Solitons in Liquid Crystals

A thesis submitted to The University of Manchester for the degree of Doctor
of Philosophy in the Faculty of Science and Engineering

2022

Yuan Shen

Department of Physics & Astronomy

Contents

Number of words: 79183
Number of pages: 231

List of Figures

List of Supplementary Figures

List of Tables

Abstract

From the ocean to the sky, from physical to biological systems, solitons are ubiquitous and have been observed in different kinds of nonlinear systems. Liquid crystals (LCs), well known for their applications in electro-optics and displays, have been broadly used as a perfect platform for studying solitons over the last five decades due to the simple fabrication and characterization of the solitons in LCs. The solitons in LCs show various structures which surprisingly resemble the ones in other physical systems ranging from nonlinear photonics to magnetic materials, particle physics to cosmology. The aim of this thesis is to explore the possibility of generating different kinds of solitons in LC systems and then better understand the physical properties of LCs and solitons in other physical systems by investigating the formation, structure and dynamic behavior of the solitons in LC systems.

In this thesis, different types of solitons are generated and investigated in different kinds of LC systems. Dissipative dynamic solitons called directrons are generated in a chiral nematic system and are compared with the ones in the achiral nematic system; Topological solitons named torons are generated in homogeneously aligned chiral nematic systems with varied pitches by applying electric fields; Dissipative solitons that characterized with a swallow-tail-like shape are generated in a smectic A LC probably for the first time. The formation and dynamics of the solitons are characterized through polarizing optical microscope and investigated in detail.

It is found that the motion of the solitons can be easily manipulated by tuning the frequency and voltage of the applied external electric field. One can also control the trajectory of the solitons through patterned surface alignment. The solitons can even be used as vehicles to trap and transport micro-cargos. At specific experimental conditions, the solitons behave like active colloidal particles and exhibit emergent collective dynamic behavior similar to their counterparts in biological systems.

This work provides a systematic experimental investigation on the formation and dynamics of different kinds of solitons in LCs, which could be helpful to better understand various nonlinear phenomena of LCs as well as different solitonic field configurations in other physical systems.

Declaration

I declare that no portion of the work referred to in the thesis has been submitted in support of an application for another degree or qualification of this or any other university or other institute of learning.

Yuan Shen

20 April 2022

Copyright Statement

1. The author of this thesis (including any appendices and/or schedules to this thesis) owns certain copyright or related rights in it (the "Copyright") and he has given The University of Manchester certain rights to use such Copyright, including for administrative purposes.

2. Copies of this thesis, either in full or in extracts and whether in hard or electronic copy, may be made only in accordance with the Copyright, Designs and Patents Act 1988 (as amended) and regulations issued under it or, where appropriate, in accordance with licensing agreements which the University has from time to time. This page must form part of any such copies made.

3. The ownership of certain Copyright, patents, designs, trademarks and other intellectual property (the "Intellectual Property") and any reproductions of copyright works in the thesis, for example graphs and tables ("Reproductions"), which may be described in this thesis, may not be owned by the author and may be owned by third parties. Such Intellectual Property and Reproductions cannot and must not be made available for use without the prior written permission of the owner(s) of the relevant Intellectual Property and/or Reproductions.

4. Further information on the conditions under which disclosure, publication and commercialisation of this thesis, the Copyright and any Intellectual Property and/or Reproductions described in it may take place is available in the University IP Policy (see http://documents.manchester.ac.uk/DocuInfo.aspx?DocID=24420), in any relevant Thesis restriction declarations deposited in the University Library, The University Library's regulations (see http://www.library.manchester.ac.uk/about/regulations/) and in The University's policy on Presentation of Theses

Acknowledgement

Firstly, I would like to thank my supervisor Ingo Dierking for his careful mentoring and constant advice and support. Without your help, I will not be able to finish my PhD study successfully. It has been a real pleasure to work with you.

Secondly, I would also like to thank the Chinese Scholarship Council and The University of Manchester for financial support. Without the support, I would not have started my PhD study in Manchester at all.

I am very grateful to my best friend Adam Draude for his support not only with my research but also in my daily life. I still remember the first day that I came to the department. I remember that I was very nervous. My English was bad at that time, but you were very kind to me and introduced me the lab and the city. I also remember the time that we went to China. Although the trip was not very successful due to the outburst of the pandemic, I will never forget it. I am also looking forward to our next trip to China.

I also would like to thank my other friends and lab members: Yizhen Shao, Mingrui Liao, Xuzhi Hu, Varun Chandrasekar, Alexandra Gruzdenko, Chunghao Chen, and Omar Aljohani.

I also acknowledge my parents and my family who always stand behind me and give me courage.

Finally, I would like to give a very special thank you to my loving partner, Rongrong Qi, who stuck with me through difficult times. Thank you for your selfless support.

List of Publications

[1] **Y. Shen** and I. Dierking, Annealing and melting of active two-dimensional soliton lattices in chiral nematic films, To be submitted.

[2] **Y. Shen** and I. Dierking, Electrically tunable collective motion of dissipative solitons in chiral nematic films, *Nature Communications*, 2022, **13**, 2122.

[3] **Y. Shen** and I. Dierking, Recent progresses on experimental investigations of topological and dissipative solitons in liquid crystals, *Crystals*, 2022, **12**, 94.

[4] M. Tayu, A. Rahmanudin, G. Perry, R. Khan, D. Tate, R. M. Hernandea, **Y. Shen**, I. Dierking, Y. Janpatompong, S. Aphichatpanichakul, A. Zamhuri, I. V. Yrezabal, M. Turner, and D. Procter, Modular synthesis of unsymmetrical [1] benzothieno [3, 2-b][1] benzothiophene molecular semiconductors for organic transistors, *Chemical Science*, 2022, **13**, 421.

[5] **Y. Shen** and I. Dierking, Electrically Driven Formation and Dynamics of Skyrmionic Solitons in Chiral Nematics, *Physical Review Applied*, 2021, **15**, 054023.

[6] **Y. Shen** and I. Dierking, Electrically driven formation and dynamics of swallow-tail solitons in smectic A liquid crystals, *Materials Advances*, 2021, **2**, 4752-4761.

[7] **Y. Shen** and I. Dierking, Annihilation dynamics of reverse tilt domains in nematic liquid crystals, *Journal of Molecular Liquids*, 2020, **313**, 113547.

[8] **Y. Shen** and I. Dierking, Dynamic dissipative solitons in nematics with positive anisotropies, *Soft Matter*, 2020, **16**, 5325.

[9] **Y. Shen** and I. Dierking, Dynamics of electrically driven solitons in nematic and cholesteric liquid crystals, *Communications Physics*, 2020, **3**, 1.

[10] **Y. Shen** and I. Dierking, Annihilation dynamics of topological defects induced by microparticles in nematic liquid crystals, *Soft Matter*, 2019, **15**, 8749.

[11] **Y. Shen** and I. Dierking, Perspectives in Liquid-Crystal-Aided Nanotechnology and Nanoscience, *Applied Sciences*, 2019, **9**, 2512.

Chapter 1

Introduction

1.1 Introduction to liquid crystals

Liquid crystals (LCs) are phases with less order than crystals but more order than liquids [1-3]. More specifically, in liquids, atoms/molecules are uniformly distributed throughout space and all directions within liquids are equivalent, i.e., isotropic. On the other hand, crystals are anisotropic. The perfect positional and orientational symmetry of liquids are broken in crystals, and atoms/molecules are distributed nonuniformly, forming certain directions, i.e., the crystalline axes, along which there are increased probabilities of finding rows of atoms/molecules [4,5]. By contrast, LCs are systems that are thermodynamically intermediate between crystals and liquids. Some phases of LCs have only orientational order, for example, the nematic phase, while others may have both orientational and positional order (only in one or two dimensions, but not in all three dimensions) such as the smectic phase. The orientational order of LCs stems from their non-spherical molecules which are usually of rod-like shape. As a result, although the LC molecules are distributed randomly in space, they tend to align in a specific direction on average, i.e. the director, **n**, which is a unit apolar vector representing the main axis of nematic order [3].

The beginning goes back to 1888, when the LC phase (named later by the Germany physicist, Otto Lehmann) was first observed in cholesterol extracted from carrots by Friedrich Reinitzer who was an Austrian botanist and chemist [6]. The discovery received great attention at that time but the interest soon dropped off due to the lack of apparent practical applications. In 1911, the first electro-optic experiment was performed and reported by C. Mauguin [7]. In 1922, three kinds of LC phases, i.e., smectic, nematic, and cholesteric, are introduced by G. Friedel [8]. In 1927, W. Freederickz and A. Repiewa reported the influence of electric and magnetic fields on the different kinds of LC phases [9]. The renaissance of LCs started in 1960s. During those years, different kinds of new electro-optical effects, such as electro-convection domains [10], ferroelectric effects [11], guest-host interactions in nematics [12],

dynamic scattering [13], etc. were rediscovered and reported by W. Richards and G. Heilmeier, et al., leading to the development of LC displays (LCDs), which are now a \$500 billion per year industry.

Nowadays, apart from being used in displays, LCs have also been broadly used in various other areas [14]. For instance, different kinds of optical devices, such as tunable diffraction gratings [15], spatial light modulators [16,17], Airy beam and vector beam generators [18], microlens [19-21], tunable wave plates [22], tunable reflectors [23-25], LC lasers [26,27], smart windows [28,29], sensors [30,31], etc., have been realized by LCs. Soft robots with different kinds of functions have been realized by LC elastomer [32-35]. Lyotropic LC composed of graphene oxide has been used to assist in the manufacture of novel three-dimensional architectures [36], such as graphene oxide membranes [37]. Chromonic lyotropic LCs have been broadly used in biophysics as an anisotropic media for studying the dynamic behavior of bacteria [38,39]. Furthermore, LCs have also been broadly used as an ideal testbed for investigating different kinds of defects [40-42] and solitons [43-45].

What follows is a short discussion of some of the fundamental physical properties of LCs. These properties are well known to the physicists in the LC community, but are worth discussing here as they will be exploited in the study of solitons in LCs which forms the main body of this thesis.

1.1.1 Nematic, cholesteric and smectic phases

The simplest LC phase is the uniaxial nematic phase as shown in Figure 1-1 (a). The centers of gravity of LC molecules in the nematic phase are arranged randomly throughout space with no long-range order, just like those in isotropic liquids [1]. However, the LC molecules in the nematic phase have a long-range orientational order. The long-axes of the molecules tend to orientate in a specific direction on average, i.e. the director, **n**.

As achiral molecules can form nematic liquid crystal phases, chiral molecules instead can form the chiral nematic phase (also known as the cholesteric phase), in which the director rotates continuously from layer to layer at a constant rate, forming a helical structure with its helical axis perpendicular to the long axes of the LC molecules (Figure 1-1 (b)). The distance over which the director rotates by 2π is called a pitch, p. One can also obtain the

cholesteric phase simply by doping chiral dopants into the nematic phase, and can control the value of the pitch by tuning the concentration, *c*, of the chiral dopant as

$$p = \frac{1}{HTP \times c},$$

(1-1)

where *HTP* represents the helical twisting power of the chiral dopant.

The LC molecules in the smectic phase not only have a long-range orientational order like the nematic phase, but also have a long-range positional order in one-dimension. The centers of gravity of LC molecules are homogeneously arranged within layers and the long-axes of the molecules are on average orientated in a specific direction with respect to the layer normal. If the director **n** is parallel to the layer normal, it is called the smectic-A phase (Figure 1-1 (c); if the director is tilted by an angle *θ* with respect to the layer normal, it is called the smectic-C phase.
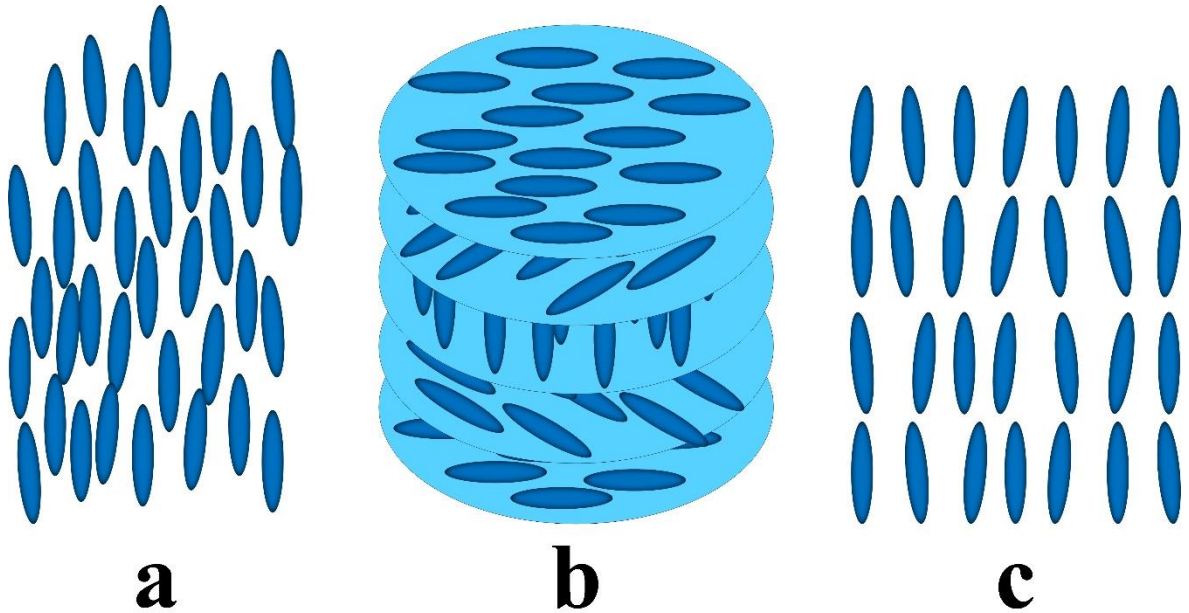
Figure 1-1 Schematic director structure of (a) the nematic phase, (b) the cholesteric phase, and (c) the smectic-A phase.

1.1.2 Nematic order parameter

Just as crystals whose positional order is described by the crystalline order parameters, the orientational order of liquid crystals can be described by the orientational order parameter. For the uniaxial nematic phase, the order parameter can be expressed by a second rank symmetric and traceless tensor *Q* as

$$Q_{ij} = S\left[\frac{3}{2}n_i n_j - \frac{1}{2}\delta_{ij}\right],$$ (1-2)

where S is the scalar order parameter which describes the amplitude of the nematic order and can be expressed by the second Legendre polynomial $P_2(u) = (3u^2-1)/2$ as

$$S = \langle P_2(\cos\theta)\rangle = \frac{1}{2}\langle 3\cos^2\theta - 1\rangle.$$ (1-3)

θ is the angle between the long axis of individual liquid crystal molecules and the director **n**. It is noted that the tensor Q_{ij} is even in **n**, which indicates **n** is apolar, i.e., $\mathbf{n} \equiv -\mathbf{n}.$ As a result, $S = 1$ if the nematic system has a perfect alignment, but vanishes ($S = 0$) in the isotropic phase due to symmetry reasons [1]. Generally, $0 < S < 1$ for typical nematic systems. The second term in equation (1-2), $[3n_i n_j - \delta_{ij}] / 2$, represents the direction of nematic order.

1.1.3 Dielectric anisotropy

The dielectric permittivity or dielectric constant, ε, represents the degree of electrical polarization of a material under an external electric field. For LCs, the dipole moment is usually orientated at an angle with the long axis of LC molecules. As a result, the dielectric permittivity can then be divided into two components: one along the long axis of the LC molecules, $\varepsilon_{\parallel}$, and the other one perpendicular to it, $\varepsilon_{\perp}$. The difference of the two components gives rise to the dielectric anisotropy

$$\Delta\varepsilon = \varepsilon_{\parallel} - \varepsilon_{\perp},$$ (1-4)

which can either be a positive value or a negative value, depending on the chemical structure of the LC molecules. The dielectric anisotropy leads to the realignment of the LCs by applying electric fields. Generally, for LCs with a positive dielectric anisotropy ($\Delta\varepsilon > 0$), the LC molecules tend to align their long axes parallel to the applied electric field. Whereas, for LCs with a negative dielectric anisotropy ($\Delta\varepsilon < 0$), the molecules tend to align their long axes perpendicular to the applied electric field.

1.1.4 Birefringence

The refractive index of LCs is dependent on the polarization and propagation direction of the incident light. In a well aligned uniaxial nematic LC, there is a special direction,

known as the "optic axis", along which there is no birefringence. For light propagating through the nematic bulk with its polarization perpendicular to the optic axis, it is governed by the ordinary refractive index n_o. On the other hand, for light that propagating with its polarization parallel to the optic axis, it is governed by the extraordinary refractive index n_e. Both n_o and n_e are related to the dielectric permittivity of the LC material in the visible range of the electromagnetic spectrum as

$$\begin{aligned} n_0 &= \sqrt{\varepsilon_\perp} \\ n_e &= \sqrt{\varepsilon_\parallel} \end{aligned} \qquad (1\text{-}5)$$

The difference of n_o and n_e gives the birefringence of the LC material as

$$\Delta n = n_e - n_o. \qquad (1\text{-}6)$$

.

1.1.5 Elasticity

LCs can be easily deformed by various factors, such as external magnetic or electric fields, surface anchoring, etc. Any deformation of the director field in the LC bulk leads to the increase of the free energy of the LC system, which can be described by the Frank free energy equation

$$F = \int d^3 r \left[\frac{1}{2} K_1 (\nabla \cdot \mathbf{n})^2 + \frac{1}{2} K_2 [\mathbf{n} \cdot (\nabla \times \mathbf{n})]^2 + \frac{1}{2} K_3 [\mathbf{n} \times (\nabla \times \mathbf{n})]^2 \right], \qquad (1\text{-}7)$$

where K_1, K_2, and K_3 are the Frank elastic constants corresponding to the splay, twist, and bend deformations (Figure 1-2). These elastic constants have dimensions of energy per length and are usually around 10^{-11} N [3].
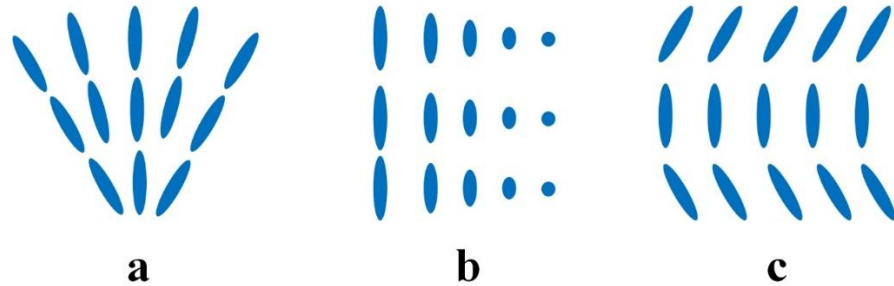
Figure 1-2 Schematic diagram for the three elastic deformations of nematic LCs. (a) Splay deformation. (b) Twist deformation. (c) Bend deformation.

1.1.6 Freedericksz transition

When an electric field **E** is applied to a nematic, due to the dielectric anisotropy of the LC system, a dielectric torque

$$\mathbf{\Gamma} = \varepsilon_0 \Delta\varepsilon \left(\mathbf{n}\cdot\mathbf{E}\right)\left(\mathbf{n}\times\mathbf{E}\right) \qquad (1\text{-}8)$$

is induced on the LC molecules, where ε_0 represents the dielectric permittivity of vacuum. If the amplitude of the applied electric field, E, is larger than a critical threshold value E_c,

$$E_c = \frac{\pi}{d}\sqrt{\frac{K_i}{\varepsilon_0 \Delta\varepsilon}}\ , \qquad (1\text{-}9)$$

where d represents the cell gap of the LC cell, this dielectric torque will overcome the elastic energy compensation and leads to a homogeneous realignment of the director field throughout the nematic system, i.e. the Freedericksz transition, named after its discoverer [1].

1.1.7 Flexoelectric effect

It is reported that a splay or bend director distortion can induce a polarization in LCs if the LC molecules have a shape polarity as well as a permanent electric dipole moment. Such a phenomenon was first described by R. B. Meyer in 1969 and was called "piezoelectric effect" [46] by him due to its similarity to the piezoelectric effect in solids. However, unlike the solids, pressure does not influence the director and cannot induce distortions and the associated polarization in nematics. As a result, such a phenomenon was later named as "flexoelectric effect" by J. Prost and P. G. De Gennes to avoid misunderstanding [1]. Later, J. Prost and J. Marcerou showed that the asymmetric molecule shape and the permanent dipole moment are not the necessary conditions for the generation of the flexoelectric effect, which can also be induced in LCs whose molecules have quadrupolar electric moments through the density gradient of the molecular quadrupolar moments [47]. As a result, one can say that the flexoelectric effect is a universal effect in LCs since almost all LC molecules have non-zero quadrupolar moments [48].
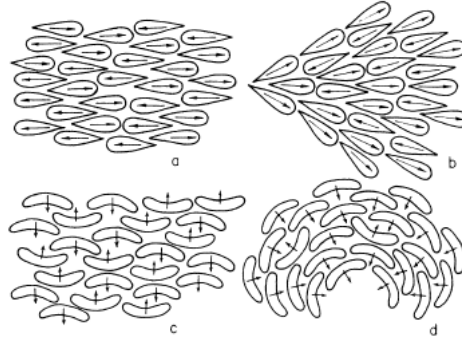
Figure 1-3 The Meyer model of flexoelectric effect in LCs. (a) and (c) The undeformed state of polar LC molecules. (b) The splay deformation of the wedge-shaped molecules induces the polarization. (d) The bend deformation of the banana-shaped molecules induces the polarization. Reproduced with permission from Ref [46]. Copyright 1969 American Physical Society.

Figure 1-3 demonstrates the physical origin of the flexoelectric effect. In the first order approximation, the flexoelectric polarization is proportional to the director deformation and can be expressed as

$$\mathbf{P}_{fl} = e_1\mathbf{n}(\nabla \cdot \mathbf{n}) + e_3(\nabla \times \mathbf{n}) \times \mathbf{n},\tag{1-10}$$

where e_1 and e_3 are the flexoelectric coefficients corresponding to splay and bend deformations, respectively [1]. In the existence of an electric field, the flexoelectric effect leads to a flexoelectric torque

$$\mathbf{\Gamma}_{fl} = \mathbf{P}_{fl} \times \mathbf{E}.\tag{1-11}$$

.

1.1.8 Electro-convections in nematics

When a nematic LC with a negative dielectric anisotropy ($\Delta\varepsilon < 0$) and a positive conductivity anisotropy ($\Delta\sigma > 0$) that is confined in a LC cell with a homogeneous alignment is applied with an electric field perpendicular to the cell substrates, a global periodic striation pattern, which is called "Williams domain", will occur at certain voltages and frequencies (Figure 1-4). At very high voltages, such a regular pattern transforms into a turbulence accompanied with intense light scattering.
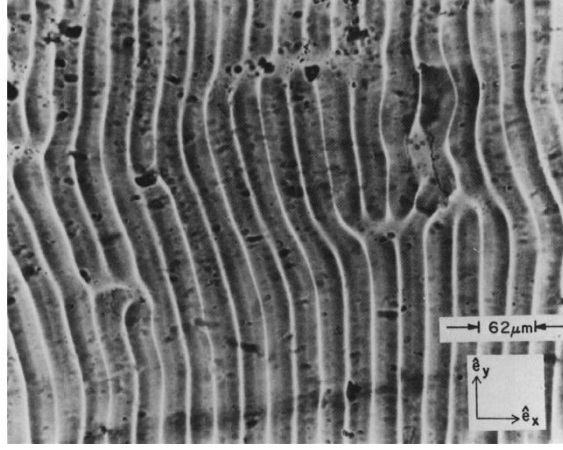
Figure 1-4 Micrograph of Williams domain. Reproduced with permission from Ref [49]. Copyright 1970 American Physical Society.

The formation of the Williams domain is due to the electro-convection effect in nematic LCs and can be well explained by the Carr-Helfrich mechanism [50,51] as demonstrated in Figure 1-5. A slab of homogeneously aligned nematic LC ($\Delta\varepsilon < 0$, $\Delta\sigma > 0$) is applied with an electric field (**E**, along the z-axis). The director, **n**, is aligned along the x-axis. The director field is slightly distorted through the bend deformation due to the thermal fluctuations. At the same time, the elastic torque and the dielectric torque tend to restore the director field. On the other hand, due to the positive conductivity anisotropy, there is a current component **J**$_t$ which moves along the x-axis and tends to accumulate a positive space charge q in the region A. The space charge gives an additional electric field. As a result, the overall electric field at point B is shifted from **E** to **E** + Δ**E**. Due to the negative dielectric anisotropy of the LC molecules, the molecules at point B tend to align perpendicular to the overall electric field, which increases the bend distortion. At the same time, the space charge is subjected to a Coulomb force **qE** which leads to a material flow. Such a flow induces a hydrodynamic torque at point B which also tends to increase the bend distortion.
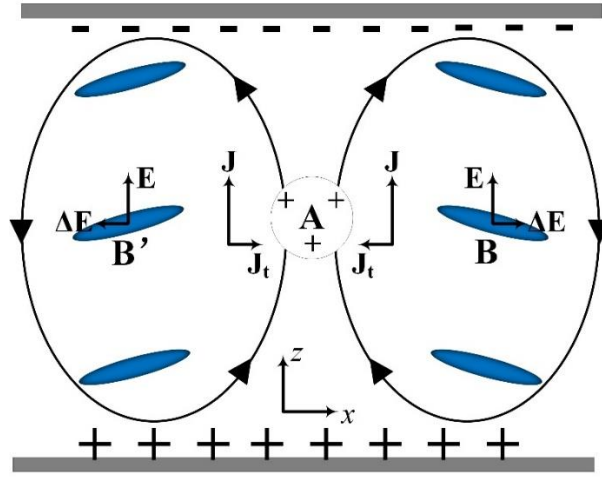
Figure 1-5 The schematic illustration of the Carr-Helfrich mechanism.

1.2 Solitons in LCs

Solitons are self-sustained localized packets of waves that propagate in nonlinear systems [44]. They can pass through each other without changing their shapes. They are ubiquitous in our daily life from water waves in rivers to storms in atmosphere. The discovery of solitons goes back to 1834 when the Scottish engineer John Scott Russell observed that "a rounded, smooth and well-defined heap of water" moved along the canal for over 2 miles without losing its identity [52]. After that, Russell named this phenomenon "the wave of translation" or "great solitary wave" [53]. He also successfully generated such waves in small water channels and derived an empirical formula $c^2 = g(h + k)$, through which he related the velocity c of the water wave with its height k above the undisturbed water surface and the undisturbed depth h [53]. Inspired by Russell's early work, in 1895, D. J. Korteweg and G. De. Vries developed an equation for the description of shallow water waves that includes both dispersive and nonlinear effects, which is now known as the Korteweg-deVries (KdV) equation and has been broadly used to describe solitary waves in nonlinear systems [54]. However, the significance of solitons was not appreciated widely until 1965 in which year the word "soliton" was coined by N. J. Zabusky and M. D. Kruskal [55] to emphasize the particle-like property of these solitary waves. Nowadays, solitons have been observed and generated in many areas of physics, including particle physics [56], Bose-Einstein condensates [57], nonlinear photonics [58], magnetic materials [59], superconductors [60],

36

and LCs [43].

1.2.1 Nematicons

Nematicons are self-focused light beams or spatial optical solitons that propagate in nematic LCs [43]. The nonlinear coefficient of nematic LC is extraordinarily large compared to many other materials, which is 10^6 to 10^{10} times larger than that of many optical materials such as CS_2, making it an ideal system for studying spatial optical solitons [43]. The first studies of this are likely the early works by E. Braun et al. in 1993 [61,62], where light beams of complicated structures, including focal light spots, transverse beam undulations, multiple beam filaments, etc. were produced by propagating a light beam through a nematic LC bulk [43]. The schematic of the generation of nematicons is shown in Figure 1-6. A light beam, whose linear polarization is parallel to the y-axis, propagates through a homogeneously aligned nematic cell along the z-axis. The wave vector ($\mathbf{k}$) of the incident light makes an angle θ with respect to the director $\mathbf{n}$. The Poynting vector $\mathbf{S}$ is deviated from the wave vector $\mathbf{k}$ at an angle of δ, along which the extraordinary waves of the light propagate. The electric field $\mathbf{E}$ of the waves is in the $\mathbf{nk}$ plane. Within the nematic, electric dipoles are induced in the nematic molecules by the beam, which interact with the electric field of the light and induce a torque Γ':

$$\Gamma' = \varepsilon_0 \Delta\varepsilon' \left(\mathbf{n} \cdot \mathbf{E} \right) \left(\mathbf{n} \times \mathbf{E} \right), \tag{1-12}$$

where $\Delta\varepsilon' = n_e^2 - n_o^2$ is the optical anisotropy, n_e and n_o are the extraordinary and ordinary refractive indices, respectively. In cases where $n_e > n_o$, director $\mathbf{n}$ is rotated towards itself by the torque Γ' and the angle θ is thus increased. As a result, the extraordinary refractive index n_e is increased

$$n_{e,\theta} = \frac{n_e n_o}{\sqrt{n_o^2 \cdot \sin^2(\theta) + n_e^2 \cdot \cos^2(\theta)}}, \tag{1-13}$$

which focuses the light and leads to the formation of a nematicon propagating along $\mathbf{S}$. Nematicons provide promising applications in nonlinear optics and photonics and have attracted great attentions. Different types of nematicons, such as vortex nematicons [63,64], have been successfully generated and investigated recently.
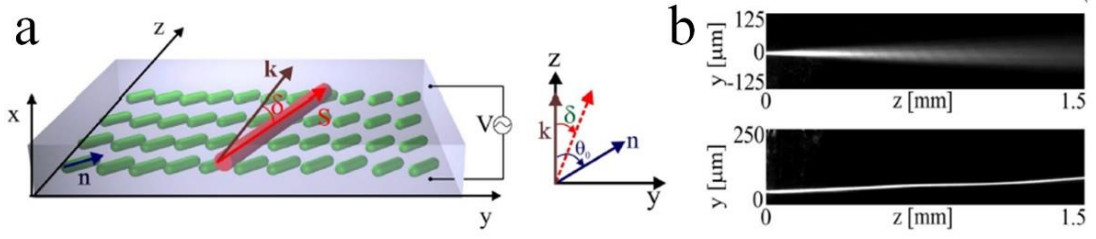
Figure 1-6 (a) Schematic of the generation of a nematicon in a nematic cell. (b) Photographs of a propagating ordinary light beam (top) and a nematicon (bottom). Reproduced with permission from Ref [65]. Copyright 2019 Optical Society of America.

1.2.2 Topological solitons

Topological solitons are topologically nontrivial field configurations embedded in a uniform far-field background that behave like particles and cannot be transformed into a uniform state through smooth deformations [66,67]. The beginning of topological solitons in LCs started about 5 decades ago with the investigations of different kinds of domain walls.

If an electric field is applied in a transverse manor to a homogenously aligned nematic with a positive dielectric anisotropy, the director can be rotated clockwise or counterclockwise to align itself parallel to the electric field. As a result, there are regions within which the director field is rotated clockwise from the perpendicular and regions where director field is rotated counterclockwise from the perpendicular. Different regions are then separated by a domain wall within which the director rotates through an angle of π [68]. Depending on the specific experimental conditions, there are three different walls, i.e., the twist wall, the splay-bend wall that parallel to the applied field and the splay-bend wall that perpendicular to the applied field. Such walls were firstly theoretically proposed by Wolfgang Helfrich in 1968 [68], and were also called planar solitons [69]. A typical example of such soliton is shown in Figure 1-7 (a), where a one-dimensional nematic twist wall is located in $\mathbb{R}^1$, which belongs to the first homotopy group, $\pi_1(\mathbb{S}^1/\mathbb{Z}_2) = \mathbb{Z}$. In the wall, the director **n** twists continuously by an angle of π, which winds around the order parameter space $\mathbb{S}^1/\mathbb{Z}_2$ once (Figure 1-7 (b)), thus giving a topological charge $|s| = 1/2$.
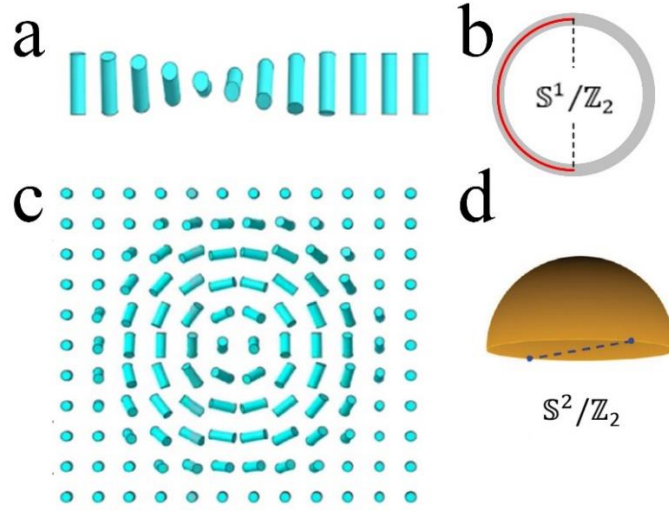
Figure 1-7 (a) Director structure of a one-dimensional nematic twist wall. (b) The order parameter space $\mathbb{S}^1/\mathbb{Z}_2$. (c) Director structure of a two-dimensional skyrmion. (d) The order parameter space $\mathbb{S}^2/\mathbb{Z}_2$.

Although the planar solitons can be stabilized easily by external fields, multidimensional topological solitons, such as particle-like three-dimensional (3D) director field configurations, in nematics are usually unstable against shrinking due to the minimization of the elastic energy [69]. Cholesteric LCs provide an ideal system for studying these high-dimensional topological solitons, whose stability is guaranteed by the helical structure of the cholesterics which maintains a fixed pitch. In this case, regions of **n** and –**n** that vary by a π rotation are separated by half of the pitch, p, of the helixes, which prevents them from getting close to each other [69,70]. Experimentally, topological solitons, such as different types of cholesteric fingers [71], baby skyrmions [72], torons [73], and hopfions [74], have been broadly observed and generated in cholesterics. Figure 1-7 (c) gives the director structure of a two-dimensional skyrmion that belongs to the second homotopy group, $\pi_2(\mathbb{S}^2/\mathbb{Z}_2) = \mathbb{Z}$. The director field of the skyrmion exhibits a π radial twist from the center to the periphery. Mapping the director field onto the order parameter space $\mathbb{S}^2/\mathbb{Z}_2$ gives the topological charge $|s| = 1$ (Figure 1-7 (d)).

1.2.3 Dissipative solitons

Dissipative solitons are localized solitary deviations of a state variable from otherwise homogeneous stable stationary background [75]. Generally, they are powered by an external

driver and disappear below a finite strength of the driver [75]. In LCs, different propagating dissipative solitary director waves driven by external fields have been reported. In many early studies, dissipative solitary director waves were induced in nematics by shearing force [76-81]. Most of these solitons are relatively large which can be observed by the naked eye, without microscopes. They can move at a constant speed over 10 cm s^{-1} through the nematic bulk in one direction (Figure 1-8 (a)).
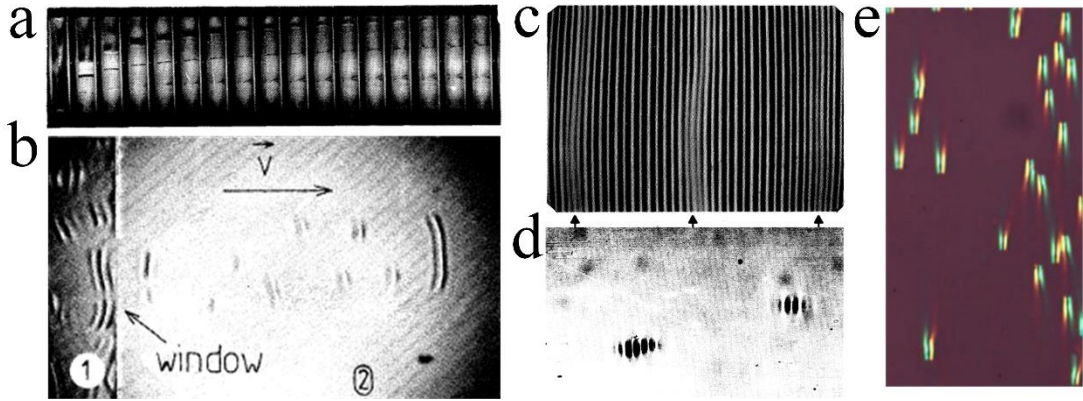
Figure 1-8 (a) Propagation of one-dimensional director waves. Reproduced with permission from Ref [77]. Copyright 1982 American Physical Society. (b) Individual convective rolls emitted from region 1 into region 2. Reproduced with permission from Ref [82]. Copyright 1979 American Physical Society. (c) Electro-convection pattern in a nematic. The solitons are indicated by black arrows at bottom. Reproduced with permission from Ref [83]. Copyright 1985 American Physical Society. (d) Localized domains of travelling convective rolls. Reproduced with permission from Ref [84]. Copyright 1988 American Physical Society. (e) Propagation of directrons. Reproduced with permission from Ref [85]. Copyright 2018 Nature.

Different dissipative solitary director waves can also be generated in LCs by applying electric fields. In 1979, R. Ribotta showed that individual connective director rolls could be induced in a nematic through electro-convection, which propagated like solitary waves from a critical zone into a subcritical zone with a uniform group velocity (Figure 1-8 (b))[82]. Later, a different kind of electrically driven soliton was reported by M. Lowe and J. P. Gollub in 1985. These solitons are called discommensurations which are regions of local compression of electro-convective rolls (Figure 1-8 (c)) [83]. In general, the electro-convection pattern composed of periodic convective rolls is stationary and spatially uniform. However, in 1988, A. Joets and R. Ribotta reported a spatially localized state of electro-convection [84]. The state is composed of elliptical localized domains of varied sizes which distribute randomly throughout the nematic bulk. Within the domains, convection rolls translate homogeneously at the same speed. But the domains do not move efficiently, instead they fluctuate around an average location (Figure 1-8 (d)). Recently, an electrically driven three-dimensional

dissipative solitary wave, called directron or director bullet, was reported by B. X. Li et al. [85,86], which has aroused great interest due to its fantastic nonlinear dynamic behavior and potential applications in nonlinear optics and micro-cargo transport. These solitons are particle-like self-confined director deformations which can propagate rapidly through the nematic bulk and survive collisions with each other (Figure 1-8 (e)). They were first reported in 1997 by H. R. Brand et al. [87], but did not receive great attention at that time probably due to the limited available techniques to characterize their structure and dynamics. The formation and dynamics of these directrons are one of the main topics of this thesis and will be introduced in details in the chapters 2 to 5.

1.3 Outline of the thesis

The scientific objective of this thesis is to investigate the formation and dynamics of different types of solitons in LC systems. For better illustration, the thesis is written in the journal format, where chapters 2 to 8 were written in the format of publications in peer-reviewed journals. Among them chapters 2, 3, 5, 6, 8 have already been published in peer-reviewed journals. Chapter 4 is ready to be submitted and chapter 7 is still in preparation. All the works are completed by myself independently with the help from my supervisor and others.

The thesis is organized as follows:

In **chapter 2**, directrons are generated in homogeneously aligned nematics as well as cholesterics by applying electric fields. The formation and dynamics of the directrons are investigated.

In **chapter 3**, hundreds and thousands of directrons are generated in a chiral nematic and their emergent collective dynamic behavior is investigated.

In **chapter 4**, the collective dynamic behavior of directrons is further investigated. Millions of directrons self-organizing into an active two-dimensional hexagonal lattice, which exhibits a non-equilibrium order-disorder transition by tuning the applied voltage.

So far the directrons have only been generated in nematics with negative dielectric anisotropy ($\Delta\varepsilon < 0$). In **chapter 5**, it shows that the directrons can also be generated in nematics with positive dielectric anisotropy ($\Delta\varepsilon > 0$). The formation, structure and dynamics

of the directrons are investigated.

In **chapter 6**, the formation and dynamics of topological solitons, called torons, are investigated in a homogeneously aligned cholesteric LC with a positive dielectric anisotropy.

In **chapter 7**, the temperature reversible transformation between torons and cholesteric fingers is investigated.

In **chapter 8**, swallow-tail solitons are generated in a smectic-A LC and their formation, structure and dynamics are investigated.

The thesis then concludes with **chapter 9**, in which open questions, opportunities and perspectives in the research field of solitons in LCs are discussed.

1.4 References

1   De Gennes, P.-G. & Prost, J. *The physics of liquid crystals (2nd Edition)*. Vol. 83 (Oxford university press, 1993).

2   Blinov, L. M. *Structure and properties of liquid crystals*. Vol. 123 (Springer Science & Business Media, 2010).

3   Selinger, J. V. *Introduction to the theory of soft matter: from ideal gases to liquid crystals*.   (Springer, 2015).

4   Borchardt-Ott, W. *Crystallography*.   (Springer Science & Business Media, 2012).

5   Powell, R. C. *Symmetry, group theory, and the physical properties of crystals*. Vol. 824 (Springer, 2010).

6   Reinitzer, F. Beiträge zur kenntniss des cholesterins. *Monatshefte für Chemie* **9**, 421-441 (1888).

7   Mauguin, C. Sur les cristaux liquides de M. Lehmann. *Bulletin de Minéralogie* **34**, 71-117 (1911).

8   Friedel, G. Les états mésomorphes de la matière. *Annales de physique* **9**, 273 (1922).

9   Fréedericksz, V. & Repiewa, A. Theoretisches und Experimentelles zur Frage nach der Natur der anisotropen Flüssigkeiten. *Zeitschrift für Physik* **42**, 532-546 (1927).

10   Williams, R. Domains in liquid crystals. *The Journal of Chemical Physics* **39**, 384-388 (1963).

11   Williams, R. & Heilmeier, G. Possible ferroelectric effects in liquid crystals and related liquids. *The Journal of Chemical Physics* **44**, 638-643 (1966).

12   Heilmeier, G. H. & Zanoni, L. guest-host interactions in nematic liquid crystals. a new electro-optic effect. *Applied Physics Letters* **13**, 91-92 (1968).

13   Heilmeier, G. H., Zanoni, L. A. & Barton, L. A. Dynamic scattering: A new electrooptic effect in certain classes of nematic liquid crystals. *Proceedings of the IEEE* **56**, 1162-1171 (1968).

14   Shen, Y. & Dierking, I. Perspectives in Liquid-Crystal-Aided Nanotechnology and Nanoscience. *Applied Sciences* **9**, 2512 (2019).

15   Shen, Y. *et al.* Photoalignment of dye-doped cholesteric liquid crystals for electrically tunable patterns with fingerprint textures. *Opt. Express* **26**, 1422-1432 (2018).

16   Varanytsia, A. & Chien, L.-C. P-134: A Spatial Light Modulator with a Two-Dimensional Array of Liquid Crystal Bubbles. *SID Symposium Digest of Technical Papers* **45**, 1492-1495 (2014).

17   Varanytsia, A. & Chien, L.-C. Photoswitchable and dye-doped bubble domain texture of cholesteric liquid crystals. *Opt. Lett.* **40**, 4392-4395 (2015).

18   Chen, P. *et al.* Chirality invertible superstructure mediated active planar optics. *Nature communications* **10** (2019).

19   Popov, P., Honaker, L. W., Mirheydari, M., Mann, E. K. & Jákli, A. Chiral nematic liquid crystal microlenses. *Scientific reports* **7**, 1-9 (2017).

20   Ma, L.-L. *et al.* Self-Assembled Asymmetric Microlenses for Four-Dimensional Visual Imaging. *ACS nano* **13**, 13709-13715 (2019).

21   Perera, K., Padmini, H. N., Mann, E. & Jákli, A. Polymer Stabilized Paraboloid Liquid Crystal Microlenses with Integrated Pancharatnam–Berry Phase. *Advanced Optical Materials*, **10**, 2101510 (2022).

22   Kragt, A. J., van Gessel, I. P., Schenning, A. P. & Broer, D. J. Temperature-Responsive Polymer Wave Plates as Tunable Polarization Converters. *Advanced Optical Materials*, **7**, 1901103 (2019).

23   Xiang, J. *et al.* Electrically Tunable Selective Reflection of Light from Ultraviolet to Visible and Infrared by Heliconical Cholesterics. *Advanced Materials* **27**, 3014-3018 (2015).

24   Lavrentovich, O. D. Electromagnetically tunable cholesterics with oblique helicoidal structure. *Opt. Mater. Express* **10**, 2415-2424 (2020).

25   Zhang, Z., Chen, Z., Wang, Y., Zhao, Y. & Shang, L. Cholesteric Cellulose Liquid Crystals with Multifunctional Structural Colors. *Advanced Functional Materials*, **32**, 2107242 (2022).

26   Xiang, J. *et al.* Electrically tunable laser based on oblique heliconical cholesteric liquid crystal. *Proceedings of the National Academy of Sciences* **113**, 12925 (2016).

27   Papič, M. *et al.* Topological liquid crystal superstructures as structured light lasers. *Proceedings of the National Academy of Sciences* **118**, 1 (2021).

28   Satapathy, P. *et al.* Switchable smart windows using a biopolymer network of cellulose nanocrystals imposed on a nematic liquid crystal. *Applied Physics Letters* **117**, 103702 (2020).

29   Jiang, Y., Shin, Y. & Yang, D.-K. Dual-Mode Switchable Liquid-Crystal Window. *Physical Review Applied* **12**, 054037 (2019).

30   Lin, I. H. *et al.* Endotoxin-Induced Structural Transformations in Liquid Crystalline Droplets. *Science* **332**, 1297 (2011).

31   Zhang, Y. P., Chodavarapu, V. P., Kirk, A. G. & Andrews, M. P. Structured color humidity indicator from reversible pitch tuning in self-assembled nanocrystalline cellulose films. *Sensors and Actuators B: Chemical* **176**, 692-697 (2013).

32   Fowler, H. E., Rothemund, P., Keplinger, C. & White, T. J. Liquid Crystal Elastomers with Enhanced Directional Actuation to Electric Fields. *Advanced Materials* **33**, 2103806 (2021).

33   Guo, Y., Zhang, J., Hu, W., Khan, M. T. A. & Sitti, M. Shape-programmable liquid crystal elastomer structures with arbitrary three-dimensional director fields and geometries. *Nature Communications* **12**, 5936 (2021).

34   Li, S. *et al.* Liquid-induced topological transformations of cellular microstructures.

Nature **592**, 386-391 (2021).

35 Li, S. *et al.* Controlling Liquid Crystal Orientations for Programmable Anisotropic Transformations in Cellular Microstructures. *Advanced Materials*, 2105024 (2021).

36 Draude, A. P. & Dierking, I. Lyotropic Liquid Crystals from Colloidal Suspensions of Graphene Oxide. *Crystals* **9**, 455 (2019).

37 Akbari, A. *et al.* Large-area graphene-based nanofiltration membranes by shear alignment of discotic nematic liquid crystals of graphene oxide. *Nature communications* **7**, 1-12 (2016).

38 Rajabi, M., Baza, H., Turiv, T. & Lavrentovich, O. D. Directional self-locomotion of active droplets enabled by nematic environment. *Nature Physics* **17**, 260-266 (2021).

39 Turiv, T. *et al.* Polar jets of swimming bacteria condensed by a patterned liquid crystal. *Nature Physics* **16**, 481-487 (2020).

40 Shen, Y. & Dierking, I. Annihilation dynamics of topological defects induced by microparticles in nematic liquid crystals. *Soft Matter* **15**, 8749 (2019).

41 Kleman, M. Defects in liquid crystals. *Reports on Progress in Physics* **52**, 555-654 (1989).

42 Chuang, I., Durrer, R., Turok, N. & Yurke, B. Cosmology in the laboratory: Defect dynamics in liquid crystals. *Science* **251**, 1336-1342 (1991).

43 Shen, Y. & Dierking, I. Recent Progresses on Experimental Investigations of Topological and Dissipative Solitons in Liquid Crystals. *Crystals* **12**, 94 (2022).

44 Lam, L. & Prost, J. *Solitons in liquid crystals*. (Springer Science & Business Media, 2012).

45 Smalyukh, I. I. knots and other new topological effects in liquid crystals and colloids. *Reports on Progress in Physics* **83**, 106601 (2020).

46 Meyer, R. B. Piezoelectric Effects in Liquid Crystals. *Physical Review Letters* **22**, 918-921 (1969).

47 Prost, J. & Marcerou, J. On the microscopic interpretation of flexoelectricity. *Journal de Physique* **38**, 315-324 (1977).

48 Chandrasekhar, S. *Liquid Crystals*. 2 edn, (Cambridge University Press, 1992).

49 Penz, P. A. Voltage-induced vorticity and optical focusing in liquid crystals. *Physical Review Letters* **24**, 1405 (1970).

50 Carr, E. F. Influence of Electric Fields on the Molecular Alignment in the Liquid Crystal p-(Anisalamino)-phenyl Acetate. *Molecular Crystals* **7**, 253-268 (1969).

51 Helfrich, W. Conduction-Induced Alignment of Nematic Liquid Crystals: Basic Model and Stability Considerations. *The Journal of Chemical Physics* **51**, 4092-4105 (1969).

52 Russell, J. S. Report on waves. *Report of the fourteenth meeting of the British Association for the Advancement of Science*, 311-390 (1844).

53 Bullough, R. Solitons. *Physics Bulletin* **29**, 78 (1978).

54 Korteweg, D. J. & De Vries, G. XLI. On the change of form of long waves advancing in a rectangular canal, and on a new type of long stationary waves. *The London, Edinburgh, and Dublin Philosophical Magazine and Journal of Science* **39**, 422-443 (1895).

55 Zabusky, N. J. & Kruskal, M. D. Interaction of "Solitons" in a Collisionless Plasma and the Recurrence of Initial States. *Physical Review Letters* **15**, 240-243 (1965).

56 Skyrme, T. H. R. A unified field theory of mesons and baryons. *Nuclear Physics* **31**,

556-569 (1962).

57 Ray, M. W., Ruokokoski, E., Kandel, S., Möttönen, M. & Hall, D. Observation of Dirac monopoles in a synthetic magnetic field. *Nature* **505**, 657-660 (2014).

58 Du, L., Yang, A., Zayats, A. V. & Yuan, X. Deep-subwavelength features of photonic skyrmions in a confined electromagnetic field with orbital angular momentum. *Nature Physics* **15**, 650-654 (2019).

59 Mühlbauer, S. *et al.* Skyrmion lattice in a chiral magnet. *Science* **323**, 915-919 (2009).

60 Blatter, G., Feigel'man, M. V., Geshkenbein, V. B., Larkin, A. I. & Vinokur, V. M. Vortices in high-temperature superconductors. *Reviews of Modern Physics* **66**, 1125 (1994).

61 Braun, E. *et al.* Filamentation and undulation of self-focused laser beams in liquid crystals. *EPL (Europhysics Letters)* **23**, 239 (1993).

62 Braun, E., Faucheux, L. P. & Libchaber, A. Strong self-focusing in nematic liquid crystals. *Physical Review A* **48**, 611 (1993).

63 Izdebskaya, Y. V., Shvedov, V. G., Jung, P. S. & Krolikowski, W. Stable vortex soliton in nonlocal media with orientational nonlinearity. *Opt. Lett.* **43**, 66-69 (2018).

64 Izdebskaya, Y., Assanto, G. & Krolikowski, W. Observation of stable-vector vortex solitons. *Opt. Lett.* **40**, 4182-4185 (2015).

65 Laudyn, U. A., Kwaśny, M., Karpierz, M. A. & Assanto, G. Electro-optic quenching of nematicon fluctuations. *Opt. Lett.* **44**, 167-170 (2019).

66 Shen, Y. & Dierking, I. Electrically Driven Formation and Dynamics of Skyrmionic Solitons in Chiral Nematics. *Physical Review Applied* **15**, 054023 (2021).

67 Manton, N. & Sutcliffe, P. *Topological solitons*. (Cambridge University Press, 2004).

68 Helfrich, W. Alignment-Inversion Walls in Nematic Liquid Crystals in the Presence of a Magnetic Field. *Physical Review Letters* **21**, 1518-1521 (1968).

69 Lavrentovich, O. D. Design of nematic liquid crystals to control microscale dynamics. *Liquid Crystals Reviews* **8**, 59-129 (2020).

70 Leonov, A. O., Dragunov, I. E., Rößler, U. K. & Bogdanov, A. N. Theory of skyrmion states in liquid crystals. *Physical Review E* **90**, 042502 (2014).

71 Baudry, J., Pirkl, S. & Oswald, P. Topological properties of singular fingers in frustrated cholesteric liquid crystals. *Physical Review E* **57**, 3038 (1998).

72 Ackerman, P. J., Trivedi, R. P., Senyuk, B., van de Lagemaat, J. & Smalyukh, I. I. Two-dimensional skyrmions and other solitonic structures in confinement-frustrated chiral nematics. *Physical Review E* **90**, 012505 (2014).

73 Smalyukh, I. I., Lansac, Y., Clark, N. A. & Trivedi, R. P. Three-dimensional structure and multistable optical switching of triple-twisted particle-like excitations in anisotropic fluids. *Nature Materials* **9**, 139 (2009).

74 Chen, B. G.-g., Ackerman, P. J., Alexander, G. P., Kamien, R. D. & Smalyukh, I. I. Generating the Hopf fibration experimentally in nematic liquid crystals. *Physical review letters* **110**, 237801 (2013).

75 Purwins, H.-G., Bödeker, H. & Amiranashvili, S. Dissipative solitons. *Advances in Physics* **59**, 485-701 (2010).

76 Cladis, P. & Torza, S. in *Hydrosols and Rheology*, 487-499 (Elsevier, 1976).

77 Guozhen, Z. Experiments on Director Waves in Nematic Liquid Crystals. *Physical Review Letters* **49**, 1332-1335 (1982).

78 Lei, L., Changqing, S., Juelian, S., Lam, P. M. & Yun, H. Soliton Propagation in

Liquid Crystals. *Physical Review Letters* **49**, 1335-1338 (1982).

79   Lei, L., Changqing, S. & Gang, X. Generation and detection of propagating solitons in shearing liquid crystals. *Journal of Statistical Physics* **39**, 633-652 (1985).

80   Shu, C. Q. *et al.* Two-dimensional axisymmetric solitons in nematic liquid crystals. *Liquid Crystals* **2**, 717-722 (1987).

81   Zheng, S. *et al.* Propagation of white ring-shaped solitons in nematic liquid crystals. *Physical Review A* **38**, 5941-5943 (1988).

82   Ribotta, R. Critical Behavior of the Penetration Length of a Vortex into a Subcritical Region. *Physical Review Letters* **42**, 1212-1215 (1979).

83   Lowe, M. & Gollub, J. P. Solitons and the commensurate-incommensurate transition in a convecting nematic fluid. *Physical Review A* **31**, 3893-3897 (1985).

84   Joets, A. & Ribotta, R. Localized, Time-Dependent State in the Convection of a Nematic Liquid Crystal. *Physical Review Letters* **60**, 2164-2167 (1988).

85   Li, B.-X. *et al.* Electrically driven three-dimensional solitary waves as director bullets in nematic liquid crystals. *Nature Communications* **9**, 2912 (2018).

86   Li, B.-X., Xiao, R.-L., Paladugu, S., Shiyanovskii, S. V. & Lavrentovich, O. D. Three-dimensional solitary waves with electrically tunable direction of propagation in nematics. *Nature Communications* **10**, 3749 (2019).

87   Brand, H. R., Fradin, C., Finn, P. L., Pesch, W. & Cladis, P. E. Electroconvection in nematic liquid crystals: comparison between experimental results and the hydrodynamic model. *Physics Letters A* **235**, 508-514 (1997).

Chapter 2

Dynamics of electrically driven solitons in nematic and cholesteric liquid crystals

Authors: Yuan Shen[1] and Ingo Dierking[1]*
[1] Department of Physics and Astronomy, School of Natural Sciences, University of Manchester, Oxford Road, Manchester, M13 9PL, United Kingdom
*Email: ingo.dierking@manchester.ac.uk

Author contributions:
Y. S. conceived and carried out the experimental investigations, analyzed the experimental results and wrote the manuscript. I. D. supervised the investigations and contributed through discussions and writing the manuscript.

Note: the format of the paper is edited. The term "directron" used to describe the solitons in the following text was named by Lavrentovich et al. in their work (B. X. Li, et al., *Phys. Rev. Res.*, 2, 013178, 2020), which was published after the publication of this work and thus was not used in the publication here in its original format. However, since the solitons in this work share the same properties of the "directrons" and to ensure the consistency of the thesis, we call these solitons "directrons" in the following text. The supplementary movies related to this work are available on the website of the journal. One can also download the movies from the figshare database: https://figshare.com/s/383c7cfb71293527fb0d.

Abstract

Investigations on solitons have been carried out for decades in various areas of physics, such as nonlinear photonics, magnetic matter and superconductors. However, producing multidimensional solitary states and manipulation of their motion are still big challenges. In this work, we describe the formation of dynamic multidimensional solitons, i.e., directrons, in a nematic and a cholesteric liquid crystal (LC). These directrons are self-confined director perturbations that propagate rapidly through the LC bulk and preserve their identities after collisions. We tune the velocity of the directrons by electric fields and control their trajectories through alignment layers. We find that the chirality of the cholesteric LC changes the interactions between the directrons and leads to a variety of fascinating dynamic behaviors which cannot be observed in the achiral nematic LC. Furthermore, we also show that these directrons can be used as vehicles for 2D delivery of micro-cargos.

2.1 Introduction

Solitons (solitary waves) are self-trapped light or matter waves that preserve their speed and shape during propagation through nonlinear media. A typical example is the soliton-like behavior of water waves observed by Russell in a shallow canal [1], which was later coined as "soliton" by Zabusky and Kruskal [2]. Since then, solitons have been brought into focus in various areas of physics, including nonlinear photonics, magnetic matter, semiconductors, superconductors, electronics, and even cosmology [3] However, in many cases, experimental observations of solitons have been reported only in effectively 1D settings [4]. It is practically important to find an efficient way to obtain stable multidimensional solitons which offer the observation of many new phenomena [5].

Liquid crystals (LCs) provide especially rich opportunities for the studies of solitons [6-8]. LCs that combine properties of isotropic liquids and crystalline solids are extremely sensitive to a variety of external stimuli, such as electric and magnetic fields, and exhibit fascinating optical behavior [9]. Studies on solitons in LCs have been carried out for over 5 decades [10]. Most early studies [11-15] were concerned with "walls" in nematics generated by magnetic fields, which actually are transition regions where the LC director smoothly

reorients by π. By rotating magnetic fields, a variety of interesting solitary waves were observed [16-18]. The coupling between director orientation and flow in a nematic LC (NLC) introduces a nonlinear term in the director equation of motion, which leads to the possible existence of solitons in a shearing NLC even without external fields [6,7,19]. Optical solitons in NLCs, called nematicons, represent self-focused, continuous wave light beams, and have received great attention in recent decades due to their promising applications in optical information technology [20,21]. Topologically structured three-dimensional (3D) solitons in the form of torons or hopfions have been experimentally created by using electric fields [22,23] or laser tweezers [24-27] in cholesteric LCs (CLCs). These solitons are basically static (although they can do squirming motions driven by electric fields [28]). They enable twist in all three spatial dimensions and are stabilized by strong energy barriers associated with nucleation of topological defects [24].

Very recently, the so-called (3+2)D solitons, i.e., directrons, where "3" refers to the 3D spatial self-confinement and "2" specifies propagation directions that are either perpendicular or parallel to the alignment direction, were observed in a NLC by Lavrentovich et al. [29,30]. These formations are nonsingular bow-like director perturbations that propagate rapidly through a slab of a uniformly aligned NLC and survive collisions with each other [30,31]. It should be noted that a similar phenomenon was earlier observed by Brand et al. [32], who reported localized formations in the shape of "butterflies" that could move in the plane of the cell. However, the dynamics and configurations of the objects were not investigated in detail in that work.

In this work, the generation of such dynamic directrons in CLCs is demonstrated. Their structure and dynamic behavior are investigated and compared with the ones in NLCs. We show that novel soliton-like features are induced by chirality. Unlike the features in NLCs reported before [29-31], the directrons in CLCs show more complex interactions that they either "pass through" each other without losing identity or collide with each other and undergo reflection. Furthermore, we show that the trajectories of their motion can be controlled by a predesignated alignment pattern allowing the realization of micro-cargo transport by directron motion.

2.2 Results

2.2.1 Generation and structure of directrons

The nematic mixture ZLI-2806 (Merck) with a negative dielectric anisotropy, $\Delta\varepsilon = \varepsilon_\parallel - \varepsilon_\perp < 0$, and a positive electric conductivity anisotropy, $\Delta\sigma = \sigma_\parallel - \sigma_\perp > 0$, is used as the soliton medium; the subscripts indicate the directions parallel and perpendicular to the director, **n**, respectively. To prepare the CLC sample, a small amount of a chiral dopant abbreviated as S811 is added to ZLI-2806. The pitch of the CLC is chosen to $P\sim 10$ μm, equal to the cell gap. Both NLC and CLC are aligned homogeneously along the alignment direction, **m** (*x*-axis), in cells with thickness $d = 10.5 \pm 0.5$ μm. A rectangular alternating current (AC) field **E** is applied to the cell perpendicular to the *xy* plane of the sample (Figure 2-1 (a)) so that the sandwich cell acts as a plate capacitor.

Independent "butterfly-like" directrons (Figure 2-1 (a)-(d)) and "bullet-like" directrons (Figure 2-1 (e)-(h)) are randomly generated in the NLC (Figure 2-2 (a)) and the CLC (Figure 2-2 (b)) samples, respectively, as the amplitude of the electric field E increases above some frequency-dependent thresholds, E_{th} (Figure 2-2 (c), (d)). In both cases the directrons move either parallel to the alignment direction, **m**, or perpendicular to it by tuning the amplitude and/or frequency of the electric fields (Figure 2-2 (e), (f), Supplementary Movie 2-1). At fixed electric field, the directrons in both the nematic and the cholesteric case preserve their shape during motion. However, when the direction of motion of the directrons changes from parallel to perpendicular to **m**, the width in the nematic case, w_N, shows a slight decrease from ~16 μm to ~13 μm, while its length l_N does not change significantly (Figure 2-1 (c) and (d)). On the other hand, in the cholesteric case, the length, l_C, increases substantially from ~6 μm to ~13 μm, while the width, w_C, shows no distinct change (Figure 2-1 (g) and (h)). The width and length of the directrons are in each case determined by the distance between the two points at which the light intensity of the directrons decreases to its half maximum, i.e., 50% in Figure 2-1 (c), (d), and 65% in Figure 2-1 (g), (h), respectively. The light intensity is defined by dividing the gray value distribution of directrons by 255. Outside the directrons, **n** in the mid-plane of samples remains parallel to the alignment direction. Inside the directrons the light intensity increases, indicating azimuthal deviations of **n** from the

initial alignment (Supplementary Figure 2-1).
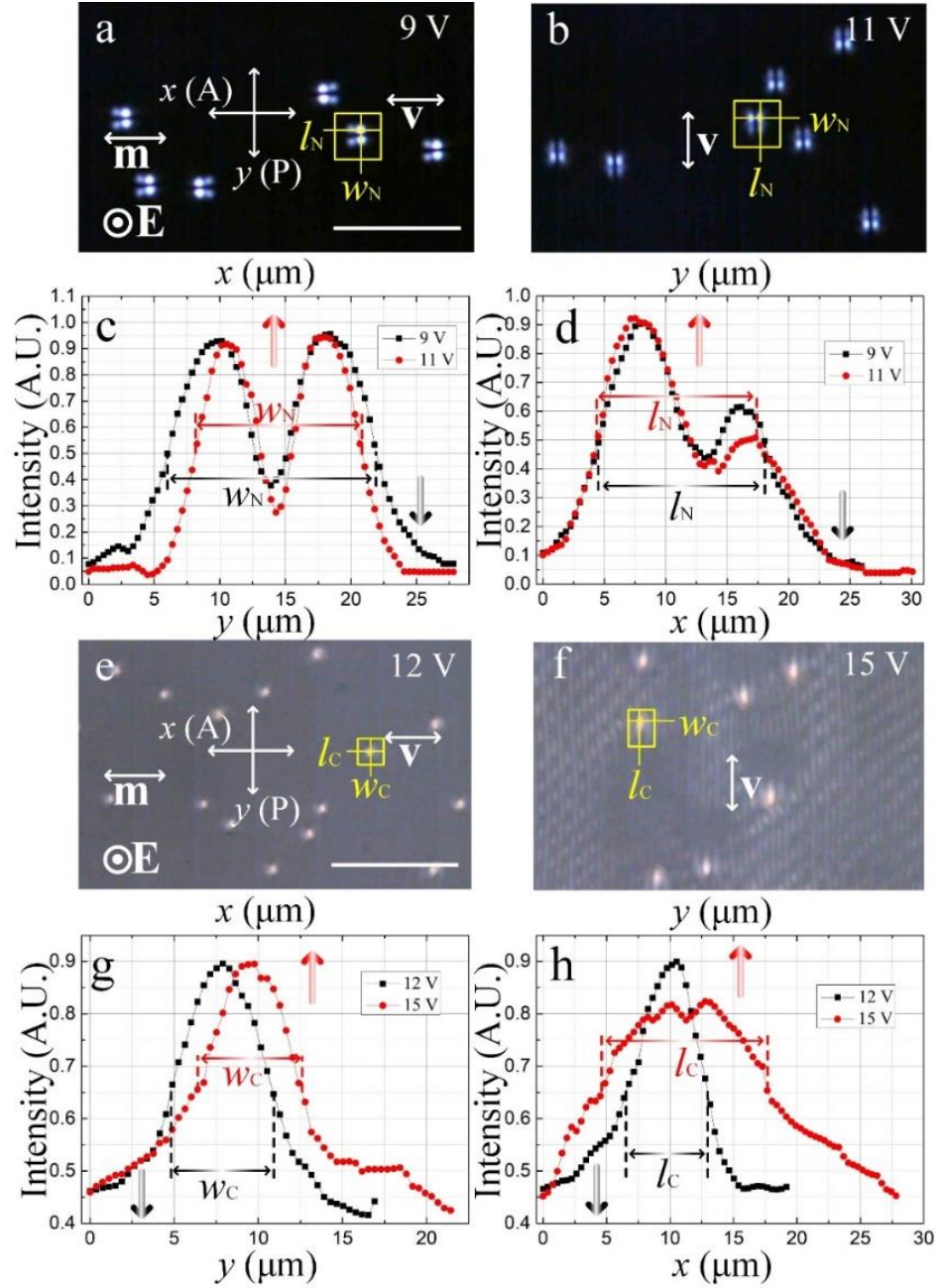
Figure 2-1 Directrons in a nematic and a cholesteric LC. Polarizing optical textures of directrons in a NLC applied with electric fields (a) 9 V, 30 Hz and (b) 11 V, 30 Hz. The widths (c) and lengths (d) of the nematic directrons. Polarizing optical textures of directrons in a CLC applied with electric fields (e) 12 V, 50 Hz and (f) 15 V, 50 Hz. The widths (g) and lengths (h) of the cholesteric directrons. The scale bars in (a) and (e) are 100 μm. **v** indicates the velocity of solitons. **m** indicates the alignment direction. The electric field **E** is perpendicular to the xy plane of the cell. A and P indicate the analyzer and polarizer, respectively. w_N, l_N, w_C, l_C represent the width and length of nematic and cholesteric directrons, respectively. The widths (c), (g) and lengths (d), (h) of the directrons are measured as the widths of the directron cross-sections normal and parallel to their velocity directions, respectively, as indicated by the yellow symbols in the corresponding polarizing optical textures.

To identify the sign of the azimuthal angle, the polarizers are decrossed with an angle β = 20 ° as shown in Supplementary Figure 2-2. By observing the directrons through a higher frame-rate at 50 fps, a periodic modulation of the light intensity is found (Supplementary Figure 2-3 and 2-4). This indicates a time-dependent oscillation of the director inside the

directrons induced by the flexoelectric effect. Such a flexoelectric effect can be further identified from the change of the light intensity transmitted through the directrons and two crossed polarizers. In Supplementary Figure 2-2, the intensity of regions 1 and 2 changes in time with the same frequency as the frequency of the AC field. The transmitted light intensity I is dependent on the angle of incidence α, the azimuthal φ and polar θ director angles in the middle plane of the sample, which can be expressed as [29,30]:

$$I \sim I_0 + \frac{4\delta^2}{\pi^2} G(\delta)\left(\varphi - \theta \tan \alpha_{LC}\right)^2, \tag{2-1}$$

where I_0 is the light intensity of the background, $\delta = 2\pi\Delta nd/\lambda \sim 4.39$ is the phase retardation of the undistorted nematic, determined by the wavelength $\lambda \sim 630$ nm, and birefringence $\Delta n = n_e - n_o \sim 0.044$ [28], n_e and n_o are the extraordinary and ordinary refractive indices, respectively. $G(\delta)$ is a slowly decaying function depends on δ. $\alpha_{LC} = \alpha/n_o$. For $\alpha = 0$, the intensity only depends on φ, the periodic change of I at $\alpha = 0$ in Supplementary Figure 2-2 (b) demonstrates that the director of the soliton experiences oscillations in the xy plane. At the same time, the director of the soliton also tilts up and down out of the xy plane by a polar angle. To demonstrate these polar oscillations, we measured I at $\alpha = 10°$. For such an oblique incidence, the polar oscillations of the director produce different intensity variations for regions 1 and 2 as shown in Supplementary Figure 2-2 (b). It should be noted that the directron in Supplementary Figure 2-2 has a mirror-symmetric structure about x-axis and y-axis and does not move efficiently. By increasing the frequency or amplitude of the field, it loses its symmetry about y-axis (Figure 2-1 (a)) or x-axis (Figure 2-1 (b)) and then moves quickly. It should be also noted that due to the limited frame rate of our camera (150 fps), to get a better intensity variation curve, the AC field applied here is a sinusoidal wave. Except here, the rest parts throughout the article are applied by rectangular wave AC fields.

The nematic directron exists in only a narrow range of amplitude and frequency of electric fields (Figure 2-2 (c)). In the range of 10-40 Hz, the texture of the nematic phase changes from a homogeneous state via a soliton state to a soliton-electrohydrodynamic (EHD) hybrid state with increasing electric field amplitude. From 40 Hz to 150 Hz, the EHD state appears ahead of the soliton state, and due to the influence of hydrodynamic flow, the motion of the directrons becomes increasingly random with higher field amplitudes and frequencies. Almost no directrons are observed when the frequency is larger than 200 Hz.

Note that it is presently unclear whether the directrons will disappear by further increasing the amplitude of electric fields in the range of 10-150 Hz, because in experiments the cells usually experience dielectric breakdown at high voltages. On the other hand, the cholesteric directrons exist in a wider range compared to their nematic counterparts (Figure 2-2 (d)). The texture of the CLC changes from a homogeneous state via a soliton state to a soliton-EHD hybrid state in the regime from 10 Hz to 800 Hz. However, when the frequency is larger than 200 Hz, the directrons do not move effectively. Instead, they oscillate locally and form chain-like structures (Supplementary Figure 2-5, Supplementary Movie 2-2). The velocity $\mathbf{v}$ of the cholesteric directrons, directed along either the x-axis or y-axis, is dependent on the amplitude and frequency of the applied electric field and increases as $v = \beta(E^2 - E_c^2)$, where $E_c(f)$ is the threshold amplitude of the applied electric field that is dependent on the frequency, $\beta \approx 90\pm10$ $\mu m^3V^{-2}s^{-1}$ (Figure 2-2 (f)). On the other hand, the amplitude of the velocity v of the nematic directrons only shows a dependence on E^2 at 30 Hz and 40 Hz, where $\beta = 72$ and 79 $\mu m^3V^{-2}s^{-1}$, respectively (Figure 2-2 (e)). At lower frequencies a saturation behavior is observed. This nonlinear dependence of the velocities of the directrons on the amplitudes of electric fields may originate from the flexoelectricity as well as the ion impurities.
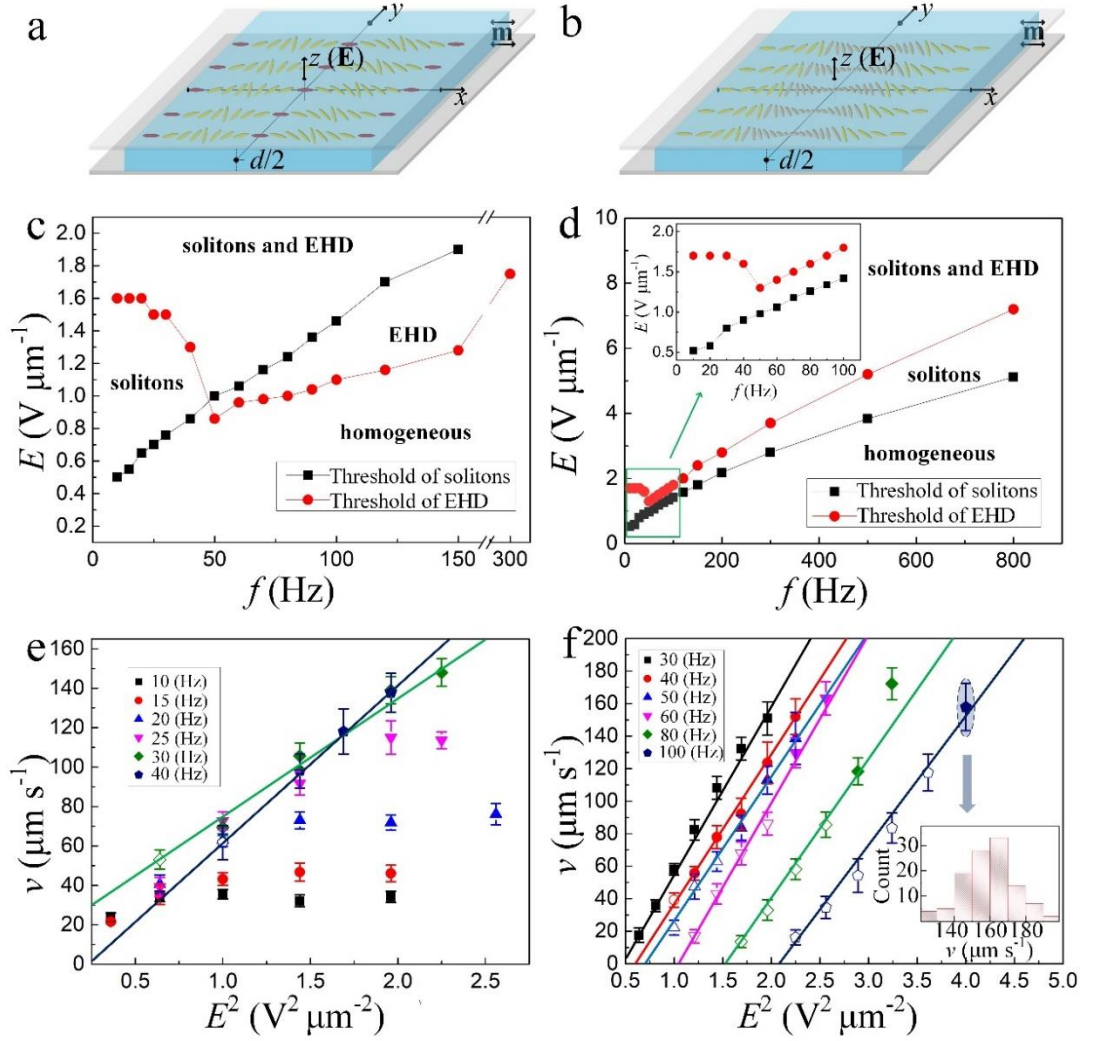
Figure 2-2 Structures of directrons and their properties as a function of the electric field. The mid-layer director configurations of directrons in the nematic (a) and the cholesteric (b) liquid crystal. **m** and **E** indicate the alignment direction and the electric field, respectively. d indicates the cell gap. Frequency dependences of thresholds of the amplitude of electric fields, E_{th}, of directrons and electrohydrodynamics (EHD) in a nematic (c) and a cholesteric liquid crystal (d), respectively. Dependences of velocities of nematic (e) and cholesteric (f) directrons on the square of the amplitude of the electric field. The solid and hollow symbols represent the velocities perpendicular and parallel to the alignment direction, respectively. The inset in (f) represents the velocity distribution of directrons at $f = 100$ Hz, $E^2 = 4$ V^2 µm^{-2}. The error bars in (e) and (f) are calculated from the standard deviation of the velocities of different directrons at the same electric fields.

According to a very recent theoretical study [33], the flexoelectric polarization of the liquid crystal is critical to the formation of the travelling directrons, and the presence of ion impurities as well as the increase of the absolute value of the conductive anisotropy will influence the travelling velocity. In addition, in ref. [31], the authors also claim that the far-field background flow may also contribute to the travelling velocity. However, in our experiments, the convective flow usually occurs at relatively high amplitudes of electric fields and we anticipate that this does not significantly contribute here. On the other hand, ionic impurities as well as flexoelectric contributions can generally not be avoided, so, in our opinion, the origin of the nonlinear travelling behavior of the directrons is most likely

54

caused by a complicated interplay between flexoelectricity and conductivity and needs further investigations to give a clear explanation.
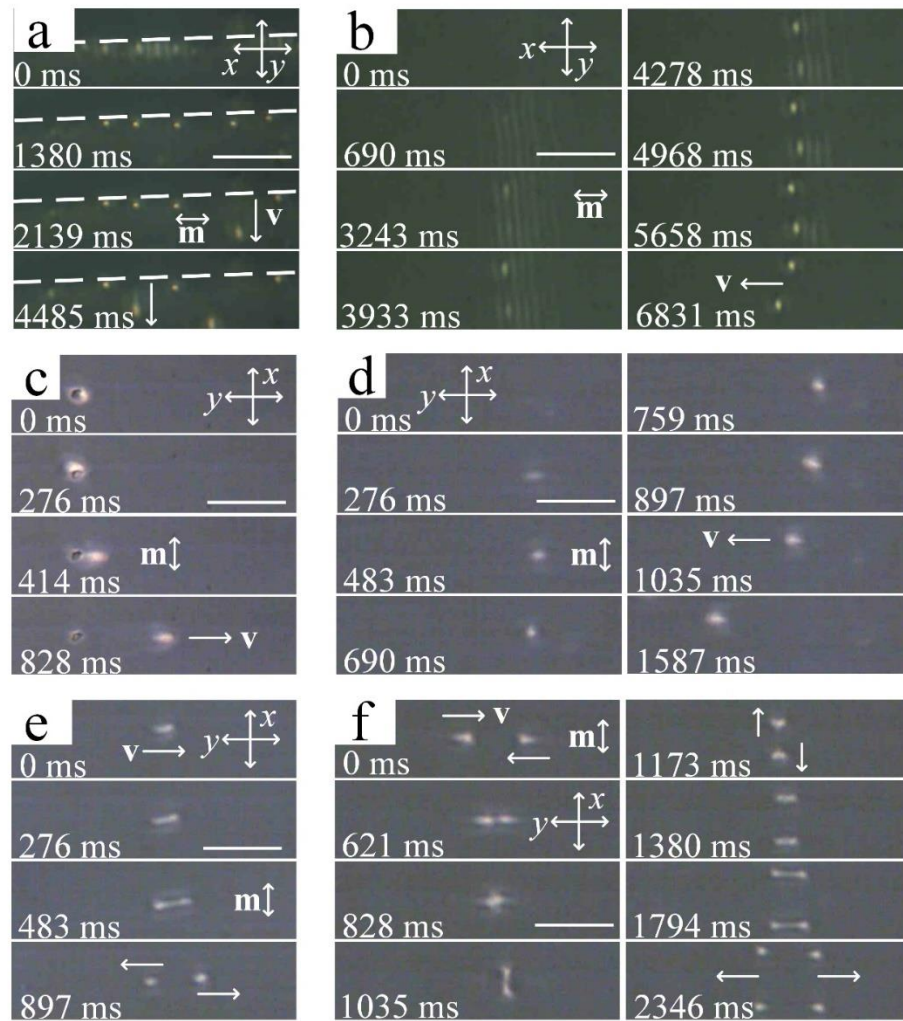
Figure 2-3 Generation of directrons in a cholesteric liquid crystal. (a) Electrode edges (marked by a dashed line) cause nucleation and reflection of directrons ($f = 40$ Hz, $E = 1.1$ V μm^{-1}). (b) Directrons may also nucleate in a local Williams domain ($f = 50$ Hz, $E = 1.1$ V μm^{-1}). Nucleation of directrons at a dust particle is shown in part (c) ($f = 40$ Hz, $E = 1.4$ V μm^{-1}), and at a site where no irregularity is observed (d) ($f = 30$ Hz, $E = 1.6$ V μm^{-1}). (e) One directron can split into two ($f = 30$ Hz, $E = 0.8$ V μm^{-1}), while (f) two directrons can collide to create two leaving directrons which in turn split again into the final four directron system ($f = 20$ Hz, $E = 0.7$ V μm^{-1}). The scale bars are 50 μm. **m** is the alignment direction and **v** indicates the velocity of the directrons. The analyzer and polarizer are parallel to the x and y axes, respectively.

Supplementary Figure 2-6 (a) and Figure 2-3 show the generation of nematic and cholesteric directrons, respectively. The directrons usually nucleate at the edges of electrodes (Supplementary Figure 2-6 (a) and Figure 2-3 (a)). Local electroconvection domains (Williams domains) can induce directrons, too, as indicated in Figure 2-3 (b). However, with the nucleation and motion of directrons, these spatially localized domains will subsequently disappear (more details of nucleation of cholesteric directrons can be found in Supplementary Movie 2-3). In addition, irregularities such as dust particles can also induce

the directrons (Supplementary Figure 2-6 and Figure 2-3 (c)). But they can also form at sites where no distinct irregularity is observed (Supplementary Figure 2-6 and Figure 2-3 (d)) which may be attributed to the localization of ions [31]. Another explanation may be the surface roughness of the indium tin oxide (ITO) electrode layer, leading locally to higher inhomogeneous electric fields. Furthermore, one cholesteric directron can even split into two or more directrons (Figure 2-3 (e)) while the collision of two cholesteric directrons may lead to the eventual creation of four (Figure 2-3 (f), Supplementary Movie 2-4). Such a proliferation phenomenon usually occurs at E_{th} and is accompanied with an elongation deformation of the directrons. During the proliferation, the directrons move slowly and obliquely, with a continuous growth of their length. When the directron length exceeds a specific value, the division occurs (Supplementary Figure 2-7).
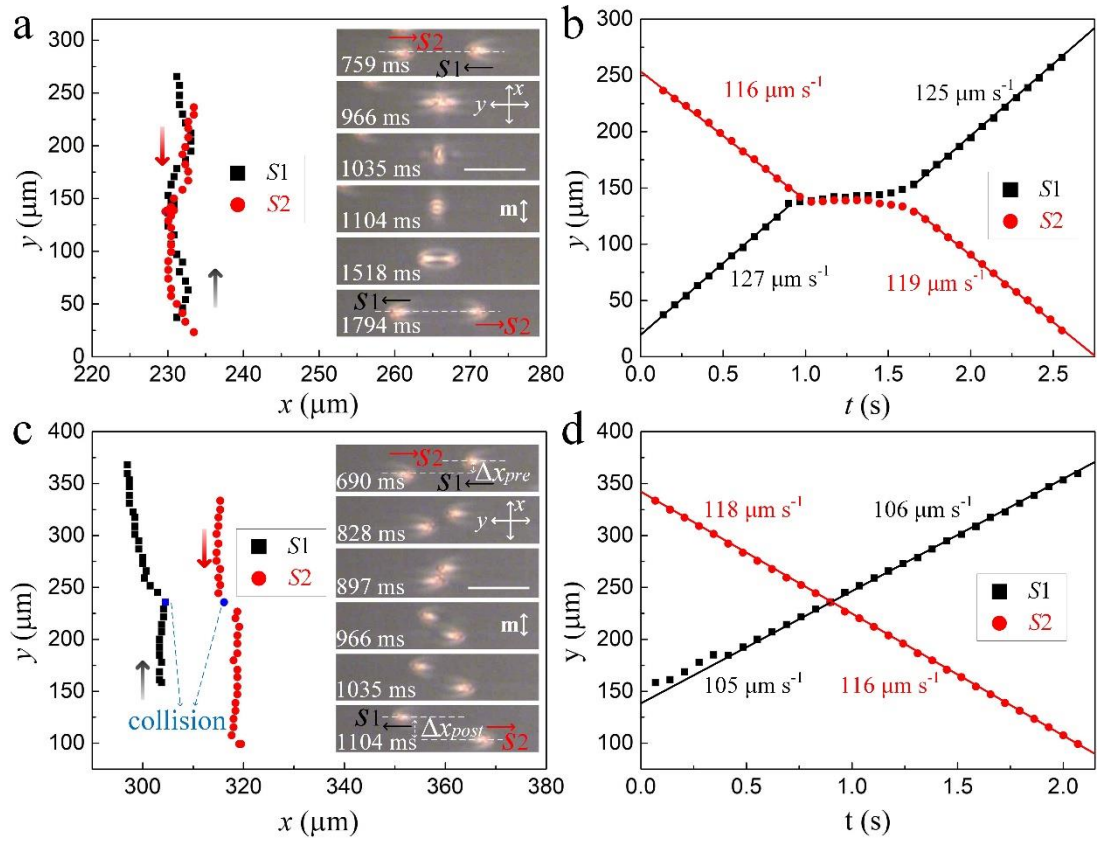
Figure 2-4 Collision behavior of cholesteric directrons. (a) and (b) show the trajectory of the collision of cholesteric directrons (s_1, s_2) in the xy-plane with offset $\Delta x_{pre} < w_C/2$ and the corresponding time dependence of the y-coordinates of the directrons, respectively. (c) and (d) show the trajectory of the collision of cholesteric directrons (s_1, s_2) in the xy-plane with offset $\Delta x_{pre} > w_C/2$ and the corresponding time dependence of the y-coordinates of the directrons, respectively. $f = 30$ Hz, $E = 1.2$ V μm^{-1}. The insets in (a) and (c) are the corresponding polarizing optical textures of the directrons, **m** indicates the alignment direction, the scale bars are 50 μm. w_C indicates the width of the cholesteric directrons. Δx_{pre} and Δx_{post} are the offsets of directrons in x-axis before and after the collision. The analyzer and polarizer are parallel to the x and y axes, respectively.

2.2.2 Collisions and interaction of directrons

In a nematic phase, two directrons moving toward each other can collide (overlap spatially and interact nonlinearly) and then "pass through" each other without losing their identity. The collision behavior is slightly different and depends on the degree of offset, Δx_{pre} (the distance between the centers of the two directrons along the x-axis) [29-31]. But the most frequent scenario is that the two directrons moving along the y-axis coalesce and form a perturbation during the collision. They then split along the x-axis, recover their structure while moving away from each other along the y-axis again at a constant velocity which may be slightly different from the velocity before the collision (Supplementary Figure 2-6). The circumstance in CLCs is more complicated. In Figure 2-4 (a), two cholesteric directrons move along the y-axis towards each other and collide. When Δx_{pre} is very small ($< 0.5w_C$), the behavior is somewhat similar to the one observed in nematics, in so far that the directrons reshape during the collision, then recover their structure and move away from each other at a constant velocity along the y-axis (Figure 2-4 (b)). The difference with regards to the collision of nematic directrons is that there is no displacement along the x-axis after coalescence, Δx_{post}, in the cholesteric case. Otherwise, if the Δx_{pre} is larger than $0.5w_C$ but smaller than w_C, the two cholesteric directrons collide and will reflect at a specific angle which is dependent on Δx_{pre} and the velocity similar to elastic particles. The directrons will then move away along the y-axis at a constant velocity (Figure 2-4 (c) and (d)). This pseudo-particle behavior may be attributed to the increased mismatch of the director field at the peripheries of the cholesteric directrons due to the helical superstructure or twist (Figure 2-2 (b)).
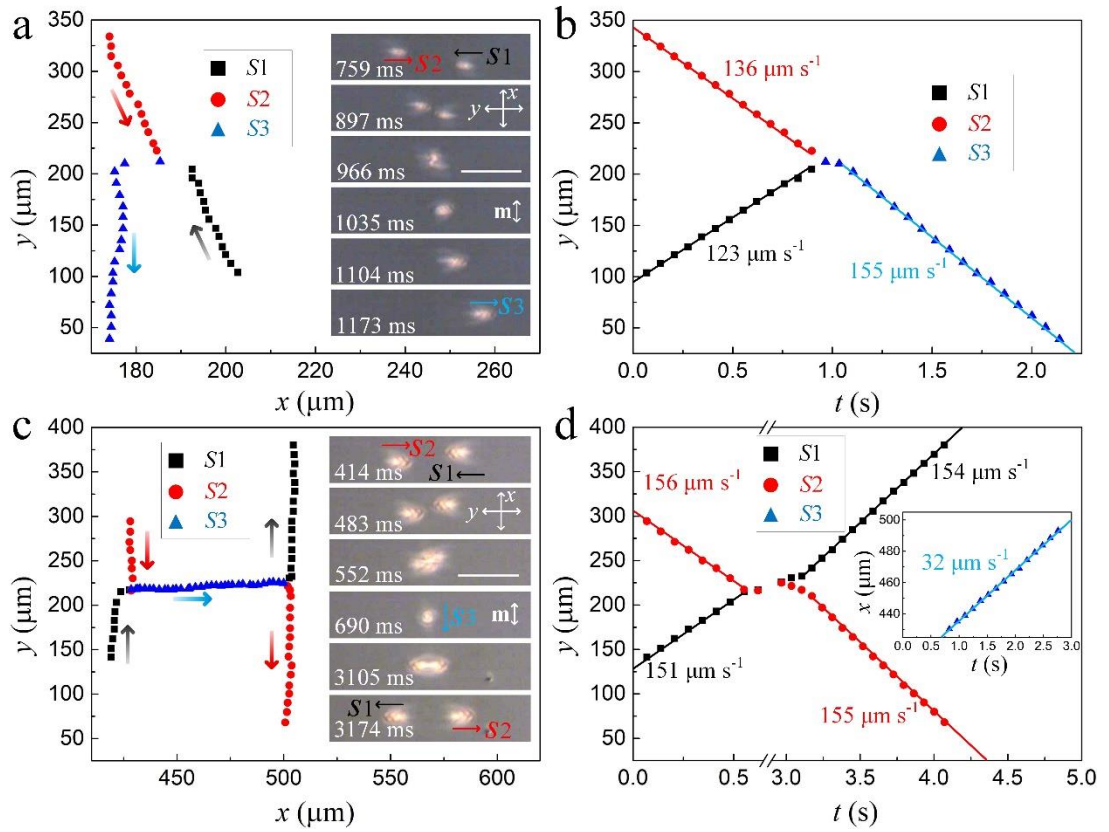
Figure 2-5 Collisions of cholesteric directrons at higher electric fields. (a) Trajectories of collision traces of cholesteric directrons (s_1, s_2, s_3) in the xy-plane (f = 40 Hz, E = 1.4 V μm^{-1}) and (b) the corresponding time dependence of the y-coordinates of the directrons. (c) Trajectories of collision traces of cholesteric directrons (s_1, s_2, s_3) in the xy-plane (f = 30 Hz, E = 1.4 V μm^{-1}) and (d) the corresponding time dependence of the y-coordinates of the directrons. The insets in (a) and (c) are the corresponding polarizing optical textures of the directrons (scale bars 50 μm. **m** indicates the alignment direction. The analyzer and polarizer are parallel to the x and y axes, respectively) The inset in (d) show the time dependence of the x-coordinate of the directron $s3$.

Further interesting phenomena occurs at higher electric fields. In Figure 2-5 (a), two cholesteric directrons are moving along the y-axis towards each other. When they collide, one directron absorbs the other and then moves away along the y-axis at a constant velocity which is slightly larger than the pre-collision velocity (Figure 2-5 (b)). In addition, at a lower frequency, upon the collision, two cholesteric directrons can merge into a single metastable one, which propagates perpendicular to its "parents" at a relatively slow speed for a short duration, and then splits into two directrons again. These then move away from each other along the initial directions (Figure 2-5 (c), (d)).

58
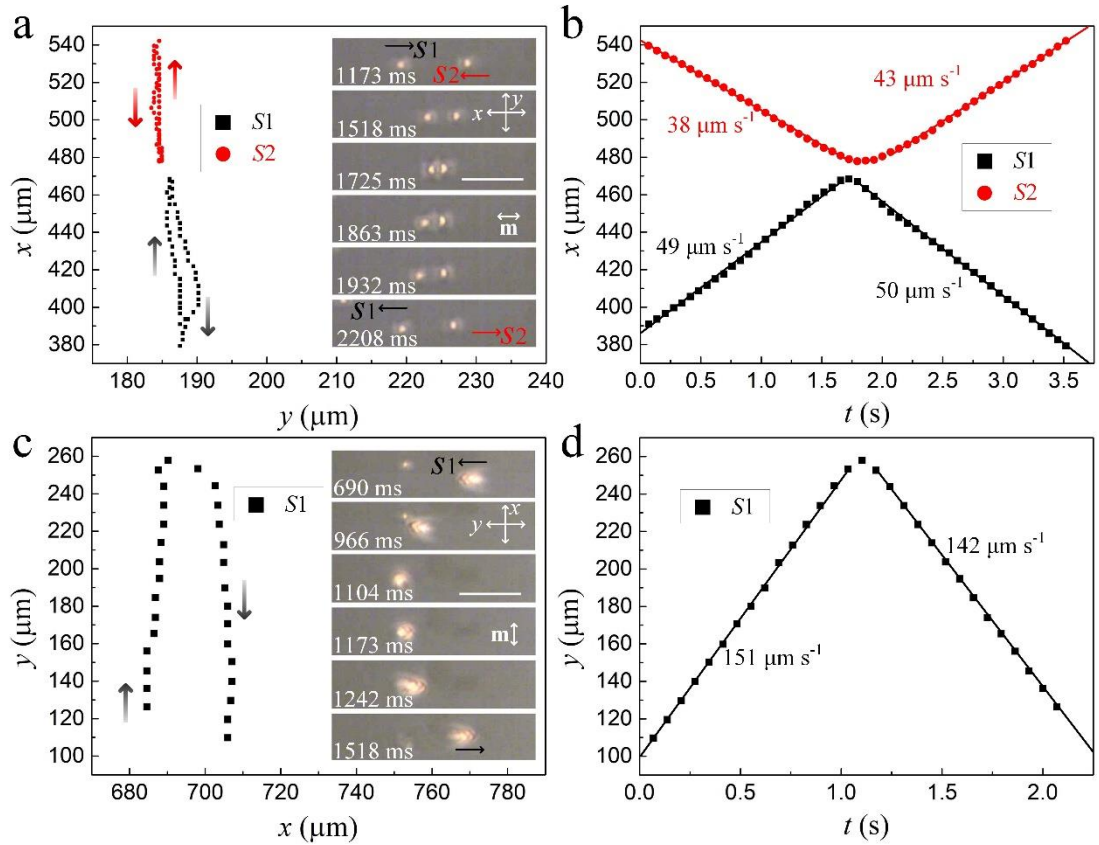
Figure 2-6 Collisions of cholesteric directrons with each other and with a dust particle. (a) The trajectory and polarizing optical textures (instes) of two directrons (s_1, s_2) colliding with each other, and (b) the corresponding time dependence of the x-coordinates of the directrons. (f = 60 Hz, E = 1.3 V μm^{-1}). (c) The trajectory and polarizing optical textures (insets) of the collision of a cholesteric directron with a dust particle, and (d) the corresponding time dependence of the y-coordinate of the directron. (f = 30 Hz, E = 1.4 V μm^{-1}). The scale bars in the insets of (a) and (c) are 50 μm. **m** indicates the alignment direction. The analyzer and polarizer are parallel to the x and y axes, respectively.

A distinguishable difference between cholesteric and nematic directrons lies in their collision behavior. When cholesteric directrons move along the alignment direction, **m**, they behave like hard body elastic particles that they cannot pass through each other. Instead, they collide with each other and then reflect into different directions (Figure 2-6 (a), (b)). Again, this phenomenon can be attributed to the increased mismatch of the director distortion along the x-axis of cholesteric directrons. Apart from the interaction between directrons introduced above, the directrons can also interact with dust particles (Figure 2-6 (c) and (d)) and the edges of electrodes (Figure 2-3 (a)). In both of these cases, the reflection of directrons is observed (more details of interactions of directrons with each other and with dust particles can be found in Supplementary Movie 2-5).

2.2.3 Photo-alignment and cargo transport

The most striking feature of the directrons is that their trajectories can be controlled not

only by electric fields, but also by the alignment layers. In Supplementary Figure 2-8, the sample is divided into three regions with different alignment directions through the photo-alignment technique [34-36]. In each region, the solitons move either parallel or perpendicular to the alignment direction, **m**, depending on the applied electric field. However, once a soliton crosses the boundaries of different regions, it will continuously change its direction to fit the alignment (Figure 2-7 (a)-(d)). Such a behavior promises a simple and viable method for manipulating directron motion, in fact along any trajectory and to any destination desired. Furthermore, it has been reported that distorted LC regions can attract colloidal particles [9,37]. Since these directrons are actually self-confined director deformations, they can even be used to transport micro-cargos. In Figure 2-7 (e), (f), a directron is induced around an impurity once the electric field is turned on, and carries the impurity moving through the bulk of the LC. When the electric field is turned off, it is found that the impurity was transported through a distance a hundred times its size in just a few seconds. More importantly, this process is repeatable and the speed and trajectory of the transport is also controllable by tuning electric fields. By combining this function with photo-alignment techniques, more sophisticated cargo transport can be realized. (More details of photo-alignment induced motions of directrons and cargo transport can be found in Supplementary Movie 2-6).
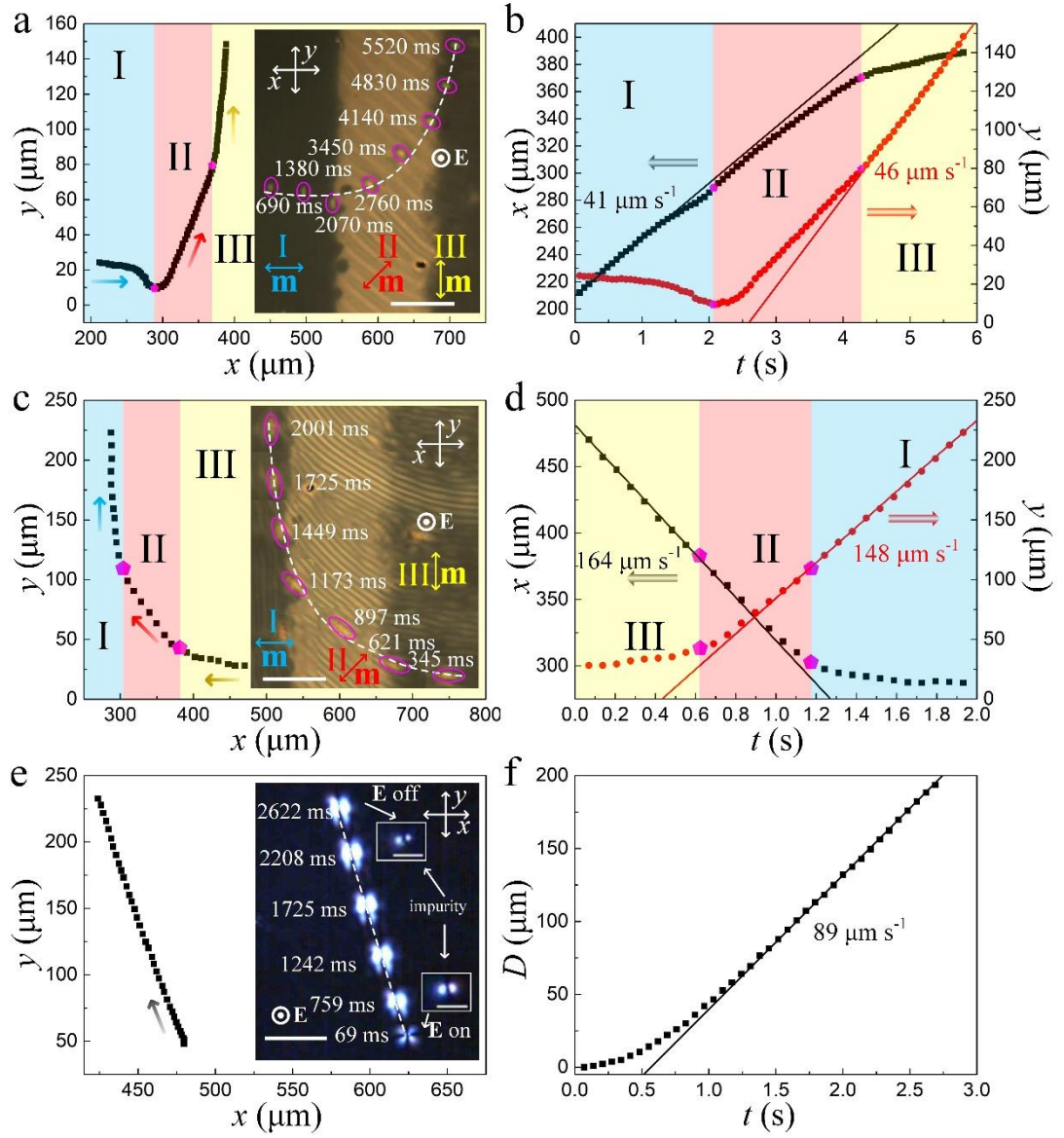
Figure 2-7 Manipulation of the trajectories of cholesteric directrons by photo-alignment and cargo-transport. (a) Trajectory of cholesteric directron in the xy-plane ($f = 40$ Hz, $E = 1.0$ V μm^{-1}) and (b) the corresponding time dependences of the x- (black) and y- (red) coordinates of the directron. (c) Trajectory of cholesteric directron in the xy-plane ($f = 40$ Hz, $E = 1.6$ V μm^{-1}) and (d) the corresponding time dependences of the x- (black) and y- (red) coordinates of the directron. Regions I, II and III are the regions in which alignment direction, **m**, is tilted with respect to the x-axis at an angle of 0°, 45°, and 90°, respectively. (e) Trajectory of the cargo (impurity, indicated in the white square in the inset. Scale bar 10 μm) carried by a nematic directron ($f = 30$ Hz, $E = 1.2$ V μm^{-1}) and (f) the corresponding time dependence of the displacement D of the cargo. The insets in (a), (c) and (e) show the corresponding optical textures of the directrons (scale bars 50 μm. The analyzer and polarizer are parallel to the x and y axes, respectively. The electric field **E** is perpendicular to the xy plane.).

2.3 Discussion

The electrically driven dynamic directrons described above represent a solitary deformation of the director field which is self-trapped in space. They can move either parallel or perpendicular to the alignment direction, depending on applied electric field conditions. In the observations through crossed polarizers, inside the directrons, the light intensity varies

spatially in the *xy* plane according to the director distribution. Along the *z* axis, the azimuthal deviation of the director field of the directrons show a parabolic-like profile, which reaches a maximum in the middle of the cell, $z = d/2$, where the boundary conditions are least influential, and diminishes at the boundary surfaces, where the anchoring is strongest, as confirmed by the observation with fluorescence confocal polarizing microscopy (FCPM) in ref. 29. The mid-plane director configuration of nematic directrons can thus be obtained by analyzing their light intensity distribution and optical textures, and the one of cholesteric directrons is deduced by adding the influence of the chirality into the achiral one as shown in Supplementary Figure 2-1. The key factor that induces the change of motion direction can be the symmetry-breaking structure of the directrons induced by the fluctuations of the director field or background flow [31]. The directrons propagating along the *x*-axis lack the symmetry with respect to the *y*-axis (Supplementary Figure 2-1 (a), (c)). And the directrons propagating along the *y*-axis lack the symmetry with respect to the *x*-axis (Supplementary Figure 2-1 (b), (d)). The formation and motion of the directrons can be attributed to the flexoelectric effect. The splay and bend of the director field leads to an induced polarization, i.e. flexo-polarization, $\mathbf{P}_f = e_1\mathbf{n}(\nabla \cdot \mathbf{n}) - e_3\mathbf{n} \times (\nabla \times \mathbf{n})$, where e_1 and e_3 are the flexoelectric coefficients. By applying an electric field, the flexo-polarization produces a flexoelectric torque on LC molecules, $\mathbf{\Gamma}_f = \mathbf{P}_f \times \mathbf{E}$. This torque is linearly dependent on $\mathbf{E}$ and induces periodic oscillations of the director. Such oscillations induced by the flexoelectric effect can be supported by their frequency-dependence behavior (Supplementary Figure 2-2 to 2-4).

Compared to the "butterfly-like" nematic directrons, which normally pass through each other during the collision (Supplementary Figure 2-4 (b)) the "bullet-like" cholesteric directrons reflect each other in collisions (Figure 2-4 (c), (d) and 2-6 (a), (b)). Such a pseudo-particle behavior is also found in the chiral samples with different pitches, 5 μm and 20 μm, representing 4π- and π-twists, in addition to the results reported here for a 2π-twist system. One may attribute this pseudo-particle behavior to the increased mismatch of the director field between cholesteric directrons due to their twist-distorted structures. On the other hand, such a particle-like behavior maybe also dependent on the velocities of the cholesteric directrons and can be tuned by the applied electric fields. At relatively low voltages, the directrons move at low speeds along the alignment direction and always collide like elastic

particles that they cannot pass through each other (Figure 2-6 (a), (b)). At relatively high voltages, the speed of the directrons increases and the directrons move perpendicular to the alignment direction. The collision between two directrons is then dependent on the degree of the offset, Δx_{pre}. When Δx_{pre} is small ($< 0.5w_C$), the directrons always (except the behaviors shown in Figure 2-5) pass through each other (Figure 2-4 (a), (b)). On the other hand, if Δx_{pre} is larger than $0.5w_C$ but smaller than w_C, the directrons will then collide like particles and reflect into different directrons (Figure 2-4 (c), (d)). However, the specific reason of this different behavior of cholesteric directrons from nematic ones is not yet clearly understood and requires further investigations.

The size of nematic directrons is mainly determined by the balance between the elastic energy, the surface anchoring and the sample thickness [31]. But in the case of the cholesteric directrons, this also depends on the pitch of the CLC. At the same conditions, the larger the pitch, the larger the directrons (Supplementary Figure 2-9 and 2-10). Besides, in the case of the $P = 10$ μm CLC, the directrons change from a motion parallel to one perpendicular to the alignment direction by increasing the applied voltage, Figure 2-1 (e), (f). This situation is opposite in the case of a $P = 20$ μm CLC, where the directrons move perpendicular to the alignment direction at low voltages but move parallel to the alignment direction at high voltages (Supplementary Figure 2-9 (a), (b)). Such a behavior is attributed to the $\pi/2$ rotation of the director field in the middle layer of the samples. As confirmed by fluorescent signal measurement [19], the structure of directrons is mainly located in the middle bulk of the sample. The increase of pitch from 10 μm to 20 μm in a $d = 10$ μm cell induces a $\pi/2$ rotation of the mid-plane director, i.e. the director field in the middle layer of the CLC with $P = 10$ μm is aligned parallel to the alignment direction but the director field in the middle layer of the CLC with $P = 20$ μm is aligned perpendicular to the alignment direction. Such a $\pi/2$ rotation of the mid-plane director leads to a $\pi/2$ rotation of the directron propagation direction. However, the situation becomes different in the case of the $P = 5$ μm CLC. The structure of the directron is distorted into a "spider-like" shape as indicated in the inset of Supplementary Figure 2-9 (f), and they move randomly without preferred direction. Interestingly, it is found that the directrons absorb "baby directrons" (small bright dots which vibrate locally) and switch their directions subsequently, leading to the irregular motion (Supplementary Movie 2-7). Such a random motion of directrons maybe attributed to the small pitch of the CLC and

warrants further investigations. Furthermore, the dependencies of E_{th} on frequency in all three CLC systems of varying pitch are similar to each other (Figure 2-2 (d), Supplementary Figure 2-11).

Previous studies have shown that the generation of the directrons is due to flexoelectric polarization and is dependent on the dielectric and conductive properties of LC [29-31]. Generally, according to de Gennes [38], the combination of dielectric properties and conductivity can be classified as (+ +), (+ -), (- -) and (- +), where the plus and minus symbols represent the sign of the dielectric ($\Delta\varepsilon$) and conductivity ($\Delta\sigma$) anisotropies, respectively. In the experiment, directrons are observed in a (- +) LC in the range where electro-convective patterns are normally observed. This is attributed to the moderately low conductivity anisotropy ~1.3×10^{-8} $\Omega^{-1}m^{-1}$ of our sample, which is much smaller than the ones usually reported in most studies of electro-convection in (- +) nematics [39,40]. The significance of this small conductivity anisotropy can be understood by considering the coupling between the electric field **E** and the space charge Q. According to the classic Carr-Helfrich electro-convection mechanism [41,42], the positive conductivity anisotropy and the bend fluctuation in a NLC induces ion segregation and forms Qs which are high and uniformly distributed in space. These Qs produce transverse Coulomb forces which offset the normal elastic and dielectric torques and cause instability, usually in the form of space-filling periodic stripes. However, due to the relatively low conductivity of our samples, there is not sufficient charge accumulation to produce a strong enough dielectric torque to induce a uniform electro-convective effect. Instead, independent solitary structures form at the localization of ions due to the flexoelectric effect [31]. However, once the applied electric field amplitude is large enough, a uniform electro-convection accompanied with directrons can be observed.

2.4 Conclusion

In conclusion, we demonstrate the structure, generation and dynamic behavior of directrons in CLCs and compare them with the ones generated in NLCs. Compared to nematic directrons, cholesteric directrons show more complicated interactions during pair-wise collisions. The helical superstructure (twist) increases the incompatibility between cholesteric directrons and makes them either pass through or reflect each other during

collisions. The speed and propagation direction of the directrons can be tuned by electric fields, and their trajectories can be predesignated through photo-alignment. Our work not only provides a feasible method for generating and controlling multidimensional solitons, but also shows that these solitons can be used for targeted 2D delivery of micro-cargos.

2.5 Materials and methods

Materials. A commercial nematic LC mixture, ZLI-2806 (Merck), was used. Chiral samples with pitches, $P = 5$ μm, 10 μm, and 20 μm, were obtained by doping different concentrations of a chiral dopant S811 (ZLI-811) (Xianhua, China) with a helical twisting power of HTP=-8.3 μm^{-1} [43] into ZLI-2806. The concentrations of S811 were 2.4 wt%, 1.2 wt%, and 0.6 wt%, respectively. For the photo-alignment process, a 0.3% solution of sulfonic azo dye SD1 (Dai-Nippon Ink and Chemicals, Japan) in dimethylformamide (DMF) was used [35]. The components of dielectric permittivity and conductivity of ZLI-2806 are $\varepsilon_\parallel = 3.0$, $\varepsilon_\perp = 7.6$, $\sigma_\parallel = 1.9 \times 10^{-8} \Omega^{-1} m^{-1}$, $\sigma_\perp = 6 \times 10^{-9} \Omega^{-1} m^{-1}$, respectively, at 4 kHz and room temperature, measured by use of an LCR meter E4980A (Agilent) using commercial cells with planar and homeotropic alignment, respectively.

Sample preparation. The cell is composed of two glass substrates coated with ITO. The glass substrates were first ultrasonically bathed, plasma cleaned, and then spin-coated with SD1. Afterwards, the empty cell was illuminated by polarized Ultraviolet (UV) light of wavelength λ = 395 nm. Cells were filled by capillary action of either the NLC or the CLC being heated to 80 °C.

Generation of solitons. The sample was kept at 80 °C on a hot stage (LTSE350, Linkam) controlled by a controller (TP 94, Linkam). The AC voltage is applied using a waveform generator (33220A, Agilent) and a home-built amplifier.

Optical characterization. The sample was observed through a polarizing microscope (Leica OPTIPOL) equipped with a digital camera (UI-3360CP-C-HQ, uEye Gigabit Ethernet) with tunable frame rate from 14.43 fps to 50 fps. The velocity and light intensity distribution of solitons were analyzed by an open-source software ImageJ and its plugin TrackMate.

2.6 Acknowledgements

2.7 References

1   Dauxois, T. & Peyrard, M. *Physics of solitons*. (Cambridge University Press, Cambridge, 2006).

2   Zabusky, N. J. & Kruskal, M. D. Interaction of "Solitons" in a Collisionless Plasma and the Recurrence of Initial States. *Physical Review Letters* **15**, 240-243 (1965).

3   Kartashov, Y. V., Astrakharchik, G. E., Malomed, B. A. & Torner, L. Frontiers in multidimensional self-trapping of nonlinear fields and matter. *Nature Reviews Physics* **1**, 185-197 (2019).

4   Malomed, B. A., Mihalache, D., Wise, F. & Torner, L. Spatiotemporal optical solitons. *Journal of Optics B: Quantum and Semiclassical Optics* **7**, R53 (2005).

5   Malomed, B., Torner Sabata, L., Wise, F. & Mihalache, D. On multidimensional solitons and their legacy in contemporary atomic, molecular and optical physics. *Journal of Physics B: Atomic, Molecular and Optical Physics* **49**, 170502 (2016).

6   Lei, L., Changqing, S., Juelian, S., Lam, P. M. & Yun, H. Soliton Propagation in Liquid Crystals. *Physical Review Letters* **49**, 1335-1338 (1982).

7   Lei, L., Changqing, S. & Gang, X. Generation and detection of propagating solitons in shearing liquid crystals. *Journal of Statistical Physics* **39**, 633-652 (1985).

8   Lam, L. Solitons in liquid crystals: Recent developments. *Chaos, Solitons & Fractals* **5**, 2463-2473 (1995).

9   Shen, Y. & Dierking, I. Perspectives in Liquid-Crystal-Aided Nanotechnology and Nanoscience. *Applied Sciences*, **9**, 2512 (2019).

10   Lam, L. & Prost, J. *Solitons in liquid crystals*. (Springer Science & Business Media, New York, 2012).

11   Helfrich, W. Alignment-Inversion Walls in Nematic Liquid Crystals in the Presence of a Magnetic Field. *Physical Review Letters* **21**, 1518-1521 (1968).

12   Leger, L. Observation of wall motions in nematics. *Solid State Communications* **10**, 697-700 (1972).

13   Leger, L. Static and dynamic behaviour of walls in nematics above a Freedericks transition. *Solid State Communications* **11**, 1499-1501 (1972).

14   Léger, L. Walls in Nematics. *Molecular Crystals and Liquid Crystals* **24**, 33-44 (1973).

15   Turner, R. Twist walls in nematic liquid crystals. *The Philosophical Magazine: A Journal of Theoretical Experimental and Applied Physics* **30**, 13-20 (1974).

16   Migler, K. B. & Meyer, R. B. Solitons and pattern formation in liquid crystals in a rotating magnetic field. *Physical Review Letters* **66**, 1485-1488 (1991).

17   Frisch, T., Rica, S., Coullet, P. & Gilli, J. M. Spiral waves in liquid crystal. *Physical Review Letters* **72**, 1471-1474 (1994).

18   Zheng, C. & Meyer, R. B. Thickness effects on pattern formation in liquid crystals in a rotating magnetic field. *Physical Review E* **55**, 2882-2887 (1997).

19   Guozhen, Z. Experiments on Director Waves in Nematic Liquid Crystals. *Physical Review Letters* **49**, 1332-1335 (1982).

20   Peccianti, M. & Assanto, G. Nematicons. *Physics Reports* **516**, 147-208 (2012).

21   Assanto, G. *Nematicons: Spatial Optical Solitons in Nematic Liquid Crystals*. Vol. 74 (John Wiley & Sons, Hoboken, 2012).

22   Haas, W. E. L. & Adams, J. E. Electrically variable diffraction in spherulitic liquid crystals. *Applied Physics Letters* **25**, 263-264 (1974).

23   Kawachi, M., Kogure, O. & Kato, Y. Bubble domain texture of a liquid crystal. *Japanese Journal of Applied Physics* **13**, 1457 (1974).

24   Smalyukh, I. I., Lansac, Y., Clark, N. A. & Trivedi, R. P. Three-dimensional structure and multistable optical switching of triple-twisted particle-like excitations in anisotropic fluids. *Nature Materials* **9**, 139 (2009).

25   Ackerman, P. J., van de Lagemaat, J. & Smalyukh, I. I. Self-assembly and electrostriction of arrays and chains of hopfion particles in chiral liquid crystals. *Nature Communications* **6**, 6012 (2015).

26   Ackerman, P. J. & Smalyukh, I. I. Diversity of Knot Solitons in Liquid Crystals Manifested by Linking of Preimages in Torons and Hopfions. *Physical Review X* **7**, 011006 (2017).

27   Foster, D. *et al.* Two-dimensional skyrmion bags in liquid crystals and ferromagnets. *Nature Physics* **15**, 655-659 (2019).

28   Ackerman, P. J., Boyle, T. & Smalyukh, I. I. Squirming motion of baby skyrmions in nematic fluids. *Nature Communications* **8**, 673 (2017).

29   Li, B.-X. *et al.* Electrically driven three-dimensional solitary waves as director bullets in nematic liquid crystals. *Nature Communications* **9**, 2912 (2018).

30   Li, B.-X., Xiao, R.-L., Paladugu, S., Shiyanovskii, S. V. & Lavrentovich, O. D. Three-dimensional solitary waves with electrically tunable direction of propagation in nematics. Nature Communications **10**, 3749 (2019).

31   Aya, S. & Araoka, F. Kinetics of motile solitons in fluid nematics. *arXiv preprint arXiv:1908.00316* (2019).

32   Brand, H. R., Fradin, C., Finn, P. L., Pesch, W. & Cladis, P. E. Electroconvection in nematic liquid crystals: comparison between experimental results and the hydrodynamic model. *Physics Letters A* **235**, 508-514 (1997).

33   Calderer, M.-C. & Earls, A. Three-dimensional solitons in nematic liquid crystals: Linear analysis. *arXiv preprint arXiv:1910.05959* (2019).

34   Li, S.-S. *et al.* Dynamic cholesteric liquid crystal superstructures photoaligned by one-step polarization holography. *Applied Physics Letters* **111**, 231109 (2017).

35   Shen, Y. *et al.* Photoalignment of dye-doped cholesteric liquid crystals for electrically tunable patterns with fingerprint textures. *Opt. Express* **26**, 1422-1432 (2018).

36   Ma, L.-L. *et al.* Rationally Designed Dynamic Superstructures Enabled by Photoaligning Cholesteric Liquid Crystals. *Advanced Optical Materials* **3**, 1691-

1696 (2015).

37   Shen, Y. et al. Annihilation dynamics of topological defects induced by microparticles in nematic liquid crystals. *Soft Matter* **15(43)**, 8749-8757 (2019).

38   De Gennes, P.-G. & Prost, J. *The physics of liquid crystals*. (Oxford university press, 1995).

39   Smith, I., Galerne, Y., Lagerwall, S., Dubois-Violette, E. & Durand, G. Dynamics of electrohydrodynamic instabilities in nematic liquid crystals. *Le Journal de Physique Colloques* **36**, C1-237-C231-259 (1975).

40   Huh, J.-H., Akasako, Y. & Kai, S. New characteristics of electrohydrodynamic instability in a nematic liquid crystal doped with a cholesteric one. *Journal of the Physical Society of Japan* **73**, 2975-2978 (2004).

41   Carr, E. F. Influence of Electric Fields on the Molecular Alignment in the Liquid Crystal p-(Anisalamino)-phenyl Acetate. *Molecular Crystals* **7**, 253-268 (1969).

42   Helfrich, W. Conduction-Induced Alignment of Nematic Liquid Crystals: Basic Model and Stability Considerations. *The Journal of Chemical Physics* **51**, 4092-4105 (1969).

43   Sohn, H. R. O. *et al.* Dynamics of topological solitons, knotted streamlines, and transport of cargo in liquid crystals. *Physical Review E* **97**, 052701 (2018).

2.8 Supplementary Information

2.8.1 Supplementary Figures:
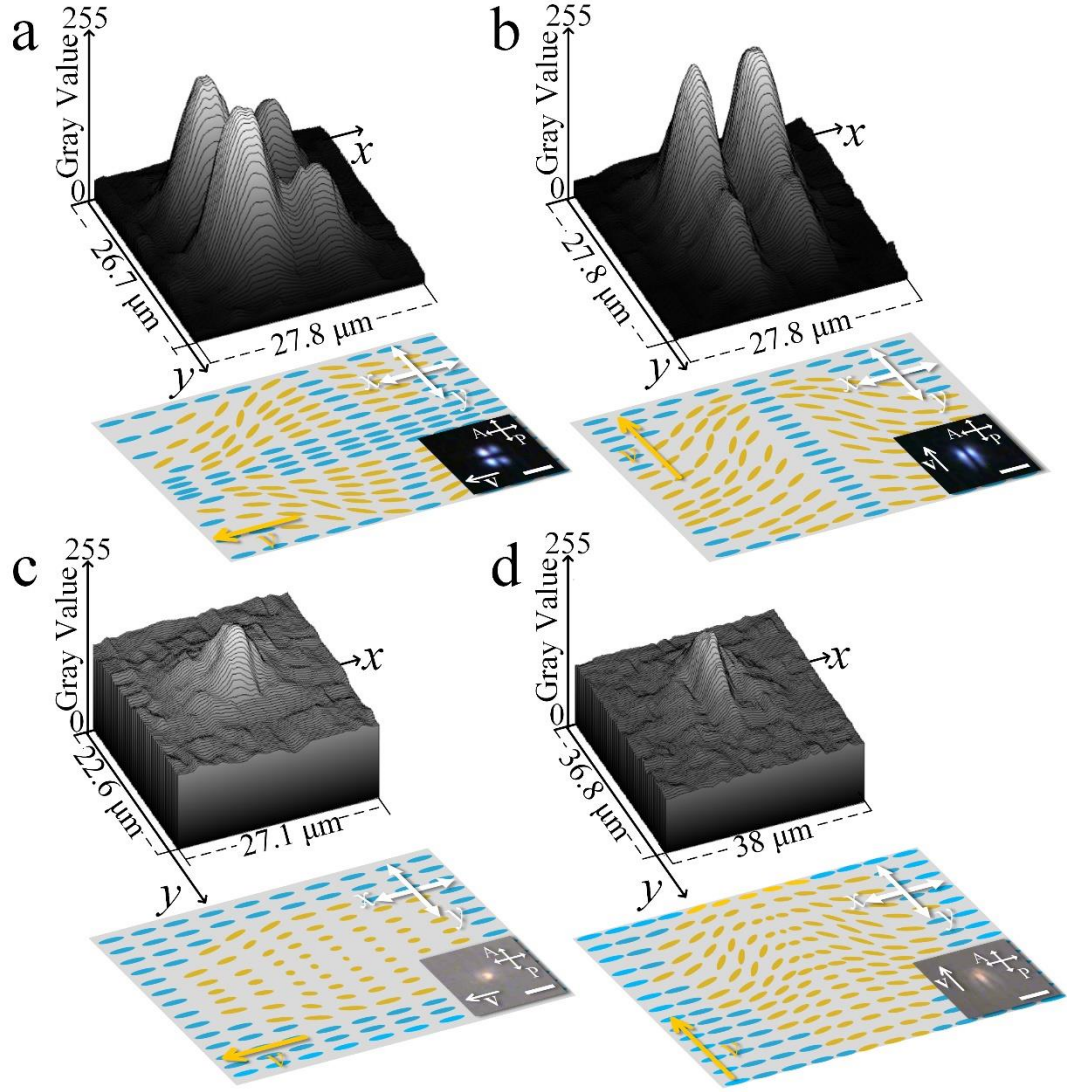
Supplementary Figure 2-1 Gray value distributions and corresponding mid-layer director configurations of nematic and cholesteric directrons. Nematic directrons that move along the x-axis (a) ($f = 30$ Hz, $E = 0.8$ V μm^{-1}) and along the y-axis (b) ($f = 30$ Hz, $E = 1.1$ V μm^{-1}) respectively. Cholesteric directrons that move along the x-axis (c) ($f = 60$ Hz, $E = 1.4$ V μm^{-1}) and along the y-axis (d) ($f = 30$ Hz, $E = 1.1$ V μm^{-1}), respectively. The insets show the polarizing optical texture of directrons. The scale bars in the insets are 20 μm. A and P indicate the analyzer and the polarizer. **v** indicates the velocity of the directrons.
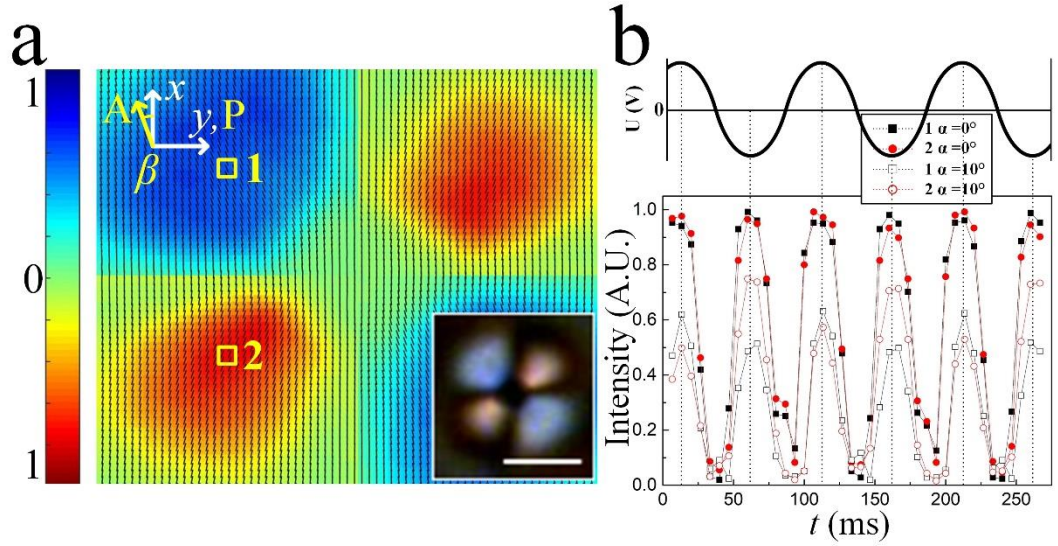
Supplementary Figure 2-2 Nematic directron driven by a low frequency electric field. (a) Transmitted light intensity map and mid-layer director distortions in the xy plane within a nematic directron. The color bar shows a linear scale of transmitted light intensity. A and P indicate the analyzer and the polarizer. The inset shows the optical texture of the corresponding nematic directron observed through polarizers that are decrossed with an angle $\beta = 20\,°$. The scale bar is 10 μm.(b) Dynamics of the transmitted light intensity at regions 1 and 2 indicated in (a) for normal, $\alpha = 0°$ and oblique, $\alpha = 10°$ incidence of light. The intensity is obtained by dividing the gray value by 255. $E = 1.5\ \mathrm{V\ \mu m^{-1}}$, $f = 10$ Hz, sinusoidal wave. $\beta = 20\,°$ in (a) and $0\,°$ in (b).
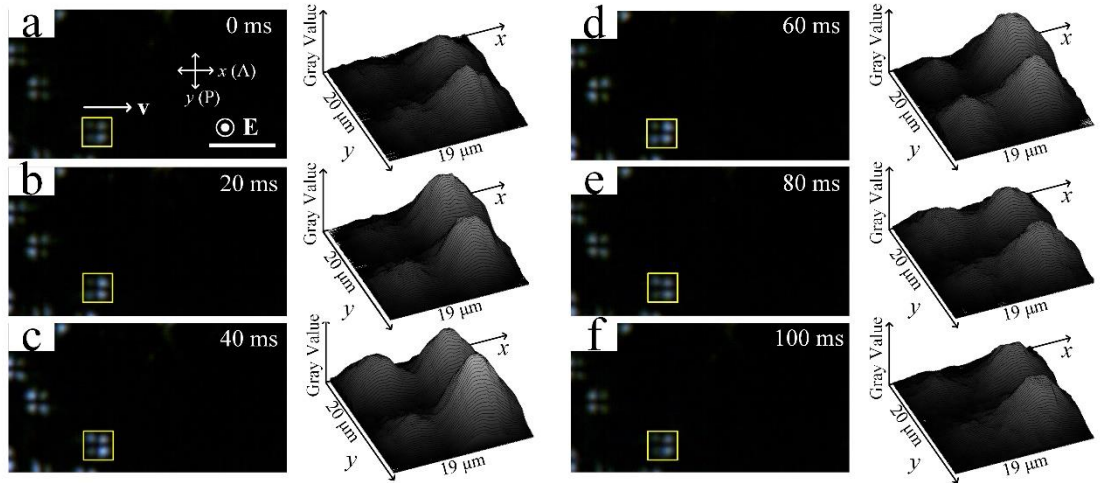
Supplementary Figure 2-3 Nematic directrons observed through a high frame rate camera. Polarizing optical textures of nematic directrons (left) and the corresponding gray value distributions (right) of the directrons outlined in the yellow rectangle at different moments. (a) $t = 0$ ms, (b) $t = 20$ ms, (c) $t = 40$ ms, (d) $t = 60$ ms, (e) $t = 80$ ms, and (f) $t = 100$ ms. $f = 20$ Hz, $E = 0.8\ \mathrm{V\ \mu m^{-1}}$. The scale bar is 50 μm. A and P indicate the analyzer and the polarizer, respectively. **v** indicates the velocity of the directrons. The electric field **E** is perpendicular to the xy plane.
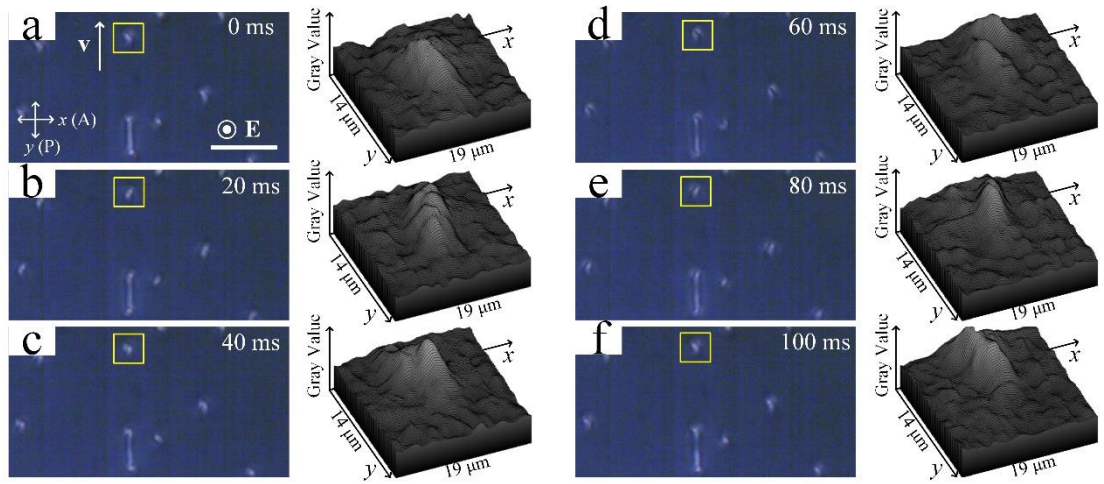
Supplementary Figure 2-4 Cholesteric directrons observed through a high frame rate camera. Polarizing optical textures of cholesteric directrons (left) and the corresponding gray value distributions (right) of the directrons outlined in the yellow rectangle at different moments. (a) $t = 0$ ms, (b) $t = 20$ ms, (c) $t = 40$ ms, (d) $t = 60$ ms, (e) $t = 80$ ms, and (f) $t = 100$ ms. $f = 20$ Hz, $E = 0.8$ V μm^{-1}. The scale bar is 50 μm. A and P are the analyzer and the polarizer, respectively. **v** indicates the velocity of the directrons. The electric field **E** is perpendicular to the xy plane.

Supplementary Figure 2-5 Cholesteric directrons driven by a higher frequency electric field. Polarizing optical texture of the cholesteric liquid crystal at $f = 200$ Hz, $E = 3$ V μm^{-1}. Some of the individual directrons and chains of directrons are labelled by the red circles and ellipses, respectively. Scale bar 100 μm. **m** indicates the alignment direction. A and P are the analyzer and the polarizer, respectively. The electric field **E** is perpendicular to the xy plane.
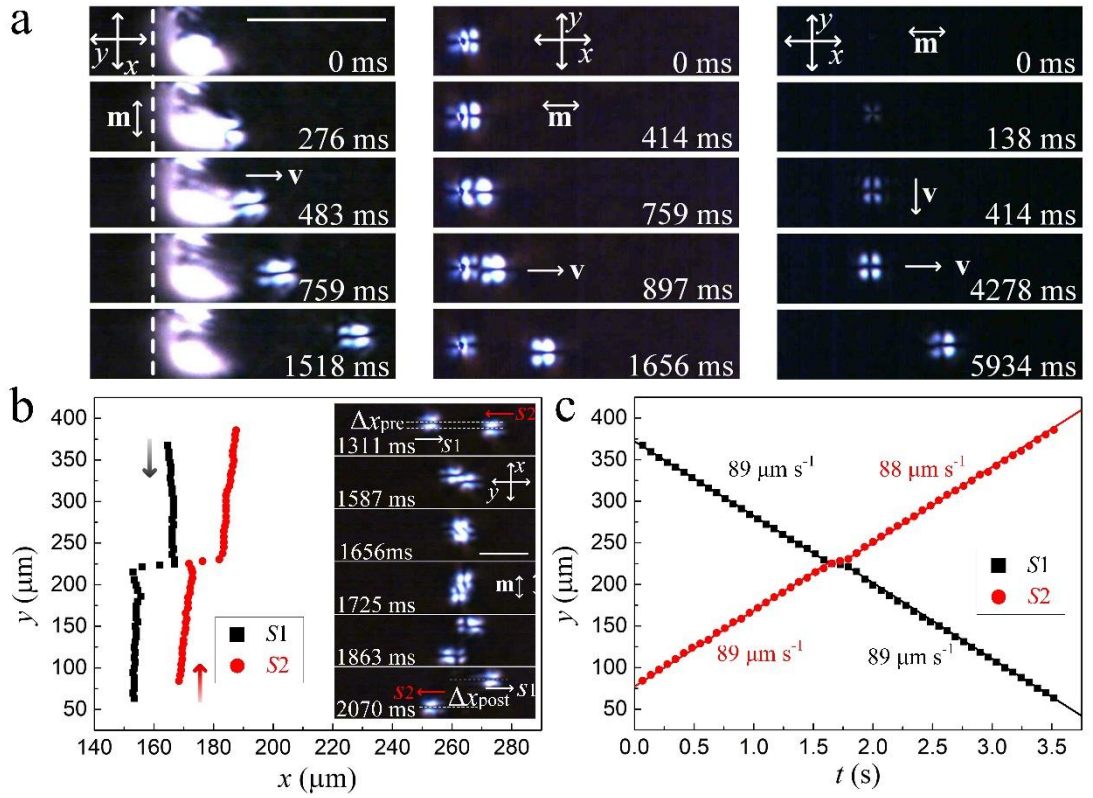
Supplementary Figure 2-6 The generation and interaction of nematic directrons. (a) Generation of nematic directrons. Columns from left to right: nucleation at the edge of an electrode $f = 30$ Hz, $E = 1.2$ V μm^{-1}, at a dust particle $f = 30$ Hz, $E = 0.9$ V μm^{-1}, and at a site where no irregularity is observed $f = 30$ Hz, $E = 0.9$ V μm^{-1}. The scale bar is 100 μm. (b) The trajectory and polarizing optical textures of two colliding nematic directrons with offset $\Delta x_{pre} < w_N/2$ and (c) the corresponding time dependence of the y-coordinates of the directrons. $f = 30$ Hz, $E = 1.2$ V μm^{-1}. The scale bar is 50 μm. **m** is the alignment direction and **v** indicates the velocity of the directrons. w_N indicates the width of the nematic directrons. Δx_{pre} and Δx_{post} are the offsets of the directrons in x-axis before and after the collision. The analyzer and polarizer are parallel to the x and y axes, respectively.
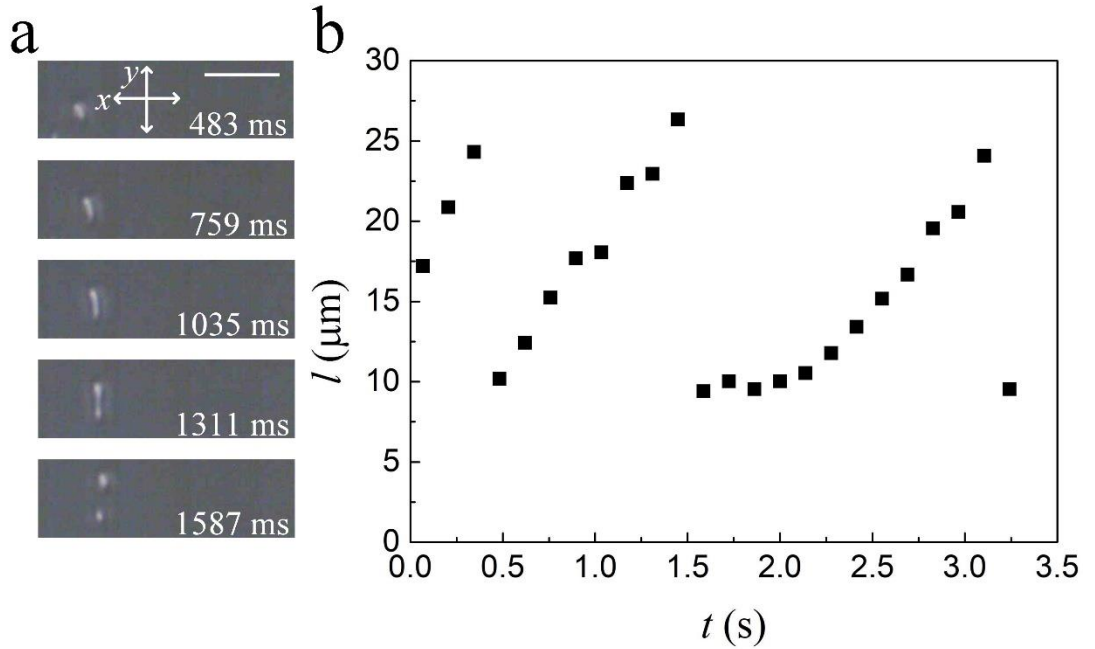
Supplementary Figure 2-7 Proliferation of a cholesteric directron. (a) Polarizing optical textures of the process of a cholesteric directron splitting into two. Scale bar 50 μm. The analyzer and polarizer are parallel to the x and y axes, respectively. (b) Time dependence of the length of the cholesteric directron. $f = 30$ Hz, $E = 0.8$ V μm^{-1}.
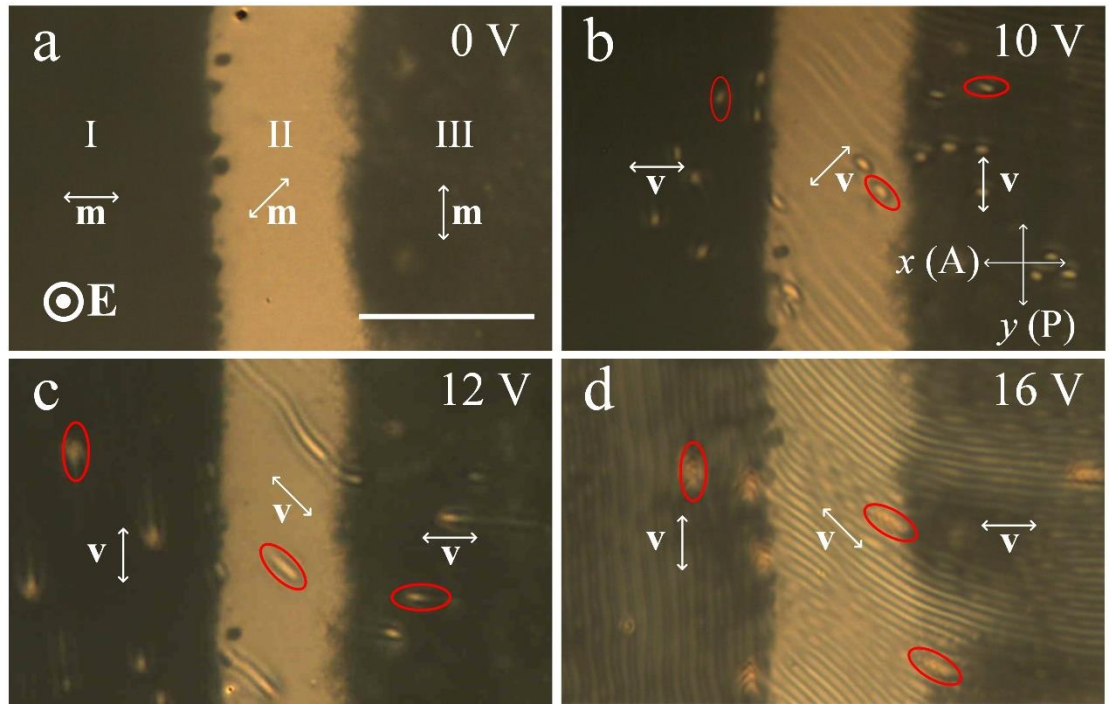
Supplementary Figure 2-8 Manipulation of the trajectories of cholesteric directrons by photo-alignment. Polarizing optical textures of the cholesteric liquid crystal divided into three regions with different alignment direction indicated by **m** (In regions I, II, and III, **m** is tilted with respect to the x axis at an angle of 0 °, 45 °, and 90 °, respectively.) at different voltages (a) 0 V, (b) 10 V, (c) 12 V, (d) 16 V. Frequency of the electric field f = 40 Hz. Scale bar 100 μm. A and P are the analyzer and the polarizer, respectively. **v** indicates the velocity of the directrons. The electric field **E** is perpendicular to the xy plane. The directrons are highlighted by red ellipses.
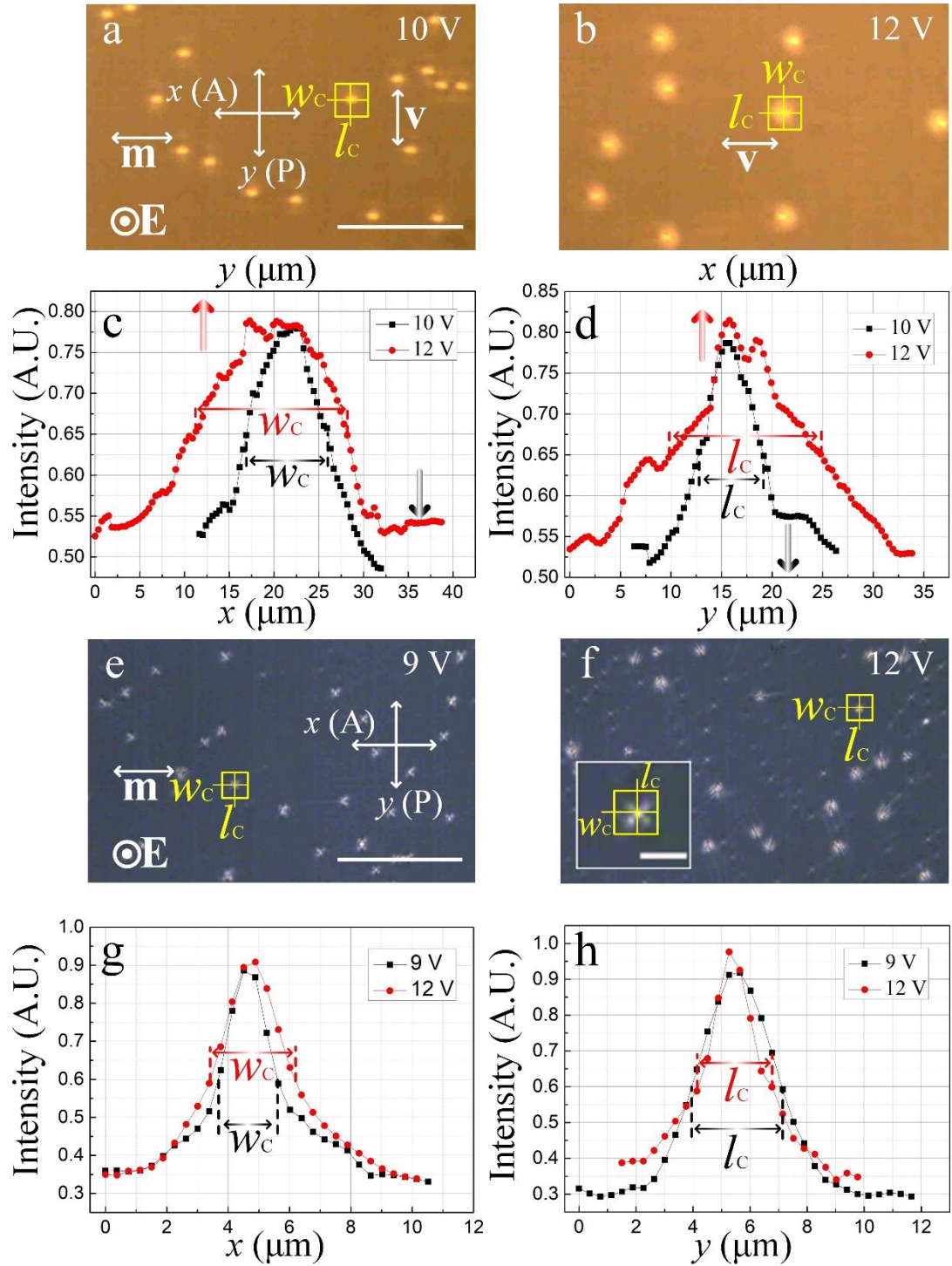
Supplementary Figure 2-9 Directrons in cholesteric liquid crystals with different pitches. Polarizing optical textures of directrons in a cholesteric liquid crystal with a 20 μm pitch driven by electric fields (a) 10 V, 50 Hz and (b) 12 V, 50 Hz. (c) and (d) show the widths and lengths of the corresponding directrons, respectively. Polarizing optical textures of directrons in a cholesteric liquid crystal with a 5 μm pitch driven by electric fields of (e) 9 V, 30 Hz and (f) 12 V, 30 Hz. (g) and (h) show the widths and lengths of the corresponding directrons, respectively. Scale bars in (a) and (e) are 100 μm. The scale bar in the inset of (f) is 10 μm. **v** indicates the velocity of directrons. **m** indicates the alignment direction. The electric field **E** is perpendicular to the xy plane of the cell. A and P indicate the analyzer and polarizer, respectively. w_C, l_C represent the width and length of cholesteric directrons, respectively. The width and length in (c) and (d) are measured as the widths of the directrons cross-sections normal and parallel to their velocity directions, respectively, as indicated by yellow symbols in the optical textures. The width and length in (g) and (h) are measured as the widths of the directron cross-sections along the x-axis and the y-axis, respectively. The widths and lengths of the cholesteric directron are determined by the distance between the two points at which the light intensity of the directrons drops to its half maximum, i.e., 65% in (c), (d), and 60% in parts (g), (h), respectively.

74
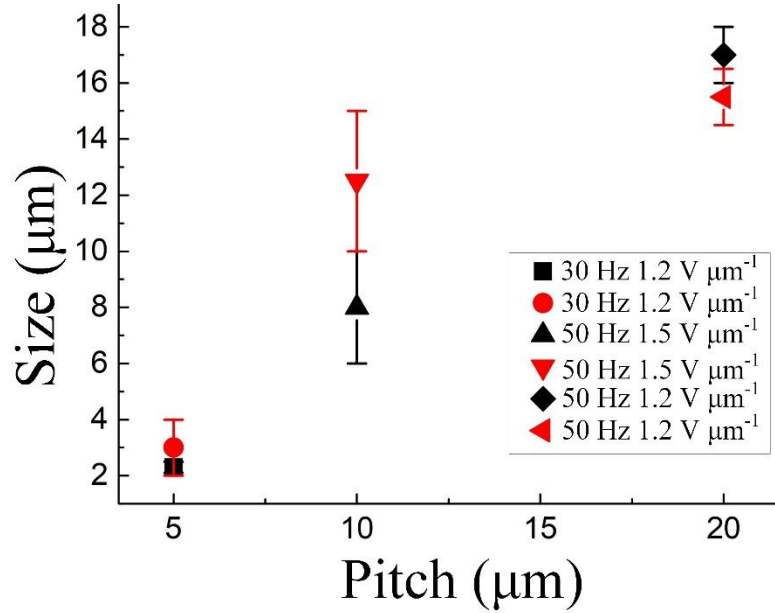
Supplementary Figure 2-10 Pitch dependence of width and length of cholesteric directrons. The widths (black) and lengths (red) of directrons in cholesteric liquid crystals with different pitches, P = 5 μm, 10 μm, 20 μm, respectively. The error bars are determined from the variation in widths and lengths of different directrons at the same conditions.
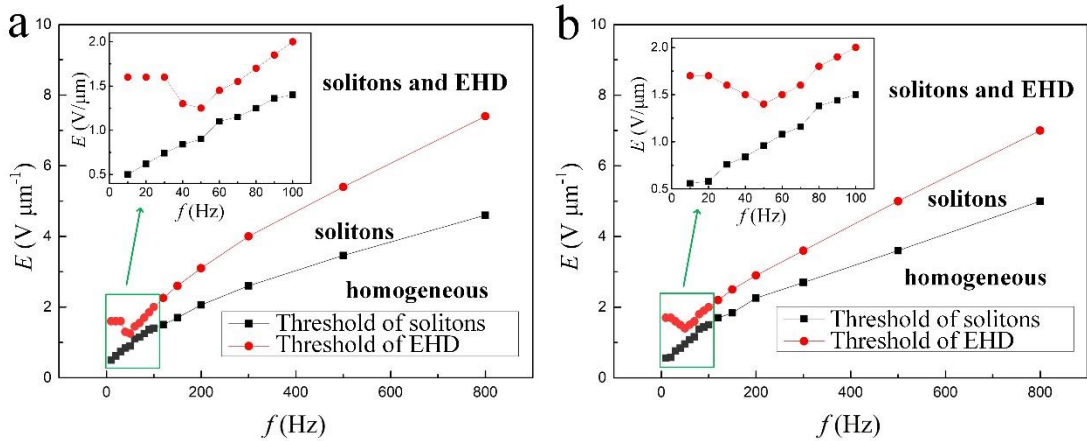
Supplementary Figure 2-11 Phase diagram of cholesteric liquid crystals as a function of the electric field. Frequency dependences of thresholds of the amplitude of electric fields, E_{th}, of directrons and electrohydrodynamics (EHD) in cholesteric liquid crystals with pitches P = 20 μm (a) and P = 5 μm (b), respectively.

2.8.2 Supplementary Movies:

File Name: Supplementary Movie 2-1

Description: **Motion of directrons in a NLC and a CLC**. Directron in a NLC moving parallel to the alignment direction, **m**, f = 30 Hz, E = 0.9 V μm⁻¹. Directron in a NLC moving perpendicular to **m**, f = 30 Hz, E = 1.1 V μm⁻¹. Directron in a CLC moving parallel to **m**, f = 50 Hz, E = 1.2 V μm⁻¹. Directron in a CLC moving perpendicular to **m**, f = 50 Hz, E = 1.5 V μm⁻¹. Real time video rate.

File Name: Supplementary Movie 2-2

Description: **Cholesteric directrons form chain-like structures at high frequency.** $f = 200$ Hz, $E = 3.0$ V μm^{-1}. Real time video rate.

File Name: Supplementary Movie 2-3

Description: **Nucleation of cholesteric directrons**. Nucleation and reflection of directrons at the edge of electrodes, $f = 40$ Hz, $E = 1.1$ V μm^{-1}. Nucleation of directrons in local Williams domains, $f = 50$ Hz, $E = 1.1$ V μm^{-1}. Nucleation of a directron at a dust particle, $f = 40$ Hz, $E = 1.4$ V μm^{-1}. Nucleation of directrons at sites where no irregularity is observed, $f = 30$ Hz, $E = 1.6$ V μm^{-1}. Real time video rate.

File Name: Supplementary Movie 2-4

Description: **Proliferation of cholesteric directrons.** A directron split into two, $f = 20$ Hz, $E = 0.7$ V μm^{-1}. Two directrons collide and split into four, $f = 20$ Hz, $E = 0.7$ V μm^{-1}. Real time video rate.

File Name: Supplementary Movie 2-5

Description: **Interactions of cholesteric directrons with each other and with dust particles**. Collision of two directrons with a small offset $\Delta x < w_C/2$, $f = 30$ Hz, $E = 1.2$ V μm^{-1}. Collision of two directrons with a largel offset $w_C/2 < \Delta x < w_C$, $f = 30$ Hz, $E = 1.2$ V μm^{-1}. Collision of two directrons results in absorption of one, $f = 40$ Hz, $E = 1.4$ V μm^{-1}. Two directrons collide and merge into a metastable directron which reverses its propagation direction, $f = 30$ Hz, $E = 1.4$ V μm^{-1}. Collision of two directrons resulting in reflection, $f = 60$ Hz, $E = 1.3$ V μm^{-1}. Reflection of a directron from a dust particle, $f = 30$ Hz, $E = 1.4$ V μm^{-1}. Real time video rate.

File Name: Supplementary Movie 2-6

Description: **Photo-alignment and cargo transport.** Cholesteric directrons propagate along **m** in regions with different alignment, $f = 40$ Hz, $E = 1.0$ V μm^{-1}. Cholesteric directrons propagate perpendicular to *m* in regions with different alignments, $f = 40$ Hz, $E = 1.6$ V μm^{-1}. Cargo transport by a nematic directron, $f = 30$ Hz, $E = 1.2$ V μm^{-1}. The cargo can be observed after electric field removal as a tiny bright spot, due to causing director field deformations. Real time video rate.

File Name: Supplementary Movie 2-7

Description: **Irregular motion of directrons in a CLC with a 5μm pitch.** $f = 30$ Hz, $E = 1.2$ V μm^{-1}. Real time video rate.

Chapter 3

Electrically tunable collective motion of dissipative solitons in chiral nematic films

Authors: Yuan Shen[1] and Ingo Dierking[1]*
[1] Department of Physics and Astronomy, School of Natural Sciences, University of Manchester, Oxford Road, Manchester, M13 9PL, United Kingdom
*Email: ingo.dierking@manchester.ac.uk

Author contributions:
Y. S. conceived and carried out the experimental investigations, analyzed the experimental results and wrote the manuscript. I. D. supervised the investigations and contributed through discussions and writing the manuscript.

Note: the format of the paper is edited. The supplementary movies related to this work are available on the website of the journal. One can also download the movies from the figshare database: https://figshare.com/s/383c7cfb71293527fb0d.

Abstract

From the motion of fish and birds, to migrating herds of ungulates, collective motion has attracted people for centuries. Active soft matter exhibits a plethora of emergent dynamic behaviors that mimic those of biological systems. Here we introduce an active system composed of dynamic dissipative solitons, i.e. directrons, which mimics the collective motion of living systems. Although the directrons are inanimate, artificial particle-like solitonic field configurations, they locally align their motions like their biological counterparts. Driven by external electric fields, hundreds of directrons are generated in a chiral nematic film. They start with random motions but self-organize into flocks and synchronize their motions. The directron flocks exhibit rich dynamic behaviors and induce population density fluctuations far larger than those in thermal equilibrium systems. They exhibit "turbulent" swimming patterns manifested by transient vortices and jets. They even distinguish topological defects, heading towards defects of positive topological strength and avoiding negative ones.

3.1 Introduction

Collective motion of animals is one of the most fascinating phenomena in our daily life. In spite of discrepancies in the size scales and the cognitive abilities of constituent individual components, systems such as schools of fish, flocks of birds, insect swarms, vertebrate herds and even human crowds produce analogous motion patterns with extended spatiotemporal coherence, indicating underlying universal principles [1]. Understanding these principles is not only interesting to physicists and biologists, but also vital to solving problems such as spreading of diseases, risk prevention at mass events, traffic jams, ecological environment problems, etc. However, it is difficult to study collective behavior by directly performing quantitative measurements in conventional macroscopic systems such as mammal herds, where tracking individual motions of a large population over long periods of time is extremely challenging. As an alternative, great achievement has been made through numerical modeling [2-4]. Moreover, different kinds of micro-scale experimental systems have also been developed to utilized as active models for studying collective behavior[5-7].

Active soft matter, in which constituent building elements convert ambient free energy into mechanical work, is becoming increasingly recognized as a promising system for studying various out-of-equilibrium phenomena [8]. It shows rich emergent dynamic behaviors that are inaccessible to systems at thermal equilibrium. Recent works show that active systems, such as bacteria systems [9] and active colloidal systems [10], can serve as promising alternatives to conventional macroscopic systems to investigate the general behavior of collective motion. However, such systems are generally difficult to prepare and control. The bacteria may be harmful to the human body and the synthesis of active colloidal particles is usually complex. Very recently, Sohn et al., reported schools of skyrmions, particle-like two-dimensional (2D) topological solitons [11]. However, only limited types of emergent collective behavior are realized because the individual skyrmions immediately synchronize their motions within seconds at a scale of the whole sample.

Solitons are self-sustained localized packets of waves that propagate in nonlinear media without changing shape, such as nerve pulses in living beings. They were firstly observed as water waves in a shallow canal by John Scott Russell in 1834 [12], but their significance was not widely appreciated until 1965 when the word "soliton" was coined by Zabusky and Kruskal [13]. Nowadays, solitons have been investigated in many areas of physics such as nonlinear photonics [14], Bose-Einstein condensates [15], superconductors [16], magnetic materials [17], just to name a few. However, creating multidimensional solitons is still a great challenge in many physical systems due to their instability [18]. Liquid crystals (LCs) have been an ideal testbed for studying solitons for decades [19]. Different kinds of solitons have been produced in LCs [19], both immobile [20-24] and mobile ones [11,25-28]. Recently, electrically driven 3D dissipative solitons coined as "director bullets" or "directrons" have received increasing attention[29-35]. These directrons were firstly reported by Brand et al. in 1997, which were called "butterflies" by the authors, but did not receive great attention at that time [36]. The directrons represent nonsingular director perturbations that propagate through a uniform nematic bulk without losing their identities. Within the directron, the director field oscillates with the frequency of the applied electric field due to the flexoelectric effect, breaking the mirror symmetry of the directrons and driving them to move.

Here we show an emergent collective motion of such directrons. Individual directrons consume electric energy and convert it into mechanical motions. Depending on the applied

voltage, they exhibit different dynamic behaviors. At low voltages, the directrons self-organize into chains, loops, flocks and swarms that move coherently like, for example, schools of fish (Figure 3-1 (a) and (b)). At high voltages, the density of the directrons increases dramatically. Tens of thousands of directrons start from random orientations and motions, but then synchronize their motions through collisions and short-range interactions with each other and develop ferromagnetic-like order within tens of seconds, as described by the well-known "Vicsek model"[3]. Further increasing the voltage leads to a dynamic transition of the collective motion from a wavy motion regime to linear motion and eventually ends into chaotic, incoherent motion. The directrons also exhibit an emergent "turbulent" swimming pattern which is manifested by recurring transient vortices and jets. Furthermore, we show that the collective motion of the directrons can be controlled by topological defects, where directrons swirl around defects of positive topological strength and avoid the ones of negative strength, in accordance with the behavior of bacteria reported before by Lavrentovich and co-workers [37]. Our findings show that active soft matter formed by directrons exhibits rich emergent collective dynamic behaviors that mimic those of living systems and provide a tunable model for studying collective motion.

3.2 Materials and methods

Materials. The chiral nematic is obtained by mixing a nematic liquid crystal ZLI-2806 (Merck) and a chiral dopant ZLI-811 (Xianhua, China). The nematic ZLI-2806 shows a phase sequence on cooling of Isotropic (100°C) Nematic (-20°C) Crystal [38]. The components of the dielectric permittivity and conductivity of ZLI-2806 at f = 4 kHz and room temperature are $\varepsilon_\parallel$ = 3.0, $\varepsilon_\perp$ = 7.6, $\sigma_\parallel$ = 1.9 × 10^{-8} Ω^{-1}m^{-1}, $\sigma_\perp$ = 6.0 × 10^{-9} Ω^{-1}m^{-1}, respectively [31].

The pitch of the LC mixture $p \sim 2$ μm is calculated according to the equation $p = 1/(HTP \times c)$, where c is the weight concentration of the chiral dopant, and HTP = -8.3 μm^{-1} represents the helical twisting power of the chiral dopant [31]. The weight concentration of chiral dopant is ~ 6% in chiral nematic mixture of $p \sim 2$ μm and ~ 1.2% in chiral nematic mixture of $p \sim 10$ μm. The experimental cells (AWAT, Poland) are prepared with a planar alignment layer. The inner surfaces of the cells are covered with polyimide and rubbed in a specific direction

(along the *x*-axis). The cell gaps are measured by the thin-film interference method [39]. In the experiments of circular motion of directrons induced by umbilic defects, the pitch of the LC mixture $p \sim 10$ μm and the cells (North LCD) used are prepared with homeotropic alignment with a cell gap $d \sim 9.4$ μm.

Generation of directrons. The LC mixture is heated to the isotropic phase and filled into cells by capillary action. The filled sample is kept at 80 °C on a hot stage (LTSE350, Linkam) controlled by a temperature controller (TP 94, Linkam). The directrons are generated by applying an AC electric field directly to the LC cell using a waveform generator (33220A, Agilent) and a home-built amplifier.

Brownian motion of colloidal micro-particles. A small amount of micro-particles with a homogeneously distributed diameter (~ 3 μm) are dispersed in the chiral nematic media ($p = 2$ μm). The sample is kept at 75 °C and the motion of the micro-particles is tracked by the camera for ~2 min. The frame rate of the camera is tuned to 150 frames per second, which gives, overall, ~18000 trajectory steps for measurement. The mean square displacement ($\Delta r^2(\tau)$) of the micro-particle is calculated which grows linearly with time lag τ as $\Delta r^2(\tau) = 6L\tau$, where L is the diffusion coefficient.

Microscopic observations. All images and movies are captured through polarizing transmission-mode optical microscopy using a Leica OPTIPOL microscope equipped with a charge-coupled device camera (UI-3360CP-C-HQ, uEye Gigabit Ethernet).

Measurement of fluid flows. To detect the potential fluid flows, small amounts of a fluorescent dye (0.04 wt%) is doped in the LC system. However, the formation of the directrons is closely related to the conductivity of the LC material and the fluorescent dye usually greatly changes the conductivity of LCs. As a result, no directron is observed, instead a global 2D grid convective pattern is formed in the doped system.

We then doped quantum dots (0.005 wt%) into the LC media. The voltage thresholds of the directrons are greatly decreased by the doping and once the voltage is larger than 20 V, electro-convection patterns emerge and fill up the whole sample. The sample is then characterized by fluorescent microscope, however, nothing is observed. We then increased the concentration of quantum dots to 0.1 wt%. At such a high concentration, no directron is generated and the sample is exhibiting electro-convection patterns throughout. Although the concentration is too high to induce the directrons, nothing is observed under the fluorescent

microscope, except a very weak blueish background. This maybe because the quantum dots are too small to be seen.

We then doped micro-particles (diameter 3 μm) into the LC system. The doping slightly decreases the voltage threshold of the directrons. We find that individual micro-particles are very easily pinned on the glass substrates of the cell by applying the electric field. On the other hand, some aggregates of micro-particles and dusts move at relatively high voltages. However, it is always observed that there are directrons attached on those. The directrons always firstly nucleated at particles or dusts and then move them. Such a behavior has been reported by Li et al. [40] and is called "soliton-induced liquid crystal enabled electrophoresis". So it is not clear whether the particles are moved by the directrons or some fluid flows, or both. However, no obvious motion of particles is observed before the emergence of directrons. The moving aggregates also stop moving once the directrons disappear by slightly decreasing the applied voltage. So one can at least conclude that before the formation of the directrons, there is no obvious fluid flow.

Data analysis. The movies are analyzed for positions of directrons using open-source software ImageJ-FIJI and its plugin "TrackMate". The position data is then processed by ORIGIN and MATLAB to characterize the dynamics of the directrons. The velocity order parameter is defined as $S_v = |\sum_j^N \mathbf{v}_j| / (N \times v_s)$, where N is the total number of directrons in the field of view and v_s is the absolute value of the velocity of coherently moving directrons [28]. The spatial velocity correlation function is defined as $g_v(r) = \langle \sum_{i,j}^N (\mathbf{v}_i \times \mathbf{v}_j) \delta[r - r_{ij}] \rangle / \langle \sum_i^N \mathbf{v}_i \times \mathbf{v}_i \rangle$ [9]. The temporal velocity correlation function is defined as $C_v(\Delta t) = \langle \sum_i^N \mathbf{v}_i(t) \times \mathbf{v}_i(t + \Delta t) \rangle / \langle \sum_i^N \mathbf{v}_i(t) \times \mathbf{v}_i(t) \rangle$. The giant number fluctuations and the scaling trend for each voltage in Figure 3-8 (a) are obtained by analyzing the directron number density versus time for 30 areas of different sizes, ranging from 53 μm × 53 μm to 367 μm × 367 μm. The time period over which the fluctuations are characterized for each data point in Figure 3-8 (a) is 500 s [28]. The hexatic bond orientational correlation function is defined as $g_6(r) = \langle \sum_{i,j}^N \psi_6^*(\mathbf{r}_i) \psi_6(\mathbf{r}_j) \delta(r - r_{ij}) \rangle$ [41], where $\psi_6(\mathbf{r}_j) = \left(\frac{1}{m_j}\right) \sum_{k=1}^{m_j} e^{i6\theta_{jk}}$ is the local hexatic bond orientational order parameter. m_j runs over the neighbors of directron j (defined as being closer than a threshold distance), and θ_{jk} is the angle between the j-k bond and an

arbitrary axis. The radial distribution function is defined as $g_v(r) = \frac{S}{2\pi r N^2} \langle \sum_{i,j,i\neq j}^{N} \delta(r - r_{ij}) \rangle$, where S is the area [9]. The pair interaction potential function ($U(r)$) is evaluated from the Boltzmann distribution $U(r) = -k_B T \ln[g(r)]$ [11,42]. We first measured the radial distribution function ($g(r)$) at very low density (low applied voltages) and then calculated the pair interaction function through the Boltzmann distribution. The critical frequency $f_c = \sqrt{\xi^2 - 1}/\tau_M$, where $\tau_M = \varepsilon_0 \varepsilon_\perp / \sigma_\perp$ is the Maxwell relaxation time for planar cells, $\varepsilon_0 = 8.85$ * 10^{-12} Fm^{-1}. $\xi^2 = \left(1 - \frac{\sigma_\perp}{\sigma_\parallel} \frac{\varepsilon_\parallel}{\varepsilon_\perp}\right)\left(1 + \frac{\alpha_2}{\eta_c} \frac{\varepsilon_\parallel}{\Delta\varepsilon}\right)$ is the material parameter that depends on conductivities ($\sigma_\perp$ and $\sigma_\parallel$), permittivities ($\varepsilon_\perp$ and $\varepsilon_\parallel$), and viscous coefficients (α_2 and η_c). Using the material data of ZLI-2806 measured at $f = 4$ kHz and room temperature, $1/\tau_M \sim 89$ Hz. The factor $\sqrt{\xi^2 - 1}$ is hard to determine exactly since both α_2 and η_c are not known. $\left(1 - \frac{\sigma_\perp}{\sigma_\parallel} \frac{\varepsilon_\parallel}{\varepsilon_\perp}\right) \sim 0.875$ and $\frac{\varepsilon_\parallel}{\Delta\varepsilon} \sim -0.65$. We assume the ratio $-\frac{\alpha_2}{\eta_c}$ being on the order of 1 as Li et al. did in their work [30], the critical frequency $f_c \sim 128$ Hz.

3.3 Results

3.3.1 Formation of directrons
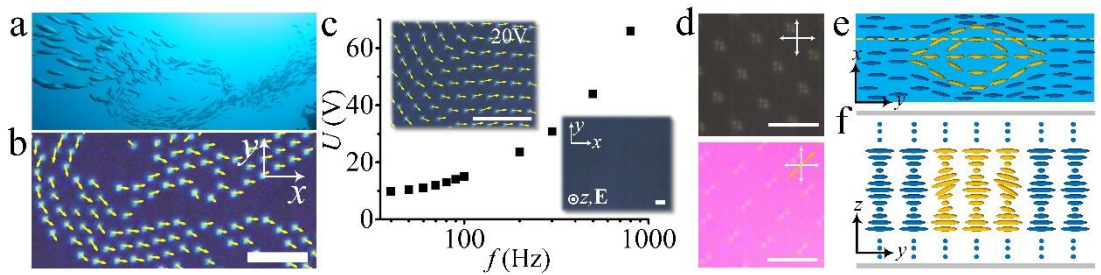
Figure 3-1 Collective motion of directrons. (a) Photograph of schools of fish. Figure from Joanna Penn, Flickr: https://www.flickr.com/photos/38314728@N08/3997721496/in/dateposted/ (b) Polarizing micrograph of collectively moving directrons with their velocities indicated as yellow arrows. $U = 16$ V, $f = 100$ Hz. Scale bar 50 μm. The polarizers are parallel to the x- and y-axes, respectively. (c) Frequency dependence of the threshold for generation of directrons. The insets show the micrographs below (0 V) and above the thresholds ($U = 20$ V, $f = 100$ Hz) of the generation of the directrons. The yellow arrows represent the velocities of the directrons. Scale bars 50 μm. (d) The polarizing micrograph of directrons at $f = 100$ Hz, $U = 20$ V. Scale bars 20 μm. The white crossed arrows represent the polarizers and the yellow arrow represent the optical axis of the λ-plate. (e) The schematic director structure of a directron in the middle layer of the chiral nematic sample. (f) The schematic director structure of a directron in the yz plane of the cross section along the dashed yellow

line in (e). The director field within the directron is represented as yellow ellipses and the homogeneous director field outside the directron is represented as blue ellipses. The top and bottom sections of the sample in (f) are homogeneously aligned helical structures and are represented by blue dots.

Collective motion, like it is exhibited by schools of fish (Figure 3-1 (a)), is accompanied with inhomogeneities and the formation of dynamic groups whose volume and shape change as the groups turn and arc but remain cohesive. Similar behavior is found in our rather unusual active soft matter system formed by hundreds and thousands of dynamic particle-like solitonic director field configurations within a cholesteric LC film (Figure 3-1 (b)), which exhibits complex, coordinated, spatiotemporal dynamical patterns. The experimental setup is similar to that in LC displays, where a thin film of cholesteric LC is sandwiched between two pieces of glass substrates which is coated with an indium tin oxide (ITO) layer as electrodes and a rubbed polyimide layer as the planar alignment layer, i.e. the director near the glass substrates aligns along the rubbing direction (along the x-axis, Figure 3-1 (b)). Along the normal to the glass substrates, the director twists continuously along a helical axis at a constant rate. The cell gap $d \sim 9.5$ μm. An alternating-current (AC) electric field, **E**, is applied perpendicular to the LC film (along the z-axis). The directrons emerge when the applied voltage exceeds a frequency dependent threshold (Figure 3-1 (c)). The formation mechanism of the directrons is not completely understood yet and requires further experimental and theoretical investigations. Recent publications by Pikin suggested that the generation of the directrons may be due to the interaction of injected electron clouds with nematic molecules [43,44]. However, the charge injection usually happens under a DC electric field or AC electric field with low frequency, which is suppressed as soon as the oscillation frequency of the applied field exceeds a few cycles [45]. Although, the directrons here exist at relatively high frequencies (up to 800 Hz, Figure 3-1 (c)), one cannot exclude the possibility of charge injection since it may still occur at high voltages. To totally exclude the possibility of charge injection, further experiments are required, for instance, one can make a cell with "blocking" electrodes [46]. On the other hand, according to previous investigations [29-31,34,35], the formation of the directrons is closely dependent on the dielectric and conductivity anisotropies of the LC materials. the directrons only occur in the limited range of moderate conductivity. If the conductivity is higher than the range, only global electro-convective patterns are observed [34]. The conductivity anisotropy of the LC in present study is $\Delta\sigma =$

1.3×10^{-8} $\Omega^{-1}\text{m}^{-1}$ (*Methods*), which is relatively small compared to the ones used in studies of electro-convections ($\sim 10^{-7}$ $\Omega^{-1}\text{m}^{-1}$) [47,48]. The significance of this small conductivity anisotropy can be understood by considering the coupling between the electric field and the space charges. According to the Carr–Helfrich electro-convection mechanism [49,50], the positive conductivity anisotropy and the bend fluctuation in a nematic induce ion segregation and form space charges which are high and uniformly distributed in space. These space charges produce transverse Coulomb forces which offset the normal elastic and dielectric torques and cause instability, usually in the form of space-filling periodic stripes. However, due to the relatively low conductivity, there is not sufficient charge accumulation to produce a strong enough dielectric torque to induce a global electro-convection pattern. Instead, the director field around the space charges is locally deformed, inducing the flexoelectric polarization. As a result, the director within the local deformations oscillates with the frequency of the applied electric field [29-31], leading to the formation of the directrons.

3.3.2 Dynamics of directrons
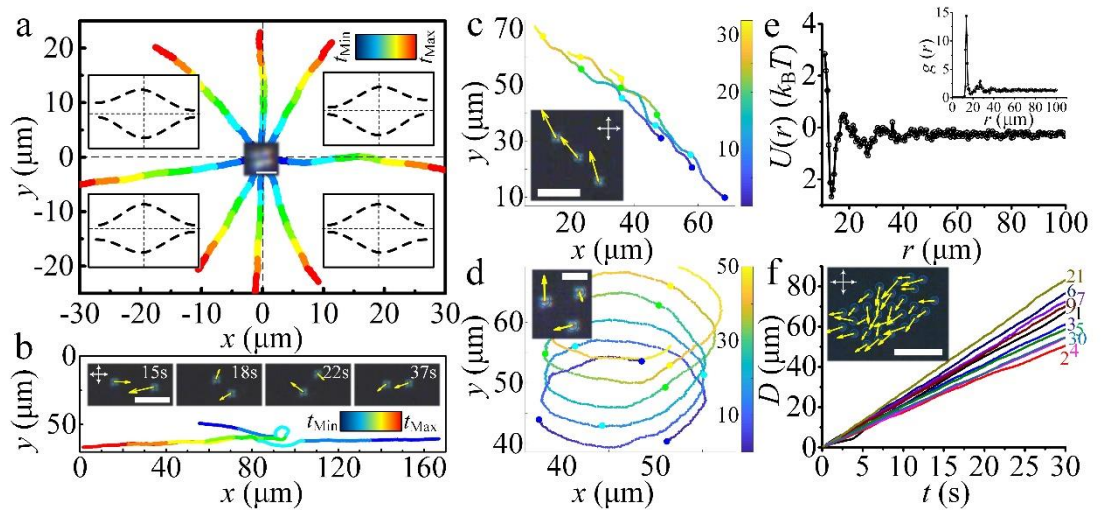
Figure 3-2 Dynamics of directrons. (a) Trajectories of 8 individual directrons at $U = 15.4$ V, $f = 100$ Hz, colored with time corresponding to the color bar ($t_{\text{Min}} = 0$ s, $t_{\text{Max}} = 10$ s). The insets in four quadrants show the schematic symmetry-breaking middle-layer director structures of the directrons. The inset in the middle shows the polarizing micrograph of a directron. Scale bar 5 μm. (b) Trajectories of two directrons at $U = 15.4$ V, $f = 100$ Hz colliding with each other, colored with time corresponding to the color bar ($t_{\text{Min}} = 0$ s, $t_{\text{Max}} = 67$ s). The insets show the time sequences of micrographs of the two directrons with yellow arrows representing the velocities, scale bar 20 μm. (c) and (d) Trajectories of three directrons at $U = 15.4$ V, $f = 100$ Hz, colored with time corresponding to the color bars (unit (s)). The directrons demonstrate linear motion (c) and circular motion (d). The insets show the micrographs of the three directrons with their velocities represented as yellow arrows. Scale bars 20 μm in (c) and 10 μm in (d). (e) Pair interaction potential function (extracted from the radial distribution function $g(r)$ shown in the inset) of the directrons at $U = 15.2$ V, $f = 100$ Hz. (f) Dependence of displacements (D) of groups of different number of directrons on time (t). The inset

shows the micrograph of the group composed of 30 directrons with their velocities representing as yellow arrows. Scale bar 50 μm. The white crossed arrows in the micrographs indicate the polarizers.

Unlike the directrons in achiral nematics reported previously, which move either parallel or perpendicular to the alignment direction [29,31], the directrons here travel in random directions in the *xy* plane independent of the alignment direction (Figure 3-2 (a)). Such a behavior may be attributed to the rotational symmetry of the small pitch helical structure of the LC system which suppresses the influence of the rubbing alignment. Moreover, the director deformation of the directrons reaches maximum in the middle layer of the LC media, and gradually diminishes as one moves toward the top and bottom cell substrates [29], which further reduces the influence of the rubbing alignment. Such a speculation can be demonstrated by the isotropic Brownian diffusion of colloidal micro-particle in our system (Supplementary Figure 3-1), which always exhibits anisotropic diffusion behavior in achiral nematics [51]. The structure of the directrons is deduced from the polarizing micrograph which shows a quadrupolar symmetry (Figure 3-1 (d)). Within the directron, the director deviates from the uniform state due to the transverse Coulomb forces provided by space charges as well as the flexoelectric polarization (Figure 3-1 (e) and (f)). Unlike the topological solitons, such as skyrmions [23], in which the director field cannot be continuously transformed into a uniform state, the directrons are topologically trivial. The director also oscillates, both in the *xy* plane and out of the plane (Figure 3-1 (e) and (f)), with the frequency of the applied electric field due to the flexoelectric effect [29-31], which leads to the periodic deformation of the directron structure (Supplementary Figure 3-2) and propels the directrons to move. The moving direction of the directrons is determined by the breaking of the quadrupolar symmetric structure (Figure 3-2 (a) insets), i.e. the directrons moving along the *x*-axis lack the left-right symmetry with respect to the *yz* plane; vice versa, the directrons moving along the *y*-axis lack the fore-aft symmetry about the *xz* plane [29-32]. One may suspect that there are some kind of fluid flows that carry the directron's motion. However, since the dielectric anisotropy of the LC material is negative ($\Delta\varepsilon = -4.6$), there is no backflow generated by the rotation of the director field. No electro-convection pattern is observed which can exclude the electro-convective flows. The isotropic flows generated by the injection of ions usually occur at very low frequencies [45]. The only possibility left is the flow generated by ion motion. However, this flow also usually happens at relatively low frequencies, i.e., the conductive

86

regime, which is limited from above by the critical frequency, f_c [52]. According to our calculation, $f_c \sim 128$ Hz in our system (*Methods*). However, the directrons can move effectively at relatively high frequencies (up to 800 Hz or even higher). Furthermore, particle tracking does not show obvious existence of flows (*Methods*). So, as far as we can conclude, it appears that there is no such kind of flows which can carry the directron's motion. The directrons can also switch their moving directions during motion due to the change of the asymmetry of their structures induced by, for instance, director fluctuations, or collisions with other directrons and inhomogeneities, such as dust particles. It is found that the directrons cannot pass through each other as reported for those in achiral nematics [29-31]. Instead, the directrons attract each other at relatively long ranges but repel at short distances (Figure 3-2 (e)). Since the directrons are nonsingular director deformations, such an interaction is more likely to stem from the elastic distortion of the director field. Figure 3-2 (b) shows that two directrons move in opposite directions collide and repel each other into different directions like true particles, but then attract each other and form a linear chain which moves coherently along a spontaneously chosen direction (Supplementary Movie 3-1). If more directrons get close to each other, they can not only form linear chains but also form closed loops (where the head and the tail of the linear chains are connected) which rotate continuously in the *xy* plane about their rotation axes along the *z*-axis (Figure 3-2 (c) and (d), Supplementary Figure 3-3 and Supplementary Movie 3-2). To probe how the dynamics of directrons changes with increasing number density, we measure the displacement of directron flocks of different sizes (different number of directrons, *n*) within a specific duration, but no obvious dependence is observed (Figure 3-2 (f)).

3.3.3 Flocks of directrons
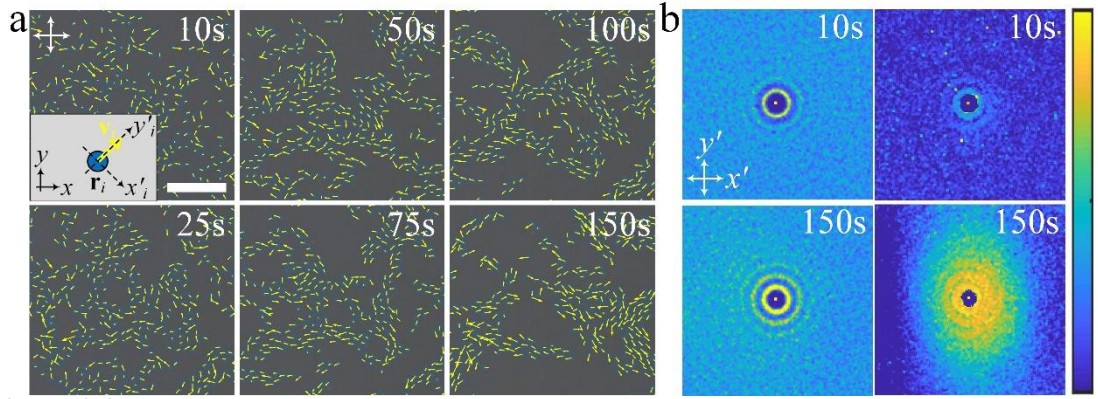
Figure 3-3 Formation of directron flocks. (a) Polarizing micrographs of directrons ($U = 16.2$ V, $f = 100$ Hz.) with their velocities represented as yellow arrows at different times after applying the electric field. Scale bar 100 μm. The crossed polarizers are indicated as white arrows. The time after the application of the electric field is indicated. A laboratory coordinate frame (x y) and a local coordinate frame (x' y') are defined in the inset. (b) 2D radial distribution functions (g) (first column) and 2D spatial velocity correlation functions (g_v) (second column) of the directrons colored according to the color bar at 10 s and 150 s after applying the electric field, respectively. The color bar changes linearly from 0 (dark blue) to 4 (light yellow) for g and from 0 (dark blue) to 1 (light yellow) for g_v. Image sizes are 200 μm × 200 μm. The 2D spatial velocity correlation functions are averaged over 5 seconds (10 frames).

Hundreds of directrons emerge after increasing the voltage over the critical value (Figure 3-1 (c)). At relatively low voltages, they form a gas-like phase in which they are distributed sparsely throughout the whole sample and move in random directions, occasionally experiencing collisions, depending on the directron density. Due to the long-range attractive pairwise interaction, the directrons gradually travel towards each other and form dynamic flocks of different sizes which move in different directions (Supplementary Movie 3-3). Within each flock, the directrons move coherently on average in the same direction (Figure 3-3 (a)). To quantify the correlation between the directrons, we compute spatial correlation functions in a "local coordinate frame" with the y-axis (y_i') along the velocity vector of the ith directron ($\mathbf{v}_i$) and the x-axis (x_i') perpendicular to it (Figure 3-3 (a) inset). The radial distribution function, $g(r)$, quantifies the probability of finding another directron in a unit area at the point (x,y) away from the reference directron, where r represents the distance between directrons. It shows an excluded volume with a radius of approximately 10 μm due to the short-range repulsive interaction and a peak at $r \sim 13$ μm (Figure 3-3 (b)), which is consistent with the pairwise interaction between directrons (Figure 3-2 (e)). Close neighbors show similar velocity to the reference directron as evidenced by the peak corresponding to the first nearest neighbor of the spatial velocity correlation function, $g_v(r)$.

The peak corresponding to the second nearest neighbor of $g_v(r)$ is indiscernible at $t = 10$ s, indicating the short-range velocity correlation between directrons at an early stage. With motion progressing, both $g(r)$ and $g_v(r)$ become increasingly long-range with an increased number and value of peaks, indicating the formation of flocks (Figure 3-3 (b)). The spatial velocity correlation function at $t = 150$ s is anisotropic with respect to the direction of collective motion which shows a longer correlation along the y'-axis (Figure 3-3 (b)). Such an anisotropy of the spatial correlation functions has been identified as one of the key properties of collective motion [53]. It has also been observed in other active systems, such as bacteria suspensions [9] and driven filament systems [54], which stems from the anisotropic shape of the individual components. However, the directrons here are basically circular in the xy plane and the anisotropy of the velocity correlation function is due to the anisotropic shape of the directron flocks which are relatively elongated along their moving directions (Figure 3-3 (a)). The radial distribution functions do not show obvious anisotropy due to the short-range pair correlation between the directrons.
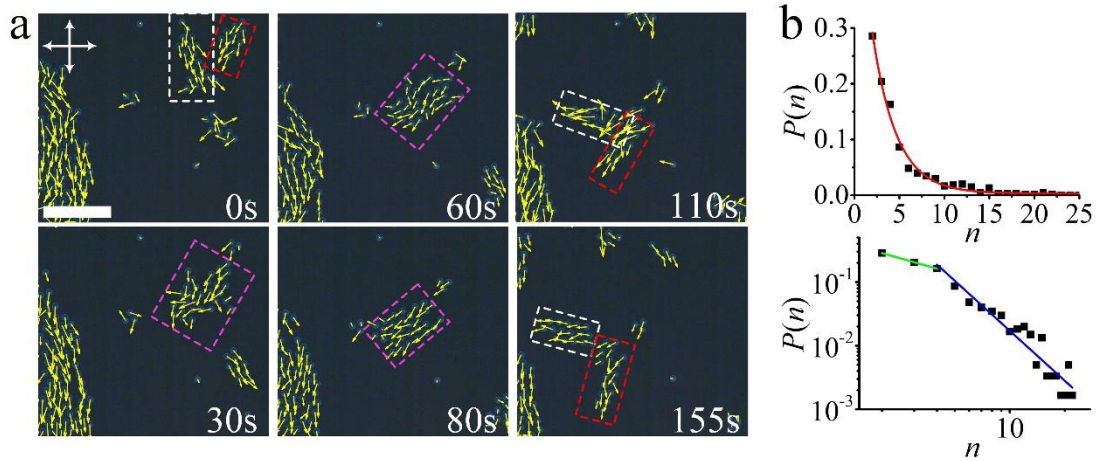
Figure 3-4 Directron flocks. (a) Polarizing micrographs of fusion and fission of directron flocks at different times. Directron flocks are indicated by dashed squares with different colors. Scale bar 100 μm. The crossed polarizers are indicated as white arrows. $U = 15.4$ V, $f = 100$ Hz. (b) Frequency distribution of directron flock sizes (number of individual directrons, n, in each flock) at $U = 15.5$ V, $f = 100$ Hz. The top figure demonstrates the probability of finding a directron flock composed of n directrons. The red line represents the exponential fit of the experimental data (black squares). The bottom figure shows the log-log plot of the distribution. The green and blue lines are linear fits of the experimental data with slopes $\beta_1 = -0.8$ and $\beta_2 = -2.6$, respectively.

The directron flocks change their size through fusion and fission processes as shown in Figure 3-4 (a). Two directron flocks moving in different directions collide with each other and then combine into a larger flock. Right after the collision, the motions of the directrons within the flock become slightly disordered with a relatively large velocity deviation, but they quickly synchronize their motions and move coherently in a specific direction. The large

flock is not stable, after travelling a certain distance, it fragments into two smaller flocks which move away from each other in different directions (Supplementary Movie 3-4). Figure 3-4 (b) shows the size distribution of directron flocks at a fixed electric field, which is exponentially distributed. Such an exponential distribution is consistent with the group size distribution of fish schools as reported by Flierl et al. [55], and predicted by Okubo [56]. However, Niwa argued that the group size distributions fit a truncated power law with a crossover to an exponential decay and is dependent on the cutoff size [57,58]. If the cutoff size is small, the exponential decay will be the only part of the functionality, but if the cutoff size is large, one may predict that the group size distribution would better fit a power law [57,58]. We plot the size distribution of directron flocks on a log-log scale and find a cutoff size of $n = 4$ (Figure 3-4 (b) bottom).

3.3.4 Electrically controllable collective dynamic behavior
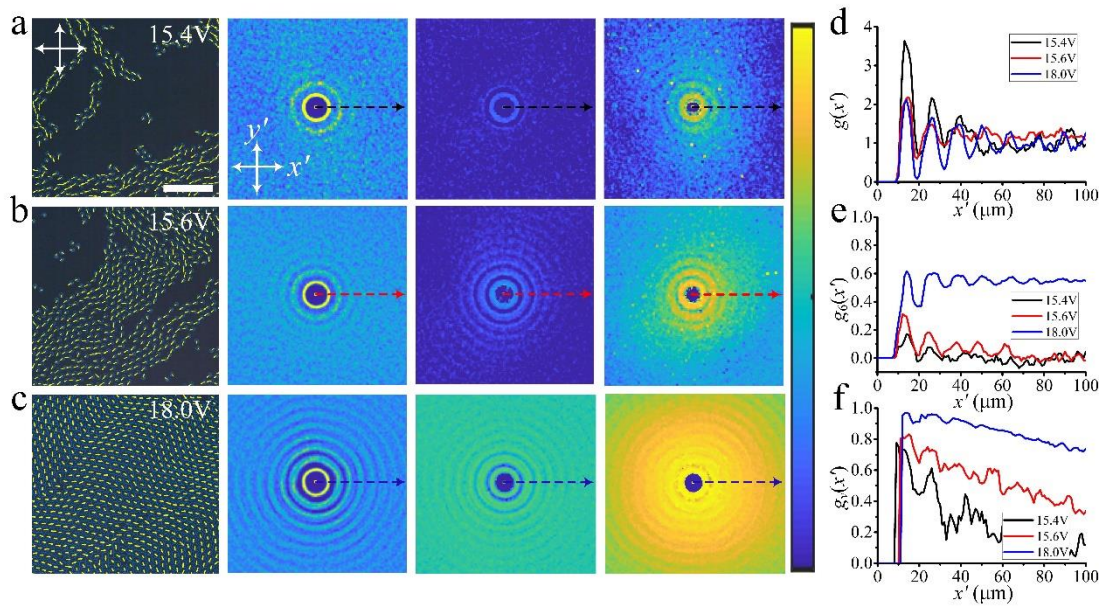
Figure 3-5 Collective motion of directrons at different voltages. Micrographs (first column, scale bar 100 μm), 2D radial distribution functions (g, second column), 2D hexatic bond orientational correlation functions (g_6, third column) and 2D spatial velocity correlation functions (g_v, forth column) of the directrons at different voltages, (a) $U = 15.4$ V, (b) $U = 15.6$ V, and (c) $U = 18.0$ V. The frequency is fixed at $f = 100$ Hz. The image sizes of the 2D correlation functions are 200 μm × 200 μm. The color bar changes linearly from 0 (dark blue) to 3 (light yellow) for g, and from 0 (dark blue) to 1 (light yellow) for g_6 and g_v. The transverse profiles (as indicated by the dashed arrows) of the corresponding (d) radial distribution functions ($g(x')$), (e) bond orientational correlation functions ($g_6(x')$) and (f) spatial velocity correlation functions ($g_v(x')$). The spatial velocity correlation functions are averaged over 10 seconds (20 frames).

The number of the directrons depends on the applied voltage. By increasing the voltage, more and more directrons emerge. Figure 3-5 shows the dynamic steady states of the

collectively moving directrons at varied voltages. It is found that by increasing the directron population density, the radial distribution function (g), hexatic bond orientational correlation functional (g_6) and spatial velocity correlation function (g_v) become more and more long-range. This is because at low density, the directrons form small flocks which move incoherently in random directions. By increasing the directron density, small flocks collide with each other and form large flocks within which the directrons pack into hexagonal structure and move coherently. At $U = 18$ V, the whole sample plane is filled with directrons which are orderly arranged due to the short-range repulsive interaction and on average move coherently in the same direction. The correlation lengths of the spatial correlation functions are of the order of tens or even hundreds of micrometers and are much larger than those of bacteria suspensions, which are usually only several micrometers [9]. Such a difference may be due to the short-range repulsive and long-range attractive interaction between the directrons which is absent among bacteria. The spatial velocity correlation functions in Figure 3-5 (b) and (c) do not show obvious anisotropic profiles which is because the directrons do not form anisotropic flocks, instead they form large-scale or even global directron flows which extend hundreds and thousands of micrometers due to the high directron density.
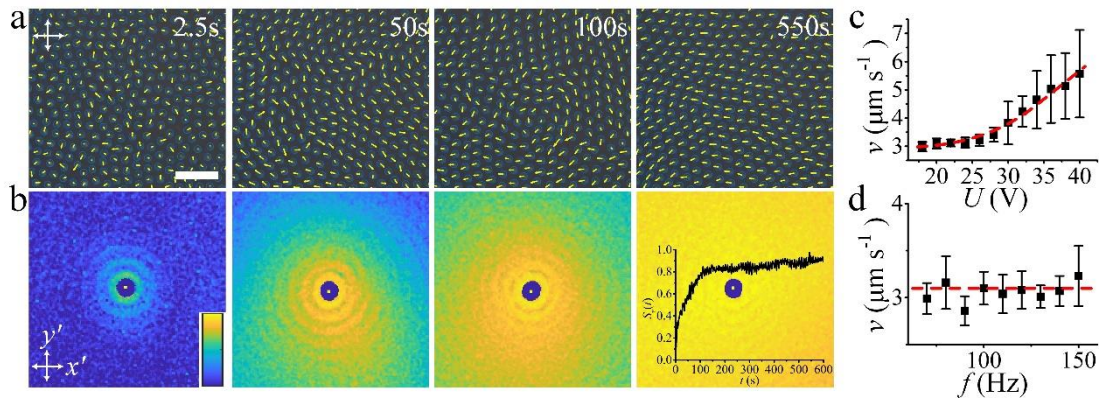
Figure 3-6 Temporal evolution of directron velocities and their dependence on electric fields. (a) Polarizing micrographs of directrons at $U = 20$ V, $f = 100$ Hz, with their velocities represented as yellow arrows. Scale bar 50 μm. The crossed polarizers are indicated as white arrows. The time after the application of the electric field is indicated in each image. (b) 2D spatial velocity correlation functions corresponding to (a) colored according to the color bar which changes linearly from 0 (dark blue) to 1 (light yellow). Image sizes represent 200 μm × 200 μm. The inset shows the temporal evolution of the velocity order parameter, $S_v(t)$. The 2D spatial velocity correlation functions are averaged over 5 seconds (10 frames). (c) The dependence of directron velocity on voltage at fixed frequency ($f = 100$ Hz). (d) The dependence of directron velocity on frequency at fixed voltage ($U = 20$ V). The error bars are calculated from the standard deviation of velocities of hundreds of different directrons.

At high packing fractions, the applied **E** initially induces random motion of directrons.

Unlike the behavior at relatively low population density where dynamic flocks of directrons form with time (Figure 3-3), the directrons here collide and interact with each other, leading to a large-scale emergent coherent directional motion (Figure 3-6 (a), Supplementary Movie 3-5). This behavior arises from many-body interactions between directrons as predicted by the "Vicsek model" where active, point-like particles interact so that they tend to align their velocities with those of their neighbors. The velocity order parameter, S_v, which characterizes the degree of ordering of directron velocities, gradually increases from ~0.1 to ~0.8 within tens of seconds and saturates at $S_v \sim 0.9$ (Figure 3-6 (b) inset), indicating the emergence of coherent unidirectional motion of directrons. As a result, the spatial velocity correlation function becomes more and more long-range (Figure 3-6 (b)). Such a phenomenon is usually seen in everyday life as one walks towards a group of pigeons. The pigeons are startled and take off en masse. Initially, they fly in random directions, but soon the flock orders and moves away coherently.
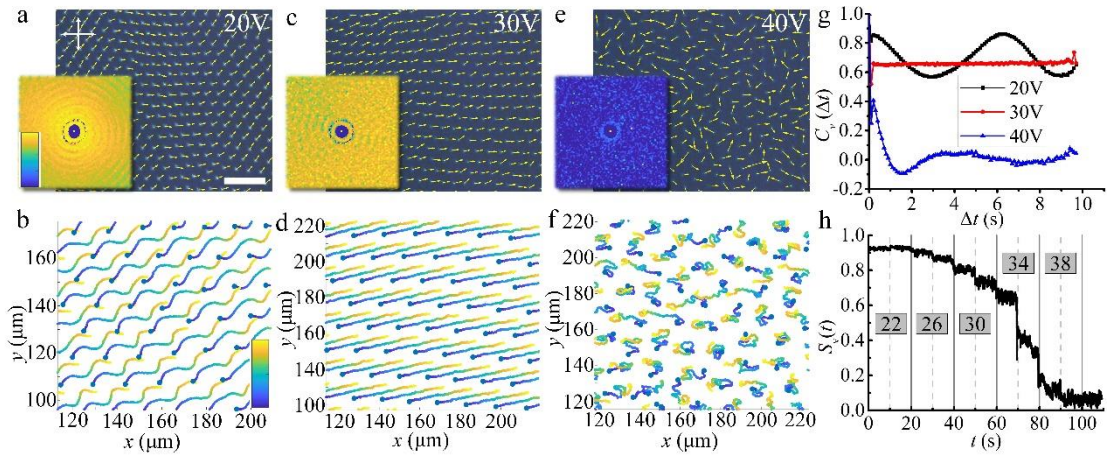
Figure 3-7 Voltage dependence of collective motion. Polarizing micrographs of directrons at (a) U = 20 V, (c) U = 30 V, and (e) U = 40 V, respectively, with their velocities represented as yellow arrows. The frequency is fixed at f = 100 Hz. Scale bar 50 μm. The crossed polarizers are indicated as white arrows. The insets are the corresponding 2D spatial velocity correlation functions colored according to the color bar which changes linearly from 0 (dark blue) to 1 (light yellow). The image sizes represent an area of 200 μm × 200 μm. The 2D spatial velocity correlation functions are averaged over 10 seconds (20 frames). Trajectories of directrons at (b) U = 20 V, (d) U = 30 V, and (f) U = 40 V, respectively, colored with time corresponding to the color bar which changes linearly from t = 0 s (dark blue) to t = 10 s (light yellow). (g) The temporal velocity correlation functions ($C_v(\Delta t)$) of directrons at different voltages corresponding to (a), (c), and (e). (h) Time dependence of the velocity order parameter, S_v, with the applied voltage (indicated as numbers in gray squares) gradually increasing from 20 V to 40 V in a steps of 2 V every 10 s.

The velocity of the directrons is also dependent on the electric field. The amplitude of the directron velocity, v, increases with increasing applied voltage but shows no obvious dependence on the frequency of the electric field (Figure 3-6 (c) and (d)). At the same time, by tuning the applied voltage, the directrons show different collective dynamic behaviors

(Figure 3-7, Supplementary Movie 3-6). It is observed that the collective motion of directrons gradually transforms from a wavy motion (Figure 3-7 (a) and (b)) to a linear motion (Figure 3-7 (c) and (d)) with increasing voltage. Although, the spatial velocity correlation functions at $U = 20$ V and $U = 30$ V are similar to each other which show strong long-range correlation (insets in Figure 3-7 (a) and (c)), the temporal velocity correlation functions ($C_v(\Delta t)$) are very different from each other. The $C_v(\Delta t)$ at $U = 20$ V changes periodically and forms a sinusoidal wave, which is due to the wavy motion of the directrons (Figure 3-7 (g)). At $U = 30$ V, the $C_v(\Delta t)$ keeps constant which is in accordance with the linear motion of the directrons (Figure 3-7 (g)). At $U = 40$ V (Figure 3-7 (e) and (f)), a chaotic incoherent motion is observed where the directrons move randomly with only weak velocity correlation at very short ranges (Figure 3-7 (e) inset). The $C_v(\Delta t)$ firstly decays to zero within 1 second and then develops a negative correlation with a minimum at $\Delta t \sim 1.5$ s, which then gradually increases to 0 (Figure 3-7 (g)). The temporal velocity correlation functions at varied voltages all show a two-step relaxation. The first relaxation always occurs immediately within 0.1 seconds, which is barely resolved. Such a two-step relaxation has also been observed in bacteria suspensions [59]. The velocity order parameter, S_v, gradually decreases with increasing voltage at first, but then suddenly decreases from ~0.7 to ~0.4 at $U = 34$ V and eventually falls to 0 at $U = 38$V (Figure 3-7 (h)). Such an order-disorder transition is due to the increase of the background noise of the system [3], which can be caused by different reasons, such as the increase of the velocity of the directrons, the distortion of the directron structures, the ion injection, the hydrodynamic flow induced by the motion of directrons, etc. Such a phenomenon is also observed in other active systems, such as granular systems in which the systems show an order-disorder transition by increasing the amplitude of the vibration of the system [60].
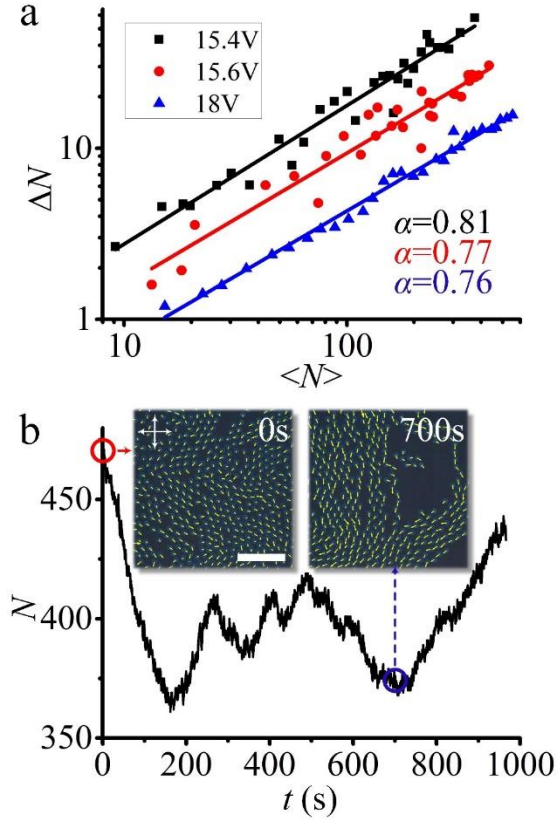
Figure 3-8 Anomalous density fluctuations in collectively moving directrons. (a) The log-log plot of the standard deviation ΔN verses the mean directron number $<N>$ for three different voltages: $U = 15.4$ V (black squares), $U = 15.6$ V (red circles) and $U = 18.0$ V (blue triangles). The frequency is fixed at $f = 100$ Hz. Solid lines are the linear fits of the experimental data. (b) Total number of directrons, N, in the field of view (306 μm * 306 μm) as a function of time. The insets show the polarizing micrographs of the directrons at $t = 0$ s (red circle) and $t = 700$ s (blue circle), respectively, with their velocities represented as yellow arrows. $U = 15.6$ V, $f = 100$ Hz. Scale bar 100 μm. The crossed polarizers are indicated as white arrows.

Directrons in flocks are packed closely, which cause high local density. At the same time, these flocks are mobile and they usually leave empty space in regions they just travel through, leading to low density in those regions. As a result, dynamic flocks produce large density fluctuations, as shown by the time evolution of the total number of directrons, N, in the whole viewing area in Figure 3-8 (b). This measurement shows a maximum about 1.4 times as large as the minimum and a standard deviation of $\Delta N \sim 31$, which is about 7.6% of the mean $<N>$ = 406. Apart from the large magnitude, the standard deviations scale with the means differently from those in thermodynamic equilibrium systems, where fluctuations obey the central limit theorem, $\Delta N \propto <N>^{1/2}$ [61-63]. In Figure 3-8 (a), it is found that directrons in flocks exhibit anomalous density fluctuations, also called giant number fluctuations [61]. For three different directron densities (voltages), the standard deviation ΔN grows more rapidly than $<N>^{1/2}$ and scales as $\Delta N \propto <N>^{\alpha}$, where $\alpha \sim 0.785 \pm 0.025$. Such giant number fluctuations have been reported in numerical simulations of self-propelled polar particles

94

where $\alpha = 0.8$ is found [62] as well as in collective motion of bacteria where $\alpha = 0.75$ is reported [9], which are close to the values measured for directrons here.

3.3.5 Recurring transient vortices and jets
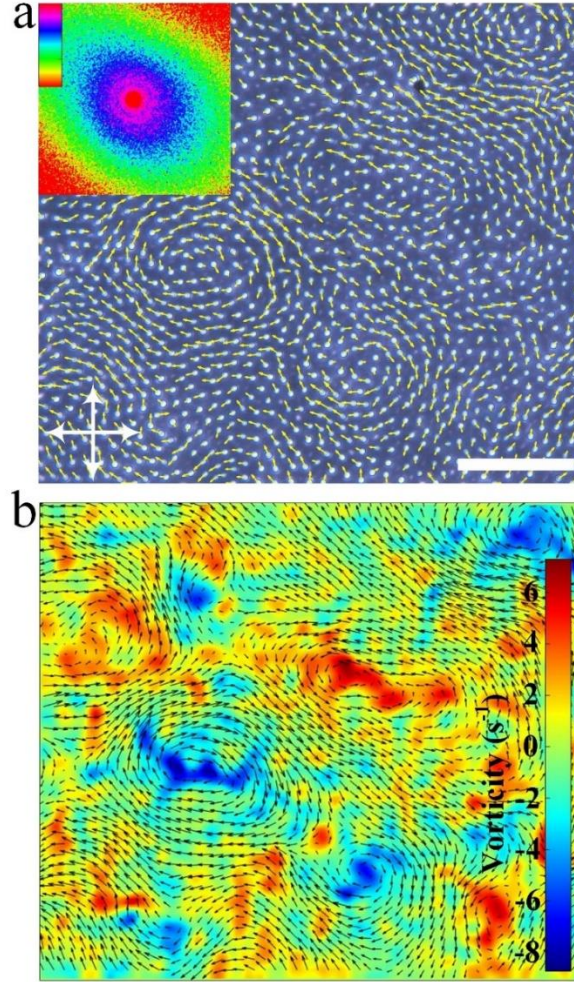
Figure 3-9 Instantaneous velocity field of directrons. (a) Polarizing microscopy of directrons with their velocities represented as small yellow arrows. $U = 100$ V, $f = 500$ Hz. The crossed white arrows indicate the polarizers. Scale bar 200 μm. The inset represents the corresponding 2D spatial velocity correlation function colored according to the color bar which changes linearly from -0.2 to 1. The image size of the 2D velocity spatial correlation function represent an area of 400 μm × 400 μm. The 2D spatial velocity correlation functions are averaged over ~1.4 seconds (20 frames). (b) Color map of vortices. The bar shows a linear scale of vorticity. The black arrows show the PIV flow field.

The emergence of transient vortices and jets in ensembles of self-propelling agents has been observed in various active systems, such as swarming bacteria [59], vibrating granular particles [64], and active colloidal systems [65]. We show that similar patterns can also be generated in our system. Here, the same LC material is filled into a homogeneous cell with a larger cell gap ($d \sim 19.7$ μm). By increasing the applied voltage to some specific values, hundreds and thousands of directrons emerge and exhibit a "turbulent" swimming pattern

manifested by recurring transient vortices and jets (Figure 3-9). The size of the directrons is slightly larger than the ones mentioned above (Supplementary Figure 3-4). The instantaneous velocity field of the directrons in Figure 3-9 reveal intense vortices with the length scales over hundreds of micrometers which are significantly exceeding the size of individual directions. The vortices spontaneously form from time to time throughout the sample. However, they are not stable as they gradually move through the nematic bulk and disappear within seconds (Supplementary Movie 3-7). The directrons show strong short-range but weak long-range velocity correlation during motion (Figure 3-9 (a) inset). The spatial velocity correlation function ($g_v(r)$) also develops an anisotropic profile and shows strong negative correlations at distances $r \sim 200$ μm which corresponds to the characteristic length scale of the vortices. Such negative velocity correlations are due to the formation of the vortices and have also been reported in turbulent bacteria suspensions [59] and active colloidal systems [66]. The temporal velocity correlation function ($C_v(\Delta t)$) also shows a two-step relaxation (Supplementary Figure 3-5) like the ones in Figure 3-7 (g), which firstly decreases to ~0.75 within 0.1 seconds, and then gradually decays to 0. The second relaxation demonstrates the process of the disintegration of coherent structures, which decays slowly within seconds (Supplementary Figure 3-5). Figure 3-9 (b) shows the instantaneous distribution and amplitude of the vortices obtained through particle image velocimetry (PIV). The formation of such a "turbulent" swimming pattern in cells with larger cell gap can possibly be attributed to the larger space between the directrons and the larger velocity of the directrons which induce complicated hydrodynamic interactions between directrons. More details about such a turbulent collective behavior will be reported elsewhere.

3.3.6 Circular collective motion of directrons commanded by topological defects
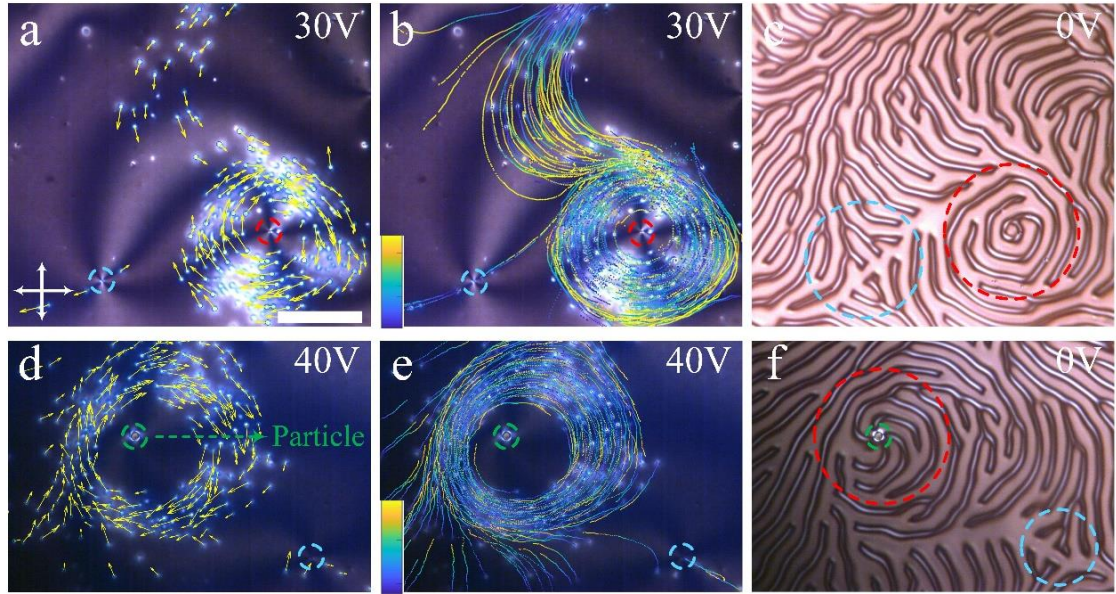
Figure 3-10 Circular motion of directron flocks. Polarizing micrographs of circulating motion of directrons around (a) a $s = +1$ defect at $f = 100$ Hz, $U = 30$ V and (d) a micro-particle at $f = 60$ Hz, $U = 40$ V with their velocities represented as yellow arrows. Polarizing micrographs of circulating motion of directrons around (b) a $s = +1$ defect and (e) a micro-particle with their trajectories colored with time corresponding to the color bar. The color bars change linearly from (b) $t = 0$ s (dark blue) to $t = 10$ s (light yellow) and (e) $t = 0$ s (dark blue) to $t = 8.6$ s (light yellow), respectively. (c) and (f) Polarizing micrographs of the fingerprint textures at $U = 0$ V. Scale bar 100 μm. The crossed polarizers are indicated as white arrows. The $s = +1$ defects and $s = -1$ defects are circled with red and blue dashed lines, respectively. The micro-particle is circled with a green dashed line.

It was reported that bacteria can sense the topological strength of defects and move around defects of a positive topological strength ($s > 0$) and avoid negative strength defects ($s < 0$) [37]. A similar phenomenon is also observed in this soliton system. Here, the LC sample is confined between two substrates with homeotropic anchoring conditions (cell gap $d \sim 9.4$ μm). It should be noted that the LC material used here has a pitch ($p = 10$ μm) larger than the ones used in previous experiments ($p = 2$ μm). The reason that we choose a larger pitch here is because there will be a lot of complicated topological defects and disclinations if the pitch is small, which will trap and hinder the motion of directrons. By applying an electric field normal to the cell substrates, due to the negative dielectric anisotropy ($\Delta\varepsilon < 0$) of the LC molecules, the director field is reoriented into the xy plane parallel to the cell substrates, leading to the formation of umbilic defects with topological strength, $s = \pm1$ [38,67]. One may suggest that these defects are the dowser textures [68] since they look similar to the umbilic defects in polarizing microscopy. However, the core of the dowser texture is a hedgehog

point defect whose size cannot be tuned by the electric field (although it can be transformed into a looped line defect) [69]. The size of the defect core observed here can be continuously changed by tuning the applied electric field (Supplementary Figure 3-6 and 3-7) which is consistent with the property of umbilic defects whose structure is nonsingular[67]. At the same time, directrons are also generated throughout the sample. The director structure of the directions observed here maybe slightly different from the ones described above due to the larger pitch. However, they are of the same type because they show similar formation, stability and dynamics. It is found that the directrons travel towards the defects with $s = +1$ and gather into circulating flocks which move coherently around the $s = +1$ cores. In contrast, the directrons deplete from the defects with $s = -1$, moving away from them (Figure 3-10 (a) and (b), Supplementary Movie 3-8). Moreover, the pair of $s = \pm 1$ defects can also be generated by introducing micro-particles into the system, where the micro-particles act as the cores of the $s = +1$ defects and simultaneously induce an accompanied $s = -1$ defect nearby [38]. Similarly, the directrons swarm around the micro-particles and avoid the $s = -1$ defects (Figure 3-10 (d) and (e), Supplementary Movie 3-9). By turning off the electric field, the directrons disappear immediately and the sample turns into a fingerprint texture, from which the topological strength of the defects can be deduced (Figure 3-10 (c) and (f)). Guiding the motion of solitons with umbilic defects was also recently reported by Sohn et al. [70]. However, unlike the directrons here which are trapped and persistently swirling around the $s = +1$ defect but repelled by the $s = -1$ defect, the solitons, (skyrmions, in their case), are deflected and sidetracked by the umbilic defects.

3.4 Discussion and conclusion

Collective behavior has been broadly studied in different kinds of systems, including bacteria suspensions [9], driven filaments [7], granular systems [64], and various active colloidal systems [10,65]. Recently, such a behavior is also realized with topological soltions in cholesteric LC systems by Sohn et al. [11,70]. In their studies, hundreds and thousands of topological solitons, skyrmions, are generated and driven into random motions by electric fields which immediately synchronize their motions within seconds and exhibit collective motions along spontaneously-chosen directions. However, there are only limited types of

collective behavior of this electrically-driven active motion, and all skyrmions, even at very low packing fractions, tend to synchronize to move together at a constant velocity and in the same direction [11]. Although, more complicated collective behaviors of the skyrmions were realized by the authors later through optical manipulation [70], the setup of the experimental system is relatively complicated which includes optical manipulations tools, such as laser tweezers, and photosensitive chiral dopants. Moreover, the types of collective behaviors in those systems are still limited where self-organization of flocks, fission and fusion process, density dependent collective motion, swirling and vortices, etc. are not reported.

One may suspect that the directrons observed here are "torons" or "skyrmions" [23]. However, the solitons here show a frequency dependent stability, i.e., the solitons disappear at fixed voltages by changing the frequency only. The voltage threshold of the generation of the solitons is also dependent on frequency (Figure 3-1 (c) and Supplementary Figure 3-8). Such a frequency dependent stability is not observed if the solitons are torons or skyrmions since their stability is guaranteed by their topological structure and is independent on the frequency of the applied electric field [28]. Moreover, the generation of torons or skyrmions usually requires a symmetry breaking transition of the LC system which can be induced by phase transition [23], Freedericksz transition [28] or strong electro-hydrodynamic instabilities [11]. However, since the dielectric anisotropy of the LC media here is negative, there is no Freedericksz transition in cells of planar alignment. For samples of homeotropic alignment, the solitons have a threshold higher than the threshold of the Freedericksz transition (Supplementary Figure 3-8), i.e., before the formation of the solitons, the LC sample has changed from the homeotropic structure to the translationally invariant configuration. Due to the conservation of the topological charge of the LC system, one cannot continuously create topological solitons from a topologically trivial homogeneous state (no electro-hydrodynamic instability is observed during the formation of solitons). Furthermore, torons or skyrmions can only exist at relatively low voltages. If the applied voltage is too high, they will either disappear (in cells of planar alignment) [28] or transform into pairs of umbilic defects (in cells of homeotropic alignment) [71]. However, the solitons here are stable even at very large voltages ($U > 60$ V at $f = 100$ Hz). Thus one can conclude that the solitons here are not torons or skyrmions, but directrons.

Topological trivial particle-like localized dissipative solitary director waves, i.e.,

directrons, have received great attention recently due to their intriguing nonlinear dynamic properties and potential applications in various areas such as microfluidics and optics [29-34]. We have shown previously that by adding chirality to the nematic LC system, the directrons can either pass through each other or collide and reflect into opposite directions during collisions [31,32]. Here, we show that by further decreasing the pitch of the LC system, the directrons can behave like true particles which collide without passing through each other and exhibit short-range repulsive but long-range attractive interactions. Unlike the directrons in achiral nematics and chiral nematics of large pitches reported earlier, which can only move in specific directions [29-31], the directrons here are equally likely to move in any direction in the xy plane and can easily change their directions during motion due to the small pitch chiral system, thus leading to the emergence of various collective behaviors. The directrons are propelled by the periodic oscillation of the director field and their moving direction is determined by their symmetry breaking structure. The directrons self-organize into finite flocks which move in random directions with no correlations. They collide and fragment during motion. Within flocks, individual directrons move coherently in the same direction. At high packing fractions, directrons start from random motion and synchronize their motion and develop polar ordering through many-body interactions. The travelling directrons even self-organize into large-scale transient vortices and jets. The motion of the directrons cause large fluctuations in population density, which exhibit an anomalous scaling with system sizes. Impressively, the collective motion of the directrons can be facilely controlled by the electric field and topological defects. Our findings show that active matter composed of directrons can be used as an excellent model system for studying general principles of collective motion. The facile fabrication, control and observation of our system also make it potentially promising for studying many other non-equilibrium phenomena, such as non-equilibrium phase transition [72], motility induced phase separation [73], out-of-equilibrium self-organization [74], etc. Since the directrons are actually self-localized director deformations and can be easily controlled through electric fields, they may even lead to new applications in microfluidics, such as micro-cargo transport [31,40], and electro-optics, such as tunable holographic optical devices.

3.5 Acknowledgement

3.6 References

1   Vicsek, T. & Zafeiris, A. Collective motion. *Physics Reports* **517**, 71-140 (2012).
2   Toner, J. & Tu, Y. Long-range order in a two-dimensional dynamical XY model: how birds fly together. *Physical review letters* **75**, 4326 (1995).
3   Vicsek, T., Czirók, A., Ben-Jacob, E., Cohen, I. & Shochet, O. Novel type of phase transition in a system of self-driven particles. *Physical review letters* **75**, 1226 (1995).
4   Helbing, D., Farkas, I. & Vicsek, T. Simulating dynamical features of escape panic. *Nature* **407**, 487-490 (2000).
5   Dombrowski, C., Cisneros, L., Chatkaew, S., Goldstein, R. E. & Kessler, J. O. Self-concentration and large-scale coherence in bacterial dynamics. *Physical review letters* **93**, 098103 (2004).
6   Cisneros, L. H., Cortez, R., Dombrowski, C., Goldstein, R. E. & Kessler, J. O. in *Animal Locomotion* 99-115 (Springer, 2010).
7   Sanchez, T., Chen, D. T. N., DeCamp, S. J., Heymann, M. & Dogic, Z. Spontaneous motion in hierarchically assembled active matter. *Nature* **491**, 431 (2012).
8   Ramaswamy, S. The mechanics and statistics of active matter. *Annu. Rev. Condens. Matter Phys.* **1**, 323-345 (2010).
9   Zhang, H.-P., Be'er, A., Florin, E.-L. & Swinney, H. L. Collective motion and density fluctuations in bacterial colonies. *Proceedings of the National Academy of Sciences* **107**, 13626-13630 (2010).
10   Bricard, A., Caussin, J.-B., Desreumaux, N., Dauchot, O. & Bartolo, D. Emergence of macroscopic directed motion in populations of motile colloids. *Nature* **503**, 95-98 (2013).
11   Sohn, H. R. O., Liu, C. D. & Smalyukh, I. I. Schools of skyrmions with electrically tunable elastic interactions. *Nature Communications* **10**, 4744 (2019).
12   Russell, J. S. Report on waves. *Report of the fourteenth meeting of the British Association for the Advancement of Science*, 311-390 (1844).
13   Zabusky, N. J. & Kruskal, M. D. Interaction of "Solitons" in a Collisionless Plasma and the Recurrence of Initial States. *Physical Review Letters* **15**, 240-243 (1965).
14   Du, L., Yang, A., Zayats, A. V. & Yuan, X. Deep-subwavelength features of photonic skyrmions in a confined electromagnetic field with orbital angular momentum. *Nature Physics* **15**, 650-654 (2019).
15   Ray, M. W., Ruokokoski, E., Kandel, S., Möttönen, M. & Hall, D. Observation of Dirac monopoles in a synthetic magnetic field. *Nature* **505**, 657-660 (2014).
16   Harada, K. *et al.* Real-time observation of vortex lattices in a superconductor by electron microscopy. *Nature* **360**, 51-53 (1992).

17	Yu, X. *et al.* Real-space observation of a two-dimensional skyrmion crystal. *Nature* **465**, 901-904 (2010).

18	Kartashov, Y. V., Astrakharchik, G. E., Malomed, B. A. & Torner, L. Frontiers in multidimensional self-trapping of nonlinear fields and matter. *Nature Reviews Physics* **1**, 185-197 (2019).

19	Lam, L. & Prost, J. *Solitons in liquid crystals*. (Springer Science & Business Media, 2012).

20	Helfrich, W. Alignment-Inversion Walls in Nematic Liquid Crystals in the Presence of a Magnetic Field. *Physical Review Letters* **21**, 1518-1521 (1968).

21	Lowe, M. & Gollub, J. P. Solitons and the commensurate-incommensurate transition in a convecting nematic fluid. *Physical Review A* **31**, 3893-3897 (1985).

22	Migler, K. B. & Meyer, R. B. Solitons and pattern formation in liquid crystals in a rotating magnetic field. *Physical Review Letters* **66**, 1485-1488 (1991).

23	Smalyukh, I. I., Lansac, Y., Clark, N. A. & Trivedi, R. P. Three-dimensional structure and multistable optical switching of triple-twisted particle-like excitations in anisotropic fluids. *Nature Materials* **9** (2009).

24	Ackerman, P. J. & Smalyukh, I. I. Diversity of Knot Solitons in Liquid Crystals Manifested by Linking of Preimages in Torons and Hopfions. *Physical Review X* **7**, 011006 (2017).

25	Leger, L. Observation of wall motions in nematics. *Solid State Communications* **10**, 697-700 (1972).

26	Guozhen, Z. Experiments on Director Waves in Nematic Liquid Crystals. *Physical Review Letters* **49**, 1332-1335 (1982).

27	Ackerman, P. J., Boyle, T. & Smalyukh, I. I. Squirming motion of baby skyrmions in nematic fluids. *Nature Communications* **8**, 673 (2017).

28	Shen, Y. & Dierking, I. Electrically Driven Formation and Dynamics of Skyrmionic Solitons in Chiral Nematics. *Physical Review Applied* **15**, 054023 (2021).

29	Li, B.-X. *et al.* Electrically driven three-dimensional solitary waves as director bullets in nematic liquid crystals. *Nature Communications* **9**, 2912 (2018).

30	Li, B.-X., Xiao, R.-L., Paladugu, S., Shiyanovskii, S. V. & Lavrentovich, O. D. Three-dimensional solitary waves with electrically tunable direction of propagation in nematics. *Nature Communications* **10**, 3749 (2019).

31	Shen, Y. & Dierking, I. Dynamics of electrically driven solitons in nematic and cholesteric liquid crystals. *Communications Physics* **3**, 1 (2020).

32	Shen, Y. & Dierking, I. Dynamic dissipative solitons in nematics with positive anisotropies. *Soft Matter* **16**, 5325 (2020).

33	Shen, Y. & Dierking, I. Electrically driven formation and dynamics of swallow-tail solitons in smectic A liquid crystals. *Materials Advances* **2**, 4752-4761 (2021).

34	Aya, S. & Araoka, F. Kinetics of motile solitons in nematic liquid crystals. *Nature communications* **11**, 1-10 (2020).

35	Lavrentovich, O. D. Design of nematic liquid crystals to control microscale dynamics. *Liquid Crystals Reviews* **8**, 59-129 (2020).

36	Brand, H. R., Fradin, C., Finn, P. L., Pesch, W. & Cladis, P. E. Electroconvection in nematic liquid crystals: comparison between experimental results and the hydrodynamic model. *Physics Letters A* **235**, 508-514 (1997).

37	Peng, C., Turiv, T., Guo, Y., Wei, Q.-H. & Lavrentovich, O. D. Command of active

matter by topological defects and patterns. *Science* **354**, 882 (2016).

38   Shen, Y. & Dierking, I. Annihilation dynamics of topological defects induced by microparticles in nematic liquid crystals. *Soft Matter* **15**, 8749 (2019).

39   Goodman, A. M. Optical interference method for the approximate determination of refractive index and thickness of a transparent layer. *Appl. Opt.* **17**, 2779-2787 (1978).

40   Li, B.-X., Xiao, R.-L., Shiyanovskii, S. V. & Lavrentovich, O. D. Soliton-induced liquid crystal enabled electrophoresis. *Physical Review Research* **2**, 013178 (2020).

41   Klamser, J. U., Kapfer, S. C. & Krauth, W. Thermodynamic phases in two-dimensional active matter. *Nature communications* **9**, 1-8 (2018).

42   Lin, B.-J. & Chen, L.-J. Phase transitions in two-dimensional colloidal particles at oil/water interfaces. *The Journal of chemical physics* **126**, 034706 (2007).

43   Pikin, S. A. On the Structural Instability of a Nematic in an Alternating Electric Field and Its Connection with Convection and the Flexoelectric Effect. *Journal of Surface Investigation: X-ray, Synchrotron and Neutron Techniques* **13**, 1078-1082 (2019).

44   Pikin, S. A. Dynamic Charged Structures in Nematics with Negative Anisotropy of Electroconductivity. *Journal of Experimental and Theoretical Physics* **132**, 637-640 (2021).

45   Nakagawa, M. & Akahane, T. A new type of electrohydrodynamic instability in nematic liquid crystals with positive dielectric anisotropy. I. The existence of the charge injection and the diffusion current. *Journal of the Physical Society of Japan* **52**, 3773-3781 (1983).

46   Arnould-netillard, H. & Rondelez, F. Electrohydrodynamic Instabilities in Cholesteric Liquid Crystals with Negative Dielectric Anisotropy. *Molecular Crystals and Liquid Crystals* **26**, 11-31 (1974).

47   Huh, J.-H. & Osoguchi, H. Formation of grid patterns in an ac-driven electroconvection system. *Physical Review E* **101**, 062701 (2020).

48   Ibragimov, T. D. Influence of fullerenes C60 and single-walled carbon nanotubes on the Carr–Helfrich effect in nematic liquid crystal. *Optik*, 166768 (2021).

49   Carr, E. F. Influence of Electric Fields on the Molecular Alignment in the Liquid Crystal p-(Anisalamino)-phenyl Acetate. *Molecular Crystals* **7**, 253-268 (1969).

50   Helfrich, W. Conduction-Induced Alignment of Nematic Liquid Crystals: Basic Model and Stability Considerations. *The Journal of Chemical Physics* **51**, 4092-4105 (1969).

51   Turiv, T. *et al.* Effect of Collective Molecular Reorientations on Brownian Motion of Colloids in Nematic Liquid Crystal. *Science* **342**, 1351 (2013).

52   De Gennes, P.-G. & Prost, J. *The physics of liquid crystals (2nd Edition)*. Vol. 83 (Oxford university press, 1993).

53   Toner, J. & Tu, Y. Flocks, herds, and schools: A quantitative theory of flocking. *Physical review E* **58**, 4828 (1998).

54   Schaller, V. & Bausch, A. R. Topological defects and density fluctuations in collectively moving systems. *Proceedings of the National Academy of Sciences* **110**, 4488-4493 (2013).

55   Flierl, G., Grünbaum, D., Levins, S. & Olson, D. From individuals to aggregations: the interplay between behavior and physics. *Journal of Theoretical biology* **196**, 397-454 (1999).

56   Okubo, A. Dynamical aspects of animal grouping: swarms, schools, flocks, and herds.

Advances in biophysics **22**, 1-94 (1986).

57   Niwa, H.-S. Migration dynamics of fish schools in heterothermal environments. *Journal of theoretical biology* **193**, 215-231 (1998).

58   Niwa, H.-S. School size statistics of fish. *Journal of theoretical biology* **195**, 351-361 (1998).

59   Zhang, H., Be'Er, A., Smith, R. S., Florin, E.-L. & Swinney, H. L. Swarming dynamics in bacterial colonies. *EPL (Europhysics Letters)* **87**, 48011 (2009).

60   Olafsen, J. & Urbach, J. Two-dimensional melting far from equilibrium in a granular monolayer. *Physical review letters* **95**, 098002 (2005).

61   Narayan, V., Ramaswamy, S. & Menon, N. Long-lived giant number fluctuations in a swarming granular nematic. *Science* **317**, 105-108 (2007).

62   Chaté, H., Ginelli, F., Grégoire, G. & Raynaud, F. Collective motion of self-propelled particles interacting without cohesion. *Physical Review E* **77**, 046113 (2008).

63   Kudrolli, A., Lumay, G., Volfson, D. & Tsimring, L. S. Swarming and swirling in self-propelled polar granular rods. *Physical review letters* **100**, 058001 (2008).

64   Blair, D. L., Neicu, T. & Kudrolli, A. Vortices in vibrated granular rods. *Physical Review E* **67**, 031303 (2003).

65   Han, K. *et al.* Emergence of self-organized multivortex states in flocks of active rollers. *Proceedings of the National Academy of Sciences* **117**, 9706-9711 (2020).

66   Zhang, B., Sokolov, A. & Snezhko, A. Reconfigurable emergent patterns in active chiral fluids. *Nature communications* **11**, 1-9 (2020).

67   Dierking, I., Marshall, O., Wright, J. & Bulleid, N. Annihilation dynamics of umbilical defects in nematic liquid crystals under applied electric fields. *Physical Review E* **71**, 061709 (2005).

68   Pieranski, P. & Godinho, M. H. Physics of the Dowser Texture. *Liquid Crystals: New Perspectives*, 193-309 (2021).

69   Gilli, J., Thiberge, S., Vierheilig, A. & Fried, F. Inversion walls in homeotropic nematic and cholesteric layers. *Liquid crystals* **23**, 619-628 (1997).

70   Sohn, H. R., Liu, C. D., Voinescu, R., Chen, Z. & Smalyukh, I. I. Optically enriched and guided dynamics of active skyrmions. *Opt. Express* **28**, 6306-6319 (2020).

71   Nagaya, T., Hotta, H., Orihara, H. & Ishibashi, Y. Observation of annihilation process of disclinations emerging from bubble domains. *Journal of the Physical Society of Japan* **60**, 1572-1578 (1991).

72   Bialké, J., Speck, T. & Löwen, H. Crystallization in a dense suspension of self-propelled particles. *Physical review letters* **108**, 168301 (2012).

73   Buttinoni, I. *et al.* Dynamical clustering and phase separation in suspensions of self-propelled colloidal particles. *Physical review letters* **110**, 238301 (2013).

74   Manoharan, V. N. Colloidal matter: Packing, geometry, and entropy. *Science* **349**, 942 (2015).

3.7 Supplementary Information

3.7.1 Supplementary Figures:
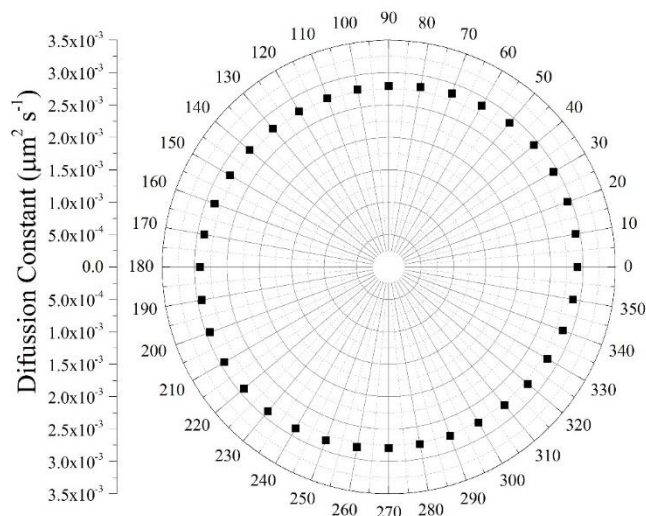
Supplementary Figure 3-1 Angular dependencies of the diffusion coefficient of a colloidal micro-particle. The colloidal micro-particle (diameter ~3 μm) is dispersed in a chiral nematic ($p \sim 2$ μm) which is filled in a cell ($d \sim 10$ μm) with planar alignment. The sample is heated to 75 ℃.
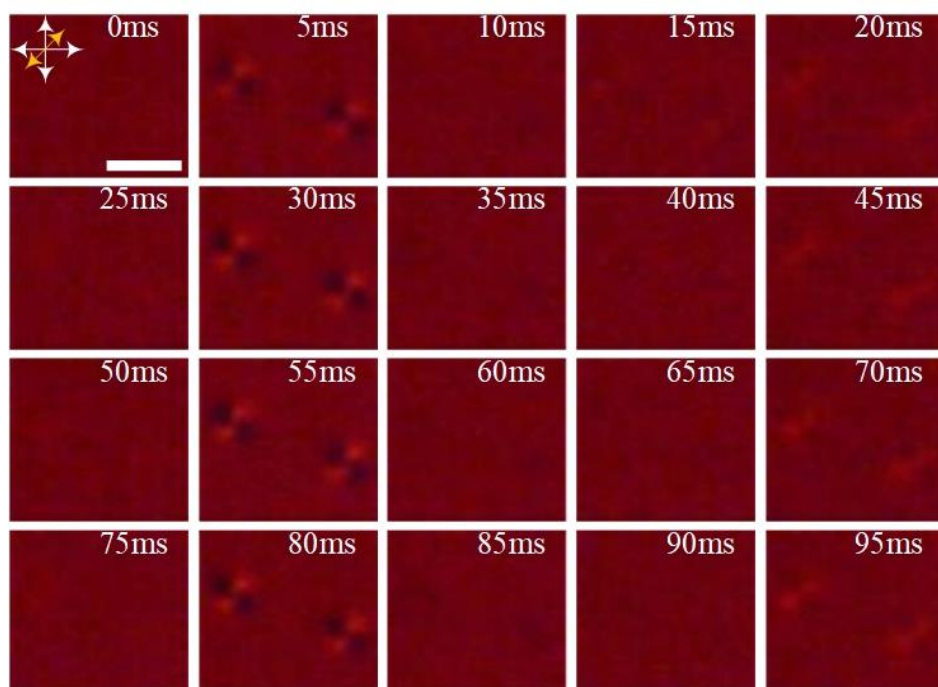
Supplementary Figure 3-2 Time series of polarizing micrographs of directrons. The directrons are modulated by an AC electric field of $U = 20$ V, $f = 20$ Hz. The corssed white arrows represent polarizers and the yellow arrow represent the optical axis of the λ-plate. Scale bar 10 μm.
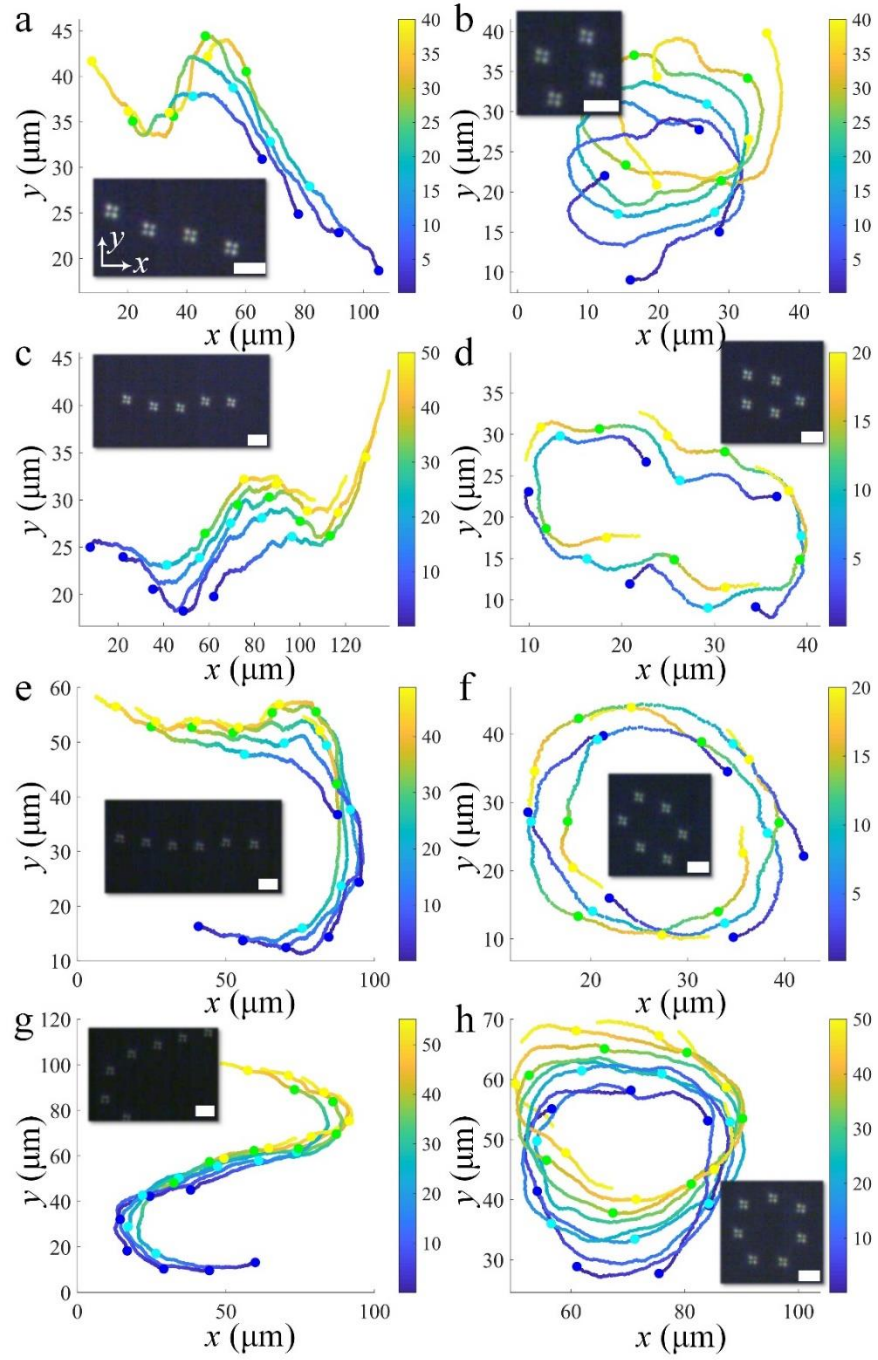
Supplementary Figure 3-3 Dynamics of directron flocks. Trajectories of different number of directrons colored with time corresponding to the color bars (unit (s)) at $U = 15.4$ V, $f = 100$ Hz. **a** and **b**, four directrons; **c** and **d**, five directrons; **e** and **f**, six directrons; **g** and **h**, seven directrons. In **a**, **c**, **e**, and **g**, the directrons form linear chains which move coherently. In **b**, **d**, **f**, and **h**, the directrons form closed loops which rotate continuously about their rotation axes. The insets show the micrographs of the corresponding directrons. Scale bar 10 μm. Polarizers are parallel to the *x*- and *y*-axes, respectively.
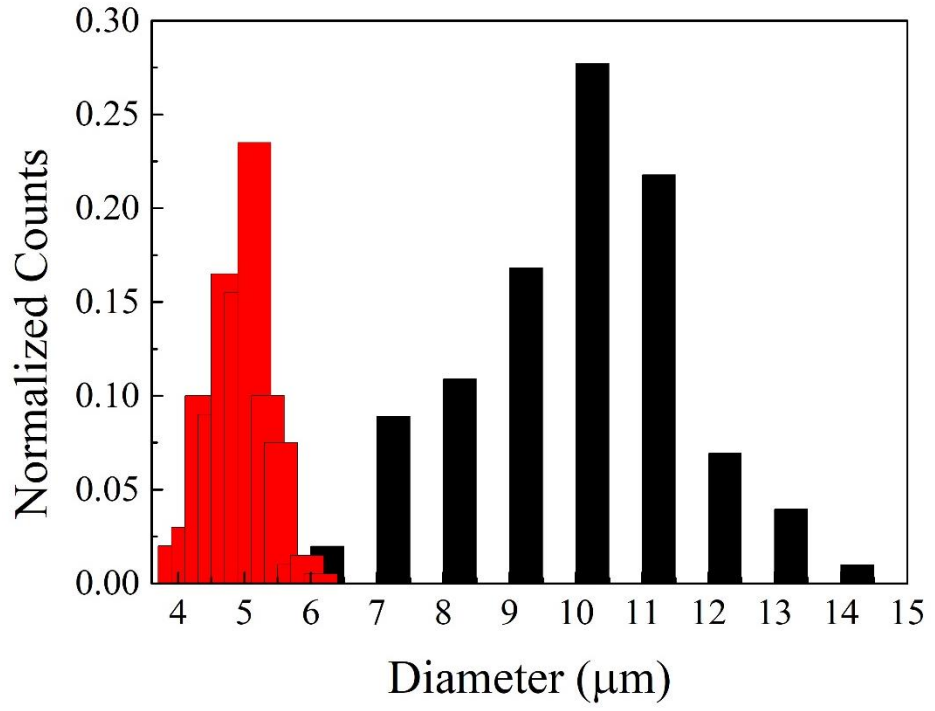
Supplementary Figure 3-4 Directron size distribution. The red bars represent the directrons in homogeneous alignment cells with cell gap $d \sim 9.5$ μm, $U = 20$ V, $f = 100$ Hz. The black bars represent the directrons in homogeneous alignment cells with cell gap $d \sim 19.7$ μm, $U = 100$ V, $f = 500$ Hz.
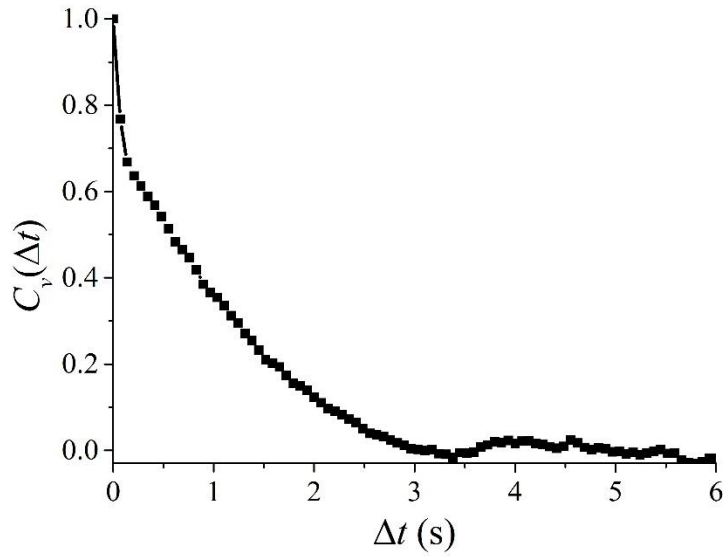
Supplementary Figure 3-5 Temporal velocity correlation function. The temporal velocity correlation function of directrons corresponding to Figure 3-9. $U = 100$ V, $f = 500$ Hz.
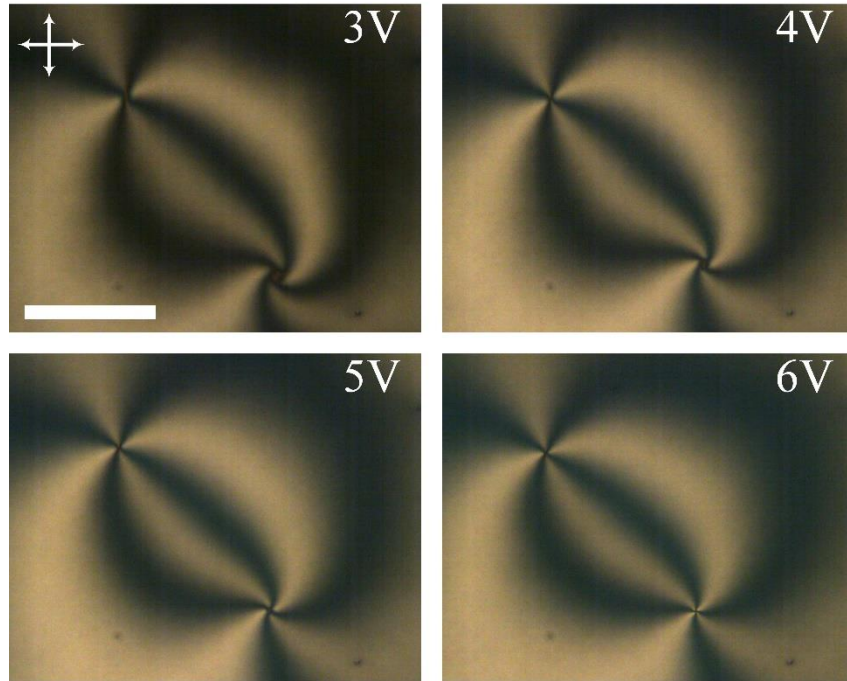
Supplementary Figure 3-6 POM image of a pair of umbilic defects at varied voltages. Demonstration of the size variation of defect cores with increasing voltage. f = 100 Hz. Scale bar 100 μm. The crossed white arrows represent the polarizers.
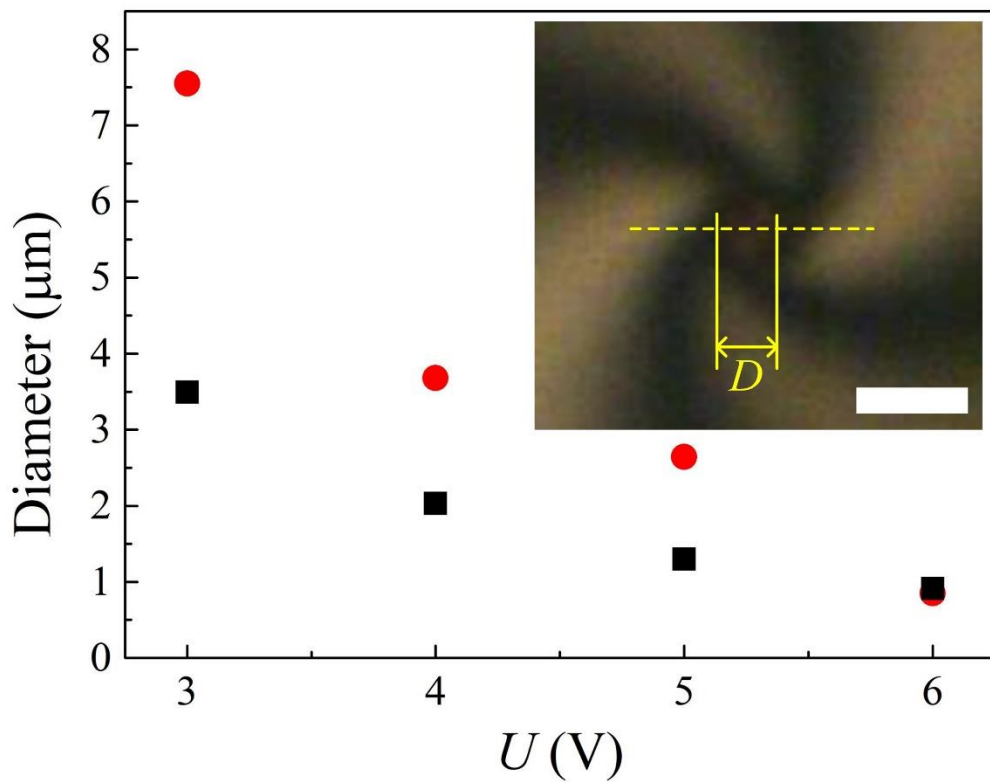
Supplementary Figure 3-7 The voltage dependence of the diameter (D) of the umbilic defect core. The red circles represent the s = +1 defects and the back squares represent the s = -1 defects. The inset shows the POM images of an umbilic defect. The diameter is measured as the width of the cross-section of the defect core as indicated by the yellow lines. Scale bar 10 μm.
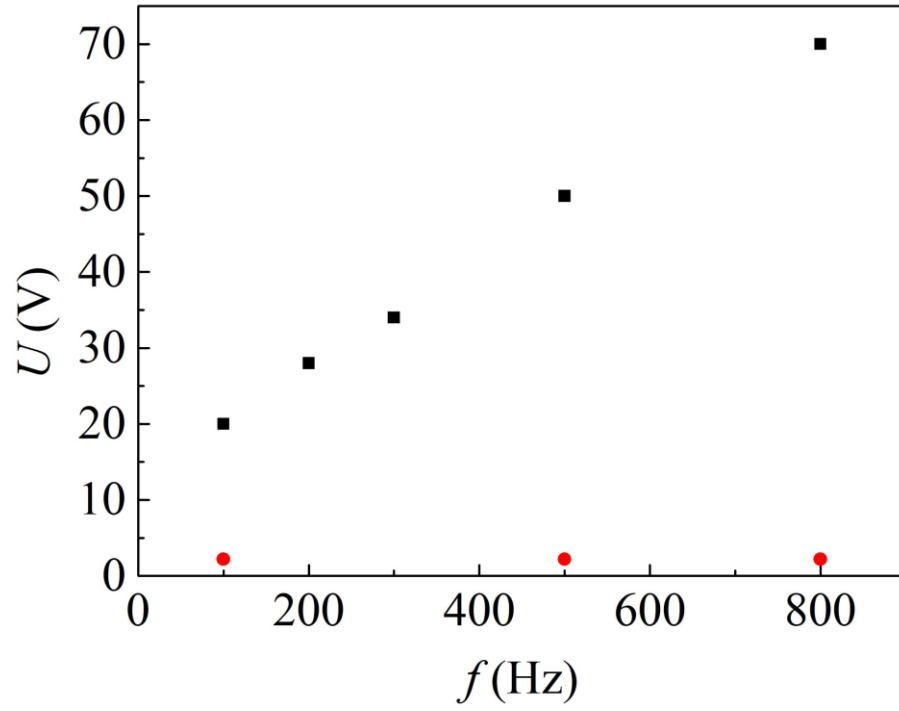
Supplementary Figure 3-8 Frequency dependence of voltage thresholds of directrons. Voltage thresholds of directrons (black squares) and Freedericksz transition (red circles) in cells of homeotropic alignment ($p \sim 10$ μm, $d \sim 9.4$ μm).

3.7.2 Supplementary Movies

Supplementary Movie 3-1. Collision of two directrons at $U = 15.4$ V, $f = 100$ Hz. The movie is played at $2\times$ the original speed.

Supplementary Movie 3-2. Dynamics of flocks of directrons composed of different number of directrons at $U = 15.4$ V, $f = 100$ Hz. The movie is played at $10\times$ the original speed.

Supplementary Movie 3-3. Formation of flocks of directrons at $U = 16.2$ V, $f = 100$ Hz. The movie is played at $5\times$ the original speed.

Supplementary Movie 3-4. Fusion and fission of directron flocks at $U = 15.4$ V, $f = 100$ Hz. The movie is played at $5\times$ the original speed.

Supplementary Movie 3-5. Emergence of large-scale coherent directional motion of directrons at $U = 20$ V, $f = 100$ Hz. The movie is played at $10\times$ the original speed.

Supplementary Movie 3-6. Dynamic motions of directrons at $U = 20$ V, $U = 30$ V and $U = 40$ V, respectively. $f = 100$ Hz.

Supplementary Movie 3-7. "Turbulent" swimming pattern of directrons at $U = 100$ V, $f = 500$ Hz.

Supplementary Movie 3-8. Circulating motion of directrons around a s = +1 defect at $U = 30$ V, $f = 100$ Hz.

Supplementary Movie 3-9. Circulating motion of directrons around a micro-particle at $U = 40$ V, $f = 60$ Hz.

Chapter 4

Annealing and melting of active two-dimensional soliton lattices in chiral nematic films

Authors: Yuan Shen[1] and Ingo Dierking[1]*

[1] Department of Physics and Astronomy, School of Natural Sciences, University of Manchester, Oxford Road, Manchester, M13 9PL, United Kingdom

*Email: ingo.dierking@manchester.ac.uk

This work is ready to be submitted.

Author contributions:
Y. S. conceived and carried out the experimental investigations, analyzed the experimental results and wrote the manuscript. I. D. supervised the investigations and contributed through discussions and writing the manuscript.

Note: the format of the paper is edited. The movies are available from the figshare database: https://figshare.com/s/383c7cfb71293527fb0d.

Abstract

From schools of fish to swarms of bacteria, active systems form self-organized structures. Here, we show that hundreds and thousands of electrically driven particle-like dissipative solitons, directrons, are generated in a cholesteric liquid crystal film and self-organizing into an active two-dimensional (2D) hexagonal lattice which moves coherently along a spontaneously-chosen direction. During the motion, the directron lattice relaxes from a disordered liquid phase to a bond-orientationally ordered hexatic phase through the motion and annihilation of topological defects, like in annealing processes of crystals. By increasing the applied voltage, the lattice gradually loses its order and exhibits a first-order hexatic-to-liquid melting transition. Our findings provide new insights into the collective dynamics of solitons in liquid crystal systems and the order-disorder transition of 2D non-equilibrium systems.

4.1 Introduction

Soft materials in which constituent building elements dissipate ambient free energy and convert it into mechanical work are generally referred to as active matter [1]. Distinct from conventional thermal systems in which self-organization usually arises from the coupling between entropy and potential interactions, the thermal energy is negligible for active matter and various complicated self-organization and collective motion stems from its primitive rules of propulsion and inter-particle interactions. Examples include large-scale vortices in bacteria suspensions [2-4], sperm cells [5], driven filaments [6-8] and artificial active particles [9-11], nematic order in vibrated rods [12] and cells [13], active crystallization of bacteria [14] and colloidal particles [15-18], clustering and phase separation of self-propelled particles [19-21], etc. However, self-organization of large scale ordered structure that experiences directional collective motion has rarely been reported so far [22].

Solitons are self-sustained localized packets of waves in nonlinear media that propagate without changing shape, such as water waves in a canal [23]. They are ubiquitous and exist in many areas of physics including nonlinear photonics [24], Bose-Einstein condensates [25], superconductors [26], magnetic materials [27] and liquid crystals [28]. The investigation of solitons

in liquid crystals have been carried out for over 5 decades. Various kinds of solitons have been reported, including different types of inversion walls [29-31], propagating solitary waves [32,33], individual convective rolls [34] and local convective domains [35], discommensurations [36,37] and breathers [38], nematicons [39], skyrmions and torons [28], swallow-tail solitons [40], etc. In 1977, Brand et al. reported an electrically driven butterfly-like soliton which moves easily and rapidly throughout the uniform nematic bulk [41], which was recently recognized as the three-dimensional (3D) dissipative solitary waves coined as "director bullets" or "directrons" by Li et al. [42-45] and received increasing attention due to their intriguing nonlinear dynamic properties and potential applications in various areas such as microfluidics and optics [46-48]. These directrons represent topological trivial particle-like localized dissipative solitary director waves. They behave like active particles that they convert the applied electric energy into translational motions and repel each other during collisions.

Here, we show that hundreds and thousands of directrons are created in a chiral nematic film by applying an electric field. The directrons start from random motions but then synchronize their motions through many-body interactions and self-organize into an active 2D hexagonal lattice which moves in a direction selected by spontaneous symmetry breaking. The lattice anneals with time from a disordered liquid phase to an ordered hexatic phase through the motion of the directrons. By increasing the applied voltage, individual directrons start exhibiting random walks, leading to a first-order hexatic-to-liquid melting transition of the 2D lattice.

4.2 Materials and methods

The samples used are the same as the ones in Chapter 3. A chiral nematic film is prepared by filling a mixture of the nematic liquid crystal ZLI-2806 (Merck) and chiral dopant ZLI-811 (Xianhua, China) into a commercial cell (AWAT, Poland). The pitch of the LC mixture $p \sim 2$ μm is calculated according to the equation $p = 1/(HTP \times c)$, where c is the weight concentration of the chiral dopant, and $HTP = -8.3$ μm^{-1} represents the helical twisting power of the chiral dopant [46]. The inner surfaces of the cell are covered with transparent indium tin oxide (ITO) layers to act as electrodes and are coated with rubbed polyimide layers to produce homogeneous alignment. The rubbing direction is along the x-axis. The cell gap d

~ 9.5 μm is measured by the thin-film interference method [49]. The sample is kept at 80 °C and an alternating-current (AC) electric field (**E**) is applied perpendicular to the cell substrates. By increasing the voltage (*U*) to a threshold value, thousands of directrons emerge and move in random directions.

4.3 Results and discussions

The directrons are the same as the ones reported in Chapter 3, which show a quadrupolar symmetric texture under the polarizing microscope (Supplementary Figure 4-1). Outside the directrons, the helical twisting structure of the director field aligns homogeneously with its helix parallel to the *z*-axis. Within the directron, the director deviates from the homogeneous state due to the transverse Coulomb forces provided by space charges as well as the flexoelectric polarization [46]. The structure of the directrons changes periodically with the frequency of the applied electric field, indicating the periodic oscillation of the director field due to the flexoelectric effect (Supplementary Figure 4-2) [46]. Once the symmetric structure of the directrons is broken, such oscillations of the director field drive the directrons to move forward [42,46]. The formation mechanism of the directrons is relatively complicated which involves many different factors, such as space charges, ion injection, flexoelectric effect, electro-convection effect, etc., and has not been completely understood yet. In our opinion, the formation of the directrons is mainly attributed to the coupling between the space charges and the flexoelectric effect (Chapter 3). Unlike topological solitons, such as skyrmions [50], whose stability is topologically protected and cannot be continuously transformed into the uniform state, the directrons are topologically trivial and immediately disappear once the electric field is off.
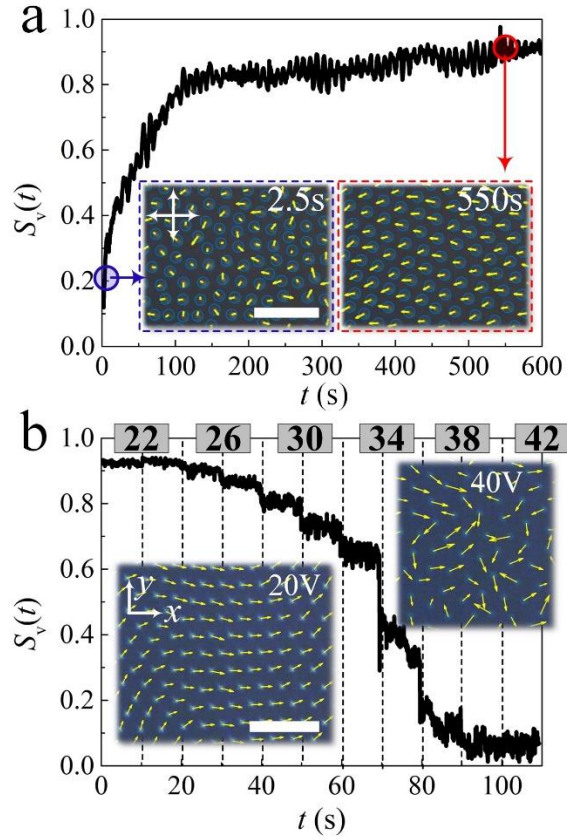
Figure 4-1 Dynamics of the solitons. (a) Time evolution of the velocity order parameter ($S_v(t)$) at U = 20 V, f = 100 Hz. The images at different times show the soliton velocities as indicated with yellow arrows. The yellow circles indicate Sv at t = 5s, 35s, and 100s, respectively. (b) Time dependence of S_v with the applied voltage being varied at a fixed frequency, f = 100 Hz. The voltage (indicated as numbers in the gray squares on top) gradually increases from 20 V to 40 V in a step of 2 V every 10 s. The insets show the micrographs of solitons at U = 20 V and 40 V, respectively, with their velocities indicated as yellow arrows. Scale bars 50 μm.

Millions of directrons start from random motions but soon synchronize their motions through interactions with each other (Figure 4-1 (a)). The velocity order parameter

$$S_v = \left|\sum_j^N \mathbf{v}_j\right| \Big/ \left(N \cdot v_s\right)$$

where N is the total number of directrons in the field of view and v_s is the absolute value of the velocity of coherently moving directrons [51], gradually increases from 0.1 to 0.8 and eventually saturates at 0.9 (Figure 4-1 (a)). The directrons distribute uniformly throughout the sample and gradually self-organize into an ordered 2D hexagonal lattice with time (Figure 4-2 (a), Supplementary Movie 4-1). Within the lattice, dislocations composed of a pair of five-and sevenfold coordinated directrons, also called disclinations, are formed randomly (Figure 4-2 (a) inset). The magnitude and direction of an isolated dislocation is given by the Burgers vector, **b**, along which the translational order of the lattice is decreased. The formaion of dislocations usually costs huge amount of free energy and destroy the

115

translational order of the crystal [52]. To better visualize the dislocations, the directron lattice is characterized by the voronoi construction (Figure 4-2 (b)). As one can see, a large amount of dislocations and dislocation pairs are formed right after the generation of directrons, which assemble into grain boundaries and clusters. As the directrons keep moving and colliding with each other, they gradually synchronize their motion. As a result, the defects gradually annihilate with each other and the lattice becomes more and more ordered. After 300 seconds, there are only small amount of dislocations left which are sparsely distributed within the lattice (Supplementary Movie 4-2). To quantify the effects of the motion on the orientational ordering, we have characterized the local and global hexatic bond orientational order parameters $\psi_6(\mathrm{r}_j)$ for soliton j and Ψ_6, respectively. The magnitude of the local bond-orientational order parameter $|\psi_6(\mathrm{r}_j)|$ varies from 0 to 1 and measures how the neighbors of soliton j fit locally on a hexagonal lattice (Figure 4-2 (c)). Ψ_6 changes with time which gradually increases and eventually saturates at late times (Figure 4-2 (f)). While the radial distribution function $g(r)$ decays exponentially to one within several peaks, it becomes more and more long-range with time, indicating the increase of the translational order of the lattice (Figure 4-2 (d) and Supplementary Figure 4-3). On the other hand, the bond orientational correlation function decays exponentially ($g_6(r) \propto e^{-r/\xi_6}$) at early times, but decays algebraically ($g_6(r) \propto r^{-\eta_6}$) at late times (Figure 4-2 (e) and Supplementary Figure 4-3). The exponent η_6 is 0.22 at $t = 150$s and 0.09 at $t = 300$s. In 2D systems, the existence of a solid featuring long-range positional order is absent due to the Mermin-Wagner theorem [53] and the transition from the solid to the liquid phase experiences two continuous phase transitions according to the Kosterlitz-Thouless-Halperin-Nelson-Young (KTHNY) theory [54-57]. The first transition driven by the dissociation of bound dislocation pairs is from the crystal with quasi-long-range positional order and long-range orientational order to the so-called hexatic phase with short-range positional order and quasi-long-range orientational order. The second transition driven by the dissociation of isolated dislocations is from the hexatic phase to a liquid phase in which both positional and orientational order show short-range correlations. While the radial distribution function ($g(r)$) decays exponentially in both liquid and hexatic phases, the bond orientational correlation function($g_6(r)$) decays exponentially in the liquid phase but algebraically in the hexatic phase. At the hexatic-liquid transition point, $g_6(r)$ decays algebraically with the exponent $\eta_6 = 0.25$, i.e., $g_6(r) \propto r^{-0.25}$ [58]. As a result, according

to the KTHNY theory, the 2D directron lattice shows a liquid phase at early time stages and transforms into a hexatic phase at t = 150s. At t = 300s, the directron lattice is deep into the hexatic phase and well ordered. One may suspect it represents a crystal phase at t = 300s, however, the exponentially decaying radial distribution function (Figure 4-2 (d)) and the divergence of the dynamic Lindemann parameter (L^2) (Supplementary Figure 4-4) exclude this possibility. The sparsely distributed free dislocations shown in Figure 4-2 (b) destroys the translational order of the lattice according to the KTHNY theory [59]. The dynamic Lindemann parameter as an improved criterion of 2D melting stays finite below a critical value L_c^2 = 0.033 in a crystal but diverges in the hexatic and liquid phases [60]. The insets in Figure 4-2 (c) show the 2D structure factors of the directron lattice at different moments which are obtained by Fourier transforming the 2D radial distribution functions before azimuthally averaging them. It transforms gradually with time from a pattern of continuous concentric rings which is typical for an isotropic liquid phase to a sixfold angular symmetric diffraction pattern which is a necessary but not sufficient condition of a hexatic phase [61].
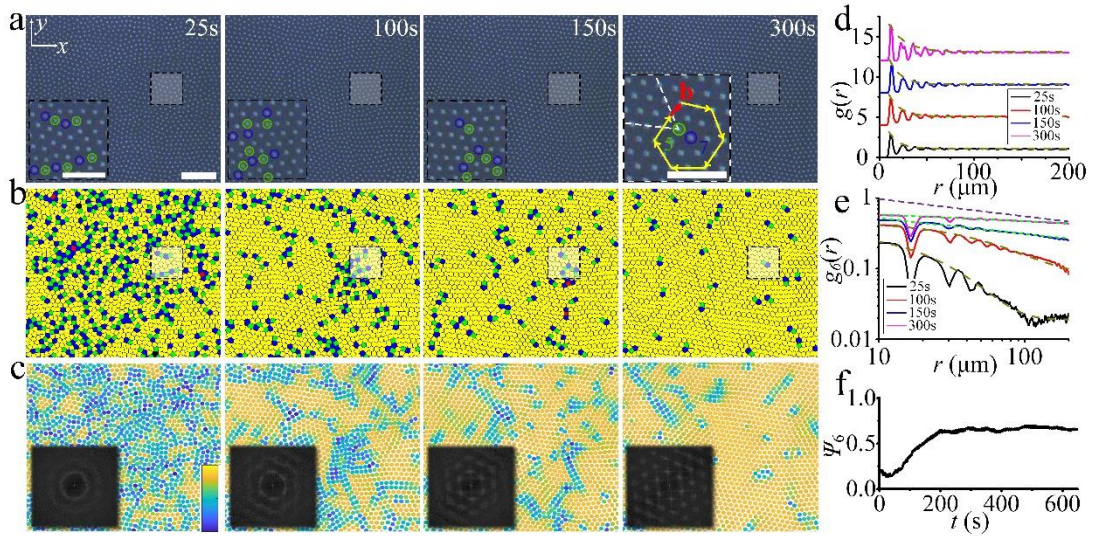
Figure 4-2 Annealing of the 2D directron lattice. (a) Micrographs of the directron lattice at different times. U = 20 V, f = 100 Hz, scale bar 100 μm. The insets show the enlarged micrographs of the regions in the black dashed squares with the five- and sevenfold coordinated directrons indicated by the green and blue circles. The orientation of the dislocation in the inset (t = 300s) is given by the Burgers vector (b) (red arrow), which is obtained from a track around the dislocation with edges comprising a constant number of solitons (yellow arrows). The lattice lines ending at the fivefold coordinated directron of the dislocation are indicated by the white-dashed lines. scale bars in the insets 50 μm. (b) Voronoi diagrams constructed with the micrographs in (a) and colored according to the number of nearest neighbors (4 = red, 5 = green, 6 = yellow, 7 = blue, others = black). The black-dashed squares are corresponding to the ones in (a). (c) Micrographs in (a) with each directron colored according to $|\psi_6|$ according to the color bar. The color bar varies linearly from 0 (deep blue) to 1 (light yellow). Insets show the corresponding 2D structure factors. (d) Radial distribution functions ($g(r)$) and (e) orientational correlation functions ($g_6(r)$) of the sample at different times. The dark-yellow-dashed and the green-dotted lines are the exponential and power law fits, respectively. The purple-short-dashed line $r^{-0.25}$ in (e) is the KTHNY prediction at the hexatic-liquid transition point. The curves in (d) have been shifted vertically for clarity. (f) Time dependence of Ψ_6.

The dynamics of the directrons depends on the applied voltage. By increasing the voltage, the velocity order parameter S_v continuously decreases from 0.9 to 0 and the collective motion of the directrons gradually transforms to a chaotic incoherent motion (Figure 4-1 (b), Supplementary Movie 4-3). Such an order-disorder transition has also been observed in granular systems by increasing the magnitude of the vibration [62] and may be attributed to the increase of the activity of directrons which destabilizes the ordered hexatic phase as numerically reported in systems of active Brownian particles [63]. As a result, the directron lattice gradually melts from the hexatic phase to the liquid phase, just as in heating of a 2D crystal (Figure 4-3 and Supplementary Movie 4-3). As the voltage gradually increases from 20 V to 32 V, the topological defects gradually increases and form grain boundaries (Figure 4-3 (b) and Supplementary Movie 4-4). At the same time, the global orientational order parameter, Ψ_6, continuously decreases (Figure 4-3 (f)). However, the directron lattice stays in the hexatic phase. This is indicated by the exponentially decaying radial distribution function and the algebraically decaying orientational correlation function whose exponent η_6 is smaller than 0.25 (Figure 4-3 (d) and (e), Supplementary Figure 4-5).
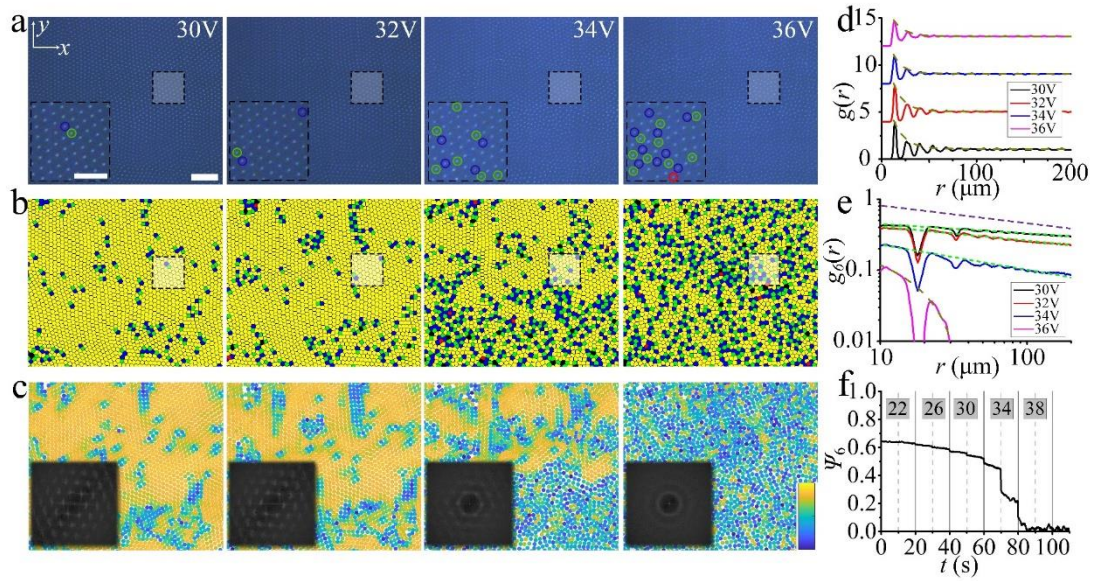
Figure 4-3 Melting of the 2D directron lattice. (a) Micrographs of the directron lattice at different voltages. $f = 100$ Hz, scale bar 100 μm. The insets show the enlarged micrographs of the regions in the black dashed squares with the four-, five- and sevenfold coordinated solitons indicated by the red, green and blue circles, respectively. scale bar 50 μm. (b) Voronoi diagrams constructed with the micrographs in (a) and colored according to the number of nearest neighbors (4 = red, 5 = green, 6 = yellow, 7 = blue, others = black). The black-dashed squares are corresponding to the ones in (a). (c) Micrographs in (a) with each directron colored according to $|\psi_6|$ according to the color bar. The color bar varies linearly from 0 (deep blue) to 1 (light yellow). Insets show the corresponding 2D structure factors. (d) Radial distribution functions ($g(r)$) and (e) orientational correlation functions ($g_6(r)$) of the sample at different voltages. The dark-yellow-dashed and the green-dotted lines are the exponential and power law fits, respectively. The purple-short-dashed line $r^{-0.25}$ in (e) is the KTHNY prediction at the hexatic-liquid transition point. The curves in (d) have been shifted vertically for clarity. (f) Time dependence of Ψ_6 with the applied voltage being varied at a fixed frequency, $f = 100$

Hz. The voltage gradually increases from 20 V to 40 V in a step of 2 V every 10 s as indicated in the gray squares.

To get a better insight into the degree of local orientational ordering, we investigate the magnitude of the projection of $\psi_6(\mathbf{r}_j)$ onto the mean local orientational field

$$n_6\left(\mathbf{r}_j\right) = \left|\psi_6^*\left(\mathbf{r}_j\right)\left\langle\psi_6\left(\mathbf{r}_k\right)\right\rangle_k\right|$$

where k represents the nearest neighbors of directron j, which takes the second nearest neighbors into account and determines how the orientation of directron j fits into the orientation of its neighbors [64]. It was shown by Larsen and Grier that the joint distribution $P(|\psi_6|, n_6)$ is unimodal if the system shows a pure phase [65], whereas a bimodal distribution is found if the system exhibits coexistence of different phases [66]. A directron with $|\psi_6| + n_6 >$ 1 is classified as belonging to the crystal phase, otherwise, it is assigned to the liquid phase. Figure 4 gives the probability distribution for the directron lattice in the $|\psi_6|$-n_6-plane at different voltages. It is noted that most of the directrons have $|\psi_6| + n_6 > 1$ and form a unimodal distribution at $U = 30$ V and 32 V, indicating a pure hexatic phase (Figure 4-4 (a) and (b)). The defects significantly increase and form chains and clusters at $U = 34$ V with a drastic decrease of the global bond orientational order, Ψ_6 (Figure 4-3 (f)). At the same time, $g_6(r)$ decays algebraically with an exponent $\eta_6 = 0.34 > 0.25$, which indicates the occurrence of a phase transition (Figure 4-3 (e)). This is inconsistent with the KTHNY theory where a continuous hexatic-to-liquid phase transition is driven by the unbinding of individual dislocations into free disclinations [55,57]. Instead, the "condensation" of defects observed in Figure 4-3 is, to some extent, in qualitative agreement with the grain-boundary-induced melting theory proposed by Chui [67]. Moreover, the joint distribution $P(|\psi_6|, n_6)$ in Figure 4-4 (c) shows a bimodal distribution indicating that the system is in a state of coexistence between hexatic and liquid phases. Such a hexatic-liquid phase seperation can also be clearly observed from the colormap of $|\psi_6|$ (Figure 4-3 (c)). The KTHNY theory is not a thermodynamically consistent theory of 2D melting and different particle-particle interactions may lead to different melting phenomena [68]. Such a first-order phase transition is similar to the motility-induced phase separation (MIPS) of active Brownian particles reported by R. Digregorio, et al. [63]. Further increase of voltage leads to an isotropic liquid phase with Ψ_6 decaying to zero (Figure 4-3 (f)). Both the radial distribution function and the orientational correlation function decays exponentially (Figure 4-3 (d) and (e)). The joint

distribution $P(|\psi_6|, n_6)$ exhibits a unimodal distribution with most of the directrons showing $|\psi_6| + n_6 < 1$ (Figure 4-4 (d)), which demonstrates that the local sixfold order up to the second shell is lost.
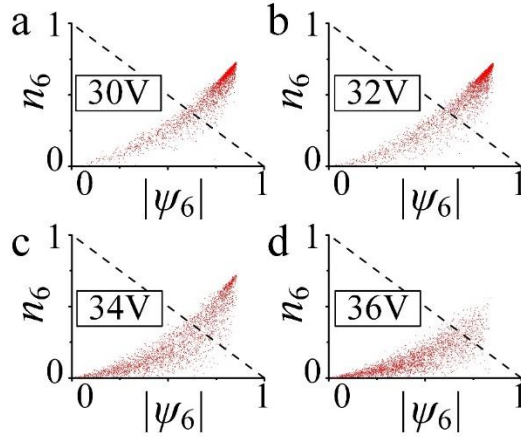
Figure 4-4 Probability distributions of $|\psi_6|$ versus n_6 of the soliton lattice at different Voltages. (a) 30 V. (b) 32. (c) 34V. (d) 36V. The black-dashed line shows $n_6 + |\psi_6| = 1$.

4.4 Conclusion

To conclude, we show that active systems formed by microscopic particle-like solitonic field configurations exhibit emergent collective dynamics inaccessible to their atomic and molecular counterparts, providing a tunable model for studying out-of-equilibrium self-organization and order-disorder transition. The large scale polar order and directional collective motion of the directrons share similarities with classical flocking models such as the Vicsek [69] and Toner-Tu modes [70,71] and is analogous to other active systems such as active colloidal particles [72]. Although it is predicted that phases known in thermodynamic equilibrium systems have their counterparts in out-of-equilibrium systems [73], only several phases have been observed so far [15,19,73,74]. Recently, the formation of active hexatic phase has been demonstrated in different numerical simulation systems [63,75-77]. However, the experimental counterpart has rarely been reported [62,78]. Our results show that dynamic directrons can self-organize into an active hexatic phase which thus extend the scenarios of 2D melting built for thermodynamic equilibrium systems to non-equilibrium systems. The facile fabrication, control and observation of our system also make it potentially promising for studying many other forms of out-of-equilibrium behavior, such as collective motion [79], MIPS [80], phase transition in non-equilirbium systems [81], etc.

120

4.5 Acknowledgement

4.6 References

1   Marchetti, M. C. *et al.* Hydrodynamics of soft active matter. *Reviews of Modern Physics* **85**, 1143 (2013).

2   Zhang, H., Be'Er, A., Smith, R. S., Florin, E.-L. & Swinney, H. L. Swarming dynamics in bacterial colonies. *EPL (Europhysics Letters)* **87**, 48011 (2009).

3   Wioland, H., Woodhouse, F. G., Dunkel, J., Kessler, J. O. & Goldstein, R. E. Confinement stabilizes a bacterial suspension into a spiral vortex. *Physical review letters* **110**, 268102 (2013).

4   Lushi, E., Wioland, H. & Goldstein, R. E. Fluid flows created by swimming bacteria drive self-organization in confined suspensions. *Proceedings of the National Academy of Sciences* **111**, 9733-9738 (2014).

5   Riedel, I. H., Kruse, K. & Howard, J. A self-organized vortex array of hydrodynamically entrained sperm cells. *Science* **309**, 300-303 (2005).

6   Schaller, V., Weber, C., Semmrich, C., Frey, E. & Bausch, A. R. Polar patterns of driven filaments. *Nature* **467**, 73-77 (2010).

7   Schaller, V. & Bausch, A. R. Topological defects and density fluctuations in collectively moving systems. *Proceedings of the National Academy of Sciences* **110**, 4488-4493 (2013).

8   Sumino, Y. *et al.* Large-scale vortex lattice emerging from collectively moving microtubules. *Nature* **483**, 448-452 (2012).

9   Bricard, A. *et al.* Emergent vortices in populations of colloidal rollers. *Nature Communications* **6**, 7470 (2015).

10   Kokot, G. & Snezhko, A. Manipulation of emergent vortices in swarms of magnetic rollers. *Nature communications* **9**, 1-7 (2018).

11   Liu, Z. T. *et al.* Activity waves and freestanding vortices in populations of subcritical Quincke rollers. *Proceedings of the National Academy of Sciences* **118**, 1-9 (2021).

12   Narayan, V., Ramaswamy, S. & Menon, N. Long-lived giant number fluctuations in a swarming granular nematic. *Science* **317**, 105-108 (2007).

13   Duclos, G., Garcia, S., Yevick, H. & Silberzan, P. Perfect nematic order in confined monolayers of spindle-shaped cells. *Soft matter* **10**, 2346-2353 (2014).

14   Petroff, A. P., Wu, X.-L. & Libchaber, A. Fast-moving bacteria self-organize into active two-dimensional crystals of rotating cells. *Physical review letters* **114**, 158102 (2015).

15   Palacci, J., Sacanna, S., Steinberg, A. P., Pine, D. J. & Chaikin, P. M. Living crystals of light-activated colloidal surfers. *Science* **339**, 936-940 (2013).

16   Grzybowski, B. A., Stone, H. A. & Whitesides, G. M. Dynamic self-assembly of magnetized, millimetre-sized objects rotating at a liquid–air interface. *Nature* **405**, 1033-1036 (2000).

17   Voth, G. A. *et al.* Ordered clusters and dynamical states of particles in a vibrated fluid. *Physical review letters* **88**, 234301 (2002).

18   Baron, M., Bławzdziewicz, J. & Wajnryb, E. Hydrodynamic crystals: Collective dynamics of regular arrays of spherical particles in a parallel-wall channel. *Physical review letters* **100**, 174502 (2008).

19   Buttinoni, I. *et al.* Dynamical clustering and phase separation in suspensions of self-propelled colloidal particles. *Physical review letters* **110**, 238301 (2013).

20   Redner, G. S., Hagan, M. F. & Baskaran, A. Structure and dynamics of a phase-separating active colloidal fluid. *Physical review letters* **110**, 055701 (2013).

21   Yan, J. *et al.* Reconfiguring active particles by electrostatic imbalance. *Nature materials* **15**, 1095-1099 (2016).

22   Sohn, H. R. & Smalyukh, I. I. Electrically powered motions of toron crystallites in chiral liquid crystals. *Proceedings of the National Academy of Sciences* **117**, 6437-6445 (2020).

23   Dauxois, T. & Peyrard, M. *Physics of solitons*.   (Cambridge University Press, 2006).

24   Du, L., Yang, A., Zayats, A. V. & Yuan, X. Deep-subwavelength features of photonic skyrmions in a confined electromagnetic field with orbital angular momentum. *Nature Physics* **15**, 650-654 (2019).

25   Ray, M. W., Ruokokoski, E., Kandel, S., Möttönen, M. & Hall, D. Observation of Dirac monopoles in a synthetic magnetic field. *Nature* **505**, 657-660 (2014).

26   Harada, K. *et al.* Real-time observation of vortex lattices in a superconductor by electron microscopy. *Nature* **360**, 51-53 (1992).

27   Yu, X. *et al.* Real-space observation of a two-dimensional skyrmion crystal. *Nature* **465**, 901-904 (2010).

28   Smalyukh, I. I., Lansac, Y., Clark, N. A. & Trivedi, R. P. Three-dimensional structure and multistable optical switching of triple-twisted particle-like excitations in anisotropic fluids. *Nature Materials* **9**, 139 (2009).

29   Helfrich, W. Alignment-Inversion Walls in Nematic Liquid Crystals in the Presence of a Magnetic Field. *Physical Review Letters* **21**, 1518-1521 (1968).

30   Leger, L. Observation of wall motions in nematics. *Solid State Communications* **10**, 697-700 (1972).

31   Migler, K. B. & Meyer, R. B. Solitons and pattern formation in liquid crystals in a rotating magnetic field. *Physical Review Letters* **66**, 1485-1488 (1991).

32   Guozhen, Z. Experiments on Director Waves in Nematic Liquid Crystals. *Physical Review Letters* **49**, 1332-1335 (1982).

33   Lei, L., Changqing, S., Juelian, S., Lam, P. M. & Yun, H. Soliton Propagation in Liquid Crystals. *Physical Review Letters* **49**, 1335-1338 (1982).

34   Ribotta, R. Critical Behavior of the Penetration Length of a Vortex into a Subcritical Region. *Physical Review Letters* **42**, 1212-1215 (1979).

35   Joets, A. & Ribotta, R. Localized, Time-Dependent State in the Convection of a Nematic Liquid Crystal. *Physical Review Letters* **60**, 2164-2167 (1988).

36   Lowe, M. & Gollub, J. P. Solitons and the commensurate-incommensurate transition in a convecting nematic fluid. *Physical Review A* **31**, 3893-3897 (1985).

37 Lowe, M., Gollub, J. P. & Lubensky, T. C. Commensurate and Incommensurate Structures in a Nonequilibrium System. *Physical Review Letters* **51**, 786-789 (1983).

38 Skaldin, O. A., Delev, V. A. & Shikhovtseva, E. S. Asymmetry of the time dynamics of breathers in the electroconvection twist structure of a nematic. *JETP Letters* **97**, 92-97 (2013).

39 Peccianti, M. & Assanto, G. Nematicons. *Physics Reports* **516**, 147-208 (2012).

40 Shen, Y. & Dierking, I. Electrically driven formation and dynamics of swallow-tail solitons in smectic A liquid crystals. *Materials Advances* **2**, 4752-4761 (2021).

41 Brand, H. R., Fradin, C., Finn, P. L., Pesch, W. & Cladis, P. E. Electroconvection in nematic liquid crystals: comparison between experimental results and the hydrodynamic model. *Physics Letters A* **235**, 508-514 (1997).

42 Li, B.-X. *et al.* Electrically driven three-dimensional solitary waves as director bullets in nematic liquid crystals. *Nature Communications* **9**, 2912 (2018).

43 Li, B.-X., Xiao, R.-L., Paladugu, S., Shiyanovskii, S. V. & Lavrentovich, O. D. Three-dimensional solitary waves with electrically tunable direction of propagation in nematics. *Nature Communications* **10**, 3749 (2019).

44 Li, B.-X., Xiao, R.-L., Shiyanovskii, S. V. & Lavrentovich, O. D. Soliton-induced liquid crystal enabled electrophoresis. *Physical Review Research* **2**, 013178 (2020).

45 Lavrentovich, O. D. Design of nematic liquid crystals to control microscale dynamics. *Liquid Crystals Reviews* **8**, 59-129 (2020).

46 Shen, Y. & Dierking, I. Dynamics of electrically driven solitons in nematic and cholesteric liquid crystals. *Communications Physics* **3**, 1 (2020).

47 Shen, Y. & Dierking, I. Dynamic dissipative solitons in nematics with positive anisotropies. *Soft Matter* **16**, 5325 (2020).

48 Aya, S. & Araoka, F. Kinetics of motile solitons in nematic liquid crystals. *Nature communications* **11**, 1-10 (2020).

49 Goodman, A. M. Optical interference method for the approximate determination of refractive index and thickness of a transparent layer. *Appl. Opt.* **17**, 2779-2787 (1978).

50 Wu, J.-S. & Smalyukh, I. I. Review: Hopfions, heliknotons, skyrmions, torons and both abelian and nonabelian vortices in chiral liquid crystals. *Liquid Crystals Reviews*, 1-91 (2022).

51 Shen, Y. & Dierking, I. Electrically Driven Formation and Dynamics of Skyrmionic Solitons in Chiral Nematics. *Physical Review Applied* **15**, 054023 (2021).

52 Gasser, U., Eisenmann, C., Maret, G. & Keim, P. Melting of crystals in two dimensions. *ChemPhysChem* **11**, 963-970 (2010).

53 Mermin, N. D. & Wagner, H. Absence of ferromagnetism or antiferromagnetism in one-or two-dimensional isotropic Heisenberg models. *Physical Review Letters* **17**, 1133 (1966).

54 Kosterlitz, J. M. & Thouless, D. J. Ordering, metastability and phase transitions in two-dimensional systems. *Journal of Physics C: Solid State Physics* **6**, 1181 (1973).

55 Nelson, D. R. & Halperin, B. I. Dislocation-mediated melting in two dimensions. *Physical Review B* **19**, 2457-2484 (1979).

56 Young, A. P. Melting and the vector Coulomb gas in two dimensions. *Physical Review B* **19**, 1855-1866 (1979).

57 Halperin, B. & Nelson, D. R. Theory of two-dimensional melting. *Physical Review Letters* **41**, 121 (1978).

58   Strandburg, K. J. Two-dimensional melting. *Reviews of modern physics* **60**, 161 (1988).

59   Brinkman, W., Fisher, D. S. & Moncton, D. Melting of two-dimensional solids. *Science* **217**, 693-700 (1982).

60   Zahn, K., Lenke, R. & Maret, G. Two-stage melting of paramagnetic colloidal crystals in two dimensions. *Physical review letters* **82**, 2721 (1999).

61   Marcus, A. H. & Rice, S. A. Observations of first-order liquid-to-hexatic and hexatic-to-solid phase transitions in a confined colloid suspension. *Physical review letters* **77**, 2577 (1996).

62   Olafsen, J. & Urbach, J. Two-dimensional melting far from equilibrium in a granular monolayer. *Physical review letters* **95**, 098002 (2005).

63   Digregorio, P. *et al.* Full phase diagram of active Brownian disks: From melting to motility-induced phase separation. *Physical review letters* **121**, 098003 (2018).

64   Dillmann, P., Maret, G. & Keim, P. Comparison of 2D melting criteria in a colloidal system. *Journal of Physics: Condensed Matter* **24**, 464118 (2012).

65   Larsen, A. E. & Grier, D. G. Melting of metastable crystallites in charge-stabilized colloidal suspensions. *Physical review letters* **76**, 3862 (1996).

66   Marcus, A. H. & Rice, S. A. Phase transitions in a confined quasi-two-dimensional colloid suspension. *Physical Review E* **55**, 637 (1997).

67   Chui, S. Grain-boundary theory of melting in two dimensions. *Physical Review B* **28**, 178 (1983).

68   Karnchanaphanurach, P., Lin, B. & Rice, S. A. Melting transition in a quasi-two-dimensional colloid suspension: Influence of the colloid-colloid interaction. *Physical Review E* **61**, 4036 (2000).

69   Vicsek, T., Czirók, A., Ben-Jacob, E., Cohen, I. & Shochet, O. Novel type of phase transition in a system of self-driven particles. *Physical review letters* **75**, 1226 (1995).

70   Toner, J. & Tu, Y. Long-range order in a two-dimensional dynamical XY model: how birds fly together. *Physical review letters* **75**, 4326 (1995).

71   Toner, J. & Tu, Y. Flocks, herds, and schools: A quantitative theory of flocking. *Physical review E* **58**, 4828 (1998).

72   Bricard, A., Caussin, J.-B., Desreumaux, N., Dauchot, O. & Bartolo, D. Emergence of macroscopic directed motion in populations of motile colloids. *Nature* **503**, 95-98 (2013).

73   Toner, J., Tu, Y. & Ramaswamy, S. Hydrodynamics and phases of flocks. *Annals of Physics* **318**, 170-244 (2005).

74   Theurkauff, I., Cottin-Bizonne, C., Palacci, J., Ybert, C. & Bocquet, L. Dynamic clustering in active colloidal suspensions with chemical signaling. *Physical review letters* **108**, 268303 (2012).

75   Klamser, J. U., Kapfer, S. C. & Krauth, W. Thermodynamic phases in two-dimensional active matter. *Nature communications* **9**, 1-8 (2018).

76   James, M., Suchla, D. A., Dunkel, J. & Wilczek, M. Emergence and melting of active vortex crystals. *Nature communications* **12**, 1-11 (2021).

77   Paliwal, S. & Dijkstra, M. Role of topological defects in the two-stage melting and elastic behavior of active Brownian particles. *Physical Review Research* **2**, 012013 (2020).

78   Seshadri, R. & Westervelt, R. Statistical mechanics of magnetic bubble arrays. II.

Observations of two-dimensional melting. *Physical Review B* **46**, 5150 (1992).

79   Vicsek, T. & Zafeiris, A. Collective motion. *Physics Reports* **517**, 71-140 (2012).

80   Cates, M. E. & Tailleur, J. Motility-induced phase separation. *Annu. Rev. Condens. Matter Phys.* **6**, 219-244 (2015).

81   Bialké, J., Speck, T. & Löwen, H. Crystallization in a dense suspension of self-propelled particles. *Physical review letters* **108**, 168301 (2012).

4.7 Supplementary Information

4.7.1 Supplementary Figures
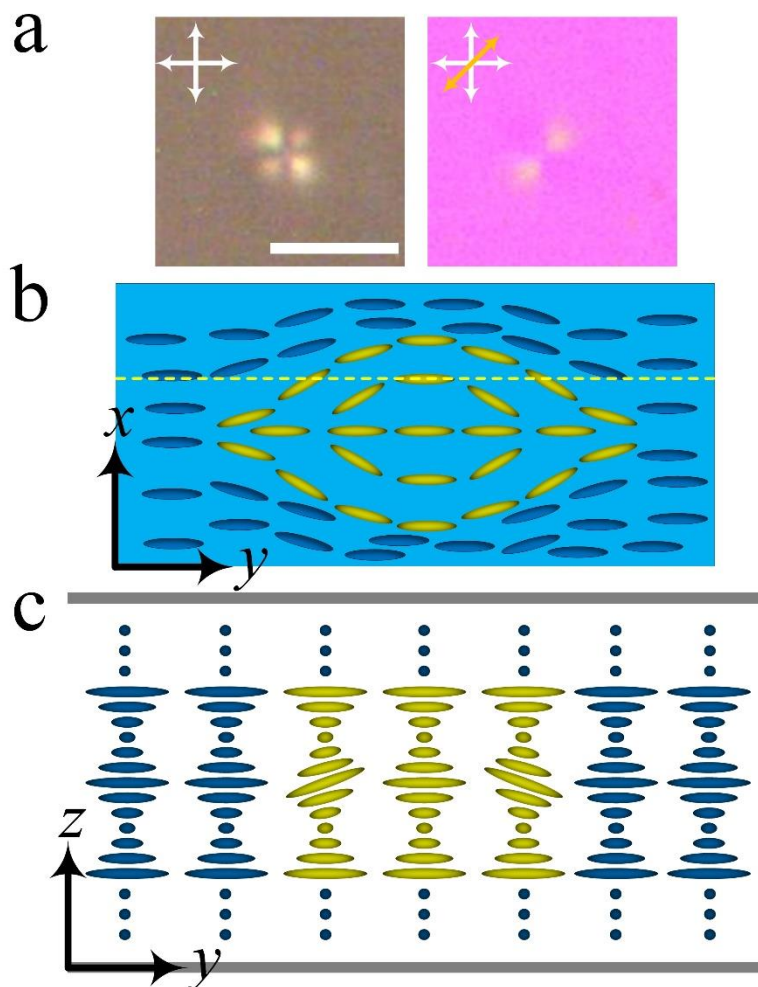
Supplementary Figure 4-1 (a) Polarizing microscopy images of a directron. The white arrows represent the polarizers and the yellow arrow represent the optical axis of the λ-plate. (b) The schematic director structure of a directron in the middle layer of the chiral nematic sample. (c) The schematic director structure of a directron in the yz plane of the cross section along the dashed yellow line in (e). The director field within the directron is represented as yellow ellipses and the homogeneous director field outside the directron is represented as blue ellipses. The top and bottom sections of the sample in (c) are homogeneously aligned helical structures and are represented by blue dots.
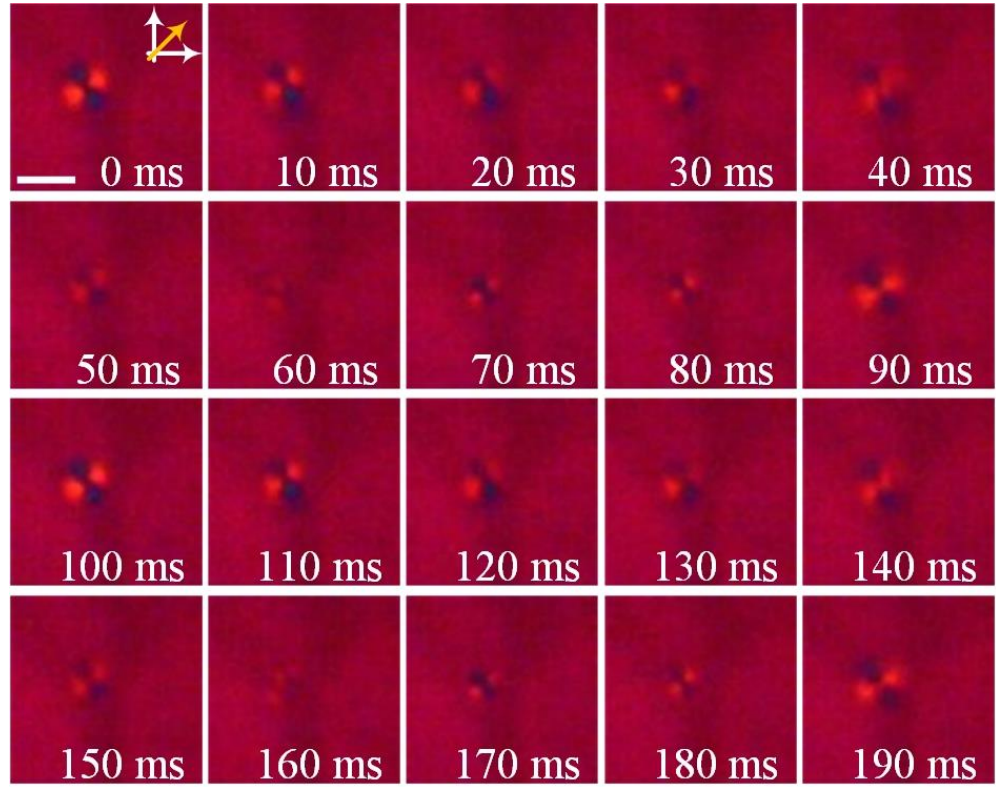
Supplementary Figure 4-2 Time series of polarizing micrographs of a directron. The directron is modulated by an AC electric field of $U = 14$ V, $f = 10$ Hz. The corssed white arrows represent polarizers and the yellow arrow represent the optical axis of the λ-plate. Scale bar 10 μm.
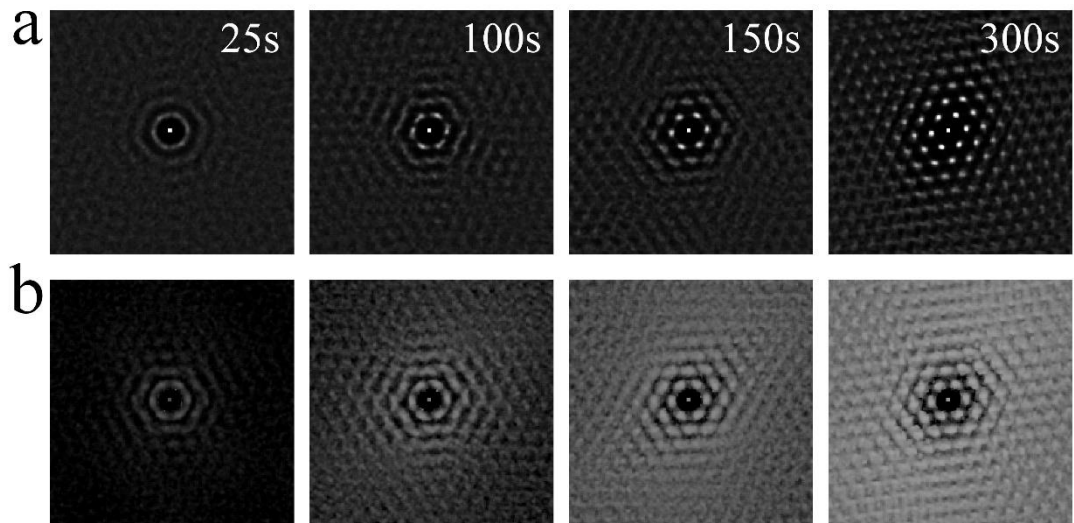
Supplementary Figure 4-3 (a) 2D radial distribution functions and (b) 2D orientational correlation functions of the soliton lattice at different moments in time as indicated in the top row of figures.
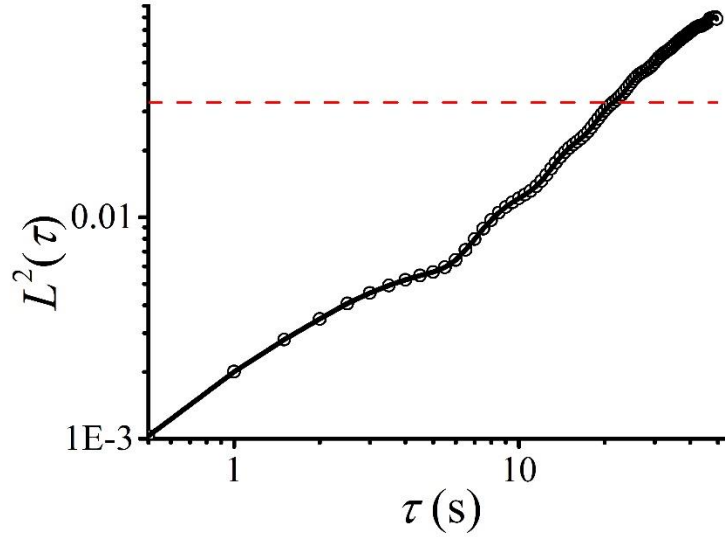
Supplementary Figure 4-4 Time lag (τ) dependence of the square of the dynamic Lindemann parameter (L^2) of the sample at $t = 300$ s. The red-dashed line indicates a critical value of $L_c^2 = 0.033$.
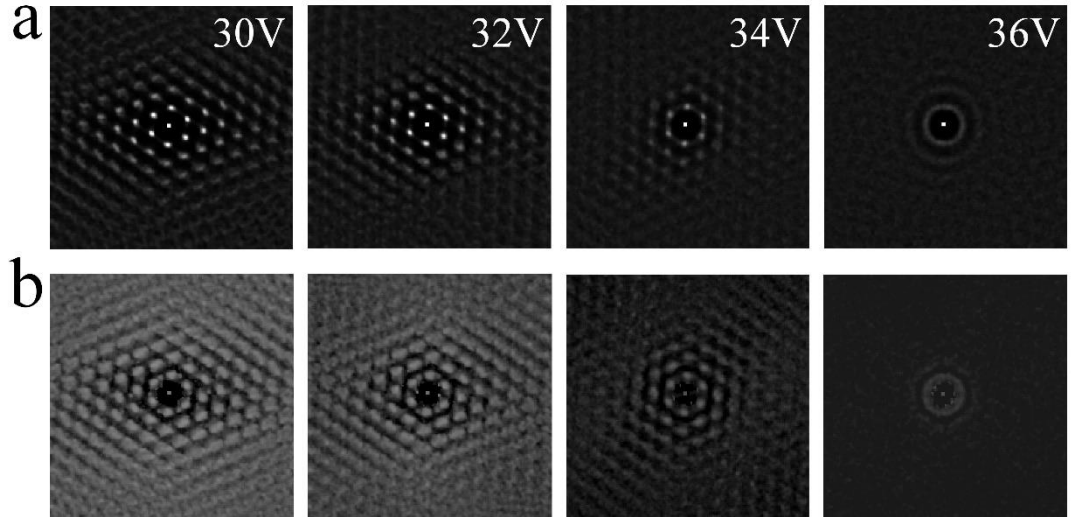
Supplementary Figure 4-5 (a) 2D radial distribution functions and (b) 2D orientational correlation functions of the soliton lattice at different applied voltages as indicated in the top row of figures.

4.7.2 Supplementary Movies

Supplementary Movie 4-1. Annealing of a 2D soliton lattice with time at $U = 20$ V, $f = 100$ Hz. The movie is played at $10\times$ the original speed.

Supplementary Movie 4-2. Voronoi diagram evolution of the soliton lattice corresponding to the one in Supplementary Movie 1, colored according to the number of nearest neighbors (4 = red, 5 = green, 6 = yellow, 7 = blue, others = black). The movie is played at $10\times$ the

128

original speed.

Supplementary Movie 4-3. Melting of a 2D soliton lattice with increasing applied voltage from 20 V to 40 V in steps of 2 V. $f = 100$ Hz. The movie is played at $2\times$ the original speed.

Supplementary Movie 4-4. Voronoi diagram evolution of the soliton lattice corresponding to the one in Supplementary Movie 3, colored according to the number of nearest neighbors (4 = red, 5 = green, 6 = yellow, 7 = blue, others = black). The movie is played at $2\times$ the original speed.

Chapter 5

Dynamic dissipative solitons in nematics with positive anisotropies

Authors: Yuan Shen[1] and Ingo Dierking[1]*
[1] Department of Physics and Astronomy, School of Natural Sciences, University of Manchester, Oxford Road, Manchester, M13 9PL, United Kingdom
*Email: ingo.dierking@manchester.ac.uk

Author contributions:
Y. S. conceived and carried out the experimental investigations, analyzed the experimental results and wrote the manuscript. I. D. supervised the investigations and contributed through discussions and writing the manuscript.

Note: the format of the paper is edited. The supplementary movies related to this work are available on the website of the journal. One can also download the movies from the figshare database: https://figshare.com/s/383c7cfb71293527fb0d.

Abstract

Electric field induced instabilities of textures of nematics are of importance for both fundamental science and practical applications. Complex electro-hydrodynamic (EHD) effects such as electro-convection, fingerprint textures, spatiotemporal chaos, and solitons in nematics have been broadly investigated and generated much attention. In this work, dissipative solitons as a novel EHD phenomenon are realized in nematics with positive anisotropies, presumably for the first time. Unlike the directrons reported recently in nematics with negative anisotropies whose formation and dynamics are mainly attributed to the flexoelectric and electro-convection effects, the solitons discussed here arise from the nonlinear coupling between the director field and the isotropic flow induced by ion motion. The structure and dynamics of the solitons are demonstrated and the influences of chirality, azimuthal anchoring and ion concentration are also investigated. Finally, we show that the propagation trajectory of solitons can be manipulated by patterned photoalignment and micro-particles can be trapped by them as vehicles for micro-cargo transport.

5.1 Introduction

Nematic liquid crystals (LCs) are self-organized anisotropic fluids with a long-range orientational order of molecules defined by the director, **n** [1]. For several decades, research has been focusing on the dynamic response of LCs to electric fields, which led to the revolutionary development of liquid crystal displays (LCDs). An elementary unit, or a pixel, of a traditional LCD is composed of two glass substrates coated with a transparent electrode and a nematic LC confined between them. Reorientation of the director **n**, which also exemplifies the optic axis, can be induced by applying an electric field across the cell, leading to the modulation of the macroscopic refractivity. Such a behavior originates from the anisotropic properties of LC molecules, such as the dielectric permittivity and electrical conductivity, i.e., the permittivity ($\varepsilon_{\parallel}$) and conductivity ($\sigma_{\parallel}$) measured along **n** are different from those (permittivity, $\varepsilon_{\perp}$, and conductivity, $\sigma_{\perp}$) measured perpendicular to **n**. The strong coupling between the reorientation of **n** and the fluid velocity also enables nonlinear responses such as electro-convection (EC) [2] and solitons (solitary waves) [3].

Solitons are localized travelling waves that were first discovered in a shallow canal by Russell in 1834 [4]. They are ubiquitous and exist in various areas of physics, such as nonlinear photonics, magnetic matter, superconductors and also LCs [5]. However, solitons of higher dimensions supported by the standard cubic nonlinearity suffer from severe instabilities [6]. Generation of multidimensional solitons and manipulation of their mobility are still grand challenges in the science of nonlinear physics and materials. Studies on solitons in LCs have been carried out for over five decades. Most early studies [7-11] were concerned with "walls" in nematics, also referred to as planar or linear solitons [12], generated by magnetic or electric fields, which actually are transition regions where **n** smoothly reorients by π. By rotating magnetic fields, a variety of interesting solitons were subsequently observed [13-15]. Due to the birefringence of LCs, optical solitons in nematic LCs, called nematicons, have received much attention. They represent self-focused, continuous wave light beams and have promising applications in optical information technology [16]. Topologically structured three-dimensional (3D) solitons in the form of torons or hopfions can be generated in cholesteric LCs by utilizing electric fields [17-19] or laser tweezers [20-22]. They are basically static but can also perform squirming motion driven by electric fields [23, 24]. They enable twist in all three spatial dimensions and are stabilized by strong energy barriers associated with the nucleation of topological defects [20].

Recently, multidimensional dissipative solitons, called directrons, driven by electric fields were observed in nematics [25-28]. These solitons represent spatially-confined director perturbations driven by electric fields that propagate rapidly through a slab of a homogeneously aligned LC and survive collisions with each other. So far, these solitons are only confirmed in LCs with a negative dielectric anisotropy, i.e., $\Delta\varepsilon = \varepsilon\| - \varepsilon\bot < 0$ and a relatively small positive, or negative, conductivity anisotropy, $\Delta\sigma = \sigma\| - \sigma\bot$. It was indicated that they cannot exist in a LC with positive $\Delta\varepsilon$ [27]. This was anticipated from the fact that a positive dielectric anisotropy $\Delta\varepsilon$ will induce a dielectric torque which strongly inhibits the flexoelectric torque at high amplitudes of electric fields. In addition, the positive $\Delta\varepsilon$ will also lead to a direct Freedericksz transition where space charges cannot form according to the Carr-Helfrich electro-convection (EC) mechanism [29, 30]. According to the reports [25-28], both flexoelectric effect and space charges are the elementary conditions for the formation of these dissipative solitons. Such stringent conditions on the LC material (negative $\Delta\varepsilon$' and

small positive or negative $\Delta\sigma$) would greatly limit broader research of these novel solitons, which are very important not only theoretically for nonlinear physics but also for practical applications such as targeted 2D delivery of optical information or mass transport via micro-cargos.

In this work, dynamic dissipative solitons are successfully generated in nematic E7 with positive $\Delta\varepsilon$ and $\Delta\sigma$. E7 is a standard liquid crystal, which has been broadly used in laboratories and industry worldwide. The nematic material is confined in cells spin-coated with a sulfonic azo dye SD1 and processed by the photoalignment technique [31]. In contrast to the conventional rubbing technique, photoalignment not only avoids problems such as mechanical damage, electrostatic charge, or dust contamination, but also produces high-resolution multidomain alignment [32, 33]. Instead of forming a quasi-homeotropic state (Freedericksz transition) as predicted by the standard model (SM) [34] or some complicated EC patterns as reported in ref. [35], dynamic dissipative solitons are observed. The formation mechanism roots in the strong coupling between **n** and the isotropic flow induced by ion motion, which is allowed by the relatively weak azimuthal anchoring strength of the photoaligned surfaces as well as the relatively high ion concentration of the sample due to a weak dissolution of the SD1 layers with time. The solitons are waves of director deformations that oscillate with the frequency of the applied alternating current (AC) electric field and can be observed *in situ* through polarizing optical microscopy (POM). The dynamics of the solitons is analyzed and tracked. They can either pass through each other in collisions or collide with each other and reflect into different directions, a behavior which depends on the amplitude (*E*) and frequency (*f*) of the applied electric field. The influence of chirality on these solitons is further investigated by doping E7 with a chiral dopant. It is shown that the trajectories of moving solitons can be manipulated by a predesignated alignment pattern and micro-cargos, such as silica particles, can be attracted and transported by the solitons. Finally, the contribution of the weak azimuthal anchoring and the influence of ion concentration are demonstrated.

5.2 Materials and methods

The nematic LC we used as the soliton medium is E7 with a positive dielectric

anisotropy of $\Delta\varepsilon \sim 12$ and a positive conductivity anisotropy of $\Delta\sigma \sim 10^{-7}$ $\Omega^{-1}\mathrm{m}^{-1}$ (measured at 1 KHz, 50 °C). The nematic is aligned homogeneously in cells with thickness $d \sim 11 \pm 3$ μm. The homogeneous alignment is realized by the photoalignment technique, in which substrates, spin-coated with SD1, are exposed to linearly polarized ultra-violet (UV) light. Either a sinusoidal or a rectangular AC field $\mathbf{E} = (0, 0, E)$ is applied along the z axis (perpendicular to the xy substrate plane of the cell, Figure 5-1) so that the sandwich cell acts as a plate capacitor. The sample is placed on a hot stage with its alignment direction, $\mathbf{m}$, parallel to the x axis, and observed through a polarizing optical microscope (POM) with crossed polarizers (the polarizer and analyzer are parallel to the x and y axes, respectively). More details about the experimental part can be found in the Experimental Section of the Supplementary Information.

5.3 Results

5.3.1 The structure of solitons

Independent "frog-egg-like" solitons are randomly generated in the nematic LC as E increases above some frequency-dependent threshold (E_N). Outside the solitons, the sample shows a homogeneous dark state. Rotating the sample by a small angle, a periodic change of light intensity (monochromatic light source) is observed (Supplementary Figure 5-1). This suggests that at low frequency f, due to the dielectric toque and its relaxation, the middle layer of $\mathbf{n}$ oscillates with f out of the xy plane by a polar angle θ_m with respect to the z axis (Figure 5-1 (b)). θ_m can be estimated from the dependence of transmitted light intensity on the polar angle, which changes from ~ 66 ° to ~ 70 ° periodically (Supplementary Figure 5-1). In the xy plane, the projection of $\mathbf{n}$ onto the xy plane aligns along $\mathbf{m}$. Inside the solitons, the light intensity increases, indicating azimuthal deviations of $\mathbf{n}$ from $\mathbf{m}$. To identify the sign of the azimuthal angle (φ_m with respect to the x axis, Figure 5-1 (b)), a first-order red plate compensator (530 nm) is inserted between the sample and the analyzer, with the slow axis λ making 45 ° with the analyzer. Either yellow or blue can be distinguished due to the subtractive or additive effect of the phase retardations of the compensator and the nematic[36]. By observing the solitons through a higher frame rate at 100 fps, a frequency-dependent

modulation of **n** is determined (Figure 5-1 (a)), which may be induced by the flexoelectric effect. Simultaneously, **n** is oscillating out of the xy plane with the polar angle θ_m due to the dielectric effect. It is also found that these solitons can move either parallel or perpendicular to **m**, which depends on their director structures. Figure 5-1 (c) shows the time-averaged structure of the solitons observed at a lower frame rate 10 fps. Solitons with a time-averaged mirror-symmetry director structure are relatively static (Figure 5-1 (c) I). As long as this symmetry is broken, which can be induced by factors such as background flows or local director distortions, the solitons start to move. Solitons propagating along the x-axis lack the symmetry with respect to the y-axis (Figure 5-1 (c) II). Vice versa, solitons propagating along the y-axis lack the symmetry with respect to the x-axis (Figure 5-1 (c) IV). A more severe deformation of **n** in region 3 also can lead to an oblique motion with respect to the x-axis (Figure 5-1 (c) III). Additionally, the time-averaged director structure of the solitons shows a static biconcave structure. This may be attributed to the longer duration of the biconcave deformation in one period of director oscillation as observed in Figure 5-1 (a). The size of the solitons is mainly dependent on the cell gap, d (Supplementary Figure 5-2). Both the width (w_N) and length (l_N) of the solitons increase with d.
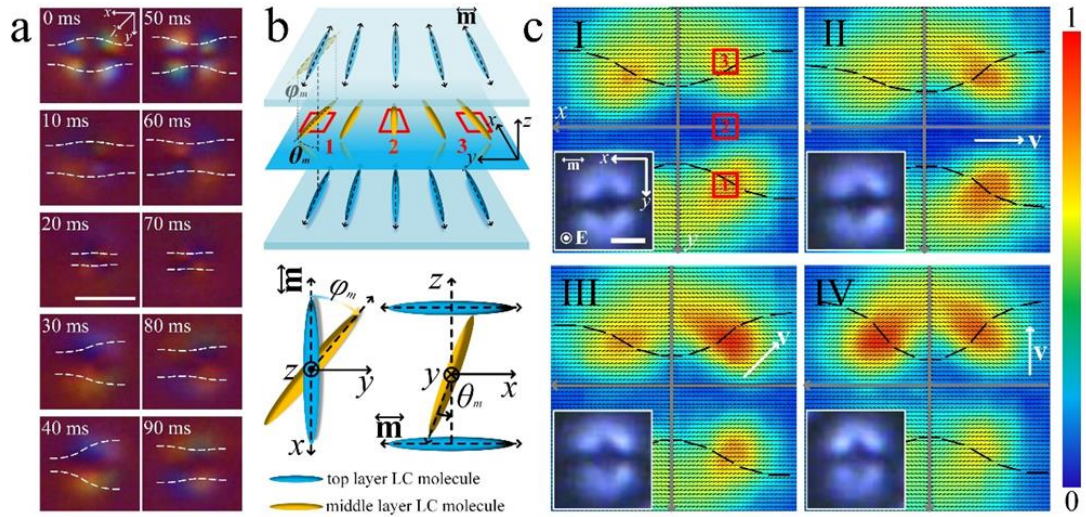
Figure 5-1 The structure of solitons. (a) POM micrographs of a soliton modulated by a rectangular AC field of $E \sim 0.4$ V μm^{-1}, $f = 10$ Hz. White dashed lines represent the director field. λ represents the slow axis of the red plate. Both polarizer and analyzer are parallel to the x and y axis, respectively. Scale bar 20 μm. (b) The schematic structure of a soliton. **m** represents the alignment direction. φ_m and θ_m represent the azimuthal angle and the polar angle of the local mid-layer director. (c) Transmitted light intensity maps and the corresponding mid-layer director fields (black dashed lines) in the xy plane within solitons. Rectangular AC field $E \sim 0.7$ V μm^{-1}, $f = 20$ Hz. **v** represents the velocity of the soliton. The color bar shows a linear scale of transmitted light intensity. Insets are the corresponding POM micrographs, scale bar 10 μm. Both polarizer and analyzer are parallel to the x and y axis, respectively. Red squares 1, 2, and 3 are corresponding to the ones in (b).

5.3.2 Generation and dynamics of solitons

As we suggested above, these dissipative solitons are driven by external AC electric field. Figure 5-2 (a) shows the threshold dependences of different states of the sample on f. Basically, the nematic firstly experiences a Freedericksz transition from the homogeneous state (inset I) to a quasi-homeotropic state where reverse-tilt domains (TIDs, inset II) are observed. These TIDs are transient and will eventually annihilate within several minutes. The threshold of the Freedericksz transition (E_F) is about 0.1 V μm^{-1}, independent on the frequency. The solitons (inset III) emerge after the Freedericksz transition and show a frequency-dependent E_N, which is proportional to $f^{1/2}$ (left-top inset). This square-root dependence of E_N on f is observed in almost all the samples throughout our experiment, which indicates that the soliton is caused by an isotropic electro-hydrodynamic (EHD) instability [37-39]. Such an interpretation is supported by the circular motion of tiny suspended dust particles observed both in the nematic and the isotropic phase at E_N [37-40]. On further increase of E, periodic domains (inset IV) that extend gradually and eventually cover the entire electrode area of the cell, are observed. Just like the dissipative solitons observed in nematics with negative dielectric anisotropy [25, 26], the ones here also show electric field dependent dynamics. Both the amplitude and the direction (either parallel or perpendicular to **m**) of the velocity (**v**) of the solitons can be tuned electrically (Figure 5-2 (b), supplementary movie 5-1). At f = const., the amplitude of soliton velocity (v) increases with E.
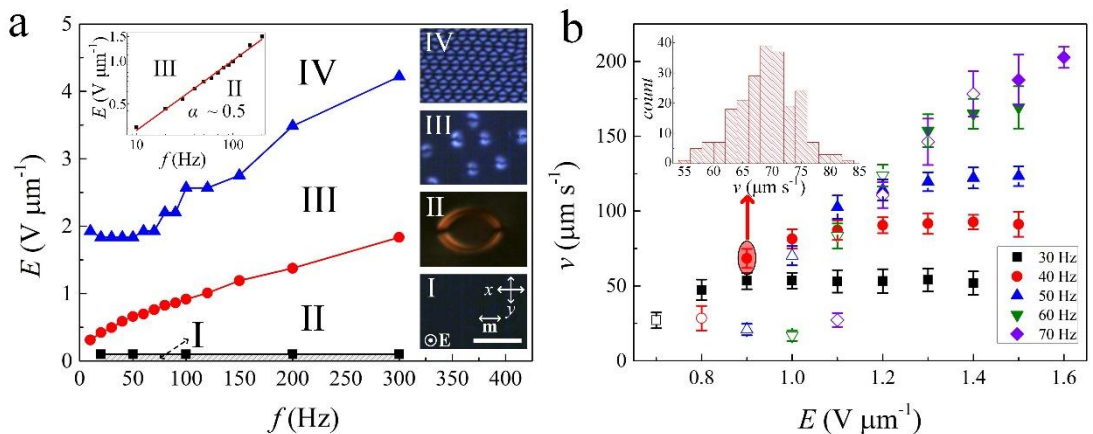
Figure 5-2 Soliton properties as a function of electric field. (a) Threshold dependence of different states (I homogeneous state, II quasi-homeotropic state, III soliton state, IV periodic domains) on the frequency of rectangular AC electric fields, f. Insets are the POM micrographs corresponding to different states (I: E = 0 V μm^{-1}; II: E ~ 0.2 V μm^{-1}, f = 20 Hz; III: E ~ 0.7 V μm^{-1}, f = 20 Hz; IV: E ~ 2.2 V μm^{-1}, f = 20 Hz). **m** represents the alignment direction. **E** represents the electric field which is perpendicular to the xy plane. Both polarizer and analyzer are parallel to the x and y axis,

respectively. Scale bar 50 μm. The inset on the top-left corner shows the square-root dependence of the threshold of solitons, $E_N(f)$, with α being the slope of this dependence. (b) Dependence of the amplitude of velocity, v, of solitons on the amplitude of a rectangular AC electric field, E. The solid and hollow symbols represent the velocities parallel and perpendicular to **m**, respectively. The error bars are calculated from the standard deviation of velocities of different solitons at the same electric field. The inset represents the velocity distribution of solitons at $f = 40$ Hz, $E \sim 0.9$ V μm^{-1}.

Generally, the solitons form randomly throughout the nematic bulk (Figure 5-3 (a) i). This may be attributed to the instabilities induced by the motion of ions since weak flow patterns are observed during the formation. With the formation and motion of solitons, these flow patterns will subsequently disappear (supplementary movie 5-2). The explanation of soliton formation via ions can be further supported by the phenomenon described below. In the experiment, we first increase E above E_N to generate solitons. At an arbitrary time, E is decreased below E_N and the solitons instantly disappear. If we increase E above E_N within ~10 s, it is found that the solitons are generated at almost the same location before the decrease of E. However, once the interval is longer (such as 30 s), new solitons are randomly generated in space. Taking a typical diffusion coefficient of ions in LCs of 2×10^{-9} m^2 s^{-1}, the delocalization of ions is about 20 s [27], which is consistent with our observation. Strong EHD flows can induce the solitons, too (Figure 5-3 (a) ii, supplementary movie 5-2). These flow patterns are usually observed at the edges of the cell or nearby disclinations. The solitons also nucleate near disclinations (yellow dashed line, Figure 5-3 (a) iii) and at irregularities, such as dust particles (Figure 5-3 (a) iv). One soliton can even split into two or more solitons (Figure 5-3 (a) v), which accompanies the elongation of the soliton. The elongation process results in a continuous accumulation of excess elastic energy, and the soliton fractionates when the energy penalty from the elastic deformation cannot be compensated by the effects of surface and dielectric interaction [27]. Furthermore, the collision of two solitons may also lead to the generation of new solitons (Figure 5-3 (a) vi). More details about the nucleation of solitons can be found in Supplementary Movie 5-2.

The solitons pass through or reflect each other during collisions, which depends on the degree of offset, δ (the distance between the centers of the two solitons) as well as their motion direction (Figure 5-3 (b)-(e), Supplementary Movie 5-3). When the solitons propagate parallel to **m** and δ is large enough ($0.5w_N < \delta < w_N$,), the two solitons pass through each other with little influence on their structure and dynamics (Figure 5-3 (b) and (c)). On the other hand, when the solitons move perpendicular to **m**, they behave like particles. Especially when $\delta < 0.5 w_N$, the two solitons collide and then reflect into opposite directions

(Figure 5-3 (d) and (e)). Such a behavior may be attributed to the increased mismatch of the director field between solitons which depends on the structure of the solitons and the offset, δ, between them.
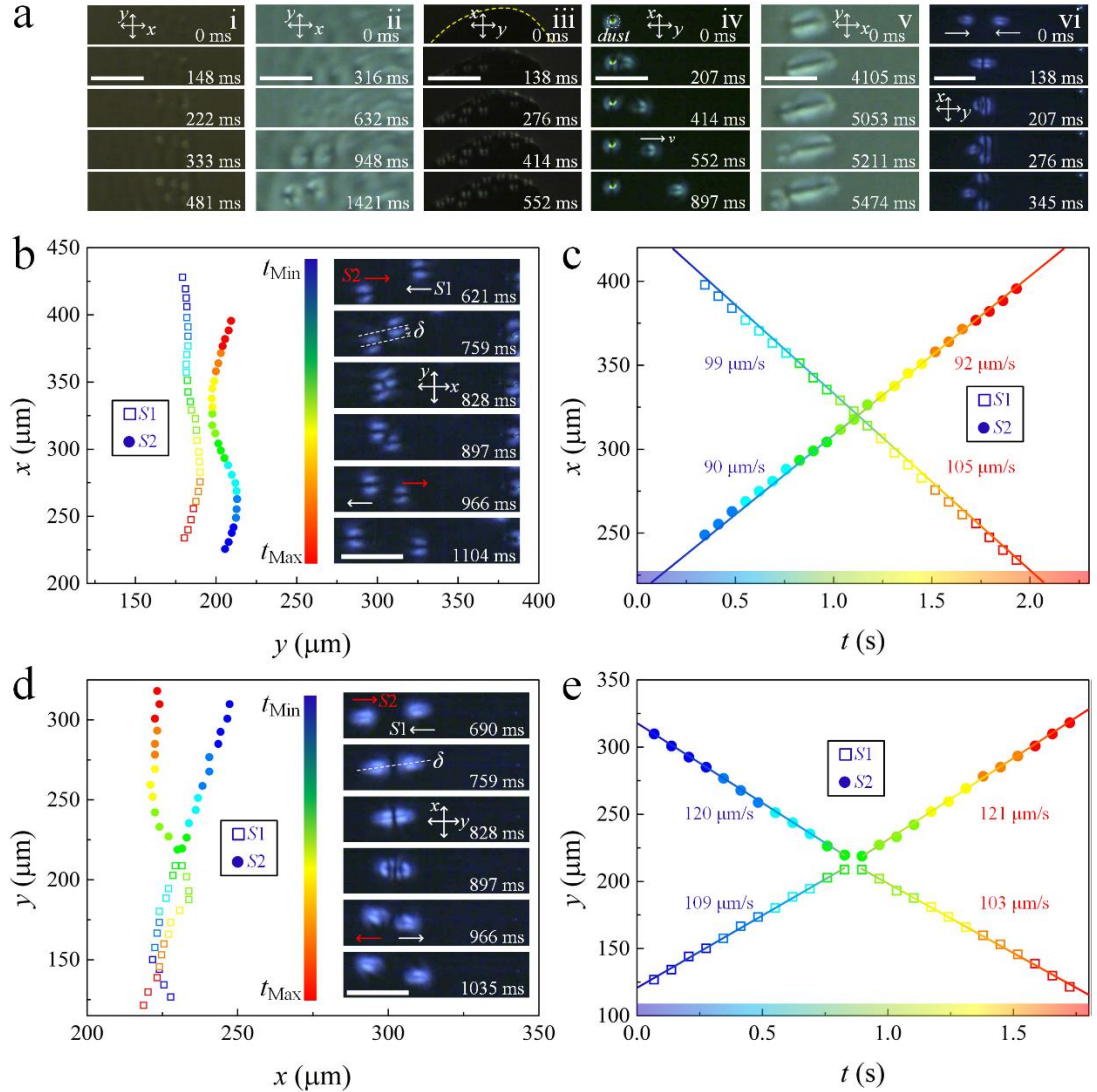
Figure 5-3 Nucleation and interaction of solitons driven by rectangular AC fields. (a) random generation of solitons ($E \sim 0.7$ V μm^{-1}, $f = 20$ Hz) (i), EHD flows induce solitons ($E \sim 0.6$ V μm^{-1}, $f = 20$ Hz) (ii), nucleation of solitons adjacent to a disclination (yellow dashed line) ($E \sim 0.7$ V μm^{-1}, $f = 20$ Hz) (iii), nucleation of a soliton at a dust particle ($E \sim 1.2$ V μm^{-1}, $f = 70$ Hz) (iv), proliferation of a soliton ($E \sim 0.5$ V μm^{-1}, $f = 20$ Hz) (v) and collision of two solitons creates a new soliton ($E \sim 1.2$ V μm^{-1}, $f = 70$ Hz) (vi). (b) The trajectories of two solitons pass through each other. $E \sim 1.1$ V μm^{-1}, $f = 40$ Hz. The color bar represents the elapsed time. $t_{Min} = 0$ s, $t_{Max} \sim 2.0$ s, time interval $\Delta t \sim 0.069$s. Insets are the POM time series micrographs of the solitons. δ represents the offset between the centers of two solitons before the collision. (c) Time dependence of x coordinates of the solitons in (b). (d) The trajectory of two solitons colliding and reflecting into opposite directions; $E \sim 1.2$ V μm^{-1}, $f = 60$ Hz. The color bar represents the elapsed time. $t_{Min} = 0$ s, $t_{Max} \sim 1.8$ s, time interval $\Delta t \sim 0.069$s. Insets are the POM time series micrographs of the solitons. δ represents the offset between the centers of two solitons before the collision. (e)Time dependence of the y coordinates of the solitons in (d). In figures (a), (b) and (d) the polarizer and analyzer are parallel to the x and y axis, respectively, with the scale bars indicating 50 μm.

5.3.3 Dissipative solitons in CLCs

The influence of chirality on the structure and dynamics of solitons was also investigated.

138

Figure 5-4 (a) shows the director structure of a CLC soliton which changes periodically with f. Figure 5-4 (b) shows the E dependence of different states of the sample on f. The CLC firstly experiences a Freederickz transition which results in the fingerprint textures (inset II) [41]. By increasing E, the fingerprint textures gradually disappear due to the unwinding effect (inset III). The CLC solitons appear after the unwinding of helixes (inset IV). Just as for achiral nematics, the threshold of CLC solitons (E_{CLC}) also shows a square-root dependence on f. Further increase of E results in the observation of a periodic domain that covers the entire sample (inset V). The velocity (both direction and amplitude) of the CLC solitons is also dependent on the electric field (Figure 5-4 (c)). At f = const, v increases with E. It is observed that in contrast to the bidirectional propagation of solitons in achiral nematics, the propagation of the CLC solitons is more unidirectional (supplementary movie 5-1), which is similar to the schools of skyrmions in CLCs reported recently [24]. However, unlike the schooling motion which is a collective phenomenon relying on the inter-skyrmion interactions, the unidirectional motion of our CLC solitons is more likely attributed to the local background flows. The dielectric oscillation of **n** as well as the motion of ions induces flows that break the symmetric structure of the solitons, and initiate their translation through the sample. The reason why the achiral solitons do not show such a unidirectional motion is not clear, but may be due to the different director structure (although the unidirectional motion of the achiral solitons can actually be induced by applying a different AC field which is additionally modulated with a higher modulation frequency f_m, such as f_m = 50 Hz, f = 10 Hz, Supplementary Movie 5-4). These flows are dependent on the local director field and can be very different in different regions. As can be seen in Supplementary Movie 5-4, two crossed disclinations divide the region into four sub-regions. The background flow in each region is perpendicular to the one nearby, leading to a fascinating circular motion of solitons. The nucleation of CLC solitons is similar to the achiral ones' (Supplementary Figure 5-3 and supplementary movie 5-5), and they can pass through or reflect each other during collisions (Supplementary Figure 5-4 and supplementary movie 5-6). One distinct difference between the chiral and achiral systems is that, the diameter (D) of the chiral solitons shows a dependence on E, which gradually decreases with increasing E (Supplementary Figure 5-5).
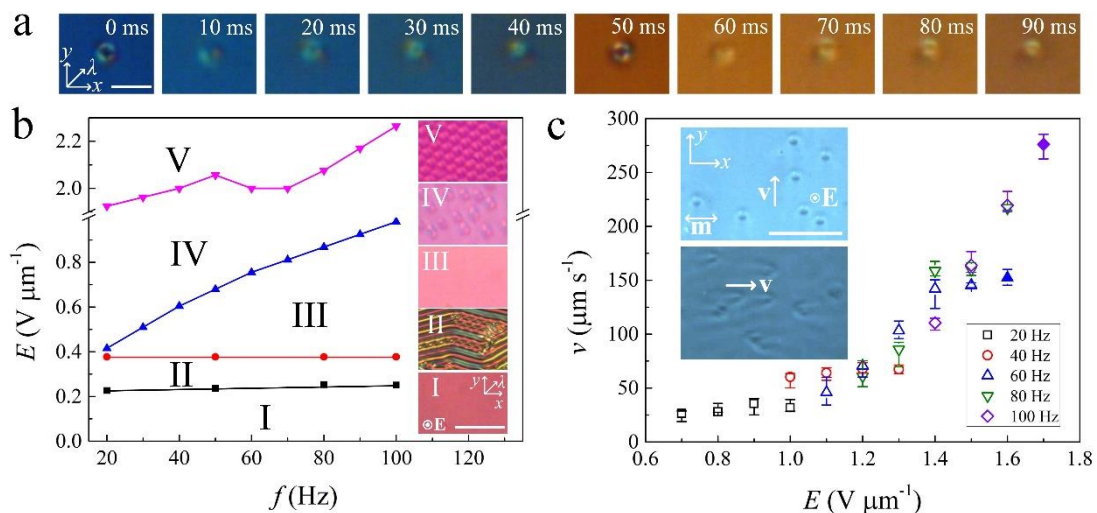
Figure 5-4 Solitons in CLCs. (a) POM micrographs of a soliton modulated by a rectangular AC field with $E \sim 0.5$ V μm^{-1}, $f = 10$ Hz. λ represents the slow axis of the red plate. Both polarizer and analyzer are parallel to the x and y axis, respectively. The scale bar is 20 μm. (b) Threshold dependence of different states (I homogeneous state, II fingerprint texture, III unwinding state, IV soliton state, V periodic domain) on the frequency of rectangular AC electric fields, f. Insets are the POM micrographs corresponding to different states (I: $E = 0$ V μm^{-1}; II: $E \sim 0.3$ V μm^{-1}, $f = 50$ Hz; III: $E \sim 0.6$ V μm^{-1}, $f = 50$ Hz; IV: $E \sim 0.8$ V μm^{-1}, $f = 50$ Hz; V: $E \sim 2.1$ V μm^{-1}, $f = 50$ Hz). **E** represents the electric field which is perpendicular to the xy plane. λ represents the slow axis of the red plate. Both polarizer and analyzer are parallel to the x and y axis, respectively. Scale bar 50 μm. (c) The dependence of the amplitude of soliton velocity, v, on the amplitude of the rectangular AC electric field, E. The solid and hollow symbols represent the velocities parallel and perpendicular to the alignment direction, respectively. The error bars are calculated from the deviation of velocities of different solitons at the same electric field. The insets show the POM micrographs of solitons travelling perpendicular ($f = 60$ Hz, $E \sim 1.2$ V μm^{-1}) and parallel ($f = 60$ Hz, $E \sim 1.6$ V μm^{-1}) to the alignment direction, **m**, respectively. The electric field **E** is perpendicular to the xy plane, and **v** represents the velocity of the solitons. Scale bar 100 μm. Both polarizer and analyzer are parallel to the x and y axis, respectively.

5.3.4 Cargo transport and trajectory manipulation

It has been reported that distorted LC regions, such as topological defects, can attract colloidal particles [42]. Since the solitons are actually self-confined director deformations, we here confirm that they too can attract particles. In Figure 5-5 (a), an aggregate of two micro-particles is attracted by a soliton nearby and trapped in its center (supplementary movie 5-7). Besides, the solitons can even be used as vehicles for micro-cargo transport. In Figure 5-5 (b), a micro-particle is carried by a soliton and moved through the nematic liquid crystal (supplementary movie 5-7). Furthermore, the propagating trajectory of the solitons can be controlled by the alignment of the cell substrates. In Figure 5-5 (c), the nematic is divided into two regions with different alignment directions perpendicular to each other. In each region, the solitons move either parallel or perpendicular to **m**, depending on the applied electric field. Once a soliton crosses the boundary of the two regions, it will transform its structure and switch its moving direction to fit the new alignment direction (supplementary

140

movie 5-6).
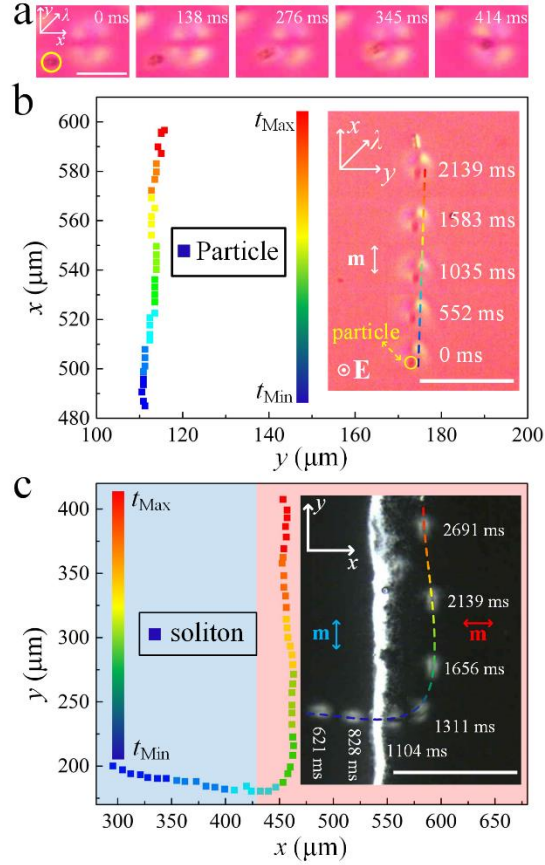
Figure 5-5 Particle trapping, cargo transport and trajectory manipulation. (a) POM time series micrographs of an aggregate of two micro-particles being trapped by a soliton (rectangular AC field $E \sim 0.5$ V μm^{-1}, $f = 20$ Hz). λ represents the slow axis of the red plate. Both polarizer and analyzer are parallel to the x and y axis, respectively. Scale bar 20 μm. The yellow circle represents the aggregate of the two micro-particles. (b) Trajectory of a micro-particle transported by a soliton (rectangular AC field $E \sim 0.9$ V μm^{-1}, $f = 40$ Hz). The color bar represents the elapsed time. $t_{Min} = 0$ s, $t_{Max} \sim 2.5$ s, time interval $\Delta t \sim 0.069$s. The inset shows the micrograph of the micro-particle transported by a soliton. **m** represents the alignment direction. The electric field **E** is perpendicular to the xy plane. The scale bar is 50 μm. λ represents the slow axis of the red plate. Both polarizer and analyzer are parallel to the x and y axis, respectively. (c) Trajectory of a soliton travelling through the boundary of two regions with perpendicular alignment. The rectangular AC field is of amplitude $E \sim 1.1$ V μm^{-1} and frequency $f = 60$ Hz. The color bar represents the elapsed time. $t_{Min} = 0$ s, $t_{Max} \sim 3.4$ s, time interval $\Delta t \sim 0.069$s. The inset shows the micrograph of the soliton. **m** represents the alignment direction. Scale bar 100 μm. Both polarizer and analyzer are parallel to the x and y axis, respectively.

5.4 Discussion

Early studies on EHD instabilities in LCs have been focused on EC effects in nematics with opposite signs of anisotropies, e.g. negative $\Delta\varepsilon$ and positive $\Delta\sigma$ [43], where EC rolls, such as "Williams domains" [44] and "chevrons" [45], are observed. In their case the destabilization is attributed to the charge separation mechanism introduced by Carr [29] and Helfrich [30], which was later extended to a three dimensional theory, i.e. the standard model (SM) [34]. Nonstandard EC effects may arise in nematics with both negative $\Delta\varepsilon$ and $\Delta\sigma$, but most of

them can be explained by adding flexoelectricity effects to the SM [46, 47]. The SM predicts no EHD instabilities in nematics with both positive $\Delta\varepsilon$ and $\Delta\sigma$. However, complex EC patterns, such as fingerprint textures [37], Maltese crosses [37] and cellular patterns [35], have been observed for homeotropic anchoring condition. Various explanations, such as charge injection (known as Felici-Benard mechanism) [48, 49], isotropic flows [37, 38, 39], flexoelectricity and surface-polarization effects [50, 51] were proposed to account for the origin of the instabilities. However, a rigorous explanation of the formation is not available yet. On the other hand, in the case of homogeneous alignment, stationary Williams domains exist for small positive values of $\Delta\varepsilon$ (normally $0 < \Delta\varepsilon < 0.4$) only, when the threshold of the EHD instability is lower than the threshold of the Freedericksz transition [52-55]. For large values of $\Delta\varepsilon$ (just as it is the situation in our case), EHD instabilities are not expected, and only a homogeneous splay Freedericksz transition is predicted [56]. However, EC patterns in the form of fingerprint textures and cellular patterns were in fact observed in ref. [35], but the authors did not give a convincing explanation for their formation.

The EHD instabilities as a form of dynamic dissipative solitary waves has been reported only very recently and only in nematics with negative $\Delta\varepsilon$ [25-28]. Their formation was attributed to flexoelectricity [25] and space charges [27]. It was not expected that such solitons can also exist in nematics with positive $\Delta\varepsilon$ since both factors are inhibited. The reason for the generation of solitons in our experiment is attributed to special conditions, namely a relatively high ion concentration in combination with weak azimuthal anchoring. The high concentration of ions induces stronger isotropic flows. These flows are the prerequisite for the solitons' generation, as they break the stability of the system (Figure 5-3 (a)). The weak azimuthal anchoring allows the periodic azimuthal oscillation of **n** in the *xy* plane and thus keeps the structure of the solitons from collapsing.

To demonstrate the influence of the azimuthal anchoring on the generation of solitons, commercial cells coated with rubbed polyimide and filled with E7 were additionally tested. It is well known that rubbed polyimide layers provide strong azimuthal anchoring for thermotropic LCs, which is of the order of 10^{-3} J m^{-2} for E7 [57]. In contrast, the azimuthal anchoring of the photoalignment layer (SD1) in our experiment is only $\sim 2.2 \times 10^{-5}$ J m^{-2} according to our measurement (Supplementary Figure 5-6). By applying an AC field to the commercial cell, it goes through a Freedericksz transition at low E and keeps a quasi-

homeotropic state at high E. At low f, by rotating the sample by a small angle with **m** deviated from the x-axis, a periodic change of light intensity is observed, which is due to the oscillation of **n** out of the xy plane. The tilting angle θ_m is estimated from the dependence of the light intensity on the polar angle, which changes with f from $\sim 67\,°$ to $\sim 72\,°$ (Supplementary Figure 5-1). No EHD instability effect is observed after the Freedericksz transition. On the other hand, E7 is also filled into a cell spin-coated with polyvinyl alcohol (PVA) solution and rubbed with velvet. It has been reported that rubbed PVA provides a relatively weak azimuthal anchoring of the order of $10^{-5}\,\mathrm{J\,m^{-2}}$ [58], which is a value comparable to our photoalignment layer. By applying an AC field to the sample, solitons are observed after the Freedericksz transition. However, unlike the ones in the cells processed by photoalignment, the ones in the PVA cell cannot move efficiently, instead, they look like they are trapped and can only vibrate locally (Supplementary Movie 5-8). This may be due to the poor rubbing alignment, dust contamination, and static electric effects produced during the rubbing process.

The influence of ion concentration is also investigated by doping different concentrations of an ionic dopant (ASE2, Supplementary Figure 5-7 (a)) into E7. We estimate the ion concentration by measuring the conductivity $\sigma\perp$ and the dielectric loss $\varepsilon\perp$" of the sample (Supplementary Figure 5-8 (a)); the higher $\sigma\perp$ and $\varepsilon\perp$", the higher the ion concentration [59]. E7 doped with 0 wt %, 0.1 wt % and 0.5 wt % ASE2, respectively, were filled into commercial cells (rubbed polyimide), and solitons are observed in the sample doped with 0.5 wt % ASE2 (Supplementary Figure 5-8 (b)). It should be noted that the solitons are only observed at the edges of the ITO electrodes (Supplementary Movie 5-8), which may be due to the stronger EHD instabilities there. At higher E, periodic EC rolls whose wave vector are parallel to the rubbing direction are observed as reported in ref. [35].

Moreover, we also find that the ion concentration of the samples processed by photoalignment technique changes with time. Both $\sigma\perp$ and $\varepsilon\perp$" increase greatly within a time period of 3 days (II) and then remain saturated (III, 10 days later) (Supplementary Figure 5-9 (a)). The increase of ion concentration could be attributed to a weak solubility of SD1, which is an ionic material, in the LC E7 (Supplementary Figure 5-7 (b)). The influence of such an increase is discussed below. As mentioned before, the solitons randomly form in space as long as E surpasses E_N which is attributed to the instabilities induced by ionic

motion. The distribution of the ion concentration throughout the sample is not homogeneous, the regions with higher ion concentration generate solitons more easily, which means that E_N in different regions is slightly different (generally the difference is smaller than 0.1 V μm^{-1}). To eliminate this difference, we confine our measurement to the same region (770 μm x 409 μm). In Supplementary Figure 5-9 (b), it is found that in the usual case (I, 0 days), the solitons firstly nucleate in the vicinity of a dust particle (inset), with most part of the region exhibiting no solitons. By slowly increasing E (~ 0.02 V μm^{-1} per 30 s), the number of the solitons increases gradually mainly due to the random generation and proliferation effect (Figure 5-3 (a)), and the solitons gradually fill up the region. It should be noted that the reason why we do not use the number density of solitons to represent the covered area is because the solitons generate randomly and inhomogeneously, i.e. the number density of soliton changes greatly in different sub-regions. The amount of solitons reaches the maximum at ~ 1.05 V μm^{-1} and then gradually decreases. In contrast, after 3 days (II), it is found that when E surpasses E_N, the solitons generate homogeneously throughout the region and the densities of solitons in different sub-regions are similar to each other. This may be caused by the increase of the overall ion concentration of the sample diminishing the differences among different sub-regions. By increasing E, more solitons generate in a rather narrow range of E and the amount of solitons reaches a maximum at ~ 0.65 V um^{-1}. The maximum is almost twice as large as the one in case I. Further increase of E, causes the amount of solitons to decrease gradually and finally reach saturation. It is also found that the threshold E_N decreases by ~ 0.1 V μm^{-1}. Such a decrease may be attributed to the increase of the ion concentration, and can be found throughout the sample. In Supplementary Figure 5-10, the E_N of a region nearby the edge of the ITO electrode is also found to be decreased, but with a smaller amplitude.

To further verify that the formation of solitons arises from the properties of the photoalignment, and is not a privilege of E7 alone, 5CB (4-cyano-4'-pentylbiphenyl), another well-studied LC which has been broadly used both in laboratories and industry, is filled into a cell spin-coated with SD1 and processed by photoalignment. Just as for E7, both $\Delta\varepsilon$ and $\Delta\sigma$ of 5CB are positive [23]. Dissipative solitons are observed at E above E_N, and the $E_N(f)$ also shows the before observed square-root dependence (Supplementary Figure 5-11 (b)). Besides, it is found that the behavior of the solitons in 5CB is similar to case II of E7

(Supplementary Figure 5-9), which may be attributed to a higher ion concentration of 5CB (Supplementary Figure 5-11 (a)).

5.5 Conclusion

In summary, dynamic dissipative solitons are realized in nematics with both positive dielectric and conductive anisotropies. The structure and dynamics of the solitons are demonstrated and the influences of chirality, azimuthal anchoring and ion concentration are investigated. The underlying mechanism of the formation of the solitons is still not very clear and requires further experimental and theoretical investigations [60,61]. However, generally, it may be attributed to the strong coupling between the director field and the isotropic flow, which is allowed by the weak azimuthal anchoring of the photoalignment as well as the relatively high ion concentration. Our work not only contributes to the investigation of EHD effects in LCs and nonlinear systems in general, but also provides a simple way for generating and manipulating multi-dimensional solitons, as well as exploiting them for micro-cargo transport.

5.6 Acknowledgements

5.7 References

1. Shen, Y. & Dierking, I. Perspectives in Liquid-Crystal-Aided Nanotechnology and Nanoscience. *Applied Sciences* **9**, 2512 (2019).
2. De Gennes, P.-G. & Prost, J. *The physics of liquid crystals*. (Oxford university press, 1995).
3. Lam, L. & Prost, J. *Solitons in liquid crystals*. (Springer Science & Business Media, 2012).
4. Dauxois, D. & Peyrard, M. *Physics of solitons*. (Cambridge University Press, 2006).
5. Kartashov, Y. V., Astrakharchik, G. E., Malomed, B. A. & Torner, L. Frontiers in multidimensional self-trapping of nonlinear fields and matter. *Nature Reviews Physics* **1**, 185-197 (2019).
6. Malomed, B., Sabata, L. T., Wise, F. & Mihalache, D. On multidimensional solitons and

their legacy in contemporary atomic, molecular and optical physics. *Journal of Physics B: Atomic, Molecular and Optical Physics* **49**, 170502 (2016).

7. Helfrich, W. Alignment-inversion walls in nematic liquid crystals in the presence of a magnetic field. *Physical Review Letters* **21**, 1518-1521 (1968).

8. Leger, L. Observation of wall motions in nematics. *Solid State Communications* **10**, 697-700 (1972).

9. Leger, L. Static and dynamic behaviour of walls in nematics above a Freedericks transition. *Solid State Communications* **11**, 1499-1501 (1972).

10. Léger, L. Walls in nematics. *Molecular Crystals and Liquid Crystals* **24**, 33-44 (1973).

11. Turner, R. Twist Walls in Nematic Liquid Crystals. *The Philosophical Magazine: A Journal of Theoretical Experimental and Applied Physics* **30**, 13-20 (1974).

12. Chandrasekhar, S. & Ranganath, G. S. The structure and energetics of defects in liquid crystals. *Advances in Physics* **35**, 507-596 (1986).

13. Migler, K. B. & Meyer, R. B. Solitons and pattern formation in liquid crystals in a rotating magnetic field. *Physical Review Letters* **66**, 1485-1488 (1991).

14. Frisch, T., Rica, S., Coullet, P. & Gilli, J. M. Spiral waves in liquid crystal. *Physical Review Letters* **72**, 1471-1474 (1994).

15. Zheng, C. & Meyer, R. B., Thickness effects on pattern formation in liquid crystals in a rotating magnetic field. *Physical Review E* **55**, 2882-2887 (1997).

16. Assanto, G. *Nematicons: Spatial Optical Solitons in Nematic Liquid Crystals* (John Wiley & Sons, 2012).

17. Haas, W. E. L. & Adams, J. E. New optical storage mode in liquid crystals. *Applied Physics Letters* **25**, 535-537 (1974).

18. Kawachi, M., Kogure, O. & Kato, T. Bubble domain texture of a liquid crystal. *Japanese Journal of Applied Physics* **13**, 1457 (1974).

19. Ackerman, P. J., Lagemaat, J. & Smalyukh, I. I. Self-assembly and electrostriction of arrays and chains of hopfion particles in chiral liquid crystals. *Nature Communications* **6**, 6012 (2015).

20. Smalyukh, I. I., Lansac, Y., Clark, N. A. and Trivedi, R. P. Three-dimensional structure and multistable optical switching of triple-twisted particle-like excitations in anisotropic fluids. *Nature Materials* **9**, 139 (2009).

21. Ackerman, P. J., Qi, Z. & Smalyukh, I. I. Optical generation of crystalline, quasicrystalline, and arbitrary arrays of torons in confined cholesteric liquid crystals for patterning of optical vortices in laser beams. *Physical Review E* **86**, 021703 (2012).

22. Sohn, H. R. O., Liu, C. D., Wang, Y. & Smalyukh, I. I. Light-controlled skyrmions and torons as reconfigurable particles. *Opt. Express* **27**, 29055-29068 (2019).

23. Ackerman, P. J., Boyle, T. & Smalyukh, I. I. Squirming motion of baby skyrmions in nematic fluids. *Nature Communications* **8**, 673 (2017).

24. Sohn, H. R. O., Liu, C. D. & Smalyukh, I. I. Schools of skyrmions with electrically tunable elastic interactions. *Nature Communications* **10**, 4744 (2019).

25. Li, B.-X., Borshch, V., Xiao, R.-L., Paladugu, S., Turiv, T., Shiyanovskii, S. V. & Lavrentovich, O. D. Electrically driven three-dimensional solitary waves as director bullets in nematic liquid crystals. *Nature Communications* **9**, 2912 (2018).

26. Li, B.-X., Xiao, R.-L., Paladugu, S., Shiyanovskii, S. V. & Lavrentovich, O. D. Three-dimensional solitary waves with electrically tunable direction of propagation in nematics. *Nature Communications* **10**, 3749 (2019).

27. Aya, S. & Araoka, F. Kinetics of motile solitons in nematic liquid crystals. *Nature Communications* **11**, 1 (2020).

28. Shen, Y. and Dierking, I. Dynamics of electrically driven solitons in nematic and cholesteric liquid crystals. *Communications Physics* **3**, 1-9 (2020).

29. Carr, E. F. Influence of Electric Fields on the Molecular Alignment in the Liquid Crystal p-(Anisalamino)-phenyl Acetate. *Molecular Crystals* **7**, 253-268 (1969).

30. Helfrich, W. Conduction-induced alignment of nematic liquid crystals: basic model and stability considerations. *The Journal of Chemical Physics* **51**, 4092-4105 (1969).

31. Ma, L.-L., Li, S.-S., Li, W.-S., Ji, W., Luo, B., Zheng, Z.-G., Cai, Z.-P., Chigrinov, V., Lu, Y.-Q., Hu, W. & Chen, L.-J. Rationally designed dynamic superstructures enabled by photoaligning cholesteric liquid crystals. *Advanced Optical Materials* **3**, 1691-1696 (2015).

32. Li, S.-S., Shen, Y., Chang, Z.-N., Li, W.-S., Xu, Y.-C., Fan, X.-Y. & Chen, L.-J. Dynamic cholesteric liquid crystal superstructures photoaligned by one-step polarization holography. *Applied Physics Letters* **111**, 231109 (2017).

33. Shen, Y., Xu, Y.-C., Ge, Y.-H., Jiang, R.-G., Wang, X.-Z., Li, S.-S. & Chen, L.-J. Photoalignment of dye-doped cholesteric liquid crystals for electrically tunable patterns with fingerprint textures. *Opt. Express* **26**, 1422-1432 (2018).

34. Bodenschatz, E., Zimmermann, W. & Kramer, L. On electrically driven pattern-forming instabilities in planar nematics. *Journal de Physique* **49**, 1875-1899 (1988).

35. Kumar, P., Heuer, J., Tóth-Katona, T., Éber, N. & Buka, Á. Convection-roll instability in spite of a large stabilizing torque. *Physical Review E* **81**, 020702 (2010).

36. Hartshorne, H. N. *The Microscopy of Liquid Crystals* (*Microscope Publications Ltd.*, 1974).

37. Barnik, M. I., Blinov, L. M., Grebenkin, M. F. and Trufanov, A. N. Dielectric regime of electrohydrodynamic instability in nematic liquid crystals. *Molecular Crystals and Liquid Crystals* **37**, 47-56 (1976).

38. Barnik, M., Blinov, L., Pikin, S. & Trufanov, A. Instability mechanism in the nematic and isotropic phases of liquid crystals with positive dielectric anisotropy. *Sov Phys JETP* **45**, 396-398 (1977).

39. Trufanov, A., Barnik, M., Blinov, L. & Chigrinov, V. Electrohydrodynamic instability in homeotropically oriented layers of nematic liquid crystals. *Sov Phys JETP* **53**, 355-361 (1981).

40. Oh, J., Gleeson, H. F. and Dierking, I. Electric-field-induced transport of microspheres in the isotropic and chiral nematic phase of liquid crystals. *Physical Review E* **95**, 022703 (2017).

41. Li, W.-S., Shen, Y., Chen, Z.-J., Cui, Q., Li, S.-S. & Chen, L.-J. Demonstration of patterned polymer-stabilized cholesteric liquid crystal textures for anti-counterfeiting two-dimensional barcodes. *Appl. Opt.* **56**, 601-606 (2017).

42. Shen, Y. & Dierking, I. Annihilation dynamics of topological defects induced by microparticles in nematic liquid crystals. *Soft Matter* **15**, 8749-8757 (2019).

43. Goossens, W. in *Advances in Liquid Crystals*. Elsevier, 1978, vol. 3, pp. 1-39.

44. Smith, I., Galerne, Y., Lagerwall, S., Dubois-Violette, E. & Durand, G. Dynamics of electrohydrodynamic instabilities in nematic liquid crystals. *Le Journal de Physique Colloques* **36**, C1-237-C231-259 (1975).

45. Ribotta, R., Joets, A. & Lei, L. Oblique roll instability in an electroconvective anisotropic

fluid. *Physical Review Letters* **56**, 1595-1597 (1986).

46. Tóth-Katona, T., Cauquil-Vergnes, A., Éber, N. & Buka, Á. Nonstandard electroconvection with Hopf bifurcation in a nematic liquid crystal with negative electric anisotropies. *Physical Review E* **75**, 066210 (2007).

47. Krekhov, A., Pesch, W., Éber, N., Tóth-Katona, T. & Buka, Á. Nonstandard electroconvection and flexoelectricity in nematic liquid crystals. *Physical Review E* **77**, 021705 (2008).

48. Nakagawa, M. & Akahane, T. A New Type of Electrohydrodynamic Instability in Nematic Liquid Crystals with Positive Dielectric Anisotropy. I. The Existence of the Charge Injection and the Diffusion Current. *Journal of the Physical Society of Japan* **52**, 3773-3781 (1983).

49. Nakagawa, M. & Akahane, T. A New Type of Electrohydrodynamic Instability in Nematic Liquid Crystals with Positive Dielectric Anisotropy. II. Theoretical Treatment. *Journal of the Physical Society of Japan* **52**, 3782-3789 (1983).

50. Monkade, M., Martinot-Lagarde, P. & Durand, G. Electric polar surface instability in nematic liquid crystals. *EPL (Europhysics Letters)* **2**, 299 (1986).

51. Lavrentovich, O., Nazarenko, V., Pergamenshchik, V., Sergan, V. & Sorokin, V. Surface-polarization electrooptic effect in a nematic liquid crystal. *Sov. Phys. JETP* **72**, 431-444 (1991).

52. Zenginoglou, H. & Kosmopoulos, I. On the ability of homogeneously aligned nematic mesophases with a positive dielectric anisotropy to exhibit Williams domains as a threshold effect. *Molecular Crystals and Liquid Crystals* **43**, 265-277 (1977).

53. Krishnamurthy, K. S. Electric field induced oscillatory domains in a nematic with positive dielectric anisotropy. *Japanese Journal of Applied Physics* **23**, 1165-1168 (1984).

54. Kishore, P. Electrohydrodynamic instability in nematic liquid crystal mixtures with positive dielectric anisotropy. *Molecular Crystals and Liquid Crystals* **128**, 75-87 (1985).

55. Barnik, M. I., Blinov, L. M., Grebenkin, M. F., Pikin, S. A. & Chigrinov, V. G. Experimental verification of the theory of electrohydrodynamic instability in nematic liquid crystals. *Physics Letters A* **51**, 175-177 (1975).

56. Buka, A., Éber, N., Pesch, W. & Kramer, L. *Advances in Sensing with Security Applications* (Springer, 2006).

57. Bryan-Brown, G., Wood, E. & Sage, I. Weak surface anchoring of liquid crystals. *Nature* **399**, 338 (1999).

58. Vorflusev, V. P., Kitzerow, H.-S. & Chigrinov, V. G. Azimuthal anchoring energy in photoinduced anisotropic films. *Japanese Journal of Applied Physics* **34**, L1137-L1140 (1995).

59. Garbovskiy, Y. & Glushchenko, I. Nano-objects and ions in liquid crystals: ion trapping effect and related phenomena. *Crystals* **5**, 501-533 (2015).

60. Pikin, S. A. On the structural instability of a nematic in an alternating electric field and Its connection with convection and the flexoelectric effect. *Journal of Surface Investigation: X-ray, Synchrotron and Neutron Techniques* **13**, 1078-1082 (2019).

61. Earls, A. & Calderer, M. C. Three-dimensional soliton-like distortions in flexoelectric nematic liquid crystals: modeling and linear analysis. *arXiv preprint arXiv: 1910.05959v1* (2019).

5.8 Supplementary Information

5.8.1 Experimental Section

Materials. The nematics used are E7 (Xianhua, China) and 5CB (Fluorochem), respectively. The CLC with pitch $p \sim 5$ μm is made by doping a chiral dopant S811 (ZLI-811, Xianhua, China) into E7. The helical twisting power (HTP) of S811 to E7 is ~ -10.9 μm^{-1} [1], and the concentration of S811 and E7 are 1.83 wt% and 98.17 wt%, respectively. In the photoalignment process, a 0.3 % solution of SD1 (Dai-Nippon Ink and Chemicals, Japan) in dimethylformamide (DMF) is used. Silica micro-particles with a monodisperse diameter of 3 μm are used in the particle trapping and cargo-transport experiments. The PVA solution is made of 0.5 wt% PVA (Aldrich) and 99.5 wt% deionized water.

Cell preparation. The cells for photoalignment are made with two ITO coated glass substrates. The substrates were cleaned in an ultrasonic bath, plasma cleaned and spin-coated with SD1. They were assembled using 10 μm spacers. The thicknesses of the cells, d, are measured by the thin film interference method [2], which vary from $d = 8.6$ μm to $d = 14.7$ μm. During the photoalignment process, the empty cells were exposed to linearly polarized ultraviolet (UV) light of wavelength $\lambda = 395$ nm. The cell for PVA alignment was made in an analogous fashion. The ITO coated glass substrates were firstly subjected to an ultrasonic bath, plasma cleaned and spin-coated with PVA. The substrates were then unidirectionally rubbed several times with a velvet cloth. The rubbed substrates were assembled with the rubbing directions **m** being anti-parallel to each other. The cell gap was measured to be $d = 9.7$ μm. Finally, either nematics or CLC were heated into the isotropic phase and filled into the cells by capillary action.

Generation of solitons. The samples were heated to 50 °C (E7, both nematic and CLC) or 30 °C (5CB) by a hot stage (LTSE350, Linkam) controlled by a temperature controller (TP 94, Linkam). An AC field was applied across samples by a waveform generator (33220A, Agilent) and a home-built power amplifier.

Optical characterization. Samples were observed through a polarising optical microscope (Leica OPTIPOL) equipped with a digital camera (UI-3360CP-C-HQ, uEye Gigabit Ethernet) with tunable frame rate from 10 fps to 100 fps.

Threshold measurement. The thresholds of the solitons (E_N and E_{CLC}) are measured as discussed below. A region (770 μm * 409 μm) in the center of a sample was observed through POM. An AC field was applied across the sample and increased gradually (~ 0.02 V μm^{-1} per 30 s) from an amplitude E which is far below the generation threshold of the solitons. The threshold is determined as that electric field amplitude E, at which solitons can first be distinguished through POM.

Velocity measurement. The velocity of the solitons in nematics was analyzed by an open-source software ImageJ and its plugin TrackMate. At the same electric field, the velocities of over 100 solitons were automatically measured. However, the solitons in CLCs cannot be distinguished well by the software due to the low contrast with respect to the background. So their velocities were measured manually and the error bars are determined from the deviation of velocities of 5 to 10 different solitons at the same electric field.

Calculation of the polar tilted angle of mid-layer director, θ_m. The calculation of θ_m is based on the electrically controlled birefringence effect (ECB) of nematics [3]. Firstly, the dependence of the transmitted light intensity, I_a, on E (Supplementary Figure 5-1 (a)) is measured by a photodiode. The amplitude of the applied electric field, E, is increased gradually through a programmed LCR meter E4980A (Agilent). The sample is placed between crossed polarizers and rotated by an angle ($\beta \sim 45$ °) with **m** deviated from the polarizer. A sinusoidal AC field ($f = 5$ KHz) is applied across the sample which increases automatically from 0.05 V to 16.0 V in steps of 0.025 V (0.05 V to 3.0 V) and 0.5 V (3.0 V to 16.0 V). Monochromatic light ($\lambda = 633$ nm) is transmitted through the sample and polarizers and the intensity I_a is recorded by a photo-diode detector. The light intensity before the Freedericksz transition is recorded and represented as I_{a0}.

Then a low-frequency sinusoidal AC field is applied across the sample ($E \sim 0.7$ V μm^{-1}, $f = 10$ Hz) by a waveform generator (33220A, Agilent) and a home-built amplifier. Monochromatic light ($\lambda = 633$ nm) is transmitted through the sample and the intensity (gray value), g, of a region with no solitons is recorded by a CCD camera. The intensity (gray value) at $E = 0$ V μm^{-1} is also recorded and symbolized as g_0. The intensity is then normalized as I_c (Supplementary Figure 5-1 (c))

$$I_c = \frac{g}{g_0} \times I_{a0} \tag{S5-1}$$

. The simulation of the dependence of transmitted light intensity on polar tilted angle, $\theta(z)$, is based on the calculation as discussed below. To simplify the calculation, we assume that $\theta(z)$ is independent on z, i.e. $\theta(z) = \theta_m$. The extraordinary and ordinary refractivity of E7 corresponding to wavelength $\lambda = 633$ nm at 50 °C is $n_e \sim 1.69$, $n_o \sim 1.52$ [4]. Cell gaps are $d = 10.1$ μm for the SD1 coated cell and $d = 9.5$ μm for the polyimide coated cell. In the initial position **n** is orientated along the x-axis and the nematic layers manifest a birefringence of $\Delta n = n_e - n_o \sim 0.17$. When the field exceeds the Freedericksz threshold value, **n** deviates from its orientation along the x-axis, while remaining perpendicular to the y-axis. As a result, n_o remains unchanged, but n_e decreases. The relationship between n_e and θ_m can be represented as

$$n_e' = \frac{n_e n_o}{(n_e^2 \sin^2 \theta_m + n_o^2 \cos^2 \theta_m)^{1/2}} \tag{S5-2}$$

, and the phase difference between the transmitted extraordinary and ordinary ray for monochromatic light of wavelength λ is found as

$$\Delta\psi' = \frac{2\pi d(n_e' - n_o)}{\lambda} = \frac{2\pi d \Delta n'}{\lambda} \tag{S5-3}$$

. The transmitted light intensity depends on β and can be represented as

$$I' = I_{in} \sin^2 2\beta \sin^2 \frac{\Delta\psi'}{2} \tag{S5-4}$$

, where I_{in} is the incident polarized light intensity. The intensity is then normalized as I_b (Supplementary Figure 5-1 (b))

$$I_b = \frac{I'}{I_{in} \sin^2 2\beta \sin^2 (\frac{n_e - n_o}{2})} \times I_{a0} \tag{S5-5}$$

. By comparing the electric field amplitude E in Supplementary Figure 5-1 (a) and (c), we know that the oscillation dependences in Supplementary Figure 5-1 (c) are located in the range after the third peak of the dependences in Supplementary Figure 5-1 (a). And the polar tilted angle, θ_m, can then be estimated by fitting the maximum and minimum I_c in Supplementary Figure 5-1 (c) to (b).

Azimuthal surface anchoring measurement. The azimuthal anchoring of E7 in the photoaligned cell is measured by the method described in refs. [5,6]. Two glass substrates coated with SD1 are uniformly photoaligned and assembled with a 90 ° twist. The sample is placed between two crossed polarizers and heated up to the isotropic phase to measure the

minimum transmitted light intensity (wavelength $\lambda = 590$ nm), $I_{0\perp}$. Then one of the polarizers is rotated by 90 ° to measure the maximum intensity, $I_{0//}$. Subsequently, the sample is cooled to room temperature into the nematic phase, and the light intensity, I_t, transmitted through the sample and a pair of parallel polarizers is measured when gradually rotating the sample. Then the intensity, I_t, is normalized as

$$I = \frac{I_t - I_{0\perp}}{I_{0||}} \tag{S5-6}$$

. A typical angular dependence of the normalized transmitted intensity, I, is shown in Supplementary Figure 5-6 (a). for a cell of thickness $d = 6.3$ μm. For samples with different thicknesses, the minimum, I_{Min}, and maximum I_{Max}, normalized transmitted intensity are

$$I_{Min} = [\cos \tau \cos \upsilon + \frac{1}{\sqrt{1 + X^2}} \sin \tau \sin \upsilon]^2 \tag{S5-7}$$

$$I_{Max} = [\cos \tau \cos \upsilon + \frac{1}{\sqrt{1 + X^2}} \sin \tau \sin \upsilon]^2 + [\frac{X}{\sqrt{1 + X^2}} \sin \tau]^2 \tag{S5-8}$$

, where υ is the director twist between the top and the bottom plates, $X = \Delta\psi/(2\upsilon)$ and $\Delta\psi = 2\pi\Delta nd/\lambda$ is the phase retardation, $\tau = \upsilon(1+X^2)^{1/2}$, $\Delta n = 0.22$ for E7 at 20 °C for light of wavelength $\lambda = 590$ nm [4]. By measuring I_{Min} and I_{Max} of samples of different thicknesses d, and fitting them with Equations (7) and (8), υ can be determined. Finally, the azimuthal anchoring strength W_φ can be deduced from the surface torque equation

$$W_\varphi d \cos \upsilon = 2k_{22}\upsilon \tag{S5-9}$$

, where $k_{22} \sim 10^{-11}$ J m^{-1} is the twist elastic constant of E7 [7].

References

1. S.-S. Li, Y. Shen, Z.-N. Chang, W.-S. Li, Y.-C. Xu, X.-Y. Fan and L.-J. Chen, *Applied Physics Letters*, 2017, **111**, 231109.
2. A. M. Goodman, *Appl. Opt.*, 1978, **17**, 2779-2787.
3. L. M. Blinov and V. G. Chigrinov, *Electrooptic effects in liquid crystal materials*, Springer Science & Business Media, 1996.
4. B. Bahadur, R. K. Sarna and V. G. Bhide, *Molecular Crystals and Liquid Crystals*, 1982, **72**, 139-145.
5. C. K. McGinn, L. I. Laderman, N. Zimmermann, H.-S. Kitzerow and P. J. Collings, *Physical Review E*, 2013, **88**, 062513.

6. C. Peng, Y. Guo, T. Turiv, M. Jiang, Q.-H. Wei and O. D. Lavrentovich, *Advanced Materials*, 2017, **29**, 1606112.

7. R. D. Polak, G. P. Crawford, B. C. Kostival, J. W. Doane and S. Žumer, *Physical Review E*, 1994, **49**, R978-R981.

5.8.2 Supplementary Figures
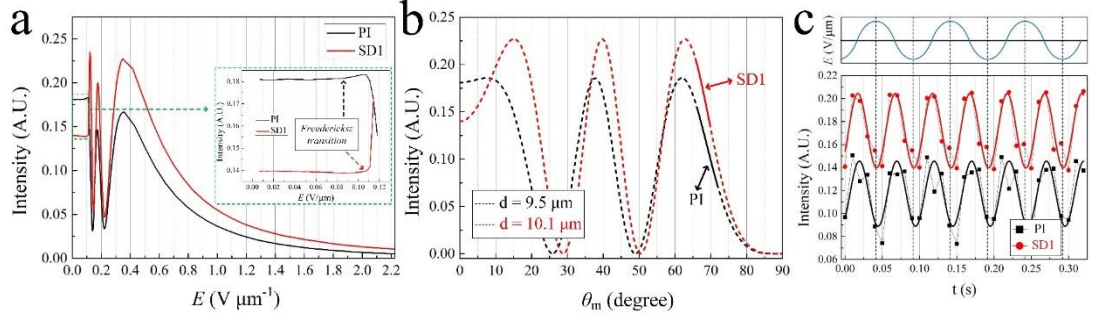
Supplementary Figure 5-1 Electro-optical properties of nematics. (a) Dependence of normalized transmitted light intensity (wavelength $\lambda = 633$ nm) through nematics in cells coated with polyimide (PI, black) and SD1 (red) on the amplitude of sinusoidal AC electric field, E. (b) Simulated dependence of normalized transmitted light intensity ($\lambda = 633$ nm) through nematics in cells with different cell gaps on the polar angle θ_m of the director. (c) Experimental measurements of normalized transmitted light intensity ($\lambda = 633$ nm) through nematics in cells coated with PI (black) and SD1 (red). $E \sim 0.7$ V μm^{-1}, $f = 10$ Hz.
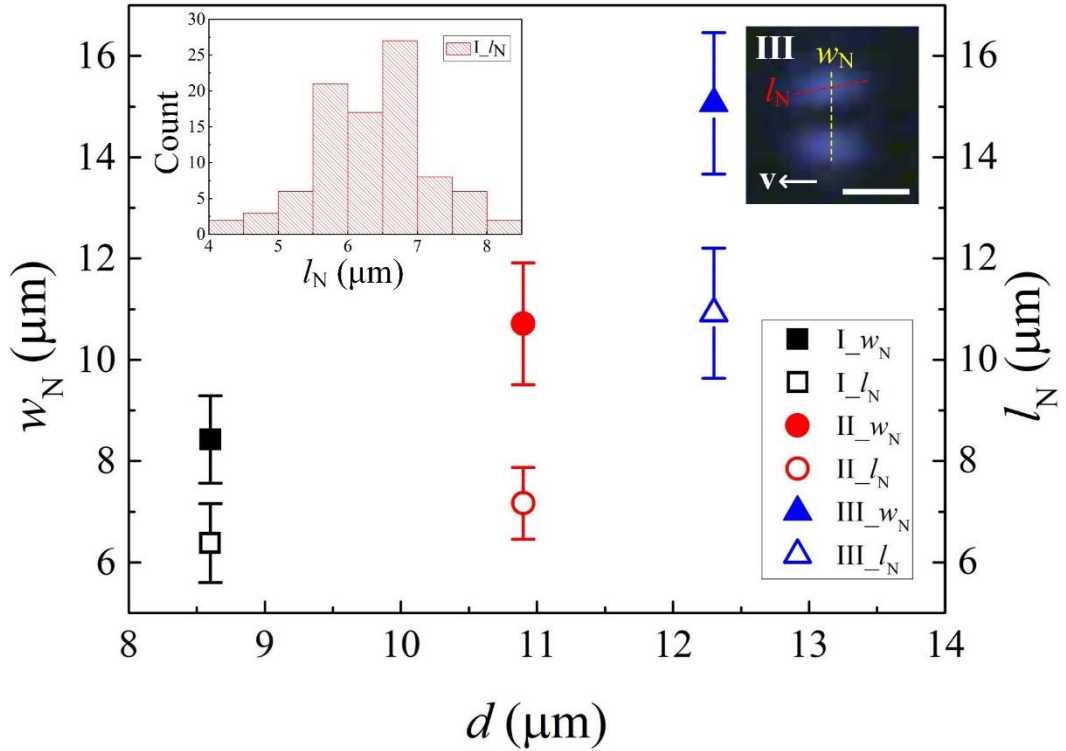
Supplementary Figure 5-2 Dependence of solitons' width (w_N) and length (l_N) on cell gap (d). w_N (yellow) and l_N (red) are represented in the inset (top-right corner, showing the micrograph of a soliton, scale bar 10 µm, **v** represent the velocity of the soliton). The inset on the top-left corner represents the length distribution of the solitons in case I. The applied rectangular AC field is $E \sim 1.0$ V μm^{-1}, $f = 30$ Hz. The error bars are calculated from the standard deviation of w_N and l_N of different solitons at the same conditions (electric fields and d).
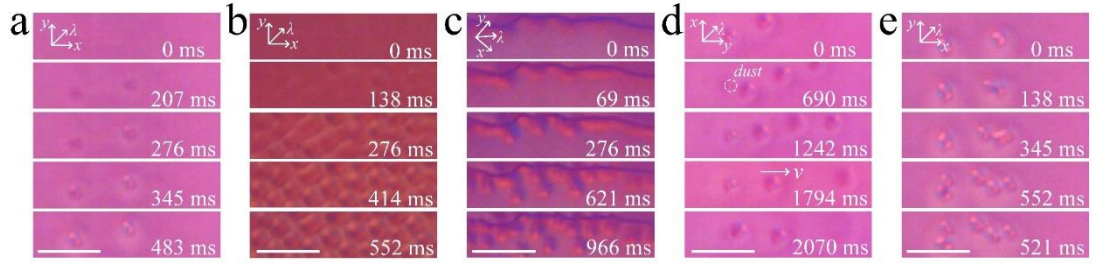
Supplementary Figure 5-3 Nucleation of solitons in CLCs applied with rectangular AC field. (a) solitons generate randomly in space ($E \sim 0.8$ V μm^{-1}, $f = 50$ Hz). (b) EHD flows induce solitons ($E \sim 1.0$ V μm^{-1}, $f = 50$ Hz). (c) nucleation of solitons adjacent to a disclination ($E \sim 0.9$ V μm^{-1}, $f = 60$ Hz). (d) nucleation of a soliton at a dust particle ($E \sim 1.0$ V μm^{-1}, $f = 60$ Hz). (e) proliferation of solitons ($E \sim 0.8$ V μm^{-1}, $f = 50$ Hz). **v** represents the velocity of solitons. Scale bars are 50 μm. λ represents the slow axis of the red plate. Polarizer and analyzer are parallel to the x and y axis, respectively.
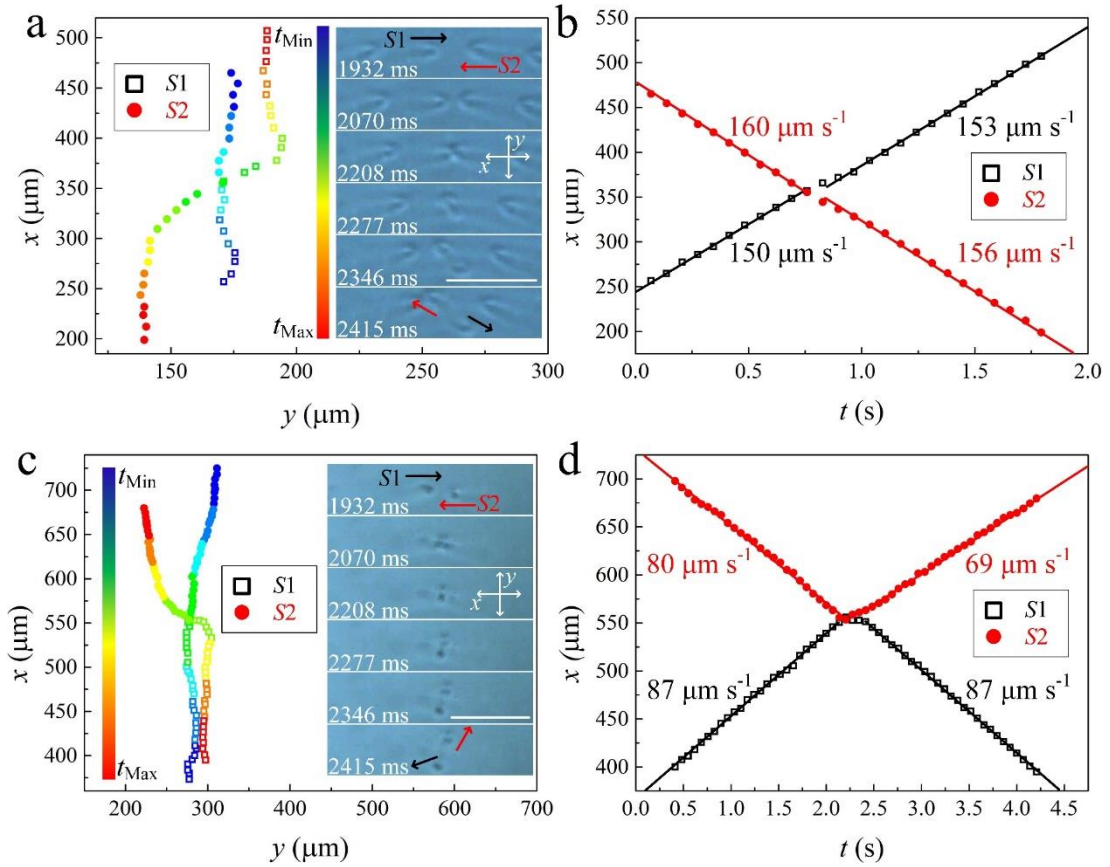
Supplementary Figure 5-4 Collision of solitons. (a) The trajectory of two solitons pass through each other. The color bar represents the elapsed time. $t_{Min} = 0$ s, $t_{Max} \sim 1.8$ s, time interval $\Delta t \sim 0.069$s. Insets are the POM micrographs of the solitons. Polarizer and analyzer are parallel to the x and y axis, respectively. The scale bar is 100 μm. The applied rectangular AC field has an amplitude of $E \sim 1.6$ V μm^{-1} and frequency $f = 60$ Hz. (b) Time dependence of x coordinates of the solitons in (a). (c) The trajectory of two solitons bump together and reflect into opposite directions. The color bar represents the elapsed time. $t_{Min} = 0$ s, $t_{Max} \sim 4.2$ s, time interval $\Delta t \sim 0.069$s. Insets are the POM micrographs of the solitons. Polarizer and analyzer are parallel to the x and y axis, respectively. Scale bar 100 μm. The rectangular AC field $E \sim 1.0$ V μm^{-1}, $f = 50$ Hz. (d) Time dependence of y coordinates of the solitons in (c).
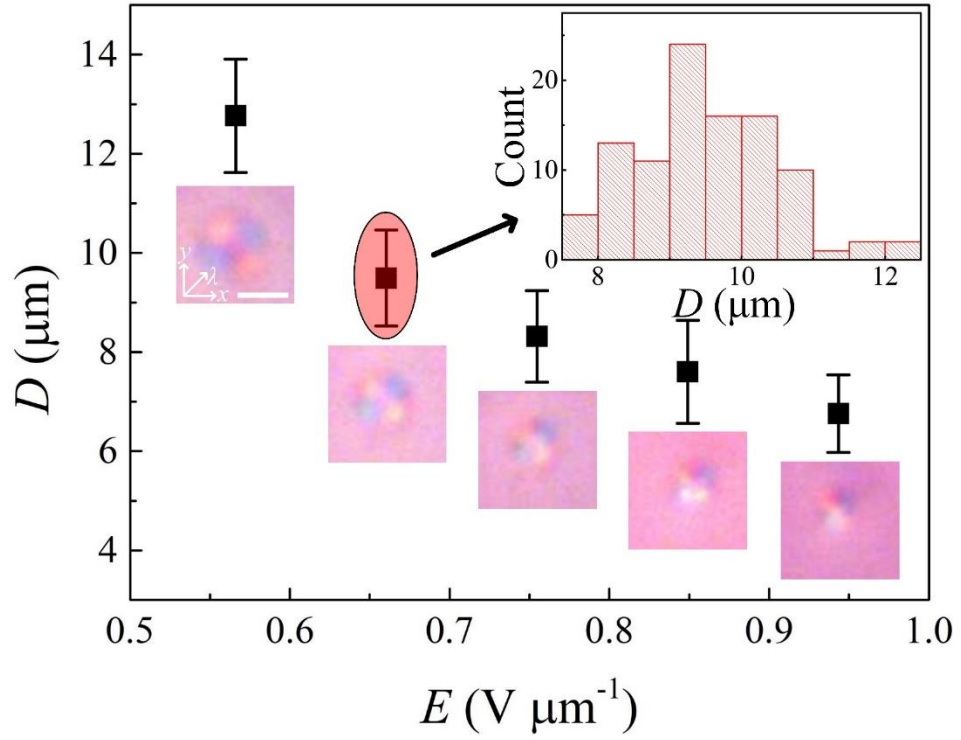
Supplementary Figure 5-5 Dependence of chiral solitons' diameter (*D*) on the amplitude of the applied rectangular AC electric field, *E*. The insets are the corresponding micrographs of the solitons at varied *E*, *f* = 30 Hz. *d* = 10.6 μm. Scale bar 10 μm. λ represents the slow axis of the red plate. Both polarizer and analyzer are parallel to the *x* and *y* axis, respectively. The inset (top-right corner) represents the diameter distribution of the soliton at *E* ~ 0.66 V μm⁻¹. The error bars are calculated from the standard deviation of diameters of different solitons at the same *E*.
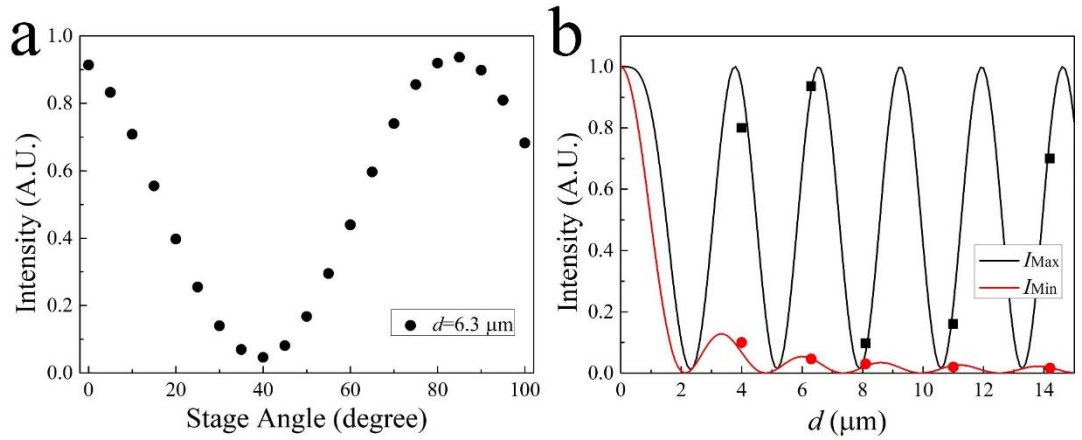
Supplementary Figure 5-6 Azimuthal surface anchoring of a photoaligned nematic (E7). (a) Angular dependence of the normalized transmitted light intensity (wavelength λ = 590 nm) for a cell with thickness of *d* = 6.3 μm, rotated between two parallel polarizers. (b) Thickness dependences of the normalized transmitted light intensities, I_{Max} (black squares) and I_{Min} (red circles). The experimental data are fitted with Equations (7) and (8) with υ ~ 83 ° (solid lines).
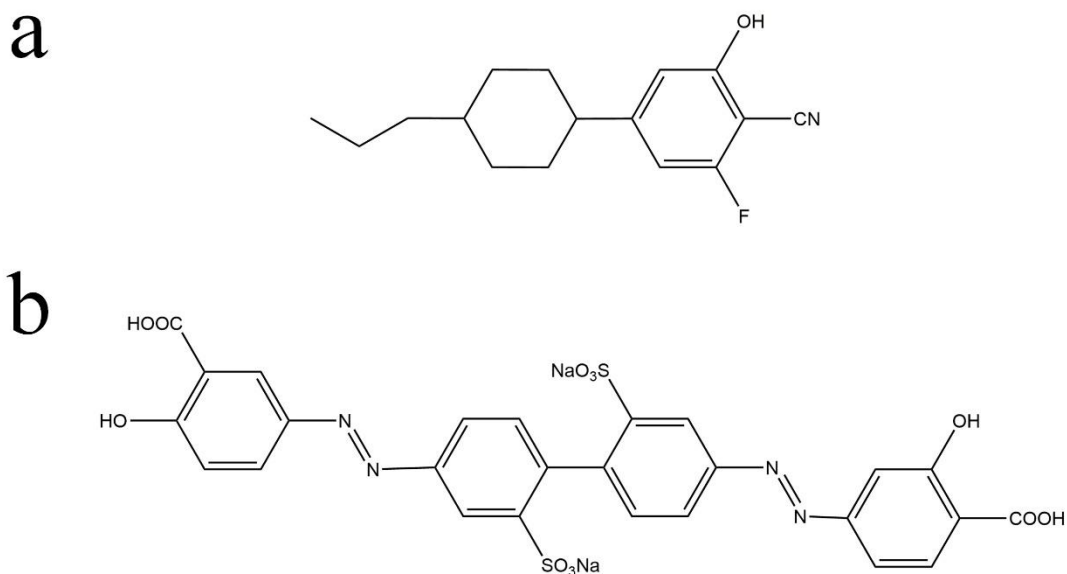
Supplementary Figure 5-7 Chemical structure of (a) ASE2 and (b) SD1.
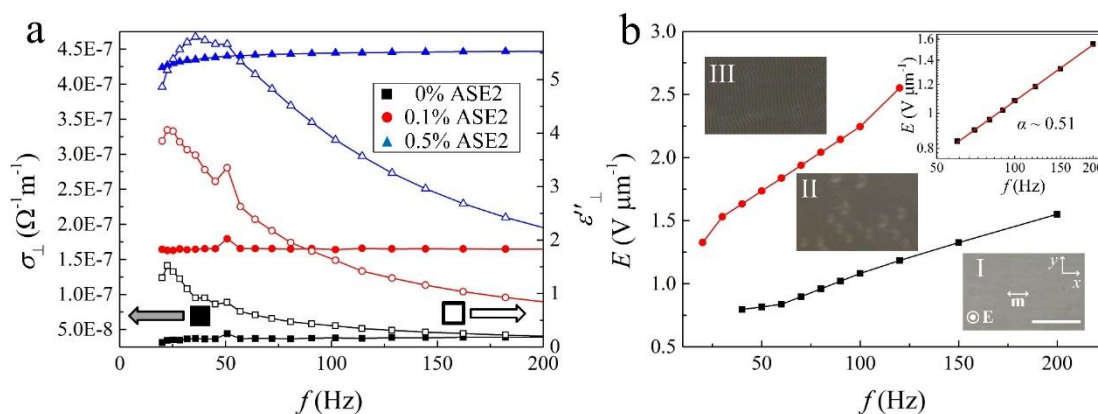
Supplementary Figure 5-8 Physical properties of nematics (E7) in commercial cells coated with rubbed polyimide. (a) Dependences of conductivity ($\sigma\perp$, solid symbols) and dielectric loss ($\varepsilon\perp$'', hollow symbols) of nematics doped with different concentrations of ionic dopant (ASE2) on frequency (*f*). (b) Threshold dependence of different states (I quasi-homeotropic state, II soliton state, III periodic EHD rolls) on the frequency of rectangular AC electric fields, *f*. Insets are the POM micrographs corresponding to different states (I: $E \sim 0.6$ V μm^{-1}, $f = 80$ Hz, II: $E \sim 1.1$ V μm^{-1}, $f = 80$ Hz, III: $E \sim 2.2$ V μm^{-1}, $f = 80$ Hz). **m** represents the alignment direction. **E** represents the electric field which is perpendicular to the *xy* plane. Both polarizer and analyzer are parallel to the *x* and *y* axis, respectively. Scale bar 100 μm. The inset on the top-right corner shows the square-root dependence of the threshold of soliton creation, E_N, on frequency. α is the slope of the dependence.
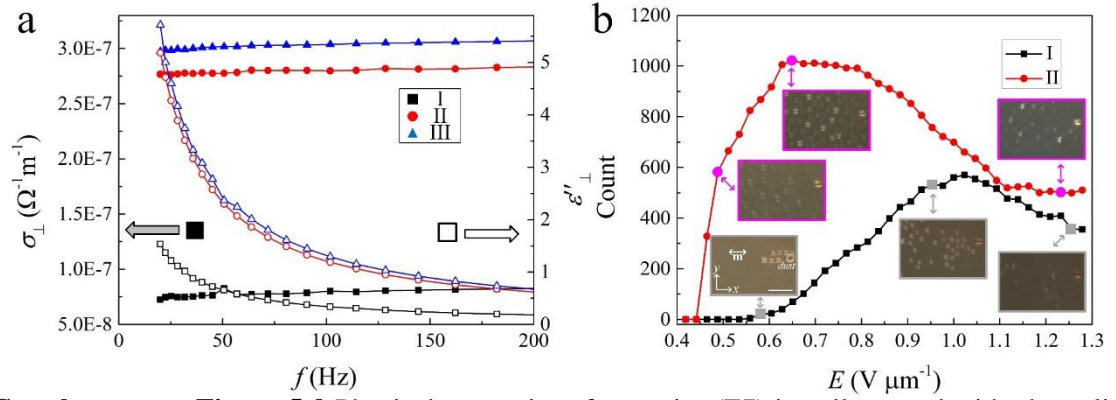
Supplementary Figure 5-9 Physical properties of nematics (E7) in cells coated with photoaligned SD1. (a) Dependences of conductivity ($\sigma_\perp$, solid symbols) and dielectric loss ($\varepsilon_\perp''$, hollow symbols) of nematics kept for I: 0 days, II: 3 days, III: 10 days, on frequency, f. (b) The number of solitons in a region (770 μm x 409 μm) as a function of the amplitude of rectangular AC electric field, E (I: 0day, II: 3 days, f = 20 Hz). The insets are the micrographs corresponding to different E, scale bar 50 μm, **m** represents the alignment direction; polarizer and analyzer are parallel to the x and y axis, respectively.
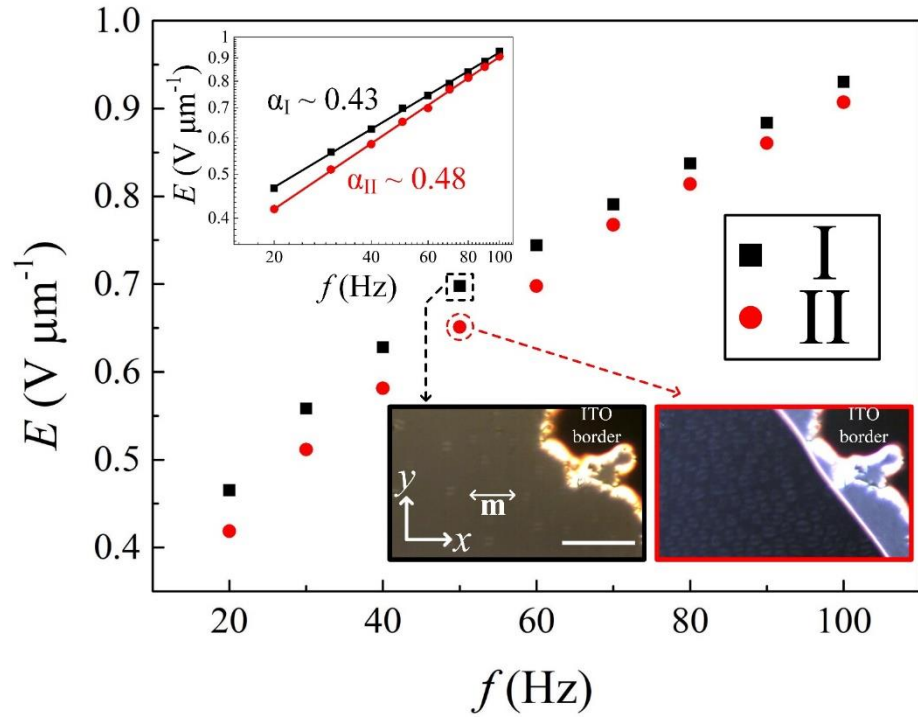
Supplementary Figure 5-10 Frequency dependence of the threshold of the solitons in the vicinity of the ITO electrode edge. I: 0 days, II: 3 days later. The inset (top-left) shows the square-root dependence of the threshold of soliton formation, E_N, on frequency (rectangular AC field). α is the slope of the dependence. The insets (bottom-right) are the corresponding micrographs of the solitons. scale bar 100 μm, **m** represents the alignment direction; polarizer and analyzer are parallel to the x and y axis, respectively.

157
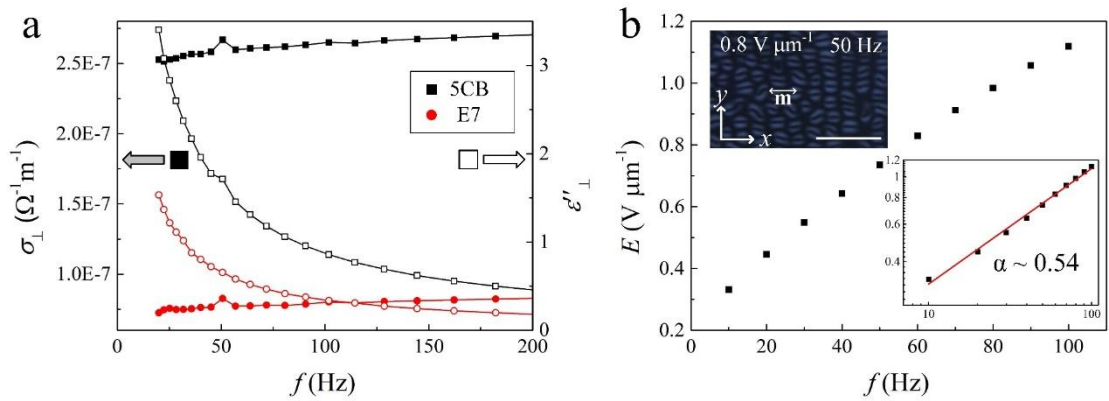
Supplementary Figure 5-11 Physical properties of nematics (5CB) in cells coated with photoaligned SD1. (a) Dependences of conductivity ($\sigma_\perp$, solid symbols) and dielectric loss ($\varepsilon_\perp''$, hollow symbols) of 5CB (black squares) and E7 (red circles) on frequency (f). (b) Frequency dependence of the threshold of solitons in 5CB (rectangular AC field). The inset (bottom-right) shows the square-root dependence of the threshold of soliton formation on frequency, α is the slope of the dependence. The inset (top-left) is a micrograph of the solitons. Scale bar 100 μm, **m** represents the alignment direction, the polarizer and analyzer are parallel to the x and y axis, respectively.

5.8.3 Supplementary Movies

File Name: Supplementary Movie 5-1
Description: Motion of solitons in a nematic LC (NLC) and a CLC at different electric fields.

File Name: Supplementary Movie 5-2
Description: Generation of solitons in NLCs. (i) random generation of solitons. (ii) EHD flows induce solitons. (iii) nucleation of solitons adjacent to a disclination. (iv) nucleation of a soliton at a dust particle. (v) proliferation of a soliton. (vi) collision of two solitons creates a new soliton.

File Name: Supplementary Movie 5-3
Description: Collisions of solitons in nematic LCs at different electric fields. (i) two solitons pass through each other, (ii) two solitons collide and reflect into opposite directions.

File Name: Supplementary Movie 5-4
Description: Unidirectional motion of solitons in a nematic LC driven by modulated AC field and circular motion of solitons in a CLC.

File Name: Supplementary Movie 5-5
Description: Generation of solitons in CLCs. (a) random generation of solitons. (b) EHD flows induce solitons. (c) nucleation of solitons adjacent to a disclination. (d) nucleation of a soliton at a dust particle. (e) proliferation of solitons.

File Name: Supplementary Movie 5-6
Description: Collisions of solitons in CLCs at different electric fields. (i) two solitons pass

through each other, (ii) two solitons collide and reflect into opposite directions.

File Name: Supplementary Movie 5-7
Description: Cargo transport and patterned photoalignment. (a) micro-particle trapping by solitons. (b) micro-particle transport by a soliton. (c) propagation of solitons in regions with different alignment directions.

File Name: Supplementary Movie 5-8
Description: (a) Solitons in a cell coated with rubbed PVA and (b) solitons at the ITO edges of a commercial cell.

Chapter 6

Electrically driven formation and dynamics of skyrmionic solitons in chiral nematics

Authors: Yuan Shen[1] and Ingo Dierking[1]*
[1] Department of Physics and Astronomy, School of Natural Sciences, University of Manchester, Oxford Road, Manchester, M13 9PL, United Kingdom
*Email: ingo.dierking@manchester.ac.uk

Author contributions:
Y. S. conceived and carried out the experimental investigations, analyzed the experimental results and wrote the manuscript. I. D. supervised the investigations and contributed through discussions and writing the manuscript.

Note: the format of the paper is edited. The supplementary movies related to this work are available on the website of the journal. One can also download the movies from the figshare database: https://figshare.com/s/383c7cfb71293527fb0d.

Abstract

Skyrmions are continuous but topologically nontrivial field configurations that behave like particles. They play an important role in fields ranging from condensed matter to nuclear physics. Realizing and manipulating different kinds of motions of skyrmions are still great challenges. Here three-dimensional skyrmions in the form of double-twist tori terminated on two topological point defects called 'torons' are produced in chiral nematic liquid crystals with varied helical pitches. The spontaneous formation of skyrmions and high-degree multi-skyrmion configurations called 'skyrmion bags' are characterized by polarizing microscopy. The skyrmions show anomalous diffusion at equilibrium state, and perform collective directional motion driven by fluid flows with a velocity controllable by electric fields as well as surface anchoring. They can be utilized as vehicles for micro-cargo transport. We also show that skyrmions can collide and form clusters with tunable shape, anisotropy and fractal dimension.

6.1 Introduction

Solitons are self-sustained localized packets of light or matter waves in nonlinear media that propagate without changing shape. They are ubiquitous and exist in various areas of physics such as nonlinear photonics, hydrodynamics of fluids, plasma, superconductors, magnetic materials, and liquid crystals (LCs) [1, 2]. Topological solitons, as a very different kind of solitons, are topologically nontrivial field configurations embedded in a uniform far-field background, that behave like particles and cannot be transformed to a uniform state through smooth deformations [3]. They emerge in theories that span many branches of physics, such as the instantons in quantum theory, vortices in superfluids, and have attracted much attention of physicists and mathematicians. The beginnings go back to Gauss who envisaged that localized knots of physical fields could behave like particles [4, 5]. As a primitive model of atoms, Kelvin suggested that various chemical elements could be represented by knotted vortices [3]. Later, Skyrme developed a nonlinear theory of pions in three spatial dimensions which can model elementary particles with different baryon numbers as topological solitons with different topological degrees [6, 7]. Due to the universality of their mathematical models

161

and physical structures, solitons with similar topological configurations can emerge in different physical systems with their physical properties being related. In condensed matter physics, low dimensional skyrme's solitons (introduced as 'baby skyrmions') have been experimentally investigated in magnets [8, 9] and LCs [10, 11], with the former showing promise for racetrack memory and spintronic devices [12] and the latter for various optical applications [13-15].

Nematic LCs are self-organized anisotropic fluids with a long-range orientational order of elongated molecules defined by the average of the long molecular axis called the director, **n**. It has been an ideal testbed for investigations of various soliton phenomena since the 1960s, which started with the studies of static linear and planar solitons induced by magnetic or electric fields [16, 17]. By rotating the applied fields, a variety of interesting behaviors of these solitons were subsequently reported [18-20]. Propagating solitary waves can be generated in nematics by shearing the samples [21-23]. Nematicons which represent self-focused, continuous wave light beams in nematic LCs are well known for their potential applications in optical information technology [24]. Recently, three dimensional dynamic dissipative solitons were reported in nematics which show various exotic dynamic behaviors and received much attention [25-29]. Further, a number of topological solitons were observed in chiral nematic LCs (CNLCs). In a ground-state CNLC, **n** twists continuously along a helical axis perpendicular to the local long molecular axis at a constant rate. The distance over which **n** rotates by a 2π is named 'pitch', p [30, 31]. This helical structure of CNLC can be deformed by applying electric fields or by confining it between surfaces with homeotropic anchoring, leading to the geometric frustration which is usually locally relieved by forming topological defects [32]. Depending on the strength of applied fields or anchoring, these defects may be relaxed into string-like structures called cholesteric fingers [33], or nonsingular solitonic structures called cholesteric bubbles or spherulitic domains [34]. It was not recognized until recently that these cholesteric bubbles are in fact topological analogs of skyrmions [35, 36]. These skyrmionic structures can be stabilized as individual particle-like excitations and arranged into crystalline arrays and linear chains [13, 37]. They are usually investigated as static field configurations [35, 38] with only a few studies being related to their out-of-equilibrium dynamics [39]. Dynamic motion of skyrmions is of paramount interest for applications such as information storage in magnets [12] and microfluidics in LCs [27]. Despite the fact that

electrically driven motion of skyrmions has been recently reported both in magnets [40] and LCs [39], realizing different kinds of motions and manipulating these motions are still topics of significant challenge.

In this work, topological solitons of elementary 2-dimensional (2D) skyrmions capped by two 3D singular point defects ("Bloch points" in the magnetic analogy [41]) called 'torons' or 'hopfions' [38] are generated in CNLCs confined between surfaces with homogeneous anchoring by applying electric fields, which were previously studied only in homeotropic confinement [11, 34]. By changing the ratio of the thickness of LC cells, d, and the pitch, p, of CNLCs, topological solitons exhibit different optical textures and dynamic behaviors. The formation process of the solitons is characterized and demonstrated in detail. In addition, the spontaneous formation of the so-called 'skyrmion bags' with a tunable topological degree is also demonstrated, which may enlighten approaches in encoding information in both optical and magnetic information storage. We find that these topologically protected skyrmionic solitons undergo anomalous diffusion at equilibrium and perform collective directional motion at non-equilibrium states. Their velocity can be controlled by tuning the electric field and the surface anchoring, enabling fascinating dynamic behaviors. Interestingly, they can even be utilized as vehicles for directed micro-cargo transport. Furthermore, we also induce skyrmionic solitons in systems of high chirality (small pitches) and show that they behave like colloidal particles and exhibit various exotic dynamic behaviors that have never been reported before. They can even form clusters with tunable shape, anisotropy and fractal dimension during inelastic collisions, which may enable mesostructured soft-matter composites with tunable mechanical and optical properties.

6.2 Results

6.2.1 Structure and formation of skyrmionic solitons ($d/p \sim 3.9$)

The torons are embedded in a background of quasi-homeotropic director field and are stabilized by an intermediate-strength electric field (Figure 6-1 (a) and (b)). The structure of a toron is derived from its optical textures (Figure 6-1 (a)), which can be represented by a baby skyrmion featured by a π radial twist from its center to periphery stabilized by the

strong energy barriers associated with the nucleation of two hyperbolic defects at its ends (Figure 6-1 (c) and (d)). The point defects of opposite hedgehog charges facilitate the transformation of the soliton to a topologically trivial uniform state. In the cases with homeotropic boundaries, the two point defects usually nucleate near the boundary surfaces [11, 36]. However, in our case, we presume that the torons are located in the middle layer of the cell with the point defects away from the boundary surfaces due to the large ratio of cell gap and pitch ($d/p \sim 3.9$). It is found that the torons cannot be stabilized in system with $d/p \sim 1$, which may be due to the incompatibility of the point defects with the homogeneous anchoring. For nonpolar director fields ($\mathbf{n} = -\mathbf{n}$), such a toron can be regarded as a baby skyrmion and can be labeled by elements of the second homotopy group, $\pi_2(S^2/Z_2) = Z$, and its topological degree, Q, can be represented by the skyrmion number that counts the integer number of times the order parameter space S^2/Z_2 is covered by its director field (Figure 6-1 (c), (d)) [42].
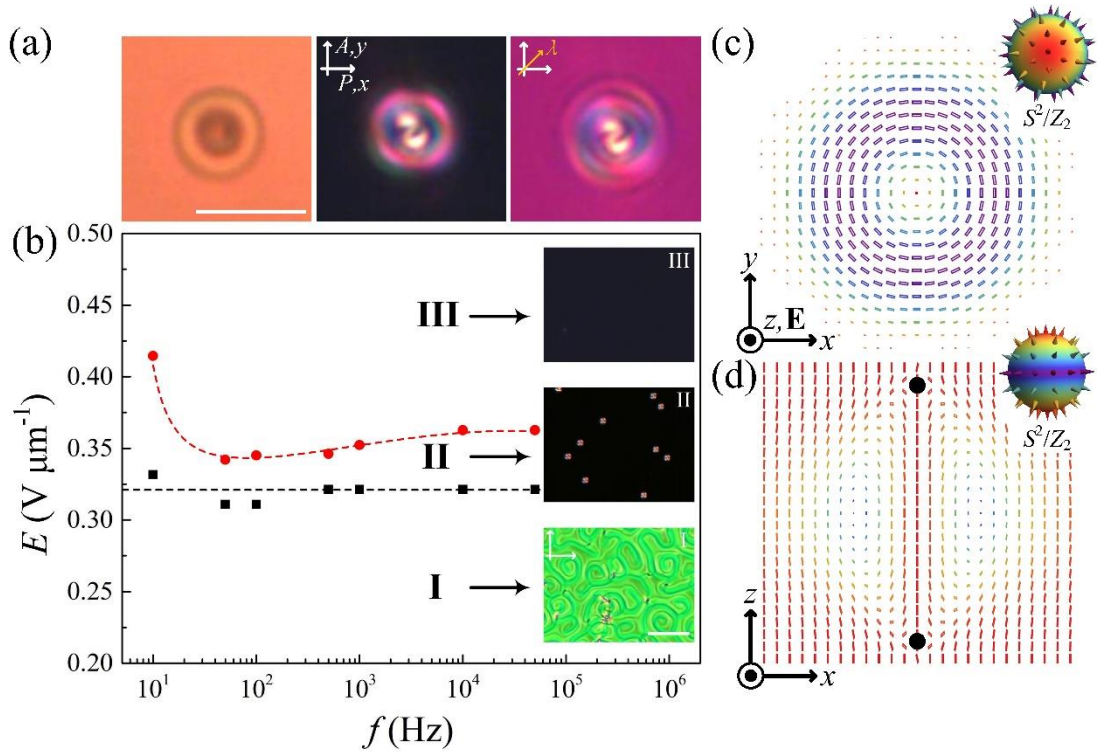
Figure 6-1 Skyrmionic solitons in CNLCs with pitch $p \sim 5$ μm confined in a cell with cell gap $d = 19.3$ μm. (a) From left to right, micrographs of a soliton ($E = 0.33$ V μm^{-1}, $f = 50$ kHz) without polarizers, with crossed polarizers, with crossed polarizers and a first-order red plate compensator (530 nm) whose slow axis λ makes an angle of 45° with the crossed polarizers. Scale bar 10 μm. (b) Threshold dependence of different states (I: fingerprint textures, II: soliton state, III: quasi-homeotropic state) on the frequency of an applied rectangular AC electric field, f. Insets are the polarizing micrographs of different states (I: $E = 0$ V μm^{-1}, II: $E = 0.33$ V μm^{-1}, $f = 50$ kHz, III: $E = 0.36$ V μm^{-1}, $f = 50$ kHz). Scale bar 50 μm. The white arrows indicate polarizers. Director configuration of a soliton in the x-y plane (c) and (x-z plane) (d), where $\mathbf{n}$ is represented as rods colored according to their orientations on target S^2/Z_2 sphere (insets).

In our experiment, the configuration of the samples is similar to that in LC displays, where the CNLC is confined between two conductive glass substrates with homogeneous alignment. The x-axis indicates the alignment direction, and the electric field is applied along the z-axis (Figure 6-1). The sample firstly shows a typical fingerprint texture [43], Figure 6-1 (b). By increasing the amplitude of the electric field, E, the fingers gradually shrink due to the unwinding effect [30]. Each finger shortens symmetrically from its two ends, and it is found that a toron forms when the two ends meet (Figure 6-2 (a)). These fingers are topologically equivalent to torons and are classified as second type cholesteric fingers (CF2) [44, 45]. We find these CF2s can drift with a constant velocity in a direction perpendicular to their long axes [46] and form dynamic spirals [47] at low frequency, f (Supplementary Figure 6-1 [48]) which is attributed to the Lehmann rotation as well as flexoelectric effects [46]. First type fingers (CF1s) are observed in a thinner cells and can crawl in a direction parallel to their long axes (Supplementary Figure 6-1 [48]), yet they cannot form solitons [47]. On the other hand, some fingers also form closed loops, which continuously shrink and eventually form topological solitons (Figure 6-2 (b)). It is noted that the solitons formed from the loops have a larger diameter than the ones formed directly from fingers, with a slightly different texture. This may indicate that they have different topological structures, which requires further investigations. Moreover, sometimes a soliton may even form inside a loop that constitutes a skyrmion bag [49]. However, such a configuration is not stable, the center soliton will get squeezed and annihilate, and the loop will collapse into a single soliton within seconds (Figure 6-2 (c)). Interestingly, such transformations are even reversible, i.e. the solitons formed from loops can transform into loops while the ones formed from fingers turn into fingers (Figure 6- 2(d), (e), Supplementary Movie 6-1 [48]). Further increase of E will destroy these topologically protected configurations and lead to a cholesteric-nematic transition (Figure 6-1 (b)).
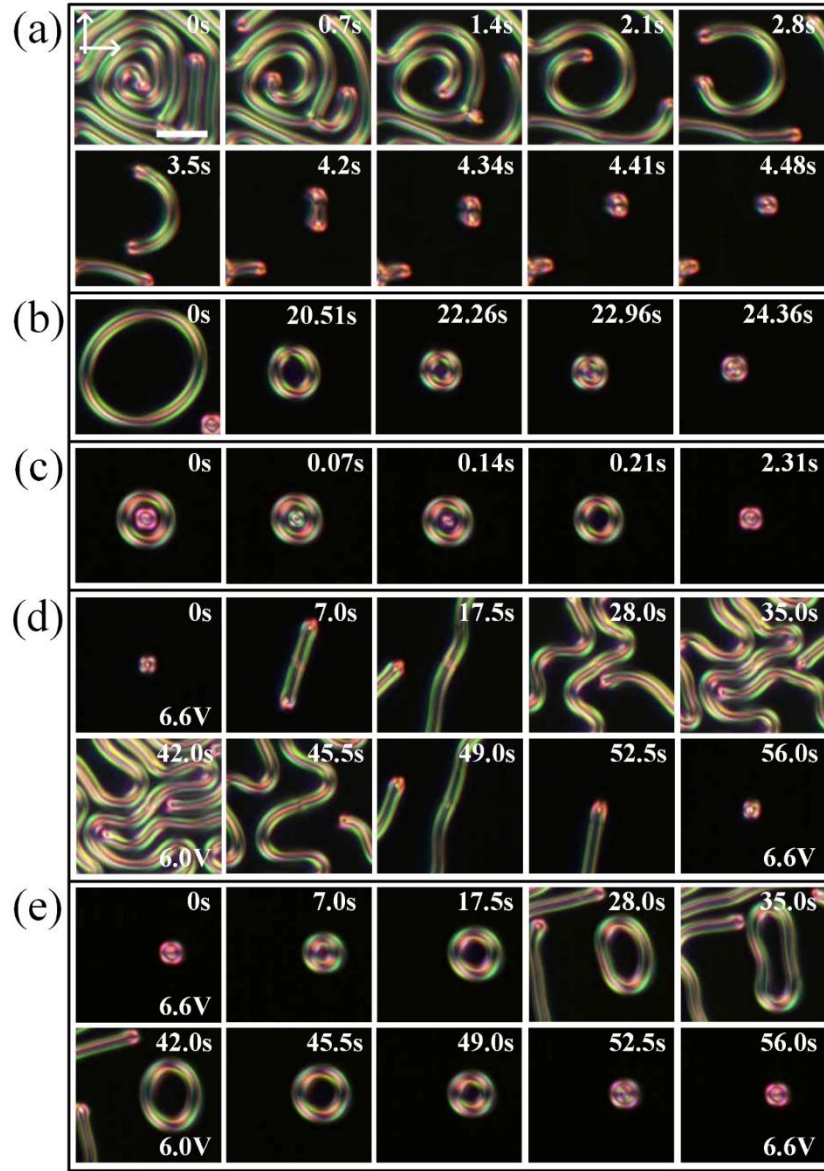
Figure 6-2 Formation of skyrmionic solitons in CNLCs with pitch $p \sim 5$ μm confined in a cell with cell gap $d = 19.3$ μm. (a) Shrinking of a cholesteric finger into a soliton ($U = 6.6$ V, $f = 50$ kHz). (b) Collapse of a looped cholesteric finger into a soliton ($U = 6.6$ V, $f = 50$ kHz). (c) Collapse of a skyrmion bag into a single soliton ($U = 6.6$ V, $f = 50$ kHz). (d) Reversible transformation between a soliton and a cholesteric finger. (e) Reversible transformation between a looped cholesteric finger and a soliton. In d, e, U gradually changes from 6.6 to 6.0 then to 6.6 V, $f = 50$ kHz. Scale bar 20 μm. The white arrows indicate polarizers.

6.2.2 Formation of skyrmion bags ($d/p \sim 3.9$)

Higher-degree skyrmion configurations are attractive to researchers due to their potential applications for high-density information storage [9, 50]. It was reported that such high-degree skyrmion configurations, also called 'skyrmion bags', could be realized in CNLCs by laser tweezers [49, 51]. Here, we show that these skyrmion bags can also form spontaneously by relaxing electro-hydrodynamic instabilities. Compared to laser tweezers, the application of electric fields is more flexible and convenient. In addition, as an analog of

166

magnetic skyrmions, it is also more practical and acceptable to applications for information storage. Figure 6-3 (a) shows skyrmion bags $S(1)$ to $S(4)$, $S(16)$ and $S(29)$ which are stabilized by a low frequency modulated electric field. As reported in [49], we denote skyrmion bags as $S(N_S)$, where N_S is the number of (anti)skyrmions inside the large bag skyrmion. However, unlike the skyrmion bags reported in Ref. [49], where the bag skyrmion is formed by twisted wall loops and has a topological degree of $Q = -1$, the bag skyrmion in our case is formed by a looped CF2 with $Q = 2$ [47, 49]. Hence, the total topological degree Q of a skyrmion bag $S(N_S)$ in our case is $N_S + 2$. In Figure 6-3 (b), we demonstrate that the topological degree of a skyrmion bag can be changed by simply tuning the frequency, where Q changes continuously from 7 to 16, and then from 16 to 23 (Supplementary Movie 6-2 [48]). Figure 6-3 (c) shows the reversible transformation between a skyrmion bag and cholesteric fingers with $Q = $ constant. Finally, we show that these skyrmion bag configurations can also be easily cleared. In Figure 6-3 (d), a bag skyrmion is cut by a soliton located outside, leading to the annihilation of the outside soliton and the transformation of the bag skyrmion to a single soliton (yellow dashed circle).
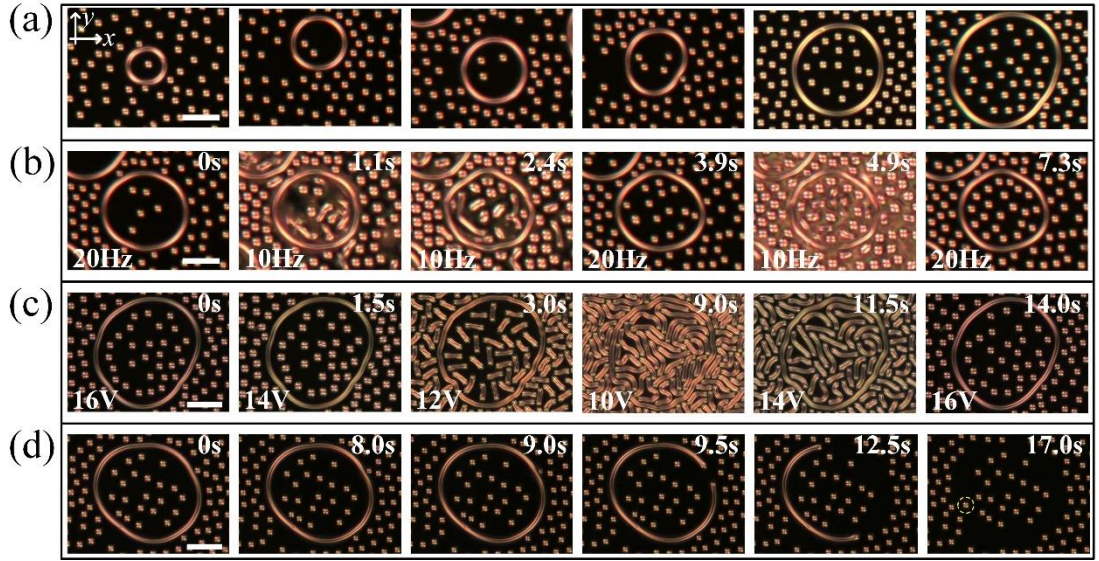
Figure 6-3 Skyrmion bags in CNLCs with pitch $p \sim 5$ μm confined in a cell with cell gap $d = 19.3$ μm. (a) Polarizing micrographs of skyrmion bags $S(1)$ to $S(4)$ ($U = 16.0$ V, $f = 50$ kHz, $f_m = 20$ Hz) $S(16)$ and $S(29)$ ($U = 12.0$ V, $f = 50$ kHz, $f_m = 30$ Hz). (b) Changing the topological degree of a skyrmion bag by tuning electric field ($U = 16.0$ V, $f = 50$ kHz, f_m is indicated at left-bottom of each figure). (c) Reversible transformation between skyrmions and cholesteric fingers ($f = 50$ kHz, $f_m = 20$ Hz, U is indicated at left-bottom of each figure). (d) Transformation of a bag skyrmion into a skyrmionic soliton ($f = 50$ kHz, $f_m = 20$ Hz. From left to right, U increases gradually from 16.0 to 18.0 V). Scale bars 50 μm. Polarizer and analyzer are parallel to the x- and y- axis, respectively.

6.2.3 Brownian motion of skyrmionic solitons ($d/p \sim 2.6$)

The dynamics of topological solitons is investigated in the system with a smaller pitch of $p \sim 2$ μm. It is found that although sharing the same field configurations, the polarizing optical textures of torons of different pitches are different (Figure 6-1, Supplementary Figure 6-2 [48]), which is due to the different phase retardations and rotations of polarization when light is traversing through the samples with different d/p ratios [52]. It is also found that it requires higher applied electric fields E to induce the torons, which is due to the larger twist energy of CNLCs with smaller pitch ($F_T = K_2 q[\mathbf{n} \cdot (\nabla \times \mathbf{n})]$, where K_2 is the twist elastic constant, $q = \pi / p$) [30] (Supplementary Figure 6-2 [48]). The solitons undergo Brownian motion at equilibrium just like colloidal particles. Translational diffusion of solitons is driven by the localized thermal fluctuations of $\mathbf{n}$ and is resisted by the LC's viscous drag associated with the rotational viscosity γ. Figure 6-4 (a) shows the dependences of the mean squared displacement (MSD) of a colloidal micro-particle, a soliton, and an immobile particle, respectively, on time lag, τ. The MSD of the particle grows linearly with τ: $\langle \Delta r^2(\tau) \rangle = 6D\tau$, where D is the diffusion coefficient [53, 54]. Interestingly, the soliton exhibits an anomalous behavior, $\langle \Delta r^2(\tau) \rangle \propto \tau^\alpha$ with the exponents $\alpha_x = 0.83$ and $\alpha_y = 0.48$ (Figure 6-4 (b) inset), where α_x and α_y are the exponents in x and y directions, respectively. Such a sub-diffusion regime can better be visualized with the velocity autocorrelation function (VACF) $C_{vx}(\tau) = \langle v_x(\tau) v_x(0) \rangle$, where v_x is the velocity of the soliton along the x-axis, and similarly $C_{vy}(\tau) = \langle v_y(\tau) v_y(0) \rangle$ for the y-direction [55, 56]. In Figure 6-4 (b), it is found that both C_{vx} and C_{vy} are negative for short time scales, indicating sub-diffusion. Furthermore, such diffusion is found to be dependent on voltage (Figure 6-4 (c), (d)). One can thus determine the half-width Δ of the histograms of displacements by fitting the data with Gaussians. The diffusivity of the soliton $D = \Delta^2/\tau$ and thus the effective viscous drag coefficients can be calculated according to Einstein's relation $\xi = k_B T/D$, where $k_B = 1.38 \times 10^{-23}$ J K^{-1} is Boltzmann's constant and T is the absolute temperature [53]. It is found that D slightly increases for increasing voltage (U) and saturates at $U = 5.5$ V (Supplementary Table 6-1 [48]), which may be attributed to the negative correlation between the diameter of solitons and applied

voltages (Supplementary Figure 6-3 [48]).
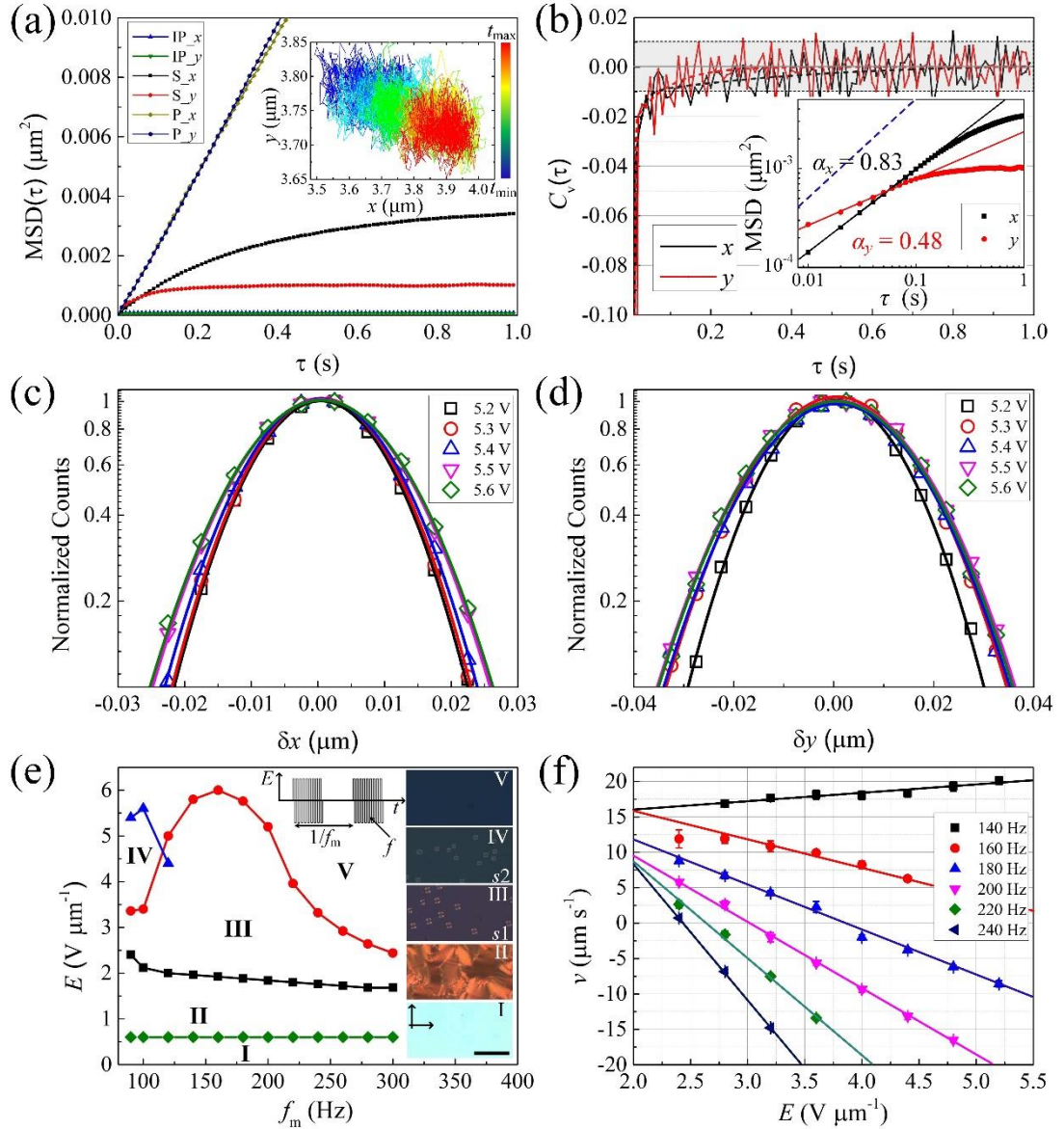
Figure 6-4 Dynamics of skyrmionic solitons in CNLCs with pitch $p \sim 2$ μm confined in a cell with cell gap $d = 5.1$ μm. (a) MSDs versus time lag τ of an immobile particle (IP), a soliton (S), and a colloidal particle (P) in the direction parallel (x) and perpendicular to (y) the alignment direction. Inset shows the trajectory of the soliton with the time corresponding to the color bar, $t_{min} = 0$s, $t_{max} = 100$ s. (b) Velocity autocorrelation functions for the soliton diffusing along x- and y-axis, respectively. The dashed lines (black/red) are polynomial fits. Inset shows the log-log plot of the MSD versus τ of the soliton. The blue dashed line indicates a slope of 1 for reference. (c), (d) Histograms of the displacement of the soliton (c) along the x-axis and (d) along the y-axis at different U for time lag of 10 ms; the solid lines are Gaussian fits of the experimental data points (open symbols, the data of the soliton at each voltage were obtained from 30000 trajectory steps). (e) Threshold dependence of different states (I: homogeneous state, II: fingerprint texture, III: dynamic topological soliton state ($s1$), IV: dissipative soliton state ($s2$), V: quasi-homeotropic state) on modulated electric field frequency, f_m. The profile of the modulating electric field is indicated as an inset. Insets (I-V) are the polarizing micrographs of different states (I: $E = 0$ V μm^{-1}, II: $E = 1.18$ V μm^{-1}, $f_m = 140$ Hz, III: $E = 2.75$ V μm^{-1}, $f_m = 140$ Hz, IV: $E = 2.75$ V μm^{-1}, $f_m = 100$ Hz, V: $E = 6.0$ V μm^{-1}, $f_m = 140$ Hz), $f = 50$ kHz. Scale bar 50 μm. The black arrows indicate crossed polarizers. (f) Dependence of the amplitude of velocity, v, of topological solitons on the amplitude of the modulated electric field, E; the solid lines are linear fits of the experimental data points (symbol). The error bar of each data point are calculated from the standard deviation of velocities of hundreds of different solitons at the same electric field.

6.2.4 Coherent directional motion of skyrmionic solitons ($d/p \sim$ 2.6)

On the other hand, directional collective motion of torons can be induced by applying an electric field modulated with a low frequency, f_m (Figure 6-5 (a)). Figure 6-4 (e) shows different states of CNLC by varying the modulated electric field. It is found that besides the torons, also dynamic dissipative solitons are induced at low f_m. Such dissipative solitons were recently reported by us [28] and are induced by the nonlinear coupling between the director field and the isotropic flow of ions. Unlike torons, they can only exist at non-equilibrium conditions. In contrast, the torons can drift (perpendicular to the alignment direction, y-axis) in a wide range of modulation frequencies f_m with a velocity that can be controlled by the applied electric field (Figure 6-4 (f), Supplementary Movie 6-3 and 6-4 [48]). Such motion is somewhat similar to the schools of skyrmions reported recently [57], but with a much larger velocity. We attribute this motion to the coupling between backflow and the squirming motion of torons. Due to the positive dielectric anisotropy, **n** tends to orient parallel to the electric field direction. At low f_m, **n** periodically rotates from its initial horizontal orientation to a vertical orientation. Such a non-reciprocal rotational dynamics of **n** induces the backflow that drives the torons. At the same time, the twisted region is squeezed and relaxed as the voltage is applied and turned off within $1/f_m$, making the torons expand, contract and morph as they move [39], resembling the squirm of active micro-swimmers [58]. By tuning E and f_m, the torons can alter their motion direction reversibly between the $+y$ and the $-y$ directions (Figure 6-4 (f), Supplementary Movie 6-5 [48]). It is well-known that the velocity profile of backflow in homogeneous confinement is bidirectional, i.e. the velocity field in the top half of the cell is an inverse mirror image of the one in the bottom half [59]. Tuning the electric field may induce a positional transition of torons [60, 61], thus leading to such a bidirectional reversal of motion. Figure 6-5 (b) shows various dynamic interactions among torons during motion. It is observed that the skyrmionic solitons disappear once they move to the electrode (i), which is different from the dissipative solitons reported before where reflection of solitons was observed [27]. However, the skyrmionic solitons can nucleate at irregularities such as surface imperfections and dust particles (ii),

which is similar to the dissipative solitons [27]. The skyrmionic solitons collide with each other like particles during motion. In (iii), a moving soliton collides with an immobile soliton which is trapped by a dust particle, and then moves away from the immobile soliton. On the other hand, if the immobile soliton is not trapped, it is pushed by the moving soliton and starts moving itself (iv). More interestingly, it is found that at some specific frequencies and voltages, there exists "two kinds" of solitons, i.e. the large ones that move more slowly towards the left and the smaller ones that move more quickly towards the right. The number of the small solitons is much smaller than that of the large ones. During the motion, the small soliton is absorbed by the large one if they collide with each other. After the collision, the larger one continuously shrinks into a small soliton and moves into the opposite direction at a larger speed (v, Supplementary Movie 6-3 [48]). The reason of such a behavior and the differences between the topological structures of these "two kinds" of solitons are not clear yet and require further investigation. One possible assumption is that these "two kinds" of solitons are actually topologically equivalent. However, the smaller ones somehow are located at a higher energy level, maybe due to the drastic symmetry breaking of the LC phase induced by the steep increase of applied voltage. The reason why this is believed is that the optical texture and the dynamic behaviors (speed and moving direction) of the small solitons are very similar to the large ones at higher voltages. Furthermore, at low f_m, dissipative solitons are induced which are absorbed by the skyrmionic solitons once they interact with each other (vi). The details of these interactions can be found in the Supplementary Movie 6-6 [48].
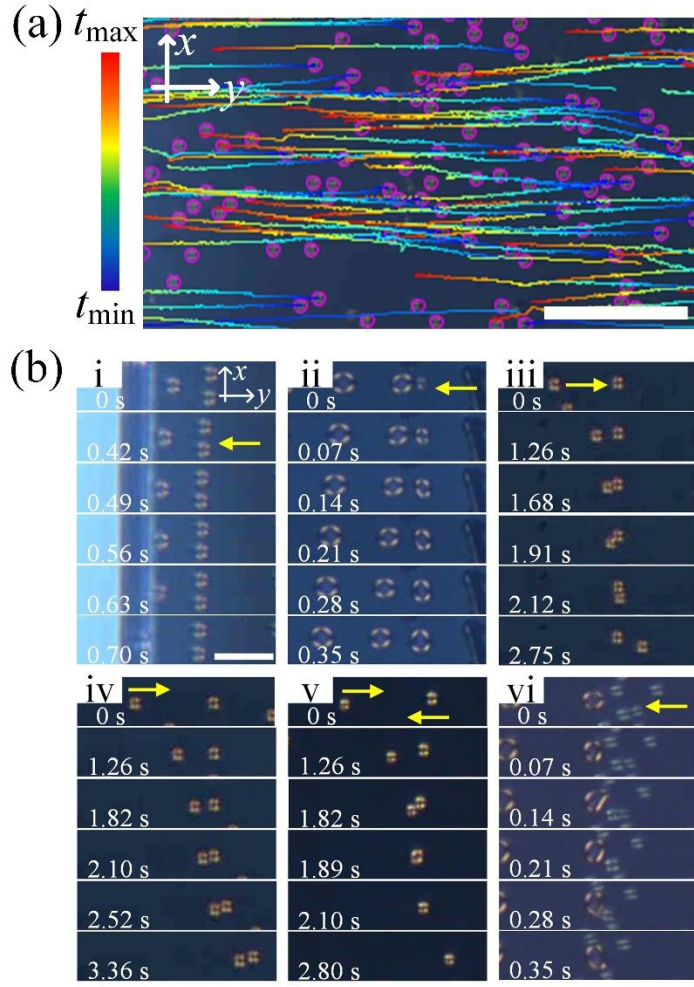
Figure 6-5 Collective motion and interactions of skytmionic solitons in CNLCs with pitch $p \sim 2$ μm confined in a cell with cell gap $d = 5.1$ μm. (a) Trajectories of skyrmionic soliton motions colored with time according to the color bar ($t_{min} = 0$ s, $t_{max} = 20$ s). Scale bar 60 μm. $E = 2.75$ V μm^{-1}, $f = 50$ kHz, $f_m = 180$ Hz. The polarizer and analyzer are parallel to the x- and y-axis, respectively. (b) Interactions of skyrmionic solitons: i. solitons disappear at the electrode edge ($E = 2.35$ V μm^{-1}, $f = 50$ kHz, $f_m = 200$ Hz); ii. solitons nucleate at an surface imperfection ($E = 3.53$ V μm^{-1}, $f = 50$ kHz, $f_m = 130$ Hz); iii. a moving soliton collides with a soliton which is pinned at a dust particle ($E = 2.35$ V μm^{-1}, $f = 50$ kHz, $f_m = 180$ Hz); iv. a moving soliton collide an immobile soliton and pushes it moving together ($E = 2.35$ V μm^{-1}, $f = 50$ kHz, $f_m = 180$ Hz); v. two solitons move in opposite directions collide and one of them is absorbed by the other ($E = 2.35$ V μm^{-1}, $f = 50$ kHz, $f_m = 220$ Hz); vi. the absorption of dissipative solitons by a topological soliton ($E = 2.75$ V μm^{-1}, $f = 50$ kHz, $f_m = 130$ Hz).

In previous studies [11, 34, 52, 62], the skyrmions are always confined between surfaces with homeotropic anchoring, and thus their direction of motion is randomly determined by the spontaneous symmetry-breaking structures [39] or many-body interactions [57]. Here, by using homogeneous alignment, the direction of motion of the torons can be easily controlled. In Supplementary Figure 6-4 (a) [48], a sample is divided into regions with different alignment directions through the photo-alignment technique [63]. It is found that the torons move perpendicular to the predesigned alignment direction in each region. Once they reach the border of the region, they are absorbed by the disclinations formed in the border regions.

Interestingly, it is found that there is a disclination splitting the left region into two sub-regions. Such a disclination is formed from the high field induced collapsing of a π-wall (a planar soliton represented by the first homotopy group $\pi_1(\mathbb{S}^2/\mathbb{Z}_2) = \mathbb{Z}_2$). The director thus twists π from the left to the right sub-region, leading to the motion of torons in opposite directions (Supplementary Movie 6-7 [48]). Furthermore, it was reported that localized distortions of director fields can attract colloidal particles to minimize the elastic free energy [31, 64]. As a result, we show that these soliton structures can be utilized as vehicles for micro-cargo transport. In Supplementary Figure 6-4 (b) [48], a toron is induced near an aggregate of two micro-particles by applying an electric field, and then carries these while moving through the nematic bulk. More importantly, such a process is repeatable and the speed and trajectory of the transport is also controllable by tuning the electric field, as well as the surface anchoring (Supplementary Movie 6-8 [48]).

6.2.5 Dynamics of skyrmionic solitons with high chirality ($d/p \sim$ 13.3)

To investigate the influence of chirality, skyrmionic solitons are induced in CNLCs with a much smaller pitch ($p \sim 0.375$ μm) compared to previous investigations. In addition to the smaller size and higher E threshold as compared to the ones with larger pitch p, the skyrmionic solitons in this case have an inhomogeneous diameter distribution (Supplementary Figure 6-5 [48]). It is found that during the formation of solitons, unstable skyrmion bags with different N_S are formed randomly. Unlike the skyrmion bags mentioned above, the loops discussed here shrink and absorb the solitons inside, thus forming solitons with extraordinarily large diameters (Supplementary Figure 6-6, Supplementary Movie 6-9 [48]). Despite the fact that the small solitons cannot be clearly distinguished by the polarizing optical microscope due to limited light intensity and optical resolution, the larger ones have polarizing optical textures analogous to the ones obtained for pitch $p \sim 2$ μm (Supplementary Figure 6-2(a) and 6-5(a) [48]). Individual solitons undergo anomalous diffusion at low f, where both sub-diffusion and super-diffusion are observed (Supplementary Figure 6-7 [48]). Such a behavior is attributed to the nonlinear coupling between backflow and the isotropic flow of ions. Directional collective motion of solitons is also observed which is however

significantly different from the one mentioned above. In the case of $p \sim 2$ μm, the ionic flows and associated hydrodynamic effects are suppressed by using a high carrier frequency, $f =$ 10 – 50 kHz. The solitons move consistently in a specific direction with a constant velocity and a velocity order parameter $S = \left| \sum_i^N v_i \right| / (N \cdot v_s)$ close to 1, where N is the number of solitons and v_s is the absolute value of the velocity of the coherently moving solitons (Supplementary Figure 6-8 [48]). In contrast, here, due to the isotropic flows of ions at low f, individual solitons move in different directions at each moment (Figure 6-6 (a)), with a much smaller velocity order parameter $S \sim 0.4$ (Figure 6-6 (c)) and an average velocity of $<v_y> \sim$ -2 μm s^{-1} pointing in the $-y$ direction (Figure 6-6 (d)) induced by backflow (Supplementary Movie 6-10 [48]). Solitons undergo hydrodynamic fluctuations, leading to a locally meandering but long-term directed trajectory (Figure 6-6 (b)), which is very different from the smooth and straight trajectory shown in Figure 6-5 (a). Generally, active fluids exhibit behaviors beyond the expectation of equilibrium statistical mechanics, such as the so-called giant number fluctuations (GNF). We analyzed the relationship between the mean number $<N>$ and the root mean square number $\Delta N = <(N - <N>)^2>^{1/2}$ of solitons within different sample areas. Unlike the case of stochastic Brownian motion of colloidal particles, where $\Delta N \propto <N>^\beta$ with $\beta = 1/2$ [65], the collective directional motion of solitons exhibit GNF with β = 1.13 (Figure 6-6 (e)). Figure 6-6 (f) shows the evolution of fluctuations in the local number density analyzed by counting the numbers of solitons within a selected sample area of 146 μm × 130 μm. It is found that the density η decreases gradually and then saturates at late stage, which is due to the coalesce of solitons at low f (Supplementary Figure 6-9 [48]). The topological protection of skyrmions is caused by the swirling director texture and is strictly enforced in the continuum. Understanding the mechanism of unwinding skyrmions is vital to the enhancement of their stability [66]. Merging of skyrmions has been reported in magnetic materials and is attributed to the proliferation and propagation of magnetic Bloch points [67]. In our case, such a coalesce may be attributed to the interactions between the hedgehog point defects or the fierce inelastic collisions among solitons that destroy the topologically protected structures.
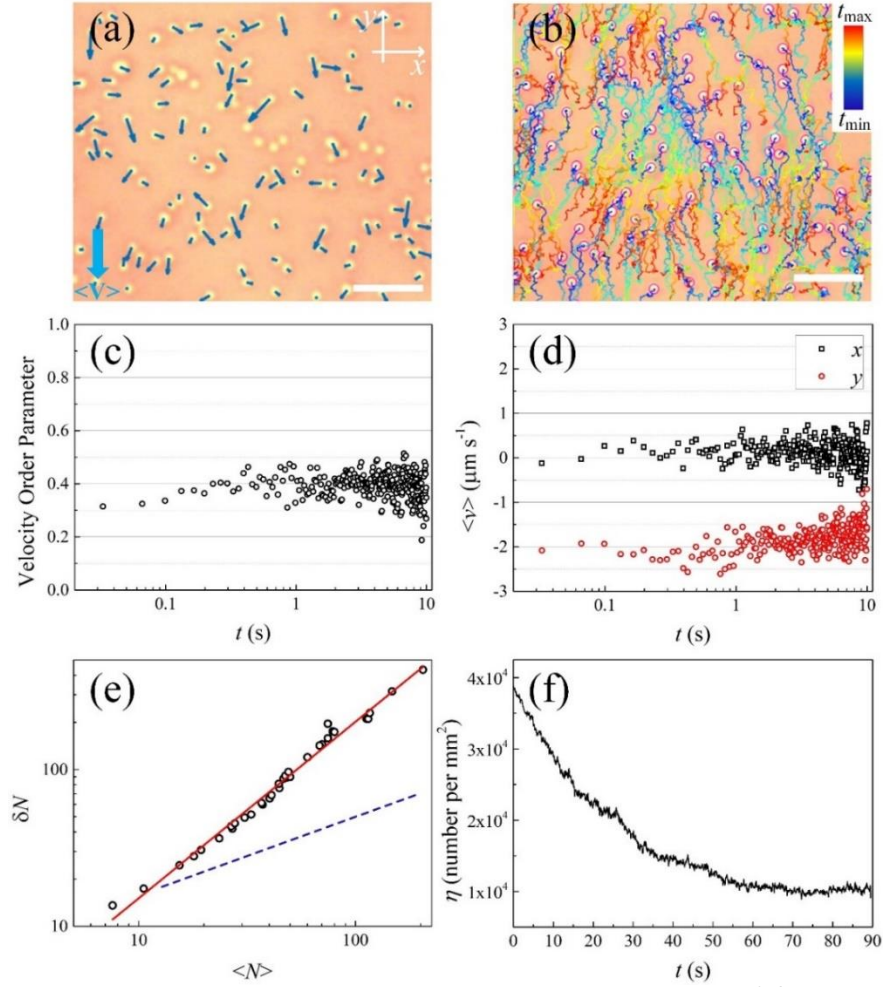
Figure 6-6 Coherent Skyrmionic soliton motion in CNLCs with pitch $p \sim 0.375$ μm confined in a cell with cell gap $d = 5.0$ μm. Micrograph of skyrmionic solitons at 0.5 s after applying an electric field (a) with their velocities marked as small blue arrows (the amplitudes of velocities are indicated as the lengths of the arrows) and (b) with their trajectories colored with time according to the color bar ($t_{min} = 0.5$ s, $t_{max} = 10$ s). Scale bars 10 μm. Evolution of (c) velocity order parameter and (d) average velocities of the solitons in (a) with time. (e) Giant-number fluctuation analysis using log-log plot of ΔN versus $<N>$; The red line is the linear fit of the experimental data points (symbol); blue dashed line indicates a slope of 0.5 for reference. (f) An example of number density fluctuation during motion for a 146 μm × 130 μm sample area. $E = 5.0$ V μm^{-1}, $f = 200$ Hz for all the measurements.

During the motion, the solitons behave like colloidal particles with a sticking probability $s < 1$, forming anisotropic clusters while they collide. We describe the geometry of aggregated soliton clusters by their fractal dimension (Figure 6-7). Despite the limited number of clusters measured (over 100 in our case), the fractal dimension still provides a reasonably accurate description of differences in the shape of clusters at different stages. We analyze the cluster structures by using the "inertia" tensor [68, 69] defined for a cluster composed of N solitons as $M_{ab} = \sum_{i=1}^{N} (\rho_a^i - \bar{\rho}_a)(\rho_b^i - \bar{\rho}_b)$, where $a, b = x, y$; $\boldsymbol{\rho^i} = \left(\rho_x^i, \rho_y^i \right)$ are coordinates of the ith soliton, and $\bar{\boldsymbol{\rho}} = N^{-1} \sum_{i=1}^{i} \boldsymbol{\rho^i}$ is the center of mass of the cluster. This allows us to define a characteristic diameter $D = 2\sqrt{\text{Tr}\mathbf{M}/N}$ and anisotropy of individual

175

clusters $q = (M_{xx} - M_{yy} + 2iM_{xy})/(M_{yy} + M_{xx}) = |q|e^{i2\phi}$, where $|q|$ and ϕ are the cluster's elongation and the azimuthal angle of the long axis, respectively. It is $|q| = 1$ for a string-like cluster and $|q| = 0$ for a disk-like cluster [69]. The statistical analysis of the relationship between N and D reveals that clusters exhibit fractal behavior $N \propto D^{d_f}$, where d_f denotes the Hausdorff dimension. Generally, a uniform object embedded in a m-dimensional space has $d_f = m$, while a loose structure with decreasing density from its center has $d_f < m$ [70]. It is found that the solitons form 1D linear chains at the beginning, which are gradually destroyed by fluid flows and turn into irregular clusters at the later stage (Figure 6-7).
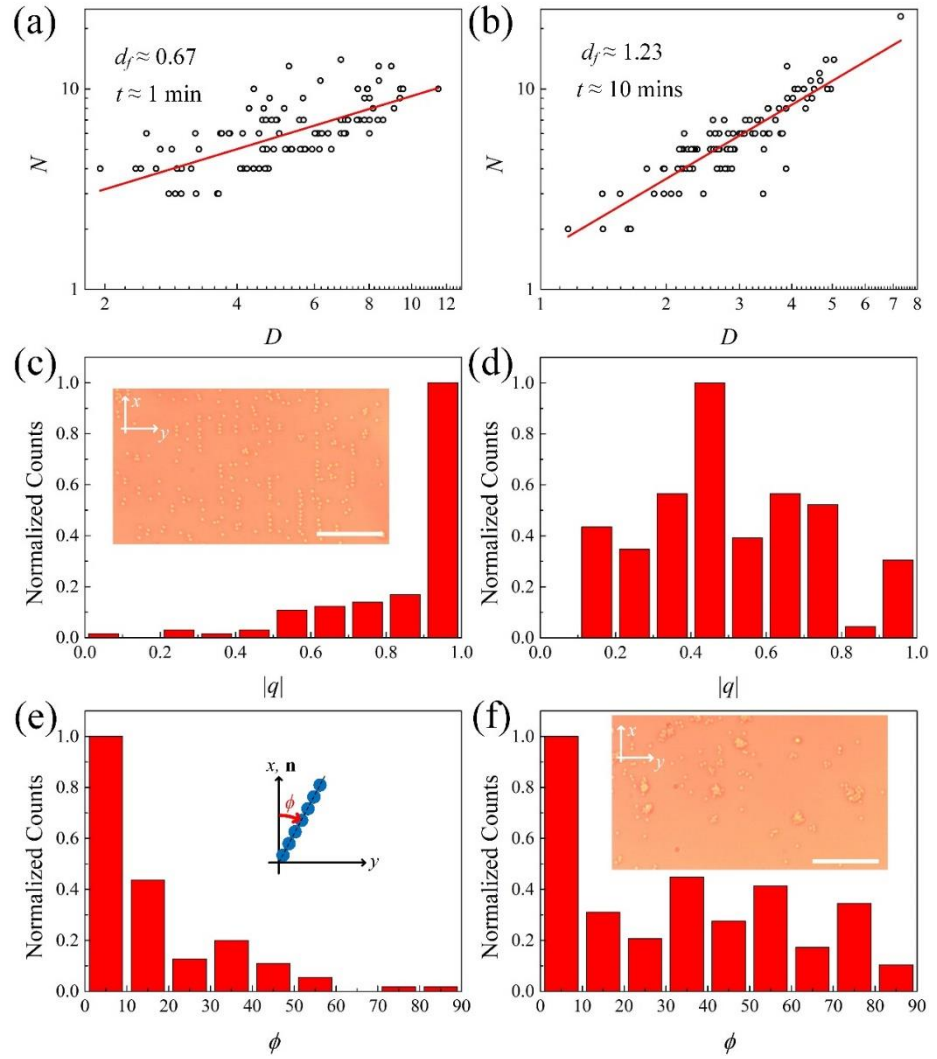
Figure 6-7 Aggregation of skyrmionic solitons in CNLCs with pitch $p \sim 0.375$ μm confined in a cell with cell gap $d = 5.0$ μm. Log-log plot of the number of solitons N and cluster diameter D at (a) 1min and (b) 10 mins after applying an electric field. The red lines are the linear fits of the experimental data points (symbol). Histograms of the cluster anisotropy $|q|$ at (c) 1 min and (d) 10 mins after applying electric field. Histograms of the angle between the long axis of clusters and the alignment direction (x-axis) ϕ at (e) 1 min and (f) 10 mins after applying an electric field. Insets in (c) and (f) are the micrographs of aggregates of solitons at 1 min and 10 mins after applying electric field, respectively. Scale bar 30 μm. $E = 4.88$ V μm^{-1}, $f = 200$ Hz.

6.3 Discussion

Recently, multi-dimensional dynamic dissipative solitons in nematics were reported by us [27, 28] and other groups [25, 26, 29] and have attracted increasing attention due to their fascinating nonlinear dynamic behaviors and potential applications in microfluidic systems. These solitons can move with a velocity which is controllable by the external electric fields. They preserve spatially confined shapes during motion and survive collisions, which is similar to the dynamics of the skyrmionic solitons described above. However, unlike the skyrmionic solitons whose existence is topologically protected and guaranteed by the helicoidal structure of cholesteric that maintains a fixed pitch, the dissipative solitons are actually self-trapped propagating solitary waves of director deformations and are thus topologically trivial and equivalent to the uniform state. They are formed by the flexoelectric effect of LC molecules and the nonlinear coupling between the electro-hydrodynamic flows and the LC director field. They require an external driving force to exist, such as provided by applied electric fields.

In previous studies [11, 34, 52, 62], skyrmionic solitons usually emerged between boundaries with homeotropic alignment as a result of geometrical frustration between surface anchoring and material chirality. In the same mechanism, skyrmions can also be formed in cells with homogeneous alignment, where their stability is supported by the subtle balance between the chirality and the electric field. Such a configuration facilitates the dynamic field control of the geometrical transformation of skyrmions. A variety of patterns can be formed in frustrated CNLCs with positive dielectric anisotropy by applying an electric field. Moreover, a first order cholesteric-nematic transition [71] can be achieved by increasing the electric field to completely unwind the helical structures, so that there exists in the parameter plane a coexistence line where two phases have exactly the same elastic energy and coexist [71]. Just below this line, different kinds of cholesteric fingers can form depending on various parameters including d/p, E, etc. CF2s as one of the most common types of fingers have a topological structure analogous to skyrmions [72]. There are point defects near each end of a CF2, which are not at the same height but are localized near the two substrates [71]. By increasing E just above the coexistence line, a CF2 continuously shortens until forming a toron. On the other hand, it was reported that closed loops of a CF1 can form skyrmionic

solitons, while a looped CF2 never forms such solitons unless it possesses point defects [44]. More importantly, such a transformation from looped CF2 to skyrmionic solitons has never been reported to be reversible. These discrepancies from our results may be attributed to the extraordinarily large value of d/p in our case. In previous studies [11, 37, 52, 71], depending on the elastic constants of LC materials, there is a very strict requirement on d/p (generally speaking, $d/p \sim 1$) in order to achieve the fragile balance between twist energy and homeotropic anchoring. This also greatly limits the investigations of topological solitons in high chirality systems, where apart from the coalescence of solitons, complicated dynamic motions, giant-number fluctuations, or anisotropic clusters that we reported here, other interesting phenomena such as half-skyrmions [73] may also be found.

Although collective directional motion of skyrmionic solitons in LCs has been reported recently [57, 74], the influence of fluid flows has not been discussed yet. Furthermore, controlling the dynamic motion of solitons has never really been achieved before. We find that the solitons in our experiments always move perpendicular to the alignment direction, and can be continuously switched to the opposite direction by tuning the electric field owing to the effects of backflow. Backflow has been notorious in LC display applications for decades as it causes flickering of display pixels. However, as an effect it begins to gain popularity in recent years due to its broad applications in microfluidics such as Non-Stokesian dynamics of colloidal particles [75], inelastic collision and aggregation of colloidal particles [68], annihilation dynamics of topological defects [64], etc. By tuning the alignment condition and the value of d/p, we may change the velocity profile of backflows [61], and thus vary the dynamic motion of the solitons. We also demonstrate that 2D micromanipulation of the dynamics of solitons can be realized by predesigned patterned alignment. With the help of the photo-alignment technique [63], various motions such as spiral motion, wavy motion, zigzag motion, etc. can be achieved, which will be reported elsewhere. Since the skyrmionic solitons interact with colloidal microparticles as shown, this enables various forms of cargo transport on micrometer scales.

6.4 Conclusion

To conclude, we demonstrate the dynamic formation of skyrmionic solitons in CNLCs

with varied pitches confined between surfaces with homogeneous anchoring. The field induced reversible transformations from cholesteric fingers to topological solitons overcome the restraint on the value of d/p, and thus facilitates the investigations in systems of high chirality. Stable skyrmion bags with a field controllable topological degree are generated spontaneously, which may be utilized as models of atomic nuclei with different baryon numbers or even for potential applications such as ultrahigh-density optical/magnetic information storage systems. Solitons undergo anomalous diffusion at equilibrium, and perform collective directional motion in response to modulated electric fields attributed to the effects of backflow. 2D micromanipulation and micro-cargo transport can be achieved through predesigned alignment. The nonlinear coupling with isotropic ion flows at low frequency induces complex super-diffusion of individual solitons and coherent meandering of hundreds and thousands of solitons. The solitons collide like colloidal particles and form anisotropic clusters. Our findings fill the missing pieces in the study of out-of-equilibrium phenomena of topological solitons, and open avenues for versatile dynamic soliton systems with potential applications in microfluidics and racetrack memory devices.

6.5 Materials and methods

Sample preparation: The CNLCs used were prepared by mixing a commercially available nematic liquid crystal E7 (Xianhua, China) with chiral dopants. Different pitches were obtained by varying the concentration, c, of chiral dopants according to the relationship $p = 1 / (\text{HTP} \times c)$, where HTP represents the helical twisting power of the chiral dopant. The CNLCs with pitch $p \sim 2.0$ μm and 5.0 μm are prepared with a chiral dopant S811 (ZLI-811) (Xianhua, China) whose HTP is -10.9 μm^{-1} [28], and the CNLC with $p \sim 0.375$ μm is prepared with a chiral dopant R5011 (Xianhua, China) that has a much larger HTP of ~110 μm^{-1} [76]. The small pitch $p \sim 0.375$ μm is further verified by measuring the Bragg's reflection of the sample as shown in Supplementary Figure 6-10. It is well known that the CNLC can Bragg reflect circularly polarized light with the same handedness as its chiral structure due to its characteristic helical super-structure [77]. The wavelength of the reflected light is dependent on the ordinary (n_o) and extraordinary (n_e) refractive indices and the pitch, p, of the CNLC as $\bar{\lambda} = \bar{n} \times p$, where $\bar{\lambda}$ is the average wavelength of the reflected light band, and

$\bar{n} = \frac{1}{2}(n_o + n_e)$ is the average refractive index [77]. According to Ref [76], the refractive indices of E7 at λ = 633 nm and temperature T = 20 °C are n_o = 1.517 and n_e = 1.741. We measured that $\bar{\lambda} \sim 611$ nm (Supplementary Figure 6-10 [48]), and thus obtained that $p \sim 375$ nm which is in accordance with the calculation. However, it should be noted that because the refractive indices of E7 in Ref [76] do not exactly match the temperature of our system, there could be slight difference between the calculated pitch and the real pitch. LC cells coated with rubbed polymide were purchased from AWAT (Poland). LC cells processed with the photo-alignment technique were composed of two glass substrates coated with transparent indium tin oxide (ITO) layers. The glass substrates were first ultrasonically bathed, plasma cleaned, and then spin-coated with a 0.3 wt% dimethylformamide (DMF) solution of sulfonic azo dye SD1 (Dai-Nippon Ink and Chemicals, Japan). The substrates were glued together, and the cell gap was set with spacers. The cell gap was measured by the thin film interference method [78]. Afterwards, the empty cells were illuminated by polarized Ultra-violet (UV) light with wavelength λ = 395 nm. Finally, LC mixtures were heated to the isotropic phase and filled into cells by capillary action.

Generation of solitons: Samples were kept at 50 °C on a hot stage (LTSE350, Linkam) controlled by a temperature controller (TP 94, Linkam). The AC voltage is applied using a waveform generator (33220 A, Agilent) and a home-built amplifier.

Optical characterization: Samples were observed through a polarizing microscope (Leica OPTIPOL). Images and movies were recorded by a charge-coupled device camera (UI-3360CP-C-HQ, uEye Gigabit Ethernet). In the measurements of the Brownian motion, the frame rate of the camera is tuned to 100 fps and each sample is tracked by the camera for 5 minutes, which gives overall 30000 trajectory steps for each measurement.

Data analysis: The motion of the solitons was tracked and analyzed by open-source ImageJ/FIJI software. The position information and number density of the solitons were extracted for each frame through a plugin of ImageJ, TrackMate. The temporal evolution of velocity order was obtained by analyzing the positon information of solitons between frames of movies. The giant-number fluctuations were analyzed by analyzing soliton number density versus time for 35 areas of different sizes, ranging from 30 μm × 25 μm to 180 μm × 145 μm.

6.6 Acknowledgements

6.7 References

1. Dauxois, T. & Peyrard, M. *Physics of solitons* (Cambridge University Press, 2006).
2. Kartashov, Y. V., Astrakharchik, G. E., Malomed, B. A., & Torner, L. Frontiers in multidimensional self-trapping of nonlinear fields and matter. *Nature Reviews Physics* **1**, 185 (2019).
3. Manton, N. & Sutcliffe, P. *Topological solitons* (Cambridge University Press, 2004).
4. Shnir, Y. M. *Topological and non-topological solitons in scalar field theories* (Cambridge University Press, 2018).
5. Kauffman, L. H. *Knots and physics* (World scientific, 2001), Vol. 1.
6. Skyrme, T. H. R. A unified field theory of mesons and baryons. *Nuclear Physics* **31**, 556 (1962).
7. Skyrme, T. H. R. in *Selected Papers, With Commentary, Of Tony Hilton Royle Skyrme* (World Scientific, 1994), pp. 195.
8. Mühlbauer, S., Binz, B., Jonietz, F., Pfleiderer, C., Rosch, A., Neubauer, A., Georgii, R., & Boni, P. Skyrmion Lattice in a Chiral Magnet. *Science* **323**, 915 (2009).
9. Yu, X., Onose, Y., Kanazawa, N., Park, J. H., Han, J. H., Matsui, Y., Nagaosa, N., & Tokura, Y. Real-space observation of a two-dimensional skyrmion crystal. *Nature* **465**, 901 (2010).
10. Bogdanov, A. N., Rößler, U. K., & Shestakov, A. A. Skyrmions in nematic liquid crystals. *Physical Review E* **67**, 016602 (2003).
11. Smalyukh, I. I., Lansac, Y., Clark, N. A. & Trivedi, R. P. Three-dimensional structure and multistable optical switching of triple-twisted particle-like excitations in anisotropic fluids. *Nature Materials* **9**, 139 (2009).
12. Krause, S., & Wiesendanger, R. Skyrmionics gets hot. *Nature materials* **15**, 493 (2016).
13. Haas, W. E. L. & Adams, J. E. New optical storage mode in liquid crystals. *Applied Physics Letters* **25**, 535 (1974).
14. Varanytsia, A. & Chien, L.-C. Photoswitchable and dye-doped bubble domain texture of cholesteric liquid crystals. *Opt. Lett.* **40**, 4392 (2015).
15. Varanytsia, A., Posnjak, G., Mur, U., Joshi, V., Darrah, K., Musevic, I., Copar, S. & Chien, L. -C. Topology-commanded optical properties of bistable electric-field-induced torons in cholesteric bubble domains. *Scientific reports* **7**, 1 (2017).
16. Helfrich, W. Alignment-inversion walls in nematic liquid crystals in the presence of a magnetic field. *Physical Review Letters* **21**, 1518 (1968).
17. Leger, L. Observation of wall motions in nematics. *Solid State Communications* **10**, 697 (1972).
18. Migler, K. B. & Meyer, R. B. Solitons and pattern formation in liquid crystals in a rotating magnetic field. *Physical Review Letters* **66**, 1485 (1991).
19. Frisch, T., Rica, S., Coullet, P. & Gilli, J. M. Spiral waves in liquid crystal. *Physical Review Letters* **72**, 1471 (1994).

20. Zheng, C. & Meyer, R. B. Thickness effects on pattern formation in liquid crystals in a rotating magnetic field. *Physical Review E* **55**, 2882 (1997).

21. Lei, L., Shu, C. Q., Shen, J. L., Lam, P. M., & Huang, Y. Soliton Propagation in Liquid Crystals. *Physical Review Letters* **49**, 1335 (1982).

22. Guozhen, Z. Experiments on Director Waves in Nematic Liquid Crystals. *Physical Review Letters* **49**, 1332 (1982).

23. Lei, L., Changqing, S. & Gang, X. Generation and detection of propagating solitons in shearing liquid crystals. *Journal of Statistical Physics* **39**, 633 (1985).

24. Peccianti, M. & Assanto, G. Nematicons. *Physics Reports* **516**, 147 (2012).

25. Li, B.-X., Borshch, V., Xiao, R. L., Paladugu, S., Turiv, T., Shiyanovskii, S. V., & Lavrentovich, O. D. Electrically driven three-dimensional solitary waves as director bullets in nematic liquid crystals. *Nature Communications* **9**, 2912 (2018).

26. Li, B.-X., Xiao, R. L., Paladugu, S., Shiyanovskii, S. V. & Lavrentovich, O. D. Three-dimensional solitary waves with electrically tunable direction of propagation in nematics. *Nature Communications* **10**, 3749 (2019).

27. Shen, Y. & Dierking, I. Dynamics of electrically driven solitons in nematic and cholesteric liquid crystals. *Communications Physics* **3**, 1 (2020).

28. Shen, Y. & Dierking, I. Dynamic dissipative solitons in nematics with positive anisotropies. *Soft Matter* **16**, 5325, (2020).

29. Aya, S. & Araoka, F. Kinetics of motile solitons in nematic liquid crystals. *Nature communications* **11**, 1 (2020).

30. Gennes, P.-G. De & Prost, J. *The physics of liquid crystals (2nd Edition)* (Oxford university press, 1993), Vol. 83.

31. Shen, Y. & Dierking, I. Perspectives in liquid-crystal-aided nanotechnology and nanoscience. *Applied Sciences* **9**, 2512 (2019).

32. Kamien, R. D. & Selinger, J. V. Order and frustration in chiral liquid crystals. *Journal of Physics: Condensed Matter* **13**, R1 (2001).

33. Oswald, P., Baudry, J., & Pirkl, S. Static and dynamic properties of cholesteric fingers in electric field. *Physics Reports* **337**, 67 (2000).

34. Kerllenevich, B. & Coche, A. Bubble Domain in Cholesteric Liquid Crystals. *Molecular Crystals and Liquid Crystals* **68**, 47 (1981).

35. Ackerman, P. J., Trivedi, R. P., Senyuk, B., Lagemaat, J. V. D. & Smalyukh, I. I. Two-dimensional skyrmions and other solitonic structures in confinement-frustrated chiral nematics. *Physical Review E* **90**, 012505 (2014).

36. Afghah, S. & Selinger, J. V. Theory of helicoids and skyrmions in confined cholesteric liquid crystals. *Physical Review E* **96**, 012708 (2017).

37. Ackerman, P. J., Lagemaat, J. van de & Smalyukh, I. I. Self-assembly and electrostriction of arrays and chains of hopfion particles in chiral liquid crystals. *Nature Communications* **6**, 6012 (2015).

38. Ackerman, P. J. & Smalyukh, I. I. Diversity of knot solitons in liquid crystals manifested by linking of preimages in torons and hopfions. *Physical Review X* **7**, 011006 (2017).

39. Ackerman, P. J., Boyle, T. & Smalyukh, I. I. Squirming motion of baby skyrmions in nematic fluids. *Nature Communications* **8**, 673 (2017).

40. Woo, S., Litzius, K., Kruger, B., Caretta, M. –Y. Im, L., Richter, K., Mann, M., Krone, A., Reeve, R. M., Weigand, M., Agrawal, P., Lemesh, I., Mawass, M. –A., Fischer, P., Klaui, M. & Beach, G. S. D. Observation of room-temperature magnetic skyrmions and

their current-driven dynamics in ultrathin metallic ferromagnets. *Nature materials* **15**, 501 (2016).

41. Zheng, F., Rybakov, F. N., Borisov, A. B., Song, D., Wang, S., Li, Z., Du, H., Kiselev, N. S., Caron, J., Kovacs, A., Tian, M., Zhang, Y., Blugel, S. & Borkowski, R. E. D. Experimental observation of chiral magnetic bobbers in B20-type FeGe. *Nature nanotechnology* **13**, 451 (2018).

42. Kleman, M. & Laverntovich, O. D. *Soft matter physics: an introduction* (Springer Science & Business Media, 2007).

43. Li, S.-S., Shen, Y., Chang, Z. N., Li, W. S., Xu, Y. C., Fan, X. Y., & Chen, L. J. Dynamic cholesteric liquid crystal superstructures photoaligned by one-step polarization holography. *Applied Physics Letters* **111**, 231109 (2017).

44. Baudry, J., Pirkl, S. & Oswald, P. Looped finger transformation in frustrated cholesteric liquid crystals. *Physical Review E* **59**, 5562 (1999).

45. Baudry, J., Pirkl, S. & Oswald, P. Topological properties of singular fingers in frustrated cholesteric liquid crystals. *Physical Review E* **57**, 3038 (1998).

46. Gil, L. & Gilli, J. M. Surprising Dynamics of Some Cholesteric Liquid Crystal Patterns. *Physical Review Letters* **80**, 5742 (1998).

47. Ribière, P., Oswald, P. & Pirkl, S. Crawling and spiraling of cholesteric fingers in electric field. *Journal de Physique II* **4**, 127 (1994).

48. See the Supplementary Information.

49. Foster, D., Kind, C., Ackerman, P. J., Tai, J. S. B., Dennis, M. R. & Smalyukh, I. I. Two-dimensional skyrmion bags in liquid crystals and ferromagnets. *Nature Physics* **15**, 655 (2019).

50. Fert, A., Cros, V. & Sampaio, J. Skyrmions on the track. Nature nanotechnology **8**, 152 (2013).

51. Loussert, C. & Brasselet, E. Multiple chiral topological states in liquid crystals from unstructured light beams. *Applied Physics Letters* **104**, 051911 (2014).

52. Tai, J.-S. B. * Smalyukh, I. I. Surface anchoring as a control parameter for stabilizing torons, skyrmions, twisted walls, fingers, and their hybrids in chiral nematics. *Physical Review E* **101**, 042702 (2020).

53. Russel, W. B., *et al.*, *Colloidal dispersions* (Cambridge university press, 1991).

54. Coffey, W. & Kalmykov, Y. P. *The Langevin equation: with applications to stochastic problems in physics, chemistry and electrical engineering* (World Scientific, 2012), Vol. 27.

55. Kenkre, V., Kühne, R., & Reineker, P. Connection of the velocity autocorrelation function to the mean-square-displacement and to the memory function of generalized master equations. *Zeitschrift für Physik B Condensed Matter* **41**, 177 (1981).

56. Turiv, T., Lazo, I., Brodin, A., Lev, B. I., Reiffenrath, V., Nazarenko, V. G. & Lavrentovich, O. D. Effect of collective molecular reorientations on Brownian motion of colloids in nematic liquid crystal. *Science* **342**, 1351 (2013).

57. Sohn, H. R. O., Liu, C. D. & Smalyukh, I. I. Schools of skyrmions with electrically tunable elastic interactions. *Nature Communications* **10**, 4744 (2019).

58. Palagi, S., Mark, A. G., Reigh, S. Y., Melde, K., Qiu, T., Zeng, H., Parmeggiani, C., Martella, D., Castillo, A. S., Kapernaum, N., Giesselmann, F., Wiersma, D. S., Lauga, E. & Fischer, P. Structured light enables biomimetic swimming and versatile locomotion of photoresponsive soft microrobots. *Nature materials* **15**, 647 (2016).

59. Kos, Ž. & Ravnik, M. Field generated nematic microflows via backflow mechanism. *Scientific Reports* **10**, 1446 (2020).

60. Xiao, K., Chen, X. & Wu, C.-X. Fréedericksz-like positional transition. *Physical Review Research* **1**, 033041 (2019).

61. Mieda, Y. & Furutani, K. Two-dimensional micromanipulation using liquid crystals. *Applied Physics Letters* **86**, 101901 (2005).

62. Kawachi, M., Kogure, O., & Kato, Y. Bubble Domain Texture of a Liquid Crystal. *Japanese Journal of Applied Physics* **13**, 1457 (1974).

63. Shen, Y., Xu, Y. C., Ge, Y. H., Jiang, R. G., Wang, X. Z., Li, S. S. & Chen, L. J. Photoalignment of dye-doped cholesteric liquid crystals for electrically tunable patterns with fingerprint textures. *Opt. Express* **26**, 1422 (2018).

64. Shen, Y. & Dierking, I. Annihilation dynamics of topological defects induced by microparticles in nematic liquid crystals. *Soft Matter* **15**, 8749 (2019).

65. Narayan, V., Ramaswamy, S. & Menon, N. Long-Lived Giant Number Fluctuations in a Swarming Granular Nematic. *Science* **317**, 105 (2007).

66. Muckel, F., Malottki, S. V., Holl, C., Pestka, B., Pratzer, M., Bessarab, P. F., Heinze, S., & Morgenstern, M., Experimental identification of two distinct skyrmion collapse mechanisms. *Nature Physics*, **17**, 395 (2021).

67. Milde, P., Kohler, D., Seidel, J., Eng, L. M., Bauer, A., Chacon, A., Kindervater, J., Muhlbauer, S., Pfleiderer, C., Buhrandt, S., Schutte, C. & Rosch, A. Unwinding of a Skyrmion Lattice by Magnetic Monopoles. *Science* **340**, 1076 (2013).

68. Pishnyak, O. P., Shiyanovskii, S. V. & Lavrentovich, O. D. Inelastic collisions and anisotropic aggregation of particles in a nematic collider driven by backflow. *Physical Review Letters* **106**, 047801 (2011).

69. Pishnyak, O. P., Shiyanovskii, S. V. & Lavrentovich, O. D. Aggregation of colloidal particles in a non-equilibrium backflow induced by electrically-driven reorientation of the nematic liquid crystal. *Journal of Molecular Liquids* **164**, 132 (2011).

70. Schaefer, D. W., Martin, J. E., Wiltzius, P. & Cannell, D. S. Fractal Geometry of Colloidal Aggregates. *Physical Review Letters* **52**, 2371 (1984).

71. Pirkl, S. Time evolution of cholesteric fingers of the second species in an electric field. *Crystal Research and Technology* **44**, 1323 (2009).

72. Pirkl, S., Ribiere, P. & Oswald, P. Forming process and stability of bubble domains in dielectrically positive cholesteric liquid crystals. *Liquid Crystals* **13**, 413 (1993).

73. Nych, A., Fukuda, J. I., Ognysta, U., Zumer, S. & Musevic, I. Spontaneous formation and dynamics of half-skyrmions in a chiral liquid-crystal film. *Nature Physics* **13**, 1215 (2017).

74. Sohn, H. R. & Smalyukh, I. I. Electrically powered motions of toron crystallites in chiral liquid crystals. *Proceedings of the National Academy of Sciences* **117**, 6437 (2020).

75. Pishnyak, O. P., Tang, S., Kelly, J. R., Shiyanovskii, S. V. & Lavrentovich, O. D. Levitation, Lift, and Bidirectional Motion of Colloidal Particles in an Electrically Driven Nematic Liquid Crystal. *Physical Review Letters* **99**, 127802 (2007).

76. Che, K.-J., Yang, Y. J., Lin, Y. L., Shan, Y. W., Ge, Y. H., Li, S. S., Chen, L. J. & Yang, C. Y. J. Microfluidic generation of cholesteric liquid crystal droplets with an integrative cavity for dual-gain and controllable lasing. *Lab on a Chip* **19**, 3116 (2019).

77. Hartshorne, N. H. *The Microscopy of Liquid Crystals* (Microscope Publications Ltd., 1974).

78. Goodman, A. M. Optical interference method for the approximate determination of refractive index and thickness of a transparent layer. *Appl. Opt.* **17**, 2779 (1978).

6.8 Supplementary Information

6.8.1 Supplementary Figures
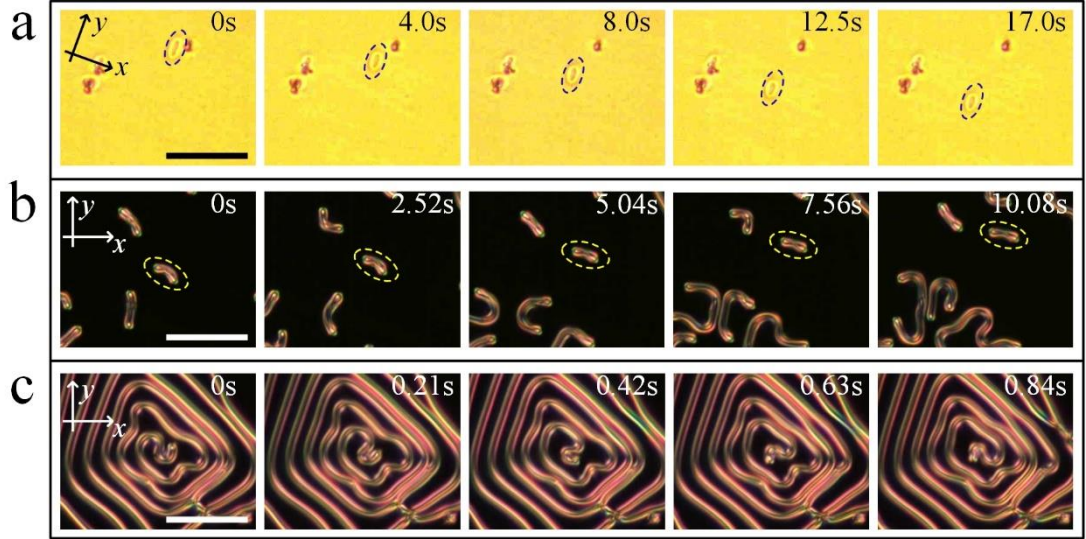
Supplementary Figure 6-1 Polarizing micrographs of dynamic cholesteric fingers. (a) Crawling of a first type cholesteric finger (CF1) (U = 3.9 V, f = 10 kHz, f_m = 15 Hz, p ~ 5.0 μm, d = 4.8 μm). (b) Drift of a second type cholesteric finger (CF2) (U = 6.4 V, f = 10 Hz, p ~ 5.0 μm, d = 19.3 μm). (c) Dynamic spiral of a CF2 (U = 6.8 V, f = 10 Hz, p ~ 5.0 μm, d = 19.3 μm). Scale bars 50 μm.
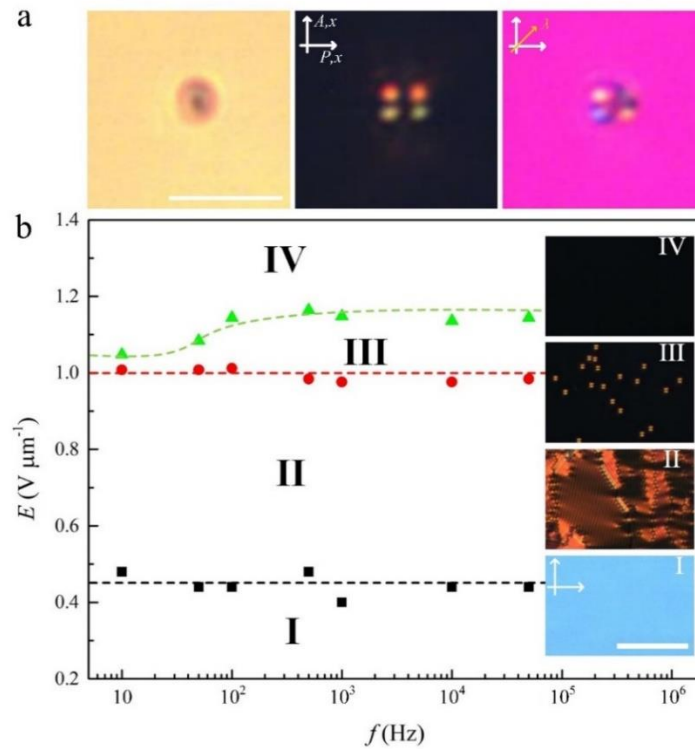
Supplementary Figure 6-2 Skyrmionic solitons in CNLCs with pitch p ~ 2 μm confined in a cell with cell gap d = 5.1 μm. (a) From left to right, micrographs of a soliton (E = 0.98 V μm^{-1}, f = 50 kHz) without polarizers, with crossed polarizers, with crossed polarizers and a first-order red plate compensator (530 nm) whose slow axis λ makes an angle of 45 ° with the crossed polarizers. Scale bar 10 μm. (b) Threshold dependence of different states (I: homogeneous state, II: focal conic texture, III: soliton state, IV: quasi-homeotropic state) on the frequency of rectangular AC electric field, f.

Insets are polarizing micrographs of the different states (I: $E = 0$ V μm^{-1}, II: $E = 0.59$ V μm^{-1}, $f = 50$ kHz, III: $E = 0.98$ V μm^{-1}, $f = 50$ kHz, IV: $E = 1.13$ V μm^{-1}, $f = 50$ kHz). Scale bar 50 μm. The white arrows indicate the polarizers.
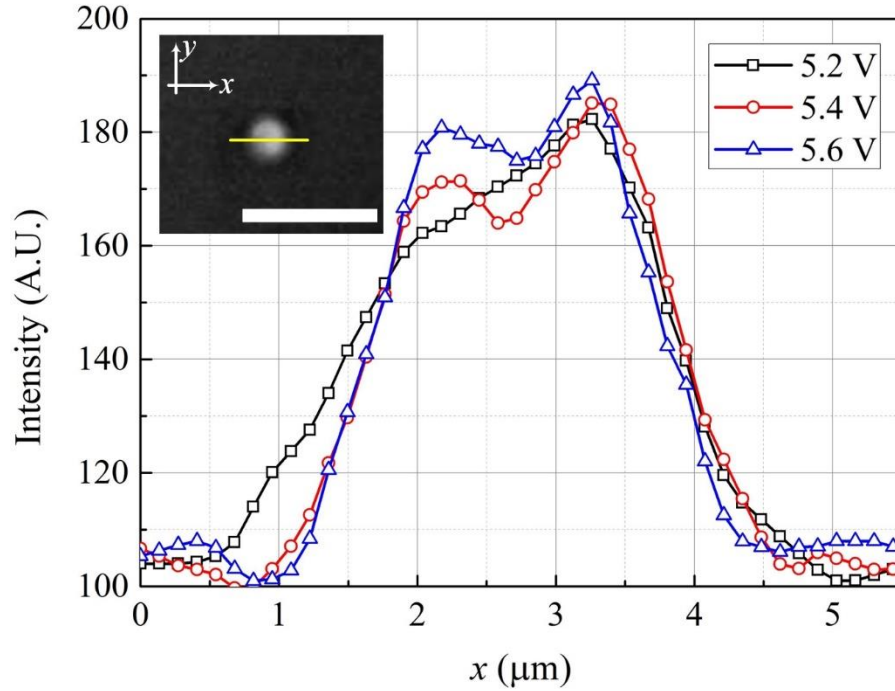
Supplementary Figure 6-3 Profile of skyrmionic solitons. The diameter of a soliton measured as the width of the cross-section of the soliton along the x-axis (yellow line in the inset) at varied voltages ($f = 50$ kHz) in CNLCs with pitch $p \sim 2$ μm confined in a cell with cell gap $d = 5.1$ μm. The inset shows the micrograph of the soliton, scale bar 10 μm.
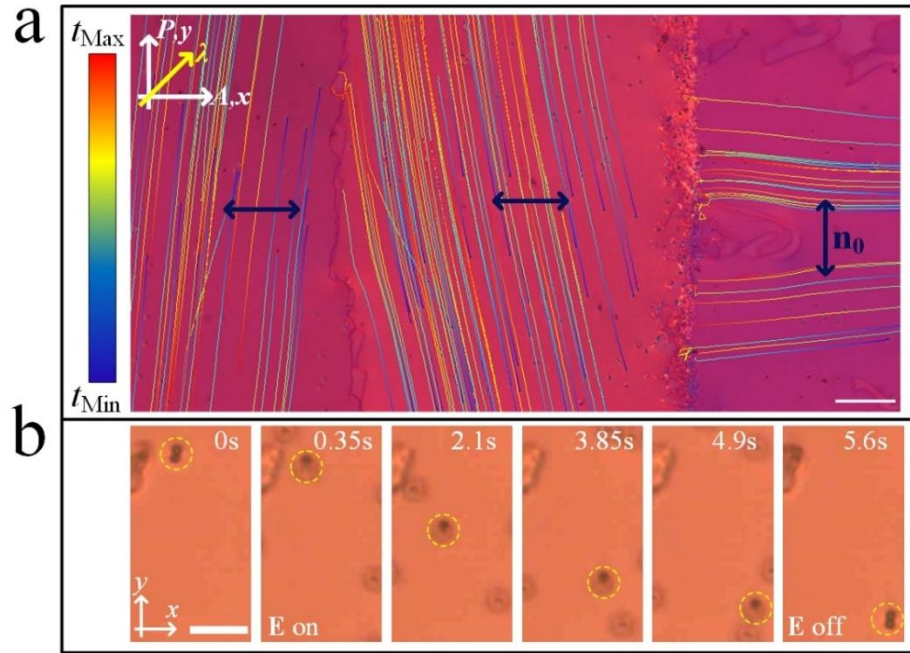
Supplementary Figure 6-4 Trajectory manipulation and cargo transport of skyrmionic solitons in CNLCs with pitch $p \sim 2$ μm. (a) Polarizing micrograph of motion of solitons in regions with different alignment directions with trajectories colored with time according to the color bar ($t_{min} = 0$ s, $t_{max} = 26$ s). The dark blue arrows indicate the alignment direction. Scale bar 60 μm. $U = 16.0$ V, $f = 50$ kHz, $f_m = 200$ Hz, $d = 6.3$ μm. (b) Micrographs of a topological soliton which is induced at an aggregate of two microparticles (diameter: 1.5 μm) by applying an electric field and then carries the microparticles moving through the LC bulk. Scale bar 10 μm. $U = 16.0$ V, $f = 100$ kHz, $f_m = 180$ Hz, $d = 5.1$ μm.
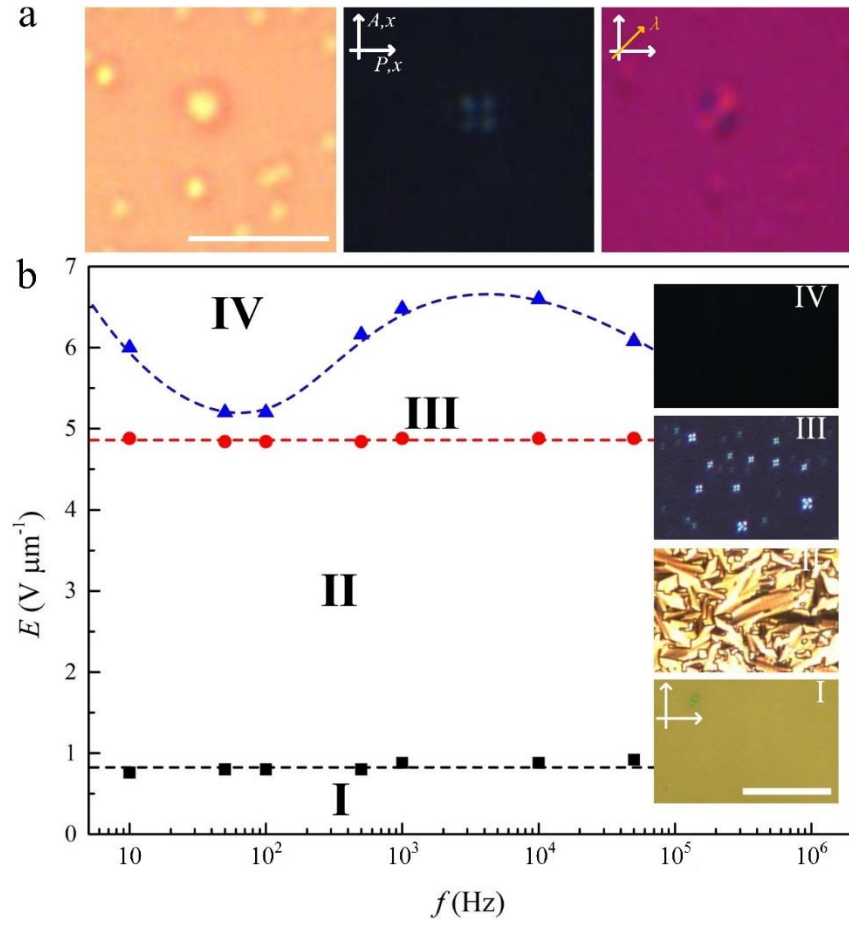
Supplementary Figure 6-5 Skyrmionic solitons in CNLCs with pitch $p \sim 0.375$ μm confined in a cell with cell gap $d = 5.0$ μm. (a) From left to right, micrographs of solitons ($E = 4.92$ V μm^{-1}, $f = 50$ kHz) without polarizers, with crossed polarizers, with crossed polarizers and a first-order red plate compensator (530 nm) whose slow axis λ makes and angle of 45 ° with the crossed polarizers. Scale bar 10 μm. (b) Threshold dependence of different states (I: homogeneous state, II: focal conic texture, III: soliton state, IV: quasi-homeotropic state) on frequency of the rectangular AC electric field, f. Insets are the polarizing micrographs of different states (I: $E = 0$ V μm^{-1}, II: $E = 2.0$ V μm^{-1}, $f = 50$ kHz, III: $E = 4.88$ V μm^{-1}, $f = 50$ kHz, IV: $E = 6.2$ V μm^{-1}, $f = 50$ kHz). Scale bar 50 μm. The white arrows indicate polarizers.
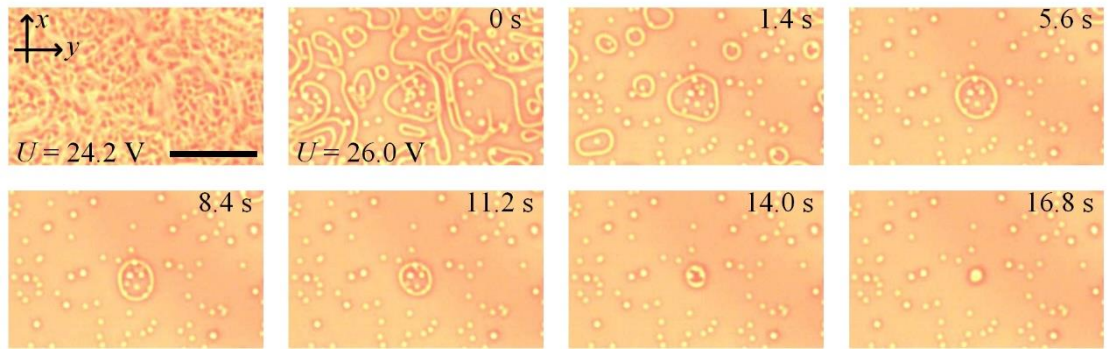
Supplementary Figure 6-6 Micrographs of formation of skyrmionic solitons in CNLCs with pitch $p \sim 0.375$ μm confined in a cell with cell gap $d = 5.0$ μm. Scale bar 20 μm.
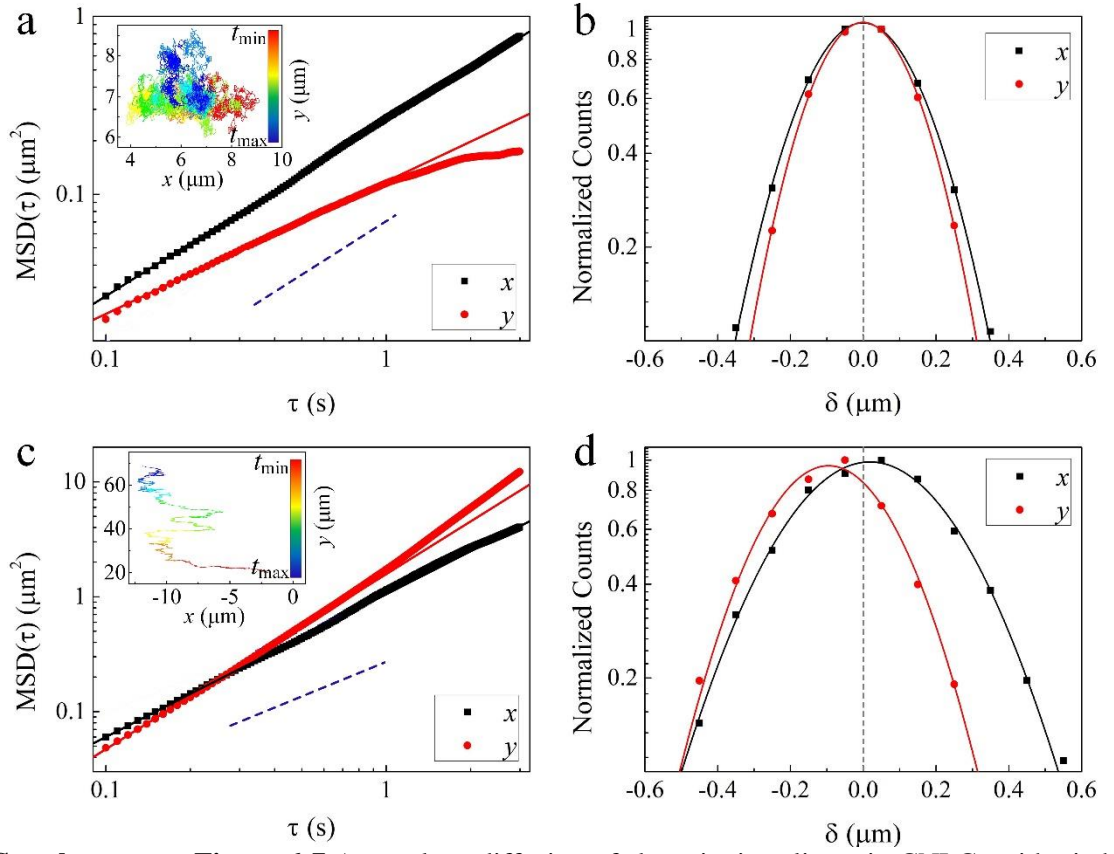
Supplementary Figure 6-7 Anomalous diffusion of skyrmionic solitons in CNLCs with pitch $p \sim$ 0.375 μm confined in a cell with cell gap $d = 5.0$ μm. MSD versus time lag τ of a soliton at (a) $U = 24.4$ V, $f = 200$ Hz and (c) $U = 25.0$ V, $f = 200$ Hz. Insets: trajectories of individual solitons with the time corresponding to the color bar $t_{\min} = 0$s, $t_{\max} = 100$ s. The blue dashed line indicates a slope of +1 for reference. (b) and (d) Histograms of displacements ($\tau = 0.1$ s) of solitons along the x- and y- axes corresponding to (a) and (b), respectively; the solid lines are Gaussian fits of the experimental data points (symbols).
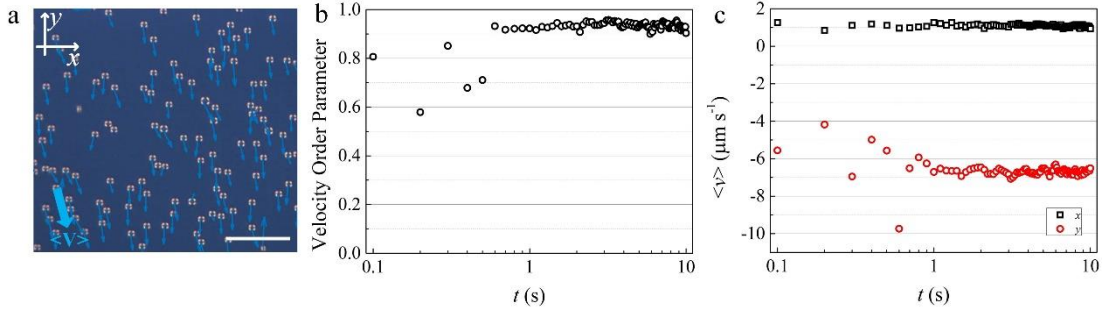
Supplementary Figure 6-8 Coherent motion of skyrmionic solitons in CNLCs with pitch $p \sim 2$ μm confined in a cell with cell gap $d = 5.1$ μm. (a) Polarizing micrograph of skyrmionic solitons at 0.5 s after applying electric field with their velocities marked as blue arrows (The amplitudes of velocities are indicated as the lengths of the arrows). Scale bar 50 μm. Evolution of (b) velocity order parameter and (c) average velocities with time. $U = 14.0$ V, $f = 50$ kHz, $f_{\mathrm{m}} = 180$ Hz.
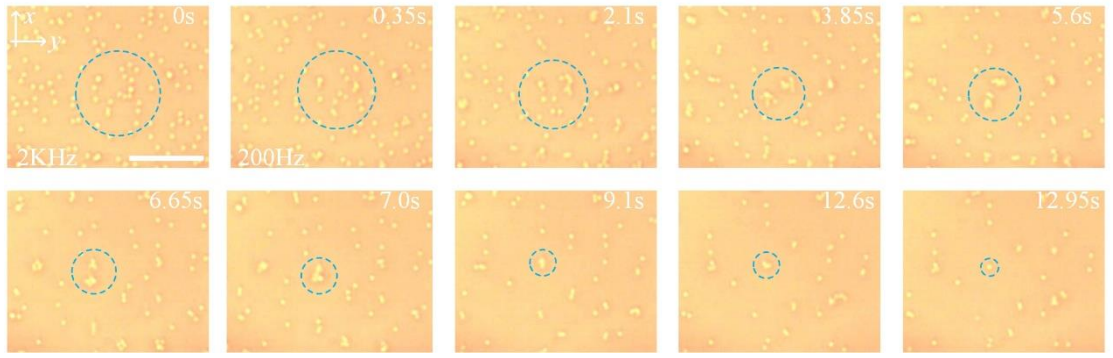
Supplementary Figure 6-9 Coalescence of skyrmionic solitons in CNLCs with pitch $p \sim 0.375$ μm confined in a cell with cell gap $d = 5.0$ μm. $U = 25.0$ V, $f = 200$ Hz. Scale bar 20 μm.
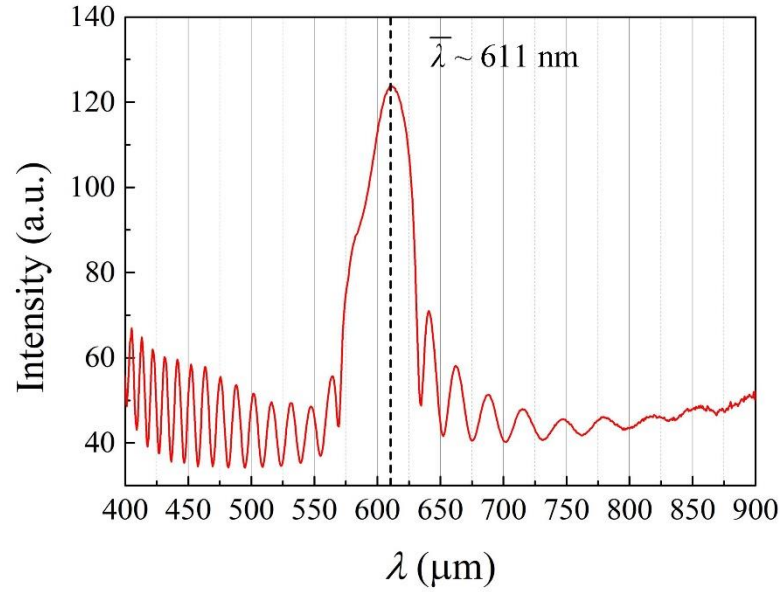
Supplementary Figure 6-10 Reflected light intensity profile of the CNLC sample with high chirality ($p \sim 0.375$ μm) confined in a cell with homogeneous alignment. $T = 50$ ℃.

	along x		along y	
U (V)	D (μm² s⁻¹)	ξ (kg s⁻¹)	D (μm² s⁻¹)	ξ (kg s⁻¹)
5.2	0.0105	4.26×10^{-7}	0.0189	2.36×10^{-7}
5.3	0.0108	4.12×10^{-7}	0.0247	1.81×10^{-7}
5.4	0.0118	3.77×10^{-7}	0.0261	1.71×10^{-7}
5.5	0.0138	3.23×10^{-7}	0.0278	1.60×10^{-7}
5.6	0.0143	3.12×10^{-7}	0.0273	1.63×10^{-7}

Supplementary Table 6-1 Lateral diffusivity D and effective viscous drag coefficient ξ of skyrmionic solitons at varied voltages. $f = 50$ kHz, $p \sim 2$ μm, $d = 5.1$ μm.

6.8.2 Supplementary Movies

File Name: Supplementary Movie 6-1
Description: Reversible transformation between skyrmionic solitons and cholesteric fingers. $P \sim 5.0$ μm, $d = 19.3$ μm, $f = 50$ kHz, U gradually decreases from 6.6 V to 6.0 V, and then increases to 6.6 V again. The movie is played at 4× the original speed.

File Name: Supplementary Movie 6-2
Description: Tuning the topological degree of a skyrmion bag by changing the modulated frequency f_m of the applied electric field. $P \sim 5.0$ μm, $d = 19.3$ μm, $f = 50$ kHz, $U = 16.0$ V, f_m changes between 20 Hz and 10 Hz. The movie is played at real speed.

File Name: Supplementary Movie 6-3
Description: Collective directional motion of skyrmionic solitons. $P \sim 2.0$ μm, $d = 5.1$ μm, $f = 50$ kHz, $f_m = 180$ Hz, $U = 14$ V. The movie is played at 2× the original speed.

File Name: Supplementary Movie 6-4
Description: Collective directional motion of skyrmionic solitons. $P \sim 2.0$ μm, $d = 5.1$ μm, $f = 50$ kHz, $f_m = 220$ Hz, $U = 18$ V. The movie is played at 2× the original speed.

File Name: Supplementary Movie 6-5
Description: Collective directional motion of skyrmionic solitons with the moving direction manipulated by the electric field. $P \sim 2.0$ μm, $d = 5.1$ μm, $f = 50$ kHz, $f_m = 200$ Hz, U increases gradually form 12 V to 18 V, and then decreases to 12 V. The movie is played at 4× the real speed.

File Name: Supplementary Movie 6-6
Description: Various interactions among skyrmionic solitons. $P \sim 2.0$ μm, $d = 5.1$ μm.
File Name: Supplementary Movie 6-7
Description: Collective directional motion of skyrmionic solitons in regions with different alignment directions. $P \sim 2.0$ μm, $d = 6.3$ μm, $f = 50$ kHz, $f_m = 200$ Hz, $U = 16.0$ V. The movie is played at 3× the real speed.

File Name: Supplementary Movie 6-8
Description: Cargo transport by a skyrmion soliton. $P \sim 2.0$ μm, $d = 5.1$ μm, $f = 100$ kHz, $f_m = 180$ Hz, $U = 16.0$ V. The movie is played at 2× the original speed.

File Name: Supplementary Movie 6-9
Description: Formation of skyrmionic solitons in CNLC with small pitch. $P \sim 0.375$ μm, $d = 5.0$ μm, $f = 4$ kHz, U gradually increase from 24.2 V to 26.0 V. The movie is played at 2× the real speed.

File Name: Supplementary Movie 6-10
Description: Collective meandering motion of skyrmionic solitons. $P \sim 0.375$ μm, $d = 5.0$ μm, $f = 200$ kHz, $U = 25.0$ V. The movie is played at 4× the original speed.

Chapter 7

Reconfigurable transformation of skyrmionic solitons in cholesteric liquid crystals

Authors: Yuan Shen[1] and Ingo Dierking[1]*
[1] Department of Physics and Astronomy, School of Natural Sciences, University of Manchester, Oxford Road, Manchester, M13 9PL, United Kingdom
*Email: ingo.dierking@manchester.ac.uk

This work is in preparation.

Author contributions:
Y. S. conceived and carried out the experimental investigations, analyzed the experimental results and wrote the manuscript. I. D. supervised the investigations and contributed through discussions.

Abstract

In this work, a reversible transformation between torons and cholesteric fingers is realized by continuously changing the pitch through temperature variation of the chiral nematic liquid crystal twist inversion system. By decreasing the pitch, the torons act as seeds from which cholesteric fingers gradually grow. By increasing the pitch, the cholesteric fingers gradually shorten and transform back to the initial state. Although the torons are severely deformed and cannot be distinguished during the transformation, the torons are very well topologically protected and cannot be destroyed.

7.1 Introduction

Topological solitons, such as skyrmions, baby-skyrmions (also refer to as two-dimensional (2D) skyrmions), are localized topologically nontrivial field configurations embedded in a uniform far-field background that behave like particles [1]. Like other topological defects, these solitons cannot be continuously deformed into a topologically trivial uniform field. They play important roles in different fields of physics, such as vortices in superconductors [2], instantons in quantum theory [3], and skyrmions in magnetic materials [4] and liquid crystals [5].

Liquid crystals are anisotropic fluids with long-range orientational order of elongated molecules defined by the average of the long molecular axis called director, **n**. The study of solitons in liquid crystals was started in 1968 by Wolfgang Helfrich who theoretically modelled alignment inversion walls as static solitons in an infinite sample of nematic order [6]. Since then, different types of solitons have been reported, including different types of inversion walls [6-8], propagating solitary waves [9,10], individual convective rolls [11] and local convective domains [12], discommensurations [13,14] and breathers [15], nematicons [16], directrons [17], swallow-tail solitons [18], etc. In addition, a number of topological solitons, such as skyrmions, torons, hopfions, heliknotons are observed or created in chiral nematic liquid crystals (CNLCs) [19-21]. The CNLC is represented by a helical superstructure in which **n** continuously twists along a helix at a constant rate. The distance over which **n** rotates by 2π is defined as a pitch, p [22]. The helical structure of CNLCs can be deformed through different

ways, such as by applying electric fields or by confining CNLCs between surfaces with homeotropic anchoring, which eventually leads to the formation of topological solitons.

In this work, topological solitons of elementary 2D skyrmions capped by two 3D singular point defects termed as "torons" are generated in a CNLC which is confined between two surfaces with homeotropic anchoring. The pitch of the CNLC is dependent on the temperature (T). By gradually decreasing the temperature from the isotropic phase, p increases. The sample slowly transforms from the focal conical texture into the fingerprint texture. Once p is of the size of the cell gap, d, the cholesteric fingers gradually relax into torons. The number of the torons can be easily controlled by manipulating the cooling rate. By gradually increasing the temperature, the torons continuously shrink and act as seeds of cholesteric fingers from which those fingers grow. We find that such a transformation is reversible and the torons are very well topologically protected during the transformation.

7.2 Materials and methods

The CNLC used is 4-[(S,S)-2,3-epoxyhexyloxy]-phenyl-4-(decyloxy)-benzoate (W46) [23,24] which shows an isotropic to nematic phase transition at $T = 97.5$ °C on cooling. The CNLC is firstly heated to the isotropic phase and then filled into a cell (North LCD) with homeotropic anchoring. The thickness of the cell, $d = 9.7$ μm, is measured through the thin-film interference method [25]. The pitch of the CNLC gradually increases with decreasing temperature. At $T = 82.5$ °C to $T = 82.3$ °C, the pitch diverges to infinity ($1/p = 0$) and the CNLC transform into a nematic phase configuration which is characterized by a completely dark texture observed in polarizing optical microscopy (POM). This helix inversion point is consistent with the previously published data (Figure 7-1) [24]. The sample then reverses its chirality from right handedness to left handedness at $T = 82.2$ °C which is characterized by the formation of cholesteric fingers and the pitch gradually decreases with further decreasing temperature [24]. The sample is observed through a polarizing microscope (Leica OPTIPOL). Images and movies are recorded by using a charge-coupled device camera (UI-3360CP-C-HQ, uEye Gigabit Ethernet). The sample is temperature controlled in a hot stage (LTSE350, Linkam) which is connected to a TP 94, Linkam temperature controller.
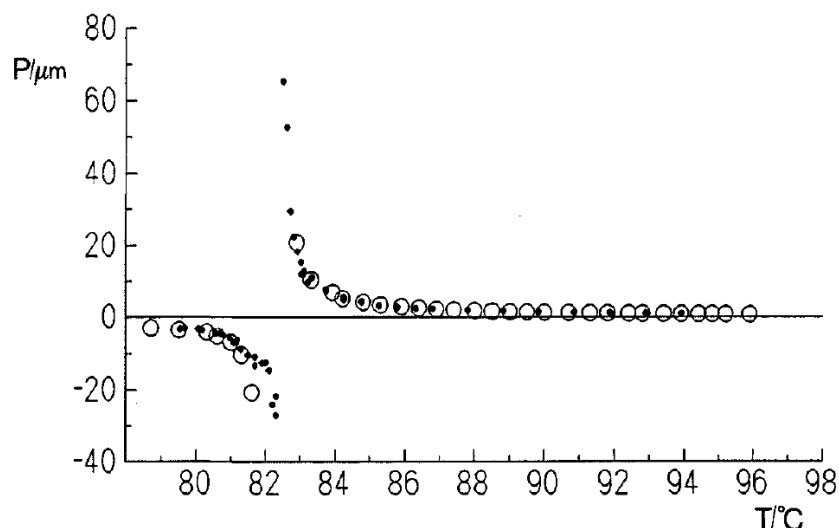
Figure 7-1 Temperature dependence of cholesteric pitch of W-46. Reproduced with permission from Ref [24]. Copyright 1993 Talor & Francis.

7.3 Results and discussion

As Figure 7-2 shows, by slowly decreasing the temperature at a rate of -0.2 °C min^{-1}, the sample firstly experiences the isotropic to cholesteric phase transition at 97.5 °C. As the pitch continuously increases with decreasing temperature, the sample gradually transforms from the focal conic texture (91.2 °C) to the fingerprint texture (85.2 °C). Further decreasing the temperature, the cholesteric fingers (CFs) become thicker, then start shrinking and some transform into torons (83.8 ℃). At $T = 83.4$ ℃, most of the fingers disappear due to the unwinding of the helical structure of the CNLC and transform into the uniform homeotropic state. However, some of the fingers shrink into torons. Normally, the fingers of CF1 type are most frequently observed in cells with homeotropic anchoring. However, despite the fact that the fingers of CF2 type do not nucleate from homeotropic anchoring as easily as those of CF1, they do nucleate at dust particles, spacers, or other irregularities [26]. It is difficult to determine the type of the CFs through the POM images at this stage because CF1 and CF2 have a similar look under POM and the CFs in our experiment are densely packed together. However, it is reported that CF1 always collapses at increasing voltage, whereas CF2 can continuously shrink and transform into torons at high voltages[27]. So, we may give a reasonable conclusion that both CF1 and CF2 exist in our system, however, only CF2 shrinks and transforms into torons. The sample texture is stable at $T = 83.2$ ℃, and is characterized by a homeotropic background sparsely embedded with torons. Further decrease the temperature will eventually destroy the torons due to the unwinding of the CNLC system.

195
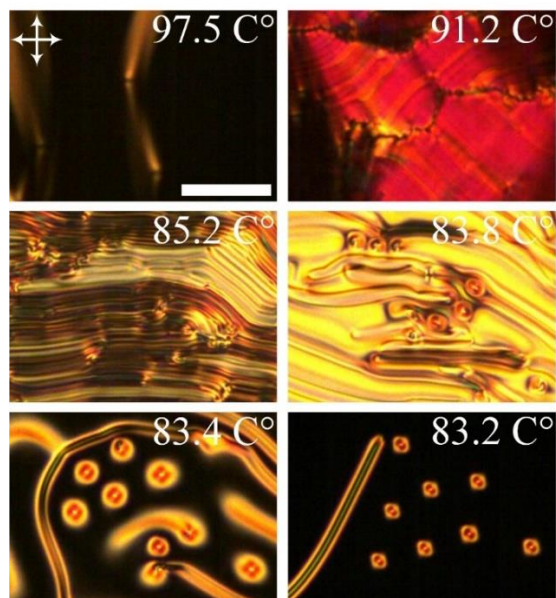
Figure 7-2 POM images of the sample at different temperatures. The sample is slowly cooled at -0.2 ℃ min^{-1} from the isotropic phase. The crossed white arrows represent the polarizers. Scale bar 50 μm.

It is observed that the number density of the torons generated is dependent on the cooling rate of the sample. Figure 7-3 shows the sample at the same temperature ($T = 83.2$ °C) but having been cooled at different rates. It is observed that the faster the temperature is decreased, the more torons are generated. It should be noted that in order to obtain the torons the sample here is firstly heated into the isotropic phase and then cooled into the cholesteric phase. In fact, the number of the torons is actually dependent on the cooling rate at which the isotropic to cholesteric phase transition is passed. No obvious difference is observed between a sample which is cooled at -5 °C min^{-1} from the isotropic phase to $T = 83.2$ °C and a sample which is firstly cooled from the isotropic phase to the cholesteric phase at -5 °C min^{-1}, and then gradually cooled (-0.2 °C min^{-1}) to $T = 83.2$ °C.
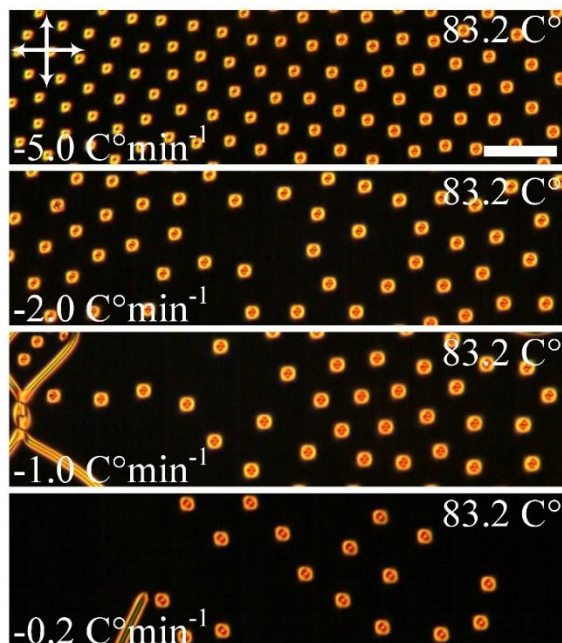
Figure 7-3 POM images of the CNLC sample at $T = 83.2$ ℃ which are obtained by cooling the sample from the isotropic phase at different cooling rate. The crossed white arrows represent the polarizers. Scale bar 50 μm.

The samples also show a reversible transformation between torons and CFs. As shown in Figure 7-4, by increasing the temperature, the toron firstly expands radially and acts as a seed from which the CFs start to grow. With continuously decreasing the pitch of the sample (increasing the temperature), the core of the toron gradually shrinks, distorts and soon the sample transforms into the fingerprint texture (Figure 7-4 (a)). Surprisingly, even though the toron is greatly distorted and can be hardly distinguished at this stage, it is very well topologically protected and can transform back to its initial state by decreasing the temperature (Figure 7-4 (b)).
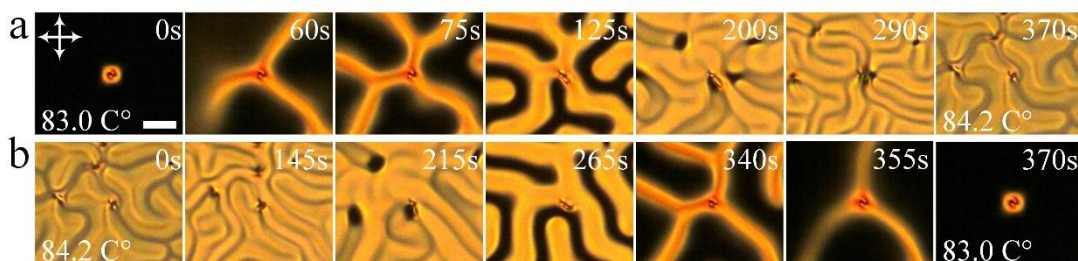
Figure 7-4 Time series of polarizing micrographs showing the transformation between a toron and cholesteric fingers on decreasing pitch (a) and back to a toron on increasing pitch (b). The temperature is gradually changes at 0.2 ℃ min[-1]. The crossed white arrows represent the polarizers. Scale bar 20 μm.

By further increasing the temperature to $T = 90.6$ °C, as shown in Figure 7-5, the toron is still stable and can be transform back from CFs by gradually decreasing the temperature.

Apart from that, an additional toron is generated.
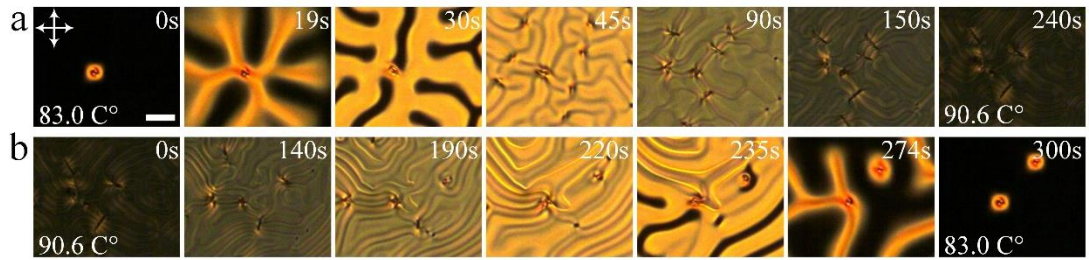
Figure 7-5 Time series of polarizing micrographs showing (a) the transformation from a toron to cholesteric fingers on decreasing pitch and (b) the transformation from cholesteric fingers back to torons on increasing pitch. The temperature is changed at a rate of 2 ℃ min^{-1}. The crossed white arrows represent the polarizers. Scale bar 20 μm.

Finally, Figure 7-6 depict a reversible transformation of a 2D lattice composed of torons. By gradually increasing the temperature, the torons firstly expands and their cores slowly move in random directions (Figure 7-6 (a), 130s). The torons then collide with each other and form aggregates of varied sizes (Figure 7-6 (a), 225s). Eventually, the aggregates continuously shrink and form a network in which the aggregates are connected via CFs (Figure 7-6 (a), 415s).
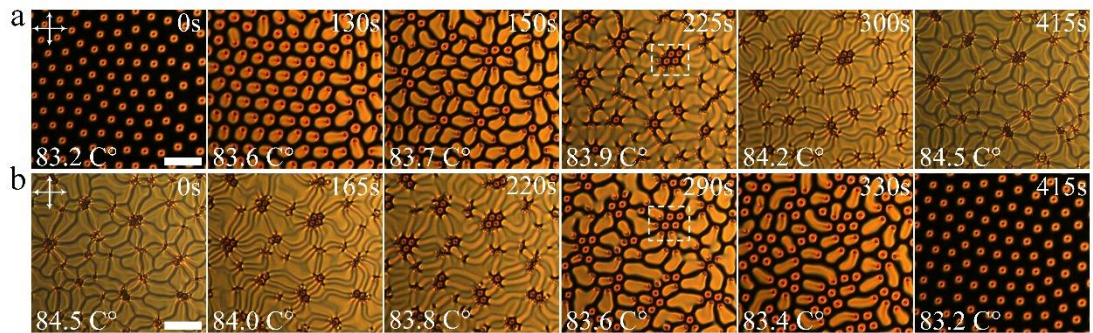
Figure 7-6 Time series of the polarizing micrographs of the sample. (a) The temperature is gradually increased at a rate of 0.2 ℃ min^{-1}. (b) The temperature is gradually decreased at a rate of -0.2 ℃ min^{-1}. The crossed white arrows represent the polarizers. Scale bar 50 μm.

By gradually decreasing the temperature, the aggregates gradually expand, disassemble and eventually transform back to the toron lattice (Figure 7-6 (b)). It is found that the number of the torons is well preserved within the aggregates. As one can see from one of the aggregates which is indicated by the white dashed square. The aggregate is composed of 8 torons by increasing the temperature (Figure 7-6 (a), 225s) and disassemble into 8 torons by decreasing the temperature (Figure 7-6 (b), 290s).

7.4 Conclusion

In this work, we show the continuous evolution from the focal conic texture to the

fingerprint texture and eventually to torons by gradually increasing the pitch of the CNLC system. The number of the generated torons can be facilely controlled by changing the speed of quenching. We further demonstrate that by decreasing the pitch of the CNLC system, the torons can act as seeds of CFs. The stability of the torons is topologically well protected so that even when they are greatly distorted at small cholesteric pitches, the torons can still transform from the CFs back to the initial state by increasing the pitch of the CNLC system. Our results not only demonstrate the reversible transformation between torons and CFs, but also provide an insight into the dependence of the stability and structure of topological solitons on chirality.

7.5 References

1   Manton, N. & Sutcliffe, P. *Topological solitons*. (Cambridge University Press, 2004).
2   Abrikosov, A. A. Nobel Lecture: Type-II superconductors and the vortex lattice. *Reviews of Modern Physics* **76**, 975-979 (2004).
3   Shuryak, E. V. The role of instantons in quantum chromodynamics:(I). Physical vacuum. *Nuclear Physics B* **203**, 93-115 (1982).
4   Roessler, U. K., Bogdanov, A. & Pfleiderer, C. Spontaneous skyrmion ground states in magnetic metals. *Nature* **442**, 797-801 (2006).
5   Smalyukh, I. I., Lansac, Y., Clark, N. A. & Trivedi, R. P. Three-dimensional structure and multistable optical switching of triple-twisted particle-like excitations in anisotropic fluids. *Nature Materials* **9**, 139 (2009).
6   Helfrich, W. Alignment-Inversion Walls in Nematic Liquid Crystals in the Presence of a Magnetic Field. *Physical Review Letters* **21**, 1518-1521 (1968).
7   Leger, L. Observation of wall motions in nematics. *Solid State Communications* **10**, 697-700 (1972).
8   Migler, K. B. & Meyer, R. B. Solitons and pattern formation in liquid crystals in a rotating magnetic field. *Physical Review Letters* **66**, 1485-1488 (1991).
9   Guozhen, Z. Experiments on Director Waves in Nematic Liquid Crystals. *Physical Review Letters* **49**, 1332-1335 (1982).
10   Lei, L., Changqing, S., Juelian, S., Lam, P. M. & Yun, H. Soliton Propagation in Liquid Crystals. *Physical Review Letters* **49**, 1335-1338 (1982).
11   Ribotta, R. Critical Behavior of the Penetration Length of a Vortex into a Subcritical Region. *Physical Review Letters* **42**, 1212-1215 (1979).
12   Joets, A. & Ribotta, R. Localized, Time-Dependent State in the Convection of a Nematic Liquid Crystal. *Physical Review Letters* **60**, 2164-2167 (1988).
13   Lowe, M. & Gollub, J. P. Solitons and the commensurate-incommensurate transition in a convecting nematic fluid. *Physical Review A* **31**, 3893-3897 (1985).
14   Lowe, M., Gollub, J. P. & Lubensky, T. C. Commensurate and Incommensurate Structures in a Nonequilibrium System. *Physical Review Letters* **51**, 786-789 (1983).
15   Skaldin, O. A., Delev, V. A. & Shikhovtseva, E. S. Asymmetry of the time dynamics

of breathers in the electroconvection twist structure of a nematic. *JETP Letters* **97**, 92-97 (2013).

16 Peccianti, M. & Assanto, G. Nematicons. *Physics Reports* **516**, 147-208 (2012).

17 Lavrentovich, O. D. Design of nematic liquid crystals to control microscale dynamics. *Liquid Crystals Reviews* **8**, 59-129 (2020).

18 Shen, Y. & Dierking, I. Electrically driven formation and dynamics of swallow-tail solitons in smectic A liquid crystals. *Materials Advances* **2**, 4752-4761 (2021).

19 Ackerman, P. J., Trivedi, R. P., Senyuk, B., van de Lagemaat, J. & Smalyukh, I. I. Two-dimensional skyrmions and other solitonic structures in confinement-frustrated chiral nematics. *Physical Review E* **90**, 012505 (2014).

20 Ackerman, P. J. & Smalyukh, I. I. Diversity of Knot Solitons in Liquid Crystals Manifested by Linking of Preimages in Torons and Hopfions. *Physical Review X* **7**, 011006 (2017).

21 Tai, J.-S. B. & Smalyukh, I. I. Three-dimensional crystals of adaptive knots. *Science* **365**, 1449 (2019).

22 De Gennes, P.-G. & Prost, J. *The physics of liquid crystals (2nd Edition)*. Vol. 83 (Oxford university press, 1993).

23 Walba, D. M. *et al.* Design and synthesis of new ferroelectric liquid crystals. 2. Liquid crystals containing a nonracemic 2, 3-epoxy alcohol unit. *Journal of the American Chemical Society* **108**, 7424-7425 (1986).

24 Dierking, I. *et al.* Investigations of the structure of a cholesteric phase with a temperature induced helix inversion and of the succeeding Sc* phase in thin liquid crystal cells. *Liquid Crystals* **13**, 45-55 (1993).

25 Goodman, A. M. Optical interference method for the approximate determination of refractive index and thickness of a transparent layer. *Appl. Opt.* **17**, 2779-2787 (1978).

26 Smalyukh, I. I. *et al.* Electric-field-induced nematic-cholesteric transition and three-dimensional director structures in homeotropic cells. *Physical Review E* **72**, 061707 (2005).

27 Baudry, J., Pirkl, S. & Oswald, P. Looped finger transformation in frustrated cholesteric liquid crystals. *Physical Review E* **59**, 5562-5571 (1999).

Chapter 8

Electrically driven formation and dynamics of swallow-tail solitons in smectic A liquid crystals

Authors: Yuan Shen[1] and Ingo Dierking[1]*
[1] Department of Physics and Astronomy, School of Natural Sciences, University of Manchester, Oxford Road, Manchester, M13 9PL, United Kingdom
*Email: ingo.dierking@manchester.ac.uk

Author contributions:
Y. S. conceived and carried out the experimental investigations, analyzed the experimental results and wrote the manuscript. I. D. supervised the investigations and contributed through discussions and writing the manuscript.

Note: the format of the paper is edited. The supplementary movies related to this work are available on the website of the journal. One can also download the movies from the figshare database: https://figshare.com/s/383c7cfb71293527fb0d.

Abstract

Electric field driven instabilities of liquid crystals, such as electro-convections, spatiotemporal chaos, backflows, and solitons are of great importance for both fundamental science and practical applications. Here we demonstrate that particle-like multidimensional solitons representing self-localized molecular director deformations can be produced in a smectic A liquid crystal by applying electric fields. These solitons are transformed from focal conic domains with a static structure topologically analogous to focal conic domains. They lack fore-aft symmetry and move perpendicular to the smectic layers and to the applied electric field direction. During motion, the solitons collide with each other and with colloidal particles and restore their speed and shape after collisions. The rich dynamic behavior and easy control of the solitons make them extremely promising for a broad range of future studies.

8.1 Introduction

Solitons are self-sustained spatially localized waves that propagate with constant speeds and shapes. They were firstly observed as water waves in a shallow canal by Russell in 1834 [1], but their significance was not widely appreciated until 1965 when the word 'soliton' was coined by Zabusky and Kruskal [2]. Nowadays, solitons have been investigated in various nonlinear systems such as nonlinear photonics, superfluids, plasma, superconductors, magnetic materials, and liquid crystals (LCs) [3,4]. A well-known example of a soliton is the Great Red Spot in Jupiter's atmosphere, which is actually a persistent high-pressure region that has been existing for centuries. Despite the ubiquity of solitons, generating multidimensional solitons is still a long-standing challenge due to their poor stabilities [4]. Solitons of higher dimensions open the way to the investigations of various new phenomena such as topological states in the form of vortex tori and rings [4] and are of practical importance such as the magnetic skyrmions in racetrack memory and spintronic devices [5]. It is thus attractive to scientists in different fields to find an efficient way to create stable multidimensional solitons and even control their motions.

Liquid crystals (LCs) provide an ideal testbed for investigations of solitons due to their

unique physical properties [6,7]. LCs are anisotropic fluids that combine the fluidity of isotropic liquids with the long range order of crystalline solids. They are generally characterized by certain symmetries in the preferred orientations of LC molecules, i.e. the director **n** [8,9]. Solitons in LCs have been investigated for decades [7]. Early studies were concentrated on the so-called planar or linear solitons, which are actually transition regions or 'walls' where **n** smoothly rotates by π [10,11]. Propagating solitary waves were generated in nematics by shearing [12,13]. Optical solitons in nematics called nematicons represent self-focused, continuous wave light beams and have received great attention in the last decade due to their promising applications in optical information technology [14]. Topological solitons in the form of baby skyrmions, torons, hopfions, etc. can be generated in chiral nematics by applying electric fields or by the use of laser tweezers [15,16]. Recently, three dimensional dissipative solitons were produced in nematics with both negative [17,18] and positive dielectric anisotropies [19].

So far, the investigations of solitons in LCs are mainly restricted to nematic phases with only rarely investigations being carried out on other phases such as fluid smectic phases. A fluid smectic phase is characterized by the existence of a lamellar arrangement of elongated molecules with orientational and one-dimensional positional order. Within each single layer, the molecules are orientated in a specific direction but the centres of mass are distributed isotropically without any further in-layer positional order [20]. In broken symmetry states, smectics usually expel deviations from equal-layer spacing in a manner which can be mapped onto the Meissner-Higgs effect [21], leading to remarkable patterns of singular ellipses, hyperbolas, and parabolas known as focal conic domains (FCDs) [22]. Within each FCDs, the equidistant smectic layers are deformed into shapes of concentric Dupin cyclides that are folded around two conjugated lines, viz., an ellipse and a confocal hyperbola (Supplementary Figure 8-1) [23]. FCDs have appealed to theorists and experimentalists since the early 20th century [24]. The investigations have gone from mere geometric curiosities [25,26] to the focus of functional applications such as matrices for self-assembly of soft microsystems [27], lithographic templates [28] and micro-lens arrays [29,30], just to name a few. However, so far, FCDs were mostly investigated as static field configurations [31], with only rare studies of their out-of-equilibrium dynamics [22].

In this work, multi-dimensional solitons are generated in a smectic A (SmA) phase by

applying a low-frequency electric field. The formation and structure of the solitons are intimately related to the FCDs. The soliton is a localized "swallow-tail"-like deformation of smectic layers with a singular defect line located at its focus. At the same time, similar to the dissipative solitons in nematics [19], the solitons in SmA break the fore-aft symmetry and move through a slab of uniformly aligned smectic LC in a direction perpendicular to the smectic layers with a constant speed and do not spread while moving over macroscopic distances hundreds times larger than their size. Both the speed and the direction of the solitons can be controlled by the frequency and amplitude of the electric field. During the motion, the solitons survive collisions with each other, restoring shape and speed. The solitons can also form linear chains that move with constant speeds and can even interact with colloidal particles. Our finding provides a facile method for generating and manipulating multi-dimensional solitons in smectic LCs which is attractive to not only physical and material scientists due to their rich nonlinear dynamic behaviors, but also engineers due to their potential applications such as targeted delivery of optical information and micro-cargo.

8.2 Materials and methods

Commercially available smectic liquid crystal 8CB (SYNTHON Chemicals) with a positive anisotropy of dielectric permittivity, $\Delta\varepsilon = \varepsilon_\parallel - \varepsilon_\perp > 0$ and a negative anisotropy of electric conductivity, $\Delta\sigma = \sigma_\parallel - \sigma_\perp < 0$ is used as the soliton medium(Supplementary Figure 8-2); the subscripts indicate whether the component is measured parallel or perpendicular to the director, **n**, respectively. The components of dielectric permittivity and conductivity of 8CB are measured at 34.0 °C through an LCR meter E4980A (Agilent) using commercial cells with planar and homeotropic alignment, respectively (Supplementary Figure 8-2). The smectic A phase is aligned homogeneously in a commercial cell (AWAT, Poland) whose inner surfaces are covered with transparent indium tin oxide (ITO) layers to act as transparent electrodes and spin-coated with polyimide that is rubbed along the x-axis (Figure 8-1 (a)) as alignment layer. The cell gap, d, is measured to be 9.5 ± 0.5 μm through the thin film interference method [32]. The sample is heated up to a temperature (T) slightly below the nematic-smectic phase transition temperature ($T < T_{\text{N-S}} \sim 35$ °C) through a hot

stage (LTSE350, Linkam) which is controlled by a temperature controller (TP 94, Linkam). A low-frequency AC field ($f < 100$ Hz), $\mathbf{E} = (0, 0, E)$, is applied perpendicular to the substrate plane (parallel to the smectic layers) of the cell to induce the solitons which are observed through a polarizing microscope (Leica OPTIPOL). Images and movies are recorded by a charge-coupled device camera (UI-3360CP-C-HQ, uEye Gigabit Ethernet). For investigation of interactions between solitons and colloidal particles, silica micro-particles with diameters (R_P) of 1.5 μm and 3.0 μm are used. A very small amount of micro-particles is firstly placed at the entrance of LC cells and then dragged into the cell by capillary filling of the LC.

8.3 Results

8.3.1 Electrically driven formation of swallow-tail solitons
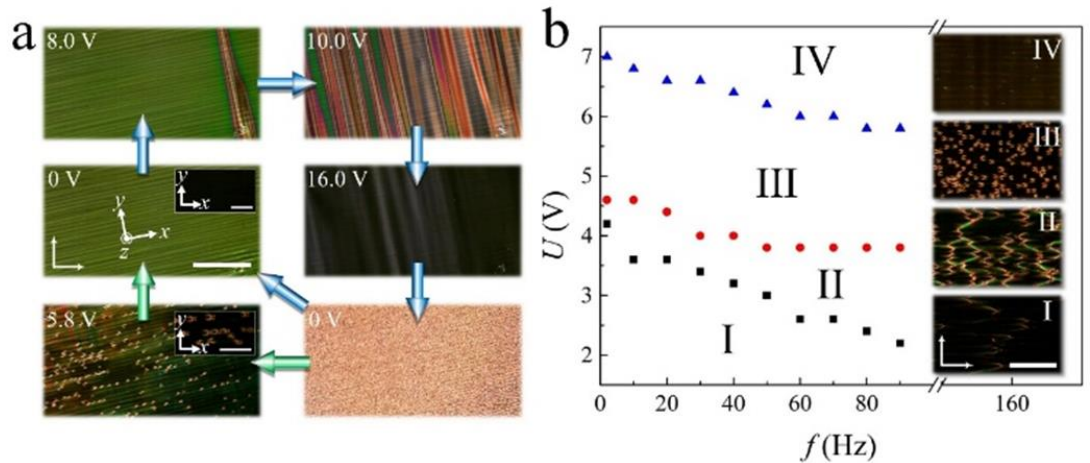
Figure 8-1 Electrically driven formation of swallow-tail solitons. (a) Evolution of different textures of SmA induced by changing the applied voltage ($f = 10$ Hz, $T = 34.8$ °C, scale bar 200 μm, the polarizers are crossed as represented by the two white arrows). The insets show the corresponding textures viewed when the x-axis is parallel to one of the polarizers (scale bars 200 μm (0V), and 50 μm (5.8V)). (b) Frequency dependence of voltage thresholds of different states transformed from the soliton state ($T = 34.8$ °C). Insets are the corresponding polarizing optical textures of different states (I. homogeneous state ($U = 3.0$ V, $f = 10$ Hz), II. PFCDs ($U = 4.2$ V, $f = 10$ Hz), III. soliton state ($U = 5.8$ V, $f = 10$ Hz), IV. homeotropic state ($U = 7.4$ V, $f = 10$ Hz)). Scale bar 100 μm. The polarizers are crossed as represented by the two white arrows.

In a homogeneously aligned nematic film with $\Delta\varepsilon > 0$, the competition between the surface anchoring and the dielectric torque on $\mathbf{n}$ induced by the electric field often leads to a uniform reversible electro-optic effect, the Freederickz transition, once the applied voltage, U, exceeds a specific threshold, U_F. In the fluid smectic phases however, due to the strong

divergence of the bend elastic constant k_{33} as well as the large layer compression modulus B, the amplitude of the distortion of the layer normal

$$\theta_m^2 \leq \frac{2\varepsilon_0 \Delta\varepsilon U^2}{Bd^2} = 2(\frac{\pi\lambda}{d})^2, \tag{8-1}$$

where λ is the smectic characteristic length, is very small, making the Freederickz transition a "ghost" effect [33]. As Figure 8-1 (a) shows, when U increases to values much larger than U_F ($U_F \sim 1.2$ V for 8CB at 36.0 °C), the homogeneous texture of SmA starts breaking up, with striations nucleating at the ITO edges and surface imperfections, which then gradually travel along the smectic layers ($U = 8.0$ V). With increasing U, these striations extend throughout the smectic phase and become more numerous, forming a striated texture ($U = 10.0$ V) [34-36]. It is assumed that there are actually small regions of homeotropic alignment lying beside the imperfections where the "seeding" starts [37]. For further increase of U, the sample turns into a quasi-homeotropic state characterized by the dark optical texture ($U = 16.0$ V). By directly turning off the voltage, a light scattering state ($U = 0$ V) is obtained, which was used as an effective way for light controls in other studies [36,38-40]. Such a texture is composed of thousands to millions of FCDs and is metastable. It will eventually relax back into a homogeneous state. The relaxation time varies from tens of seconds to several days depending mainly on the temperature of the sample. The higher the temperature ($T < T_{N-S}$), the shorter the duration. However, if a low frequency field with a mediate voltage ($U = 5.8$ V) is applied to the scattering state, the FCDs are transformed into dynamic swallow-tail solitons that move perpendicular to the SmA layers with a constant speed (Supplementary Movie 8-1). Figure 8-1 (b) shows the frequency dependence of voltage thresholds of different states transformed from the soliton state (inset III). By increasing U, the solitons disappear and the sample becomes quasi-homeotropic (inset IV). Gradually decreasing U from the solitons state, the motion of the solitons continuously slows down. Once the solitons stop moving, their structures slowly collapse and spread out, forming a number of parabolic focal conic domains (PFCDs) [41] that are tangled up (inset II). Further decreasing U, most of the PFCDs disappear, leading to the homogeneous state embed with sporadically distributed PFCDs (inset I). It is also noted that the thresholds of different states decrease with increasing frequency, f, which may be attributed to the influence of ions which will be discussed in detail below.

8.3.2 Static structure of swallow-tail solitons
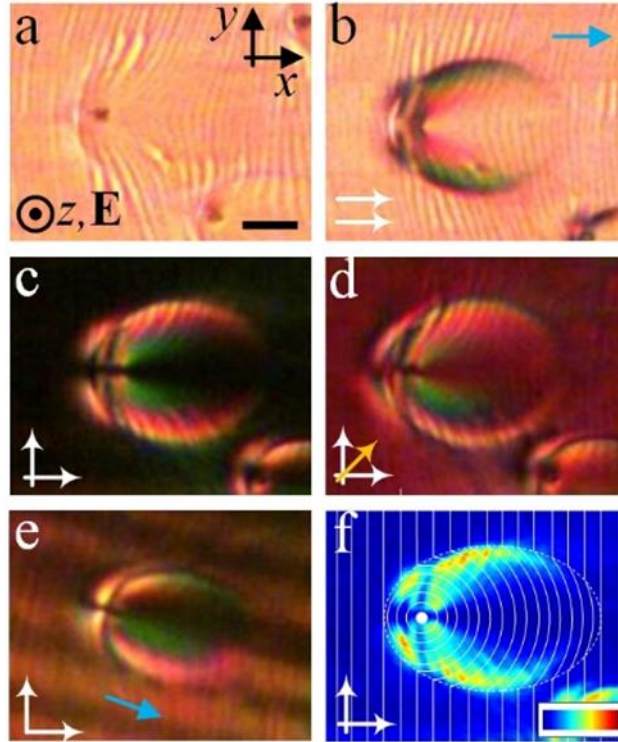
Figure 8-2 Static structure of swallow-tail solitons. (a) Optical micrograph of a typical soliton without polarizers, (b) with polarizers (white arrows) parallel to each other, (c) with crossed polarizers, and (d) with crossed polarizers and a compensator (λ-plate, yellow arrow) whose slow axis is oriented at 45 °to the polarizers. (e) Polarizing optical micrograph of a soliton which is rotated about 20 °clockwise with respect to the polarizers. The blue arrows in (b) and (e) indicate the rubbing direction of the alignment. (f)　Transmitted light intensity map and the corresponding schematic SmA layers (white lines) in the *x-y* plane within the soliton. The color bar shows a linear scale of transmitted light intensity. $U = 6.2$ V, $f = 50$ Hz, $T = 34.0$°C, scale bar 10 μm.

Figure 8-2 (a) to (e) show the optical textures of a typical swallow-tail-like soliton. It is noted that periodic light and dark stripes are produced at low-frequency voltages (Figure 8-2 (a) and (b)), which generally align along the *y*-axis (perpendicular to the alignment direction), but get distorted near and within the solitons. (Figure 8-2 (e) and (f)). The origin of these stripes are not clear yet. One may suspect these are layer undulations or periodic modulations of the director field induced by the electro-hydrodynamic instabilities. However, to give a specific explanation of the generation of the stripes requires further investigations and is out of the scope of the present study. The soliton shows a swallow-tail like texture under crossed polarizers with a structure analogous to the FCDs (Figure 8-2 (f)). The dotted line in Figure 8-2 (f) represents an elliptical contour which is generated as a result of the localization of the stress. The contour is composed of the loci of the cusps of SmA layers.

Outside the soliton, the equidistant layers align homogeneously perpendicular to the molecular alignment direction (x-axis), leading to a dark texture between crossed polarizers (Figure 8-2 (c)). Inside the soliton, the transmitted light intensity increases (Figure 8-2 (c)), indicating azimuthal deviations of the director from the alignment. As a result, the SmA layers continuously deform into curves along the y-axis, whose curvature gradually decreases as they toward the vertexes of the ellipse along the x-axis (Figure 8-2 (f)). The curvature exhibits a maximum at one of the foci of the ellipse, where a singular defect line is located and acts as the core of the soliton. This line is actually a $+2\pi$ disclination which is topologically analogous to the $+1$ radial lines of the nematic state. The line can be clearly observed as a black spot in Figure 8-2 (a) due to light scattering. Around this line, equidistant layers deform into concentric circles and encircle it, forming a cylinder [42]. According to our model, the smectic layers within the soliton are translationally invariant along the z-axis, forming a two-dimensional configuration. However, such a two-dimensional model may require further experimental measurements, such as fluorescent confocal polarizing microscopy, to prove. The soliton can also be distorted into a three-dimensional structure by tuning the electric field. In that case, the singular defect line transforms into a parabola in the x-z plane, which is analogous to the structure of FCDs [43] (Supplementary Figure 8-3). At fixed voltage U and frequency f, the solitons preserve their size during motion. By increasing U at fixed f, both the length (l) and width (w) of solitons decrease (Figure 8-3). Both l (Figure 8-3 (b)) and w (Figure 8-3 (c)) are determined from the image of the soliton taken between crossed polarizers (Figure 8-3 (a)), measured between the two points where the transmitted light intensity drops to 20% of the maximum.
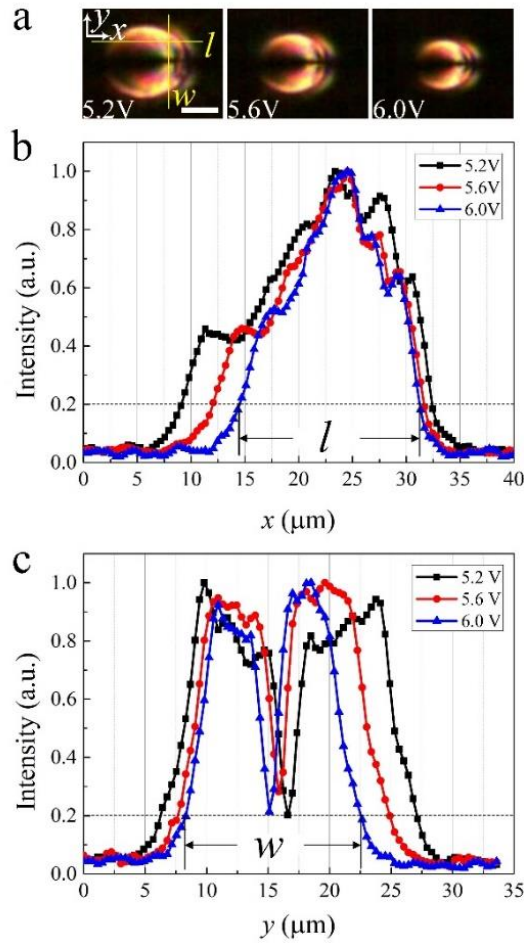
Figure 8-3 Dependence of soliton size on voltages. (a) Polarizing optical micrographs of a soliton at different applied voltages at frequency f = 1 kHz. The yellow lines intersect the soliton along the x- and y-axes indicate the length (l) and width (w) of the soliton. Transmitted light intensity profiles of the soliton measured as a function of (b) x-coordinate and (c) y-coordinate along the yellow lines in (a) at varied voltages. f = 1 kHz, T = 34.0 °C, scale bar 10 μm.

8.3.3 Dynamics of swallow-tail solitons

Figure 8-4 (a) shows the dynamic structure of a swallow-tail soliton. When driven by a low frequency voltage, the director **n** within the soliton tilts up and down relative to the x-y plane with a polar angle θ, leading to a periodic modulation of light transmission. The frequency of the oscillation of **n** is twice the frequency of the applied voltage indicating a dielectric effect. This also leads to a periodic shape transformation of the soliton of expansion, contraction and morphing during motion (Figure 8-4 (b)). It should be noted here that in order to obtain a better intensity variation curve profile, the AC field applied in (a) and (b) is a sinusoidal wave. Except for this point, the remaining investigations throughout the article were carried out with rectangular wave AC fields. Both the applied voltage and frequency control the speed of the solitons uniformly throughout the sample. In Figure 8-4 (c), it is

depicted that the speed of the solitons increases by increasing voltages at a fixed frequency. On the other hand, the speed gradually decreases as the frequency is increased. Such a decrease can be attributed to the motion of ions which depends on the external electric field and will be discussed in detail below.
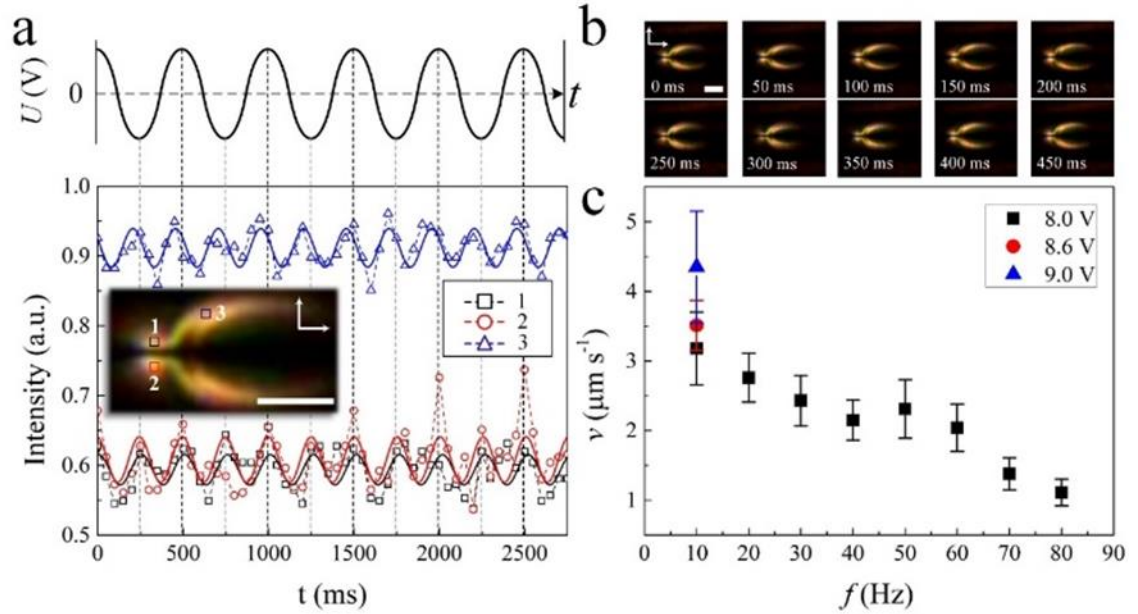
Figure 8-4 Dynamics of swallow-tail solitons. (a) Periodic oscillations of the transmitted light intensity at regions 1, 2 and 3 of a soliton (inset, scale bar 10 μm) driven by a sinusoidal wave AC voltage. $U = 7.6$ V, $f = 2$ Hz, $T = 34.8$ ℃. (b) Polarizing optical micrographs of a soliton driven by a sinusoidal wave AC voltage. $U = 7.6$ V, $f = 2$ Hz, $T = 34.8$ °C, scale bar 10 μm. The polarizers are indicated by crossed white arrows. (c) Dependence of the speed of solitons (v) on voltage (U) and frequency (f) of the applied rectangular wave AC field. The error bars are calculated from the standard deviation of velocities of hundreds of different solitons at the same electric field. $T = 34.0$ ℃.

Generally, the solitons move bidirectionally along the alignment direction (*x*-axis). However, they can also move in the *y*-axis direction in the form of edge dislocations by tuning the applied voltage. In Figure 8-5 (a), a soliton firstly moves in the *x*-axis direction. By increasing *U*, the soliton gradually shrinks and collapses into an edge dislocation (insets) which then moves along the *y*-axis. By slowly decreasing *U*, the edge dislocation transforms into a soliton (insets) again and moves in the *x*-axis direction (Supplementary Movie 8-2). It should be noted that this is not the case for all solitons, in fact some solitons annihilate during the increase of *U* while some dislocations never turn back to solitons by decreasing *U* (Supplementary Movie 8-3). As a result, the motion of the solitons can be actually switched from one spatial dimension to two spatial dimensions just by tuning the applied voltages. Figure 8-5 (b) shows the static optical textures of an edge dislocation that transforms from a soliton, which is made of a +1/2, -1/2 disclination pair. During the motion, the dislocation

oscillates from left to right periodically with the frequency of the applied voltage (Figure 8-5 (c), Supplementary Movie 8-4). Such a movement which is perpendicular to the Burgers vector **b** of the dislocation is called "climb" [44].
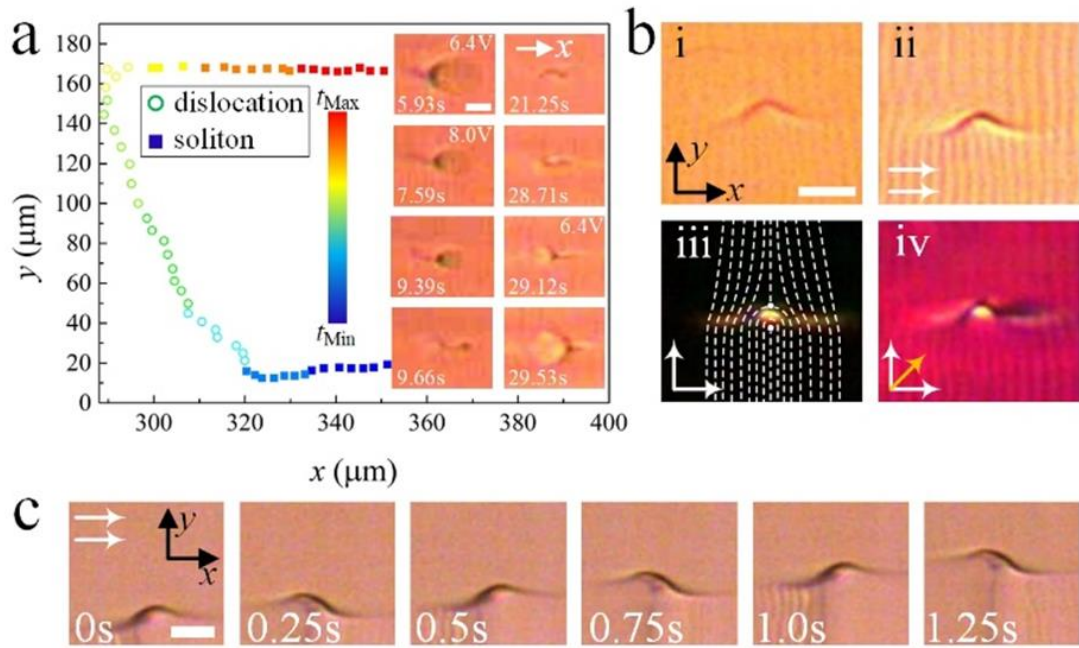
Figure 8-5 Reversible transformation from a swallow-tail soliton to an edge dislocation. (a) Trajectory of a moving soliton which transforms into an edge dislocation and back to a soliton. The insets show the evolution of the transformation (scale bar 10 μm). The voltage is changed between $U = 6.4$ V and $U = 8.0$ V. $f = 2$ Hz, $T = 34.6$ °C. (b) Optical micrographs of an edge dislocation transformed from a swallow-tail soliton (i) without polarizers, (ii) with parallel polarizers, (iii) with crossed polarizers (the white dashed lines indicate the SmA layers), (iv) with crossed polarizers and a λ-plate whose slow axis is orientated at 45 ° to the polarizers. $U = 6.6$ V, $f = 1$ kHz, $T = 34.6$ °C, scale bar 10 μm. (c) Optical micrographs of an edge dislocation moving along the y-axis. $U = 6.0$ V. $f = 2$ Hz, $T = 34.4$ °C, scale bar 10 μm. The direction of polarizers is indicated as white arrows.

It is observed that sometimes a moving soliton may split into two solitons with the other moving in the opposite direction (Supplementary Movie 8-5). Such a proliferation is also observed in the dynamics of nematic dissipative solitons [18] and may be attributed to the nonlinear coupling between the director field $\mathbf{n}(r)$ and hydrodynamic flows of ion motions (Figure 8-6 (a)). The solitons also continuously nucleate with an uncorrelated frequency at irregularities such as surface imperfections which can be clearly visible under the microscope due to the distortion of the director field $\mathbf{n}(r)$ around them (Figure 8-6 (b), Supplementary Movie 8-6). On the other hand, the solitons disappear once they get close to the edges of the ITO electrodes, which are parallel to the SmA layers (Figure 8-6 (c), Supplementary Movie 8-7). In contrast, edge dislocations are generated at the ITO electrodes which are perpendicular to the SmA layers, and move away from the electrodes along the y-axis (Figure 8-6 (d), Supplementary Movie 8-8). Furthermore, the solitons may even form

linear chains which move at a constant speed (Figure 8-6 (e) and (f), Supplementary Movie 8-9). This indicates that there may be some long-range attractions between individual solitons due to the deformation of SmA layers, which requires further investigations. At the same time, small-angle discontinuity walls [8] are formed due to the abrupt symmetry breaking transition induced by applying the electric field, along which long linear chains of solitons are moving forward (Figure 8-6 (g) and (h), Supplementary Movie 8-10).
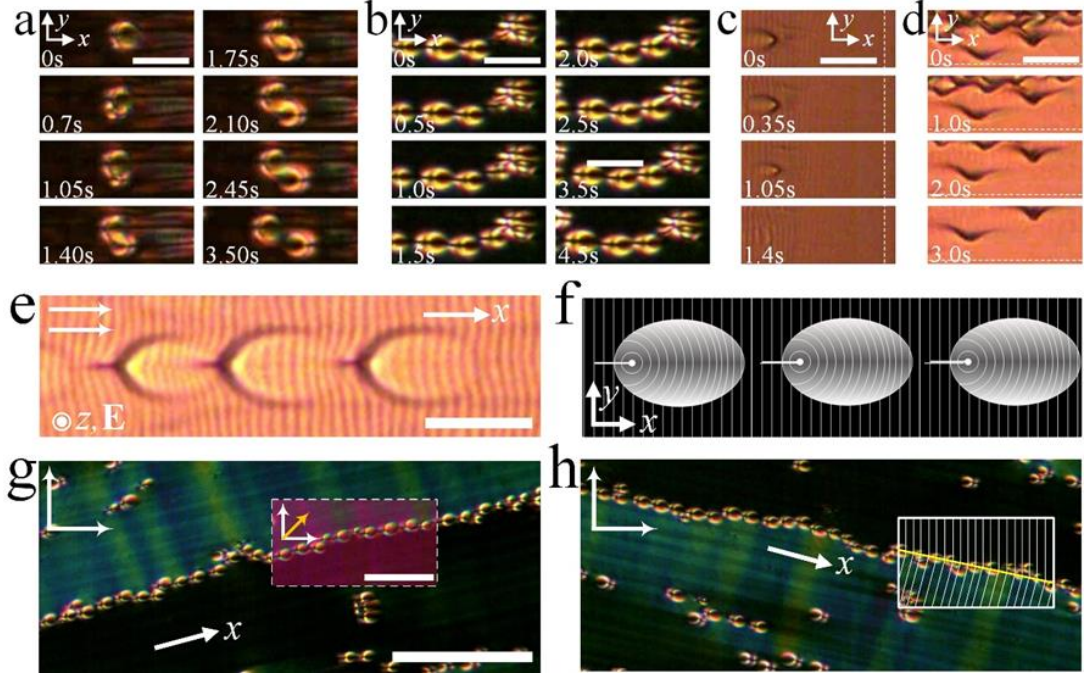
Figure 8-6 Various dynamic behaviors of swallow-tail solitons. (a) Proliferation of a soliton from a moving soliton. $U = 6.4$ V, $f = 2$ Hz, $T = 34.6$ °C, Scale bar 20 μm. (b) Nucleation of solitons from a surface irregularity. $U = 8.0$ V, $f = 20$ Hz, $T = 34.0$ °C, scale bar 20 μm. (c) Disappearance of a soliton at the ITO edge. $U = 6.8$ V, $f = 2$ Hz, $T = 34.1$ °C, scale bar 20 μm. (d) Emergence of edge dislocations at the ITO edge. $U = 6.8$ V, $f = 2$ Hz, $T = 34.1$ °C, scale bar 20 μm. (e) Micrograph of a dynamic linear soliton chain composed of three solitons. The polarizers are parallel to each other as indicated by the white arrows. $U = 6.6$ V, $f = 50$ Hz, $T = 34.6$ °C, scale bar 20 μm. (f) Schematic two-dimensional layer structure of the soliton chain in the x-y plane corresponding to (e). SmA layers are represented as equidistant white lines. (g) and (h) Micrographs of a linear chain of solitons moving on a discontinuity wall. The polarizers are crossed as represented by white arrows. $U = 8.0$ V, $f = 10$ Hz, $T = 34.0$ °C, Scale bar 100 μm. The inset in (g) shows the micrograph of the soliton chain obtained by inserting a compensator with its slow axis at an angle of 45 ° with the polarizers (scale bar 50 μm). The inset in (h) indicates the SmA layer (white lines) configuration in the proximity of the discontinuity wall (yellow line).

8.3.4 Interactions between swallow-tail solitons and colloidal micro-particles

Two swallow-tail solitons moving towards each other can collide during motion. Since the solitons are spatially two-dimensional in the x-y plane, the outcome of the collisions mostly depends on their relative locations in the plane. We define an impact parameter, Δ_y,

which is the distance between the cores of two solitons moving towards each other measured along the y-axis. When the offset, Δ_y, is much larger than the diameter of the core (singular defect line) of the solitons, R_c ($\Delta_y \gg R_c$), the two solitons pass through each other without noticeable perturbations and the offset, Δ_y, almost keeps constant after the collision (Figure 8-7 (a) and (b), Supplementary Movie 8-11). This behavior is due to the compatibility of the layer deformations along the y-axis of the two solitons in the overlapping zone (Figure 8-7 (e) i, iii, iv). On the other hand, solitons that collide head-on, i.e. where $\Delta_y \leq R_c$, behave like hard-body particles that they cannot pass through each other directly. They push against each other along the x-axis and repulse each other into opposite directions along the y-axis, and then pass through each other once $\Delta_y \gg R_c$. The offset, Δ_y, greatly increases after the collision (Figure 8-7 (c) and (d), Supplementary Movie 8-12). We attribute such a behavior to the repulsive force between the two singular defect lines with the same sign. Figure 8-7 (e) ii, iii and iv illustrate the process of the head-on collision schematically. In both cases after the collisions, the solitons recover their structures and constant speeds, which may be slightly different from the pre-collision speeds (Figure 8-7 (a) to (d)).
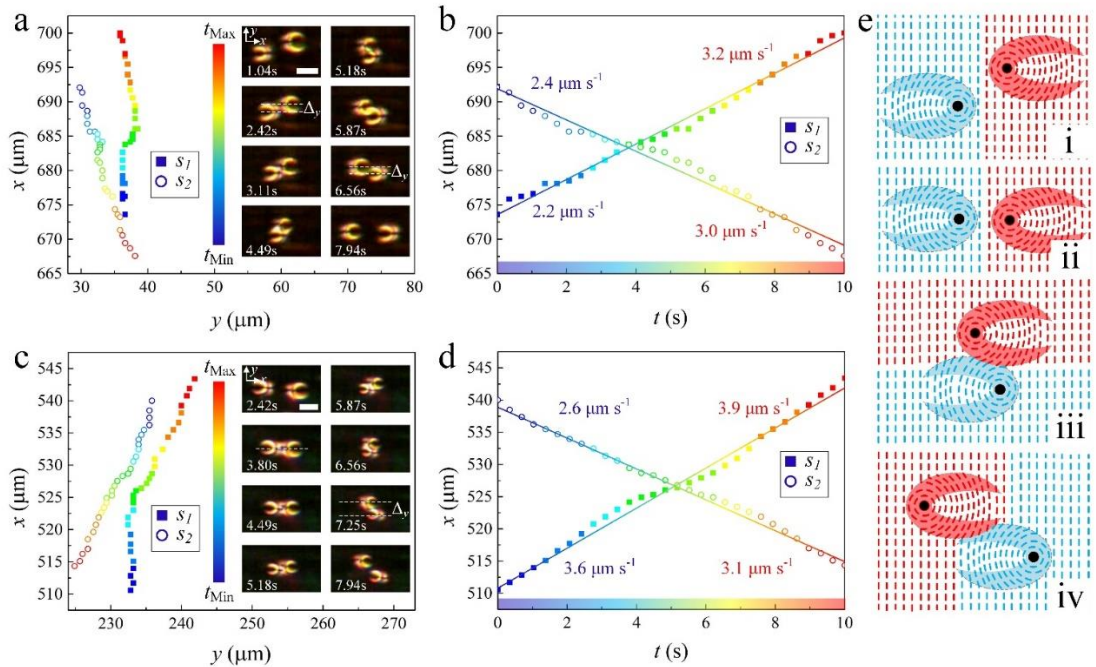
Figure 8-7 Dynamic interactions between two swallow-tail solitons. (a) and (c) Trajectories of two solitons colliding with each other. The color bar represents the elapsed time. $t_{Min} = 0$ s, $t_{Max} = 10$ s, time interval $\Delta t = 0.345$ s. Insets are time series of polarizing micrographs of the solitons during the collisions, scale bars 10 μm. (b) and (d) The corresponding time dependences of the x-coordinates of the pairs of solitons corresponding to (a) and (c), respectively. (a) and (b) $U = 5.6$ V, $f = 2$ Hz, $T = 34.8$ ℃; (c) and (d) $U = 8.0$ V, $f = 10$ Hz, $T = 34.0$ ℃. (e) Schematic layer configurations of the solitons in the collisions. i, iii and iv show the time development of two solitons pass through each other ($\Delta_y \gg R_c$) corresponding to (a) and (b); ii, iii and iv show the time development of two solitons collide head-on ($\Delta_y \leq R_c$) corresponding to (c) and (d). The blue and red dashed lines represent the SmA layers.

A swallow-tail soliton can also interact with colloidal micro-particles. In Figure 8-8 (a), a soliton moves towards an immobile micro-particle, and then suddenly sticks to the particle. The soliton cannot move forward any longer and its defect core is trapped by the particle (Supplementary Movie 8-13). However, in Figure 8-8 (b), when a soliton hits an immobile micro-particle, it is repelled by the particle along the *x*-axis and pushed away from it in the *y*-direction, before it can subsequently pass the particle (Supplementary Movie 8-14). This process is very similar to the head-on collision of two solitons described above. The micro-particles can even act as seeds for the nucleation of solitons, from which solitons are generated continuously. This looks similar to the nucleation of solitons at surface imperfections described above, however, the processes of the nucleation in these two cases are quite different. In the first case, an intact soliton is formed and released directly from a surface imperfection (Figure 8-6 (b), Supplementary Movie 8-5). In the case of a micro-particle, the deformation of the SmA layers around the particle gradually grows into a soliton. Once the soliton is matured, it moves away from the particle and a new soliton starts growing at the particle (Figure 8-9, Supplementary Movie 8-15).

8.4 Discussion

Three dimensional particle-like dissipative solitons were recently discovered in nematic LCs [17-19], which have attracted increasing attention due to their exotic nonlinear dynamic behaviors and their potential applications in microfluidic systems. They preserve their shape during motions over long distances and after collisions, which is very similar to the swallow-tail solitons described here. The solitons in nematics are propagating solitary waves of director deformations and are thus topologically nontrivial and equivalent to the uniform state. In contrast, the swallow-tail solitons are characterized by a layered multi-dimensional structure and contain a singular defect line inside, which is topologically analogous to the structure of FCDs.
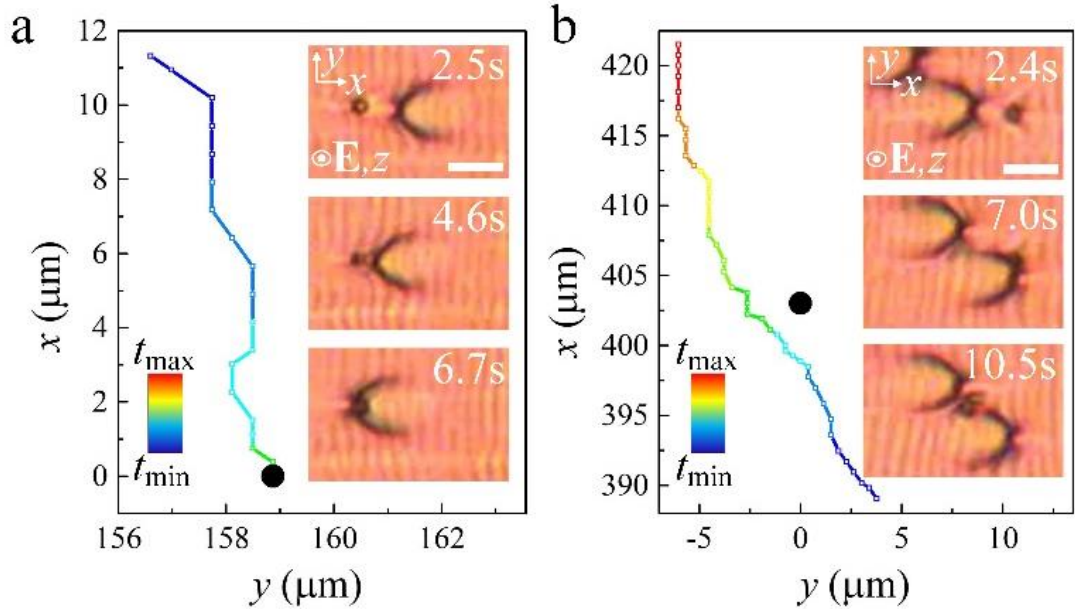
Figure 8-8 Dynamic interactions between swallow-tail solitons and colloidal micro-particles. (a) Trajectory of a soliton moving toward a micro-particle (black solid circle) and sticking to it. (b) The trajectory of a soliton which collides with a micro-particle (black solid circle) and moves away from the particle. The color bars in (a) and (b) represent the elapsed time. $t_{Min} = 0$ s, $t_{Max} = 15$ s, time interval $\Delta t = 0.345$ s. Insets in (a) and (b) are time series of optical micrographs of the solitons during the collisions with the micro-particles. $U = 5.4$ V, $f = 10$ Hz, $T = 34.4$ °C, scale bars 10 μm, micro-particle diameter $R_P = 3.0$ μm.

The FCDs are actually prototypes of the swallow-tail solitons, from which the solitons are transformed (Figure 8-1 (a)). In Supplementary Figure 8-4, it is observed that by applying a low-frequency voltage to the scattering state, the fore-aft symmetry of the tightly packed FCDs is broken by fluid flow and they start floating locally and colliding with each other, forming the solitons. Some of the solitons are annihilated during the motion and collisions. Within several seconds, the structure becomes holey and the solitons begin to move bidirectionally perpendicular to the SmA layers with constant speed (Supplementary Movie 8-16). There are several factors that can induce the motion of solitons, which are 1) hydrodynamic flows of ions, 2) backflows produced by the rotational dynamics of the director, and 3) the periodic expanding and contracting of the director structure of the solitons. However, the influence of ions can be suppressed by applying a high-frequency ($f = 5$ kHz) voltage to the scattering state, which is simultaneously modulated with a lower modulation frequency ($f_m = 10$ Hz). In this case, a periodic array of solitons is obtained (Supplementary Figure 8-5). Despite the fact that the director field oscillates with the frequency of the electric field due to the dielectric interaction, as well as the solitons expanding and contracting periodically with the modulation frequency f_m, the solitons do not move at all. This implies that the ionic motion plays an important role in the motion of the

215

solitons. Such an assumption can be further evidenced by the frequency dependence of the soliton speed, which decreases with increasing frequency. The solitons move at frequencies lower than 100 Hz. This region can be related to the so-called "conductivity regime" limited from above by the critical frequency $f_c = \tau_\sigma^{-1}(\xi^2 - 1)^{1/2}$ which is used to describe electro-hydrodynamic effects in nematic LCs [8,45]. Here $\tau_\sigma = 4\pi\varepsilon_0\varepsilon_\perp\sigma_\perp^{-1}$ is the space charge relaxation time for a homogeneous cell [20], $\varepsilon_0 = 8.85 \times 10^{-12}$ Fm^{-1} and ξ is a dimensionless parameter depending on the permittivities, conductivities, and the viscosities of the LC system. By applying the experimental data measured at $f = 100$ Hz and $T = 34.0$ °C for 8CB (Supplementary Figure 8-2), we obtain $\tau_\sigma^{-1} \sim 1$ kHz. The factor ξ is hard to determine since the viscosities of 8CB are unknown. If we assume that $(\xi^2 - 1)^{1/2}$ is of the order of 1 [46], we get $f_c \sim 1$ kHz. This indicates that the swallow-tail solitons move at frequencies below 100 Hz, corresponding to the conductivity regime in which ions move slowly under an external electric field.
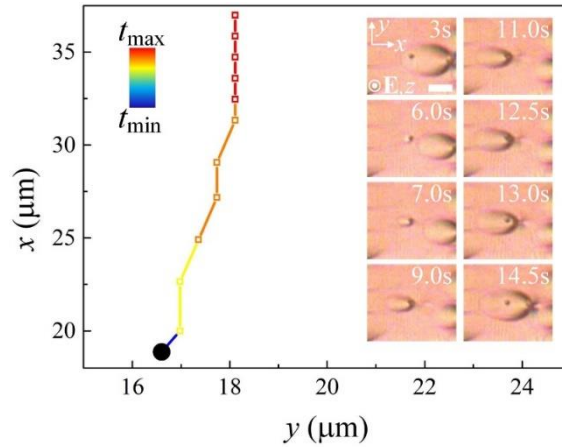
Figure 8-9 Trajectory of a swallow-tail soliton nucleated from a micro-particle. The color bar represents the elapsed time. $t_{Min} = 0$ s, $t_{Max} = 17.5$ s, time interval $\Delta t = 0.5$ s. Insets are time series of micrographs of the nucleation of a soliton at a micro-particle. $U = 7.6$ V, $f = 10$ Hz, $T = 33.5$ °C, scale bar 10 μm, micro-particle diameter $R_P = 1.5$ μm.

An ideal smectic A phase is characterized by the $D_{\infty h}$ symmetry and can be viewed as a two-dimensional fluid in planes that are parallel to the horizontal symmetry plane σ_h, or as a one-dimensional solid along the infinite rotation axis C_∞. As a result, there is an additional potential barrier W for molecules penetrating SmA layers. One typical evidence of the existence of such a barrier is the transport of micro-particles. Those move along the director in nematics [47-49], but move parallel to the layers in smectics [50,51], which indicates the larger diffusion constants within SmA layers. However, in our experiment, the solitons always move perpendicular to the SmA layers. Due to the extremely large compressibility modulus

B, the interlayer distance of SmA is almost rigidly fixed. As a result, within the swallow-tail solitons, to minimize the cost of the free energy, the elastic distortion of the SmA layers is in the form of curvature along the *y*-axis. This leads to a fore-aft symmetry breaking structure, i.e. the solitons are mirror-symmetric about the *x*-axis and lack mirror-symmetry about the *y*-axis. Such a symmetry breaking structure enables the solitons to move perpendicular to the SmA layers. Furthermore, the temperature *T* of our sample is very close to the nematic-smectic phase transition temperature $T_{\text{N-S}}$ (in most cases, $T_{\text{N-S}} - T \leq 1.0$ °C). Since the transition is of very weak first order (close to second order) [20], it can be presumed that the layer structure of the SmA phase is not very pronounced and the potential barrier *W* is relatively small at such a high temperature. This leads to a relatively pronounced permeation flow along the *x*-axis (normal to the smectic layers). In brief, the fore-aft symmetry breaking structure of the solitons determines the moving direction of the solitons and the relatively large permeation flow drives the solitons move along the *x*-axis. It is found that the motion of solitons keeps slowing down by decreasing the temperature and eventually stops when $T_{\text{N-S}} - T \sim 3.0$ °C (Supplementary Movie 8-17). This is because with decreasing temperature, the layer structure becomes more pronounced and the potential barrier *W* increases, thus leading to the decrease of the permeation flow.

The swallow-tail solitons always move along the alignment direction, which implies that one can control their motion by manipulating the alignment pattern. For instance, the photo-alignment technique is known for its flexibility and high resolution in this respect, which has been broadly applied for realizing various LC devices such as holographic gratings [52,53], terahertz microlenses [54], optical vortex processors [55], etc. Various complex two-dimensional motions of solitons can thus be realized by the photo-alignment technique, which can be utilized for realizing targeted delivery of optical information. It is also well known that the regions of molecular misalignment, such as defect cores, are energetically disfavored in LCs. Embedding particles within the cores can replace part of the energetically costly region with the particles, thus reducing the overall energy of the LC system [9,56,57]. Due to this property, FCDs have been broadly utilized as lithography templates for the self-assembly of micro-/nano-materials due to the existence of singular defect lines [27,58]. In the same way, our solitons can also be used for particle trapping and transport, and realization of various microfluidic applications by combining with the photo-alignment technique.

8.5 Conclusion

To conclude, electrically powered multi-dimensional swallow-tail solitons in the form of travelling SmA layer deformations embedded with defect cores are produced in a smectic A liquid crystal. The formation and structure of these solitons are closely related to FCDs and their dynamics are attributed to the electro-hydrodynamic fluid flows induced by ion motions. The easy generation and manipulation of the particle-like solitons and their rich nonlinear dynamic behavior should not only open the door to a broad range of theoretical studies but also pave new avenues for versatile dynamic soliton systems with potential applications in optics and microfluidics.

8.6 Acknowledgements

8.7 References

1   Scott, A. C., Chu, F. Y. F. & McLaughlin, D. W. The soliton: A new concept in applied science. *Proceedings of the IEEE* **61**, 1443-1483 (1973).
2   Zabusky, N. J. & Kruskal, M. D. Interaction of "Solitons" in a Collisionless Plasma and the Recurrence of Initial States. *Physical Review Letters* **15**, 240-243 (1965).
3   Dauxois, T. & Peyrard, M. *Physics of solitons*. (Cambridge University Press, 2006).
4   Kartashov, Y. V., Astrakharchik, G. E., Malomed, B. A. & Torner, L. Frontiers in multidimensional self-trapping of nonlinear fields and matter. *Nature Reviews Physics* **1**, 185-197 (2019).
5   Yu, X. *et al.* Real-space observation of a two-dimensional skyrmion crystal. *Nature* **465**, 901-904 (2010).
6   Kralj, M., Kralj, M. & Kralj, S. Topological Defects in Nematic Liquid Crystals: Laboratory of Fundamental Physics. *physica status solidi (a)* **218**, 2000752 (2021).
7   Lam, L. & Prost, J. *Solitons in liquid crystals*.   (Springer Science & Business Media, 2012).
8   De Gennes, P.-G. & Prost, J. *The physics of liquid crystals (2nd Edition)*. Vol. 83 (Oxford university press, 1993).
9   Shen, Y. & Dierking, I. Perspectives in Liquid-Crystal-Aided Nanotechnology and Nanoscience. *Applied Sciences* **9**, 2512 (2019).
10   Helfrich, W. Alignment-Inversion Walls in Nematic Liquid Crystals in the Presence of a Magnetic Field. *Physical Review Letters* **21**, 1518-1521 (1968).
11   Leger, L. Observation of wall motions in nematics. *Solid State Communications* **10**,

697-700 (1972).

12   Guozhen, Z. Experiments on Director Waves in Nematic Liquid Crystals. *Physical Review Letters* **49**, 1332-1335 (1982).

13   Lei, L., Changqing, S., Juelian, S., Lam, P. M. & Yun, H. Soliton Propagation in Liquid Crystals. *Physical Review Letters* **49**, 1335-1338 (1982).

14   Peccianti, M. & Assanto, G. Nematicons. *Physics Reports* **516**, 147-208 (2012).

15   Shen, Y. & Dierking, I. Electrically Driven Formation and Dynamics of Skyrmionic Solitons in Chiral Nematics. *Physical Review Applied* **15**, 054023 (2021).

16   Smalyukh, I. I. knots and other new topological effects in liquid crystals and colloids. *Reports on Progress in Physics* **83**, 106601 (2020).

17   Li, B.-X. *et al.* Electrically driven three-dimensional solitary waves as director bullets in nematic liquid crystals. *Nature Communications* **9**, 2912 (2018).

18   Shen, Y. & Dierking, I. Dynamics of electrically driven solitons in nematic and cholesteric liquid crystals. *Communications Physics* **3**, 1 (2020).

19   Shen, Y. & Dierking, I. Dynamic dissipative solitons in nematics with positive anisotropies. *Soft Matter* **16**, 5325 (2020).

20   Blinov, L. M. *Structure and properties of liquid crystals*. Vol. 123 (Springer Science & Business Media, 2010).

21   de Gennes, P. G. An analogy between superconductors and smectics A. *Solid State Communications* **10**, 753-756 (1972).

22   Liarte, D. B. *et al.* Visualization, coarsening, and flow dynamics of focal conic domains in simulated smectic-A liquid crystals. *Physical Review E* **92**, 062511 (2015).

23   Kleman, M. & Laverntovich, O. D. *Soft matter physics: an introduction*. (Springer Science & Business Media, 2007).

24   Friedel, G. & Grandjean, F. Observations géométriques sur les liquides à coniques focales. *Bulletin de Minéralogie* **33**, 409-465 (1910).

25   Bouligand, Y. Recherches sur les textures des états mésomorphes-1. Les arrangements focaux dans les smectiques: rappels et considérations théoriques. *Journal de Physique* **33**, 525-547 (1972).

26   Fournier, J. & Durand, G. Focal conic faceting in smectic-A liquid crystals. *Journal de Physique II* **1**, 845-870 (1991).

27   Yoon, D. K. *et al.* Internal structure visualization and lithographic use of periodic toroidal holes in liquid crystals. *Nature Materials* **6**, 866 (2007).

28   Kim, Y. H., Yoon, D. K., Jeong, H. S. & Jung, H.-T. Self-assembled periodic liquid crystal defects array for soft lithographic template. *Soft Matter* **6**, 1426-1431 (2010).

29   Kim, Y. H. *et al.* Fabrication of two-dimensional dimple and conical microlens arrays from a highly periodic toroidal-shaped liquid crystal defect array. *Journal of Materials Chemistry* **20**, 6557-6561 (2010).

30   Kim, Y. H. *et al.* Optically Selective Microlens Photomasks Using Self-Assembled Smectic Liquid Crystal Defect Arrays. *Advanced Materials* **22**, 2416-2420 (2010).

31   Kleman, M. & Friedel, J. Disclinations, dislocations, and continuous defects: A reappraisal. *Reviews of Modern Physics* **80**, 61 (2008).

32   Goodman, A. M. Optical interference method for the approximate determination of refractive index and thickness of a transparent layer. *Appl. Opt.* **17**, 2779-2787 (1978).

33   Rapini, A. Instabilités magnétiques d'un smectique C. *Journal de Physique* **33**, 237-

247 (1972).

34   Hareng, M., Le Berre, S. & Metzger, J. Planar-to-homeotropic structure transition under electric field in an A-phase smectic. *Applied Physics Letters* **27**, 575-576 (1975).

35   Li, Z. & Lavrentovich, O. D. Surface anchoring and growth pattern of the field-driven first-order transition in a smectic-A liquid crystal. *Physical review letters* **73**, 280 (1994).

36   Jákli, A. & Saupe, A. Electro-optic effects in smectic A phase. *Molecular Crystals and Liquid Crystals Science and Technology. Section A. Molecular Crystals and Liquid Crystals* **222**, 101-109 (1992).

37   Findon, A., Gleeson, H. & Lydon, J. Realignment of a smectic-A phase with applied electric field. *Physical Review E* **62**, 5137 (2000).

38   Coates, D., Crossland, W., Morrisy, J. & Needham, B. Electrically induced scattering textures in smectic A phases and their electrical reversal. *Journal of Physics D: Applied Physics* **11**, 2025 (1978).

39   Nawa, N. & Nuo, D. Light-scattering characteristics in smectic A liquid crystals. *Japanese journal of applied physics* **30**, 1038 (1991).

40   Steers, M. & Mircea-Roussel, A. A NOVEL ELECTRO-OPTIC STORAGE MODE IN SMECTIC A LIQUID CRYSTALS. *Le Journal de Physique Colloques* **37**, C3-145-C143-148 (1976).

41   Rosenblatt, C. S., Pindak, R., Clark, N. & Meyer, R. The parabolic focal conic: a new smectic a defect. *Journal de physique* **38**, 1105-1115 (1977).

42   Demus, D. *Textures of liquid crystals*. (John Wiley & Sons, 1979).

43   Asher, S. & Pershan, P. S. Parabolic focal conics and polygonal textures in lipid liquid crystals. *Journal de Physique* **40**, 161-173 (1979).

44   Chaikin, P. M., Lubensky, T. C. & Witten, T. A. *Principles of condensed matter physics*. Vol. 10 (Cambridge university press Cambridge, 1995).

45   Blinov, L. M. & Chigrinov, V. G. *Electrooptic effects in liquid crystal materials*. (Springer Science & Business Media, 1996).

46   Li, B.-X., Xiao, R.-L., Paladugu, S., Shiyanovskii, S. V. & Lavrentovich, O. D. Three-dimensional solitary waves with electrically tunable direction of propagation in nematics. *Nature Communications* **10**, 3749 (2019).

47   Dierking, I., Biddulph, G. & Matthews, K. Electromigration of microspheres in nematic liquid crystals. *Physical Review E* **73**, 011702 (2006).

48   Pishnyak, O. P., Tang, S., Kelly, J. R., Shiyanovskii, S. V. & Lavrentovich, O. D. Levitation, Lift, and Bidirectional Motion of Colloidal Particles in an Electrically Driven Nematic Liquid Crystal. *Physical Review Letters* **99**, 127802 (2007).

49   Lavrentovich, O. D., Lazo, I. & Pishnyak, O. P. Nonlinear electrophoresis of dielectric and metal spheres in a nematic liquid crystal. *Nature* **467**, 947 (2010).

50   Togo, T., Nakayama, K., Ozaki, M. & Yoshino, K. Electric Field-Induced Migration of SiO 2 Particles in Smectic Liquid Crystal. *Japanese Journal of Applied Physics* **36**, L1520-L1522 (1997).

51   Dierking, I., Cass, P., Syres, K., Cresswell, R. & Morton, S. Electromigration of microspheres in ferroelectric smectic liquid crystals. *Physical Review E* **76**, 021707 (2007).

52   Li, S.-S. *et al.* Dynamic cholesteric liquid crystal superstructures photoaligned by

one-step polarization holography. *Applied Physics Letters* **111**, 231109 (2017).

53   Shen, Y. *et al.* Photoalignment of dye-doped cholesteric liquid crystals for electrically tunable patterns with fingerprint textures. *Opt. Express* **26**, 1422-1432 (2018).

54   Shen, Z. *et al.* Liquid crystal tunable terahertz lens with spin-selected focusing property. *Opt. Express* **27**, 8800-8807 (2019).

55   Chen, P. *et al.* Digitalizing self-assembled chiral superstructures for optical vortex processing. *Advanced Materials* **30**, 1705865 (2018).

56   Shen, Y. & Dierking, I. Annihilation dynamics of topological defects induced by microparticles in nematic liquid crystals. *Soft Matter* **15**, 8749 (2019).

57   Ravnik, M., Alexander, G. P., Yeomans, J. M. & Žumer, S. Three-dimensional colloidal crystals in liquid crystalline blue phases. *Proceedings of the National Academy of Sciences* **108**, 5188 (2011).

58   Kim, Y. H., Yoon, D. K., Jeong, H. S., Lavrentovich, O. D. & Jung, H.-T. Smectic Liquid Crystal Defects for Self-Assembling of Building Blocks and Their Lithographic Applications. *Advanced Functional Materials* **21**, 610-627 (2011).

8.8 Supplementary Information

8.8.1 Supplementary Figures:
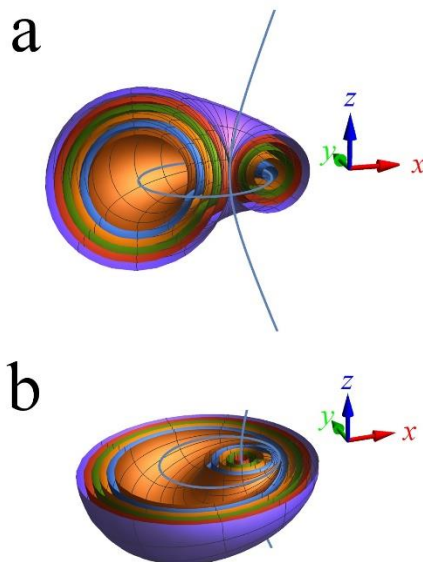
Supplementary Figure 8-1 A stack of three-dimensional Dupin cyclides cut along (a) the *xz* plane and (b) the *xy* plane. The blue lines depict the ellipse and the confocal hyperbola.
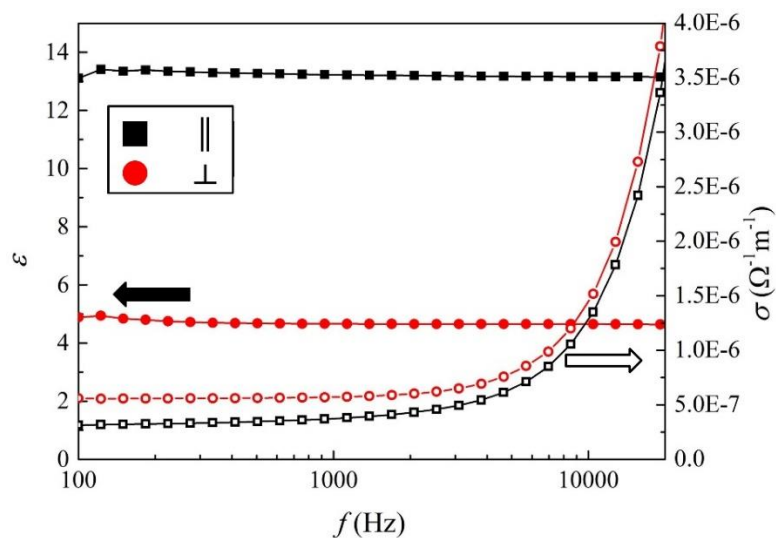
Supplementary Figure 8-2 Frequency dependence of dielectric permittivities (solid symbols) and conductivities (hollow symbols) of 8CB at $T = 34.0$ °C, $U = 0.1$ V.
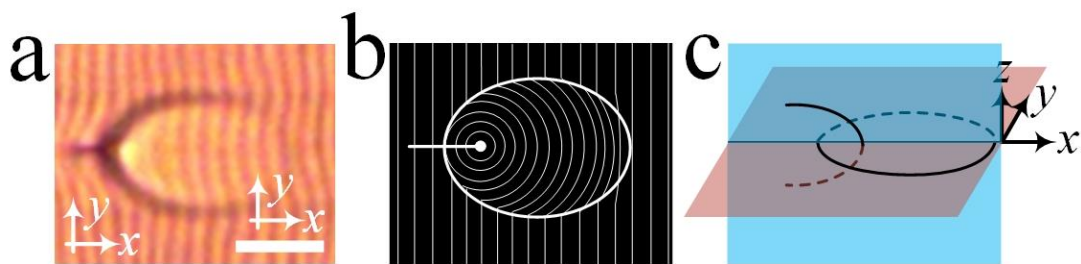
Supplementary Figure 8-3 Schematic structure of three-dimensional swallow-tail soliton. (a) Optical micrograph of a soliton at U = 6.6 V, f = 50 Hz, T = 34.6 °C, scale bar 10 μm. (b) Two-dimensional schematic structure of the soliton in the x-y plane. (c) Three-dimensional schematic locus of the cusps of the soliton.
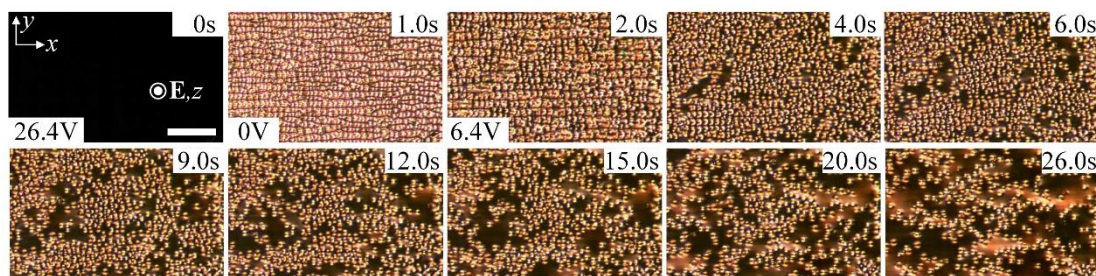
Supplementary Figure 8-4 Time series of micrographs of the dynamic transformation of the swallow-tail solitons from the focal conic domains in the scattering state. U changes from 26.4 V to 0 V to 6.4 V, f = 10 Hz, T = 34.2 °C, scale bar 50 μm.
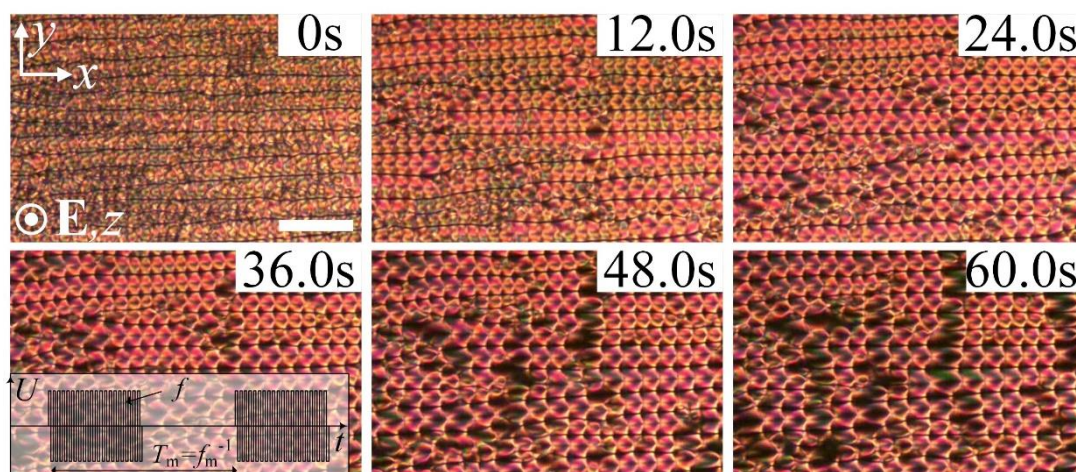
Supplementary Figure 8-5 Time series of micrographs of the dynamic transformation of the scattering state to the periodic soliton array. U = 7.0 V, f = 5 kHz, f_m = 10 Hz, T = 34.6 °C.

8.8.2 Supplementary Movies:

File Name: Supplementary Movie 8-1

Description: swallow-tail solitons move along the x-axis with a constant speed. U = 6.0 V, f = 2.0 Hz, T = 34.8 °C.

File Name: Supplementary Movie 8-2

Description: Dynamic transformation of a swallow-tail soliton into an edge dislocation and back to a soliton. The voltage is changed between U = 6.4 V and U = 8.0 V, f = 2 Hz, T = 34.6 °C.

File Name: Supplementary Movie 8-3
Description: Dynamic transformation of swallow-tail solitons into edge dislocations. The voltage is gradually increased from $U = 5.6$ V to $U = 7.2$ V, and then decreased back to $U = 5.6$ V. $f = 10$ Hz, $T = 34.6$ °C.

File Name: Supplementary Movie 8-4
Description: Dynamic motion of edge dislocations. $U = 6.0$ V, $f = 2$ Hz, $T = 34.4$ °C.

File Name: Supplementary Movie 8-5
Description: A swallow-tail soliton splits into two solitons. $U = 6.4$ V, $f = 2$ Hz, $T = 34.6$ °C.

File Name: Supplementary Movie 8-6
Description: Nucleation of swallow-tail solitons at a surface imperfection. $U = 8.0$ V, $f = 20$ Hz, $T = 34.0$ °C.

File Name: Supplementary Movie 8-7
Description: Disappearance of swallow-tail solitons at the ITO electrode. $U = 6.8$ V, $f = 2$ Hz, $T = 34.1$ °C.

File Name: Supplementary Movie 8-8
Description: Emergence of edge dislocations at the ITO electrode. $U = 6.8$ V, $f = 2$ Hz, $T = 34.1$ °C.

File Name: Supplementary Movie 8-9
Description: A chain of three swallow-tail solitons moving at a constant velocity. $U = 6.6$ V, $f = 50$ Hz, $T = 34.6$ °C.

File Name: Supplementary Movie 8-10
Description: Linear chains of swallow-tail solitons moving on discontinuity walls. $U = 8.0$ V, $f = 10$ Hz, $T = 34.0$ °C.

File Name: Supplementary Movie 8-11
Description: Two swallow-tail solitons collide and pass through each other. $U = 5.6$ V, $f = 2$ Hz, $T = 34.8$ °C.

File Name: Supplementary Movie 8-12
Description: Two swallow-tail solitons collide head-on. $U = 8.0$ V, $f = 10$ Hz, $T = 34.0$ °C.

File Name: Supplementary Movie 8-13
Description: A swallow-tail soliton collides with a micro-particle ($R_P = 3.0$ μm) and sticks to it. $U = 5.4$ V, $f = 10$ Hz, $T = 34.4$ °C.

File Name: Supplementary Movie 8-14
Description: A swallow-tail soliton collides with a micro-particle ($R_P = 3.0$ μm) and moves away from it. $U = 5.4$ V, $f = 10$ Hz, $T = 34.4$ °C.

File Name: Supplementary Movie 8-15
Description: Nucleation of swallow-tail solitons on a micro-particle ($R_P = 1.5$ μm). $U = 7.6$ V, $f = 10$ Hz, $T = 33.5$ °C.

File Name: Supplementary Movie 8-16
Description: Transformation of dynamic swallow-tail solitons from scattering state. Voltage is changed from $U = 26.4$ V to $U = 0$ V and then to $U = 6.4$ V, $f = 10$ Hz.

File Name: Supplementary Movie 8-17
Description: Dynamics of swallow-tail solitons at low temperatures. $U = 18.0$ V, $f = 10$ Hz.

Chapter 9

Conclusion and Outlook

9.1 Conclusion

Solitons are fantastic physical objects in the sense that they emerge as localized physical field configurations but behave like particles. Unlike any other solid particles, solitons are composed of the same component as the background physical system, and are due to the distortion of the field orientation. As a result, they can continuously transform their structure and dynamic behavior corresponding to different external stimuli. Liquid Crystals (LCs) as typical nonlinear systems not only provide an ideal testbed for fundamental investigations of solitons, but also serve as a versatile model for the exploration of different kinds of solitons in other physical systems.

The aim of this thesis is to explore the possibility of generating different kinds of solitons in LC systems and then better understand the physical properties of LCs and solitons in other physical systems by investigating the formation, structure and dynamic behavior of the solitons in LC systems. We successfully generated different kinds of solitons in different LC systems simply by applying electric fields and characterized the physical properties of the solitons through polarizing optical microscopes.

In chapter 2, dynamic 3D dissipative solitary waves, i.e., directrons, are generated in a nematic LC system with a negative dielectric anisotropy and then compared with the ones in a chiral nematic LC (CNLC) system by doping a small amount of chiral dopant into the achiral system. We investigate the formation, structure, interaction and dynamics of the directrons in both chiral and achiral systems. We find that the directrons in the achiral nematic system pass through each other in collisions. On the other hand, the directrons in the chiral nematic system can either pass through each other in collisions or collide and reflect into opposite directions. Both kinds of directrons can move either parallel or perpendicular to the surface alignment direction depending on the applied electric field. We also show that the motion of the directrons can be manipulated by patterned surface

alignment and the directrons can be used as vehicles for micro-cargo transport.

Then in chapter 3, by decreasing the pitch of the chiral nematic system, we show that the directrons interact with each other like particles that they repel each other at short ranges but attract each other at long ranges. The directrons move in random directions independent of the surface alignment condition. We show that by increasing the applied voltage, millions of directrons are generated randomly throughout the sample. They first move in random directions but soon synchronize their motion and self-organize into flocks and swarms. The directrons exhibit rich dynamic behaviors and exhibit "turbulent" swimming patterns that manifest as transient vortices and jets. They even distinguish topological defects, heading towards defects of positive topological strength and avoiding negative ones.

In chapter 4, we show that at high population density, the directrons in chapter 3 first show a disordered liquid phase but soon self-organize into a 2D hexagonal lattice through motion and collision. By characterizing the radial distribution function and the hexatic bond orientational correlation function of the directron lattice, we demonstrate that the lattice is in the hexatic phase. By increasing the applied voltage, the directrons starts moving randomly and the directron lattice exhibits a first-order hexatic-to-liquid phase transition.

The directrons show very interesting dynamic behavior and provide potential applications in optical information and micro-cargo transport. However, their generation requires strict requirement of the LC materials, which have to have a negative dielectric anisotropy and a negative or a small positive conductivity anisotropy. Such a requirement limits the experimental investigation and applications of the directrons. This also makes us curious if the directrons can be generated in those broadly used LC systems. In chapter 5, we show that similar dissipative solitons can also be generated in LC systems whose dielectric anisotropy and conductivity anisotropy are both positive, such as E7 and 5CB which are the most broadly used nematic LCs in labs and in industry. The solitons show similar structure and dynamic behavior to the directrons. However, their formation mechanisms are different. Unlike the directrons which are generated due to the localization of space charge and flexoelectric effect, the solitons here are generated due to the nonlinear coupling between the isotropic ion flow and the director field.

In chapter 6, we then switch our attention from the dissipative solitons to the topological solitons. Normally, topological solitons can be generated by confining CNLCs with

homeotropic anchoring surfaces due to the incompaticity between the homeotropic anchoring and the helical twisting structure of the CNLCs. Here, we show that they can also be generated in cells with homogeneous alignment by applying electric field. By tuning the electric field, the solitons can move bidirectionally perpendicular to the alignment direction at varied speeds. We investigate the formation and dynamics of the solitons in systems of different pitches. We also show that the topological solitons can also be utilized as vehicles for micro-cargo transport and can collide with each other like particles and form clusters with tunable shape, anisotropy and fractal dimension.

LCs are sensitive to external stimuli such as magnetic or electric fields and temperature. Some CNLCs can even change their pitches by tuning the temperature. In chapter 7, we investigate the dependence of the structure of topological solitons on the pitch of the CNLC system by generating torons in a temperature sensitive CNLC system. The CNLC changes its pitch greatly but continuously by tuning the temperature of the system. We find that the torons are very well topologically protected and can be reversibly transformed between torons and cholesteric fingers.

So far, most dynamic solitons are only generated in nematic LCs. We then became very curious to see if they could also be generated in other LC phases. In chapter 8, we show that particle-like dynamic solitons can be generated in a smectic A LC system. These solitons are transformed from focal conic domains with a static structure topologically analogous to the focal conic domains. They exhibit a swallow-tail-like structure under the polarizing optical microscope. They lack fore-aft symmetry and can be driven into motion perpendicular to the smectic layers through application of electric fields. They collide with each other and interact with colloidal micro-particles when in motion.

Solitons are not only fundamentally interesting to basic science but are also of great importance in various applications such as microfluidic and electro/magneto-optic devices. Understanding the physical properties of different kinds of solitons will be helpful not only to better understand the world, but also in realizing various advanced scientific techniques.

9.2 Outlook

So far, the experimental investigation of solitons in LC systems has been mainly concentrated on the nematic phase only. We found that particle-like dynamic solitons can also be generaged in smectic A LCs. This result may give the indication that similar phenomena can also be generated in other LC phases such as the ferroelectric nematic phase which was experimentally realized recently and has already received great attention [1]. The investigation of topological solitons, such as skyrmions, in those ferroelectric nematic systems will be very interesting due to the similarity of the ferroelectric nematic systems and magnetic systems, which may provide new insights into the development of racetrack memory and spintronic devices. On the other hand, the investigation of solitons in lyotropic LC systems is still limited so far. Recently, toron like director configurations were observed in a cholesteric lyotropic chromonic LC system [2] which may pave the way for the future investigations of solitons in lyotropic LC systems. So far, topological solitons of homotopy groups $\pi_1(\mathbb{S}^1)$ (twist walls), $\pi_2(\mathbb{S}^2)$ (baby skyrmions and torons), and $\pi_3(\mathbb{S}^2)$ (hopf solitons) have been realized in chiral nematic systems. However, topological solitons in higher dimensional order parameter spaces such as $\pi_3(\mathbb{S}^3)$ (Shankar skyrmions) have not been experimentally realized in LC systems [3]. Biaxial nematic LCs provide the possibility for realizing such solitons [4]. Active matter or out-of-equilibrium systems can also be a fertile ground for generation and investigation of various kinds of solitons. For instance, in active or out-of-equilibrium passive LC systems, various dynamic disclinations may tangle together to form various topological instantons or dynamic knotted structures. By considering time as the fourth spatial dimension, it is interesting to considering whether topological solitons of the fourth homotopy group can be realized [5]. The recent publication on topological structures in 3D active nematics may provide clues for such experimental investigations [6].

Apart from the fundamental questions listed above, solitons in LCs also provide promising applications in different fields. For instance, recently M. Papic et al. showed that tunable structured light lasers could be realized by using topological solitons in LCs, in which the structure and the topology of the emitted light could be controlled by varying the topology and geometry of the solitons [7]. R. Hamdi showed that the bubble domain composed

of topological solitons in LCs could be used as system of lenses whose focal length can be controlled by tuning the applied electric field [8]. A. J. Hess et al. showed that topological solitons, such as twist walls and skyrmions, could be utilized to steer light beams and serve as optical lenses and other optical elements, which can be facilely controlled by various external stimuli such as electric fields [9]. Z. J. Mai et al. showed that topological solitons, such as heliknotons, could be used as templates for spatial reorganization of nanoparticles [10]. Furthermore, we have also showed that solitons in LCs can be used as vehicle for micro-cargo transport [11-13]. It will be interesting to investigate how various practical applications can be realized by different kinds of LC solitons in future works. The detailed investigation of soliton generation and dynamics in this thesis will hopefully accelerate the growing body of work on LC soliton applications.

9.3 References

1   Chen, X. *et al.* First-principles experimental demonstration of ferroelectricity in a thermotropic nematic liquid crystal: Polar domains and striking electro-optics. *Proceedings of the National Academy of Sciences* **117**, 14021 (2020).

2   Eun, J., Pollard, J., Kim, S.-J., Machon, T. & Jeong, J. Layering transitions and metastable structures of cholesteric liquid crystals in cylindrical confinement. *Proceedings of the National Academy of Sciences* **118**, e2102926118 (2021).

3   Tai, J.-S. B. *Topological Solitons in Chiral Condensed Matters*, University of Colorado at Boulder, (2020).

4   Duda, J. Framework for liquid crystal based particle models. *arXiv preprint arXiv:2108.07896* (2021).

5   Smalyukh, I. I. knots and other new topological effects in liquid crystals and colloids. *Reports on Progress in Physics* **83**, 106601 (2020).

6   Duclos, G. *et al.* Topological structure and dynamics of three-dimensional active nematics. *Science* **367**, 1120-1124 (2020).

7   Papič, M. *et al.* Topological liquid crystal superstructures as structured light lasers. *Proceedings of the National Academy of Sciences* **118**, e2110839118 (2021).

8   Hamdi, R. Bubbles structure & droplet of glycerol forming system of lenses with tunable focal length. *Optics Communications* **505**, 127456 (2022).

9   Hess, A. J., Poy, G., Tai, J.-S. B., Žumer, S. & Smalyukh, I. I. Control of light by topological solitons in soft chiral birefringent media. *Physical Review X* **10**, 031042 (2020).

10   Mai, Z. *et al.* Nematic Order, Plasmonic Switching and Self-Patterning of Colloidal Gold Bipyramids. *Advanced Science* **8**, 2102854 (2021).

11   Shen, Y. & Dierking, I. Dynamics of electrically driven solitons in nematic and cholesteric liquid crystals. *Communications Physics* **3**, 1 (2020).

12   Shen, Y. & Dierking, I. Dynamic dissipative solitons in nematics with positive

anisotropies. *Soft Matter* **16**, 5325 (2020).

13   Shen, Y. & Dierking, I. Electrically Driven Formation and Dynamics of Skyrmionic Solitons in Chiral Nematics. *Physical Review Applied* **15**, 054023 (2021).